UNIVERSIDADE DE LISBOA

INSTITUTO SUPERIOR TÉCNICO

Thermal and structural response of pultruded GFRP profiles under fire exposure

Tiago Miguel Rodrigues Morgado

Supervisor: Doctor João Pedro Ramôa Ribeiro Correia

Co-Supervisors: Doctor Nuno Miguel Rosa Pereira Silvestre

Doctor Fernando António Baptista Branco

Thesis approved in public session to obtain the PhD degree in Civil Engineering

Jury final classification: Pass with Distinction and Honour

2018

UNIVERSIDADE DE LISBOA

INSTITUTO SUPERIOR TÉCNICO

Thermal and structural response of pultruded GFRP profiles under fire exposure

Tiago Miguel Rodrigues Morgado

Supervisor: **Doctor João Pedro Ramôa Ribeiro Correia**
Co-Supervisors: **Doctor Nuno Miguel Rosa Pereira Silvestre**
Doctor Fernando António Baptista Branco

Thesis approved in public session to obtain the PhD degree in Civil Engineering

Jury final classification: Pass with Distinction and Honour

Jury

Chairperson: **Doctor Eduardo Nuno Brito Santos Júlio**, Instituto Superior Técnico, Universidade de Lisboa

Members of the Committee:

Doctor Paulo Jorge de Melo Matias Faria de Vila Real, Universidade de Aveiro
Doctor João Pedro Ramôa Ribeiro Correia, Instituto Superior Técnico, Universidade de Lisboa
Doctor João Paulo Janeiro Gomes Ferreira, Instituto Superior Técnico, Universidade de Lisboa
Doctor José Manuel de Sena Cruz, Escola de Engenharia, Universidade do Minho

Fundings Institutions

Fundação para a Ciência e a Tecnologia (SFRH/BD/94907/2013 e PTDC/ECM/100779/2008)

2018

Abstract

Fibre reinforced polymer (FRP) materials in general and pultruded glass fibre reinforced polymer (GFRP) profiles in particular have great potential for civil engineering applications. When compared with traditional materials, the main advantages of pultruded GFRP profiles are the lightness, strength, good insulation properties, durability in aggressive environments and low maintenance requirements. However, GFRP profiles present some drawbacks, namely the relatively high initial costs, low elastic moduli, lack of design codes and poor fire behaviour. This last aspect is particularly relevant for building applications, where materials and components need to fulfil specific requirements in terms of fire reaction and fire resistance.

With the purpose of investigating the viability of the structural use of pultruded GFRP profiles in the construction industry, namely in buildings, this PhD thesis aimed at obtaining a better understanding of the thermal and structural responses of pultruded GFRP profiles exposed to fire. To achieve this goal, experimental, numerical and analytical studies were carried out, in which the following specific aspects were investigated: (i) mechanical behaviour of pultruded GFRP material at elevated temperature, in particular under compression and shear; (ii) thermal and mechanical response of pultruded GFRP profiles subjected to different types of fire exposure and comprising different fire protection systems; and (iii) numerical and analytical models to simulate the fire behaviour of GFRP structural elements.

In a first stage, experimental and analytical studies were carried out in order to characterize the compressive and shear behaviour of pultruded GFRP material at elevated temperatures (~20-180 ºC). The results obtained from these material characterization tests showed that (i) compressive strength is severely affected by temperature increase, with a reduction of 87% at 180 ºC; (ii) shear strength (from Iosipescu tests) is noticeably reduced at elevated temperature, with significant reductions (~36%) already at moderately elevated temperature (60 ºC) and a reductions of 88% at 180 ºC; and (iii) shear modulus is also significantly affected by elevated temperature, with reductions of 30% at 60 ºC and 80% at 140 ºC.

In a second stage, fire resistance tests were performed on pultruded GFRP beams and columns. The experimental results obtained confirmed the effectiveness of some fire protection systems in delaying the temperature increase of GFRP profiles and, consequently, in improving their fire resistance. As an example, for one-side fire exposure, the fire resistance of beams was increased from 36 min (unprotected) to 83 min (with passive fire protection) and 120 min (with active fire protection); the fire endurance of columns was increased from 16 min (unprotected) to 51 min (with passive fire protection) and 120 min (with active fire protection). The experimental results also showed that the number of sides exposed to fire affects severely the fire resistance behaviour of GFRP profiles. For three-side fire exposure, the fire resistance of the unprotected beams and columns was remarkably reduced (about 80% and 50%, respectively). In this case, passive fire protection was clearly more effective than active protection. Regarding the effect of load level on the fire performance of GFRP structural members, while the fire endurance of beams was moderately reduced (~15%), the fire resistance of columns was significantly affected

(~45%) by the load level increase. Failure of GFRP members was associated to approaching and/or exceeding the glass transition temperature of the material in parts under compression (axial or transverse) and/or shear. Accordingly, the GFRP columns proved to be much more susceptible to fire than GFRP beams subjected to the same type of fire exposure; this was attributed to the fact the residual strength in tension at elevated temperature is much higher than that in compression.

Aiming at simulating the thermal response of GFRP tubular profiles exposed to elevated temperatures, two- and three-dimensional finite volume models were developed, in which the entire cross-section was considered. The results obtained from this thermal analysis were in agreement with the experimental ones and highlighted the importance of considering conduction, internal radiation and convection inside the tubular section in this heat transfer problem. Three-dimensional finite element (FE) models were also developed to simulate the mechanical behaviour of the GFRP beams and columns, in which different curves were considered for the degradation of the compressive, tensile and shear properties with temperature. This numerical investigation provided interesting insights about the most relevant *kinematic* (longitudinal and transversal deformations) and *static* (stresses and failure initiation) issues of the structural response of GFRP members. Although the numerical models did not take into account the material progressive failure, the mechanical behaviour of GFRP beams was simulated with reasonable accuracy by the numerical models. On the other hand, the numerical models were less accurate in simulating the mechanical response of GFRP columns exposed to fire – although providing a fair agreement with the overall qualitative response of the columns, the calculated axial deformation rates were lower than measured and this should be related, among other effects, to the non-consideration of creep. Despite not considering the effects of delamination, the models were able to capture the main features of the failure modes. In addition to the FE models, analytical models based on beam theory were also developed to simulate the mechanical response of GFRP beams exposed to fire; in spite of the simplifying assumptions made, the results provided by these models were in close agreement with those obtained from the numerical and experimental studies.

Keywords: Glass fibre reinforced polymer (GFRP); pultruded GFRP profiles; fire behaviour; GFRP beams and columns; fire protection systems; thermal and mechanical responses; experimental tests; numerical and analytical studies.

Resumo

Os polímeros reforçados com fibras (FRP – *Fiber Reinforcer Polymer*), em particular os perfis pultrudidos de fibras de vidro (GFRP – *Glass Fibre Reinforced Polymer*), têm um grande potencial de aplicação na área de engenharia civil. Quando comparados com os materiais tradicionais (aço e betão armado), os perfis pultrudidos de GFRP apresentam reduzido peso próprio, elevada resistência, boas propriedades de isolamento, durabilidade em ambientes agressivos e reduzidos custos de manutenção. Contudo, os perfis de GFRP apresentam algumas desvantagens, nomeadamente custos iniciais relativamente elevados, reduzido módulo elástico, inexistência de regulamentação específica e deficiente comportamento ao fogo. Este último aspeto é particularmente relevante para a sua aplicação em edifícios, onde os materiais utilizados devem cumprir requisitos mínimos de reação e resistência ao fogo.

Com o intuito de estudar a viabilidade da utilização de perfis pultrudidos de GFRP na indústria da construção, especialmente em edifícios, nesta tese de doutoramento pretende-se avaliar as respostas térmicas e mecânicas dos referidos perfis quando expostos a uma situação de incêndio. Para tal, foram desenvolvidos estudos experimentais, numéricos e analíticos para investigar os seguintes aspetos: (i) comportamento mecânico do material pultrudido GFRP a temperaturas elevadas, em particular em compressão e em corte; (ii) respostas térmicas e mecânicas de perfis pultrudidos de GFRP quando sujeitos a diferentes tipos de exposição ao fogo, testando diferentes sistemas de proteção contra o fogo (passivos e ativos); e (iii) modelos numéricos e analíticos para simular o comportamento ao fogo de elementos estruturais em GFRP.

Numa primeira fase, foi realizado um estudo experimental para caracterizar o comportamento à compressão e ao corte do material GFRP quando exposto a temperaturas elevadas (~20-180 ºC), o qual foi complementado com o desenvolvimento de modelos analíticos. Os resultados obtidos nestes ensaios de caracterização mostraram que (i) a resistência à compressão é severamente afetada pelo aumento da temperatura – redução de 87% a 180 ºC; (ii) a resistência ao corte (determinada através de ensaios de Iosipescu) é também muito afetada com o aumento da temperatura – reduções de 36% e 88% para temperaturas de 60 ºC e 180 ºC, respetivamente; (iii) o módulo de distorção é também expressivamente afetado pelo aumento da temperatura – reduções de 30% e 80% para temperaturas de 60 ºC e 140 ºC, respetivamente.

Numa segunda fase, foram realizados ensaios de resistência ao fogo em perfis pultrudidos de GFRP – vigas e colunas. Os resultados obtidos confirmaram a eficácia de alguns sistemas de proteção contra o fogo em retardar o aumento da temperatura nos perfis de GFRP e, consequentemente, em melhorar o seu desempenho mecânico em situação de incêndio. Como exemplo, para a exposição ao fogo a uma face, as resistências ao fogo das vigas foram aumentadas de 36 min (não protegida) para 83 min e 120 min (com proteções passiva e ativa, respetivamente); as resistências ao fogo das colunas foram aumentadas de 16 min (não protegida) para 51 min e 120 min (com proteções passiva e ativa, respetivamente). Os resultados experimentais obtidos mostraram ainda que o número de faces expostas ao fogo afeta severamente o comportamento ao fogo dos perfis de GFRP. Para a exposição ao fogo a três

faces, as resistências ao fogo das vigas e colunas não protegidas foram drasticamente reduzidas (~80% e ~50%, respetivamente). Neste caso, o sistema de proteção passivo usado foi claramente mais eficiente que o ativo. No que diz respeito ao efeito do nível de carga no comportamento mecânico dos perfis de GFRP, enquanto a resistência ao fogo das vigas foi moderadamente reduzida (~15%), os tempos de resistência ao fogo das colunas foram significativamente afetados (~45%) pelo aumento no nível de carga aplicado. Tendo em conta os resultados obtidos, a rotura dos perfis de GFRP ocorreu quando as partes à compressão (axial ou transversal) e/ou ao corte atingiram e/ou excederam a temperatura de transição vítrea do material (~60-140 ºC). Os resultados experimentais mostraram ainda que a resistência ao fogo das colunas de GFRP é consideravelmente mais afetada (reduzida) pela exposição ao fogo do que as vigas de GFRP. Tal observação é consistente com o facto deste material ser mais suscetível à compressão do que à tração quando exposto a temperaturas elevadas.

Com o objetivo de simular a resposta térmica dos perfis de GFRP quando expostos a temperaturas elevadas, foram desenvolvidos modelos numéricos bidimensionais e tridimensionais com volumes finitos, nos quais foi modelada toda a secção transversal do perfil tubular. Os resultados obtidos nesta simulação térmica foram concordantes com os medidos experimentalmente e demonstraram ainda a importância de considerar as trocas de calor por condução, radiação e convecção no interior da cavidade neste tipo de análise. Com base na referida simulação térmica, foram desenvolvidos modelos numéricos tridimensionais com elementos finitos para simular o comportamento mecânico de vigas e colunas de GFRP expostas ao fogo, considerando diferentes curvas de degradação das propriedades mecânicas à compressão, tração e corte com a temperatura. Este estudo numérico permitiu retirar importantes ilações acerca de alguns aspetos cinemáticos (deformação longitudinal e transversal) e estáticos (tensões e iniciação da rotura) relevantes no que diz respeito à resposta estrutural de elementos em GFRP. Embora os modelos não tenham tido em conta o dano progressivo no material, o comportamento mecânico das vigas de GFRP foi modelado com razoável precisão pelos modelos numéricos. Por sua vez, os modelos numéricos foram menos precisos na modelação da resposta mecânica das colunas de GFRP – embora as respostas mecânicas obtidas numericamente tenham sido consistentes com as experimentais em termos qualitativos, as taxas de deformação axial calculadas foram inferiores às medidas experimentalmente, o que poderá estar relacionado, entre outros efeitos, com a não consideração da fluência. Apesar de também não ter sido considerado o efeito da delaminação no material, os modelos permitiram identificar e confirmar os modos de rotura experimentais. Para além dos modelos numéricos descritos, foram também desenvolvidos modelos analíticos para simular a resposta mecânica de vigas de GFRP expostas ao fogo, os quais foram baseados na teoria de vigas. Apesar das várias simplificações consideradas nestes modelos, os resultados analíticos obtidos foram concordantes com os obtidos nos estudos experimental e numérico.

Palavras-chave: Polímero reforçado com fibras de vidro (GFRP); perfis pultrudidos de GFRP; comportamento ao fogo; vigas e colunas de GFRP; sistemas de proteção contra o fogo; respostas térmica e mecânica; ensaios experimentais; estudos numérico e analítico.

Acknowledgements

The writing of this PhD thesis corresponds to the end of a long and difficult journey in my life, in which several obstacles were overcome. Here, I would like to address the next paragraphs to the people who directly or indirectly supported me during the last five years. This PhD thesis belongs to all of them.

Firstly, I would like to thank my scientific supervisors, Prof. João Ramôa Correia and Prof. Nuno Silvestre, for their tireless support, constant availability, wise advise, patience, friendship and encouragement during the past years. In fact, these two persons were, without any doubt, the main reason why I decided to do this PhD research. Also, I would like thank Prof. Fernando Branco, who has accompanied me since my MSc dissertation, for his support and helpful suggestions.

I would also like to thank the help, suggestions and friendship of all my colleagues at *Instituto Superior Técnico* (IST), particularly to Francisco Nunes, João Firmo, Mário Garrido, Mário Arruda, Cristina López, Augusto Moreira, Inês Rosa, João Sousa, Luís Valarinho, André Castelo and Lourenço Fernandes.

This PhD thesis was funded by the *Portuguese National Science Foundation* through a doctoral scholarship (SFRH/BD/94907/2013) and the FIRE-FRP (PTDC/ECM/100779/2008) and FIRE-COMPOSITE (PTDC/ECM-EST/1882/2014) projects, which financially supported this investigation.

I am also grateful to IST personnel at CERIS, DECivil, LERM and LC, namely Fernando Alves, Maria Helena Salvado, Fernando Costa, Leonel Silva and Elaine Gregório, for their help on solving administrative problems and their assistance in experimental work.

The support of Prof. Carlos Tiago, Prof. Pedro Coelho and PhD student Mahendra Paipuri was also valuable, in particular for the analysis of results and the development of numerical models.

To my best friends, Carlos Cunha, Fábio Alcário, Jorge Cruz, Luís Gonçalves, Olivier Passos, Tânia Calado and Zita Marinho, I would like to express my gratitude for their constant support, encouragement and the good moments spent outside the work.

My deepest gratitude goes to my family, Lurdes, António, Ana and Carolina. During these last years, their unconditional support and love were absolutely crucial. I am very grateful for their understanding in some periods of my PhD thesis, especially my parents and sister. To my wife Carolina, I would like to sincerely thank her support, friendship, encouragement on the critical moments, and love.

To my dear grandmother, who made me who I am.

Contents

List of figures

List of tables

Part I:

Introduction

Chapter 1:

Introduction

1.1. Context

The durability problems associated with traditional construction materials, namely reinforced concrete, steel and timber, have been promoting the study of innovative structural materials/solutions. On the other hand, the development of civil engineering has been intimately connected to the innovation in structural materials. In this context, fibre reinforced polymer (FRP) composites are promising materials, since they present several advantages over traditional materials. Although composite materials have been currently used in the construction industry during the past few decades, many issues about their behaviour for civil engineering applications still require further investigations.

FRP composites are basically constituted by a fibrous reinforcement (such as glass, carbon or aramid) embedded in a polymeric resin (most often made of polyester, epoxy or vinylester). While the first component provides the elastic and strength properties, the second one is responsible for keeping the fibres in place, in particular when the composite material is compressed, and for distributing the stresses uniformly in the material [1, 2].

Among FRP composites, pultruded glass fibre reinforced polymer (GFRP) profiles have considerable potential for civil engineering applications owing to their lightness, strength, good insulation properties, durability in aggressive environments and low maintenance requirements. Nevertheless, in addition to relatively high initial costs, low elastic moduli, brittle failure and lack of design codes, the widespread acceptance of GFRP profiles is being delayed due to concerns about their fire behaviour [3]. These concerns are relevant for various applications, especially for buildings, where materials and components need to fulfil certain requirements in terms of fire reaction and fire resistance performance.

The above-mentioned concerns are well founded. In fact, the mechanical performance of GFRP materials decreases significantly when exposed to high temperatures, especially due to the glass transition and thermal decomposition of the polymeric matrix. When exposed to moderate temperatures (~60-140 ºC), due to the glass transition of the polymer matrix, the GFRP material softens, creeps and distorts, thus presenting a severe reduction of its mechanical properties (strength and stiffness) [4]. For elevated temperatures (~300-500 ºC), the organic matrix of GFRP decomposes, releasing heat, soot and toxic volatiles [5]. Therefore, it is of paramount importance to know the influence of high temperatures on the behaviour of FRP structures, as well as the circumstances under which these materials can be safely used in building applications.

Although during the last decades some studies have been reported in the literature about the fire behaviour of pultruded GFRP profiles, further experimental and numerical investigations are needed to fully understand this relevant and complex problem. As an example, there are still several topics that are not adequately covered by the technical and scientific literature, namely (i) the characterization of the mechanical behaviour in shear and compression (in particular, the shear and compressive moduli) at elevated temperature; (ii) the variation of the thermal expansion coefficient with temperature; and (iii) the creep behaviour at elevated temperatures for different levels and types of mechanical loads (compression, shear and tensile). Moreover, the accurate prediction of the thermal and mechanical behaviour of pultruded GFRP profiles subjected to fire still remains a considerable challenge, as it involves quite demanding heat transfer and physically and geometrically nonlinear structural analyses. Comprehensive and accurate simulation tools are also not available currently.

1.2. Motivation and objectives

Presently, the knowledge about the thermo-physical and thermo-mechanical properties of GFRP material at elevated temperatures is still scarce [6]. In fact, such complexity stems, partly, from the anisotropic and temperature-dependent material properties of GFRP, most of which are still to be characterised, and the consequent complexity of the thermal and structural responses of GFRP structures in fire. Consequently, several issues are still not well understood and further studies are required at the material scale level.

At the structural scale, previous experiments about the fire response of pultruded GFRP slabs are very few. In 1994, the first large scale fire resistance test on a pultruded GFRP member was performed, in which a multicellular slab was subjected to a service load and to fire exposure from the bottom [7]. Then, in 2006, similar experiments were performed on multicellular panels [8]. In this last work, a water-cooling system was tested, which provided a significant thermal protection to the slab and considerable extension of its fire resistance.

In what concerns the fire behaviour of GFRP beams, only two experimental studies were reported in the literature, for very specific conditions. Fire resistance tests were first performed on I-section GFRP beams under four-side fire exposure and a constant load [9]. This study, in which two passive fire protection systems were tested, showed the high sensitivity of GFRP profiles to four-side fire exposure. Then, an experimental campaign about the fire behaviour of GFRP tubular beams subjected to a service load and one-side fire exposure was investigated;

this study assessed the efficacy of different active and passive fire protection systems, which were concluded to have significant potential for this specific type of fire exposure [10].

Regarding the fire behaviour of GFRP columns, the above mentioned water-cooling concept [8] was applied to full-scale pultruded GFRP columns with multicellular section, also subjected to a constant load level and exposed to fire in one-side [11]. As for the slabs, the water-cooling system was found to improve considerably the fire resistance of the columns. At a structural level, this was the only work found in the literature on columns.

The experimental work developed in this thesis addresses the fire behaviour of pultruded GFRP profiles (beams and columns) with tubular section, pursuing the author's M.Sc. dissertation [12]. The main objectives of the present study were to understand in further depth the thermal and mechanical responses of pultruded GFRP profiles subjected to fire, evaluating the influence on their fire resistance of (i) the number of sides exposed to fire, (ii) the applied load level, and (iii) using different fire protection systems. To this end, GFRP beams and columns were exposed to the time-temperature curve defined in ISO 834 [13], in either one or three sides, and simultaneously subjected to two different load levels. Although the experiments previously conducted in [9] suggest that three-side fire exposure may be much more severe compared to one-side exposure, no results are reported in the literature concerning the effect of exposing GFRP profiles (beams or columns) to fire in three-sides. Additionally, the influence of testing different load levels in the fire resistance of GFRP members has also not been reported in the literature.

The simulation of the fire behaviour of pultruded GFRP elements requires the development of thermo-mechanical models to predict their thermal and mechanical responses. In this context, a first effort comprised the development of a one-dimensional (1D) heat transfer model to estimate the evolution of temperatures in pultruded GFRP multicellular deck panels [14]. A similar 1D numerical approach, inherently quite simplistic, was used to simulate the thermal response of GFRP tubular beams exposed to fire in one-side, unprotected and protected with passive and active fire protection systems [15]. In both studies, only the bottom flange of the cross-sections was explicitly modelled. Fire resistance tests on GFRP multicellular decks (reported in [8]) were also modelled considering a two-dimensional (2D) thermal analysis [16], in which only part of the cross-section was modelled. In all these simulations, only conduction through the solid material was modelled in the heat transfer process - the air inside the cells was not taken into account, nor the radiation between the inner surfaces of the section cavities.

In a more recent work, a model to simulate the thermal response of pultruded GFRP tubular profiles exposed to fire was developed [17]. With that purpose, a 2D finite element code was developed and implemented in MATLAB. In this case, the whole cross-section was considered as well as the air inside the tubular profile by means of computational fluid dynamics. The numerical results obtained showed that it is very important to consider the radiative heat exchanges between the inner faces of the section cavity, as well as the natural convection of the air enclosed in the section. However, since the computational code developed was very time consuming, only a limited number of cases/scenarios could be successfully simulated. In this thesis, further numerical investigations about the thermal response of pultruded GFRP profiles exposed to fire were carried out. Aiming at overcoming some of the referred limitations, numerical models of the thermal response of GFRP profiles were developed using the commercial software *ANSYS Fluent 14.5* [18].

Regarding the simulation of the mechanical response of GFRP slabs and beams at elevated temperatures, only a few works concerning civil engineering applications were found in the literature. In this context, two thermo-mechanical models of GFRP slabs were developed. In the first study, three-dimensional (3D) numerical models were developed in order to determine the evolution with time of fire exposure of mid-span deflection and axial stresses; the effect of thermal expansion coefficient in the slabs' mechanical response was also evaluated [16]. In the second study, an analytical approach based on beam theory was used to investigate the fire behaviour of GFRP slabs [19]. In this case, the influence on the mid-span deflection increase of three different effects was assessed: (i) the degradation in material stiffness, (ii) thermal expansion, and (iii) the creep behaviour of the GFRP material. Later, the same analytical approach was used to estimate the evolution with time of mid-span deflection of GFRP beams exposed to fire [15]; such analytical study did not consider thermal expansion effects nor creep deformations.

In all the above-mentioned studies, the numerical/analytical models were not able to reproduce accurately the thermo-mechanical behaviour of the slabs/beams, due to the limitations of the thermal model (only part of the cross-section was considered) and the consideration of the same thermal degradation curve for compressive and tensile moduli. Despite the previous efforts in simulating the fire behaviour of pultruded GFRP beams and slabs, the referred works present some limitations and, consequently, more numerical investigations are needed in order to fully understand the fire behaviour of GFRP members. In this context, the stress analysis of GFRP members at elevated temperatures and the development of failure prediction models that consider material progressive damage require further studies.

In spite of the particular susceptibility of GFRP material to compressive loads at elevated temperature, a very limited number of works were reported in the literature about the simulation of the mechanical response of pultruded GFRP columns exposed to fire. At the material level, two studies were performed: (i) an investigation about the mechanical response of GFRP laminates loaded (in compression) and exposed to elevated temperatures, using laminate theory [20]; and (ii) numerical and analytical studies using laminate theory and finite element models, aiming at estimating the ply strains and stresses of GFRP laminates subjected to compression and elevated temperatures [21]. At the structural level, a single numerical study about the compressive behaviour of pultruded GFRP columns at elevated temperatures was developed [22]; analytical models were also used to predict the mechanical response of multicellular columns exposed to fire [11]. It is worth mentioning that in the majority of the above mentioned works (with the exception of the last one), the GFRP material was not exposed to fire, only to elevated temperatures (below the decomposition temperature). In this context, another goal of the present thesis was to develop further numerical models able to accurately simulate the mechanical response of pultruded GFRP profiles – either slabs, beams or columns - exposed to fire.

In summary, the main objective of this PhD thesis was to investigate the viability of the structural use of pultruded GFRP profiles in civil engineering applications, in particular, in buildings. To that end, the following specific goals were set: to understand in further depth (i) the mechanical behaviour of pultruded GFRP material subjected to compression and shear at elevated temperature, as well as (ii) the thermal and mechanical responses in fire of pultruded GFRP beams and columns, under different fire scenarios and using different fire protection systems; and (iii) to develop numerical and analytical models able to simulate the structural performance of GFRP members exposed to fire.

1.3. Methodology

In order to fulfil the above-mentioned goals, the methodology pursued in this thesis involved experimental, numerical and analytical investigations.

The experimental programme was developed in two stages and at two different scales. In a first stage, several tests were carried out in small-scale coupons in order to determine (i) the thermo-physical properties of GFRP and fire protection materials (dynamic mechanical analysis, DMA, and differential scanning calorimetry and thermogravimetric analysis, DSC/TGA); and (ii) the mechanical response in shear and compression of pultruded GFRP material at elevated temperature, namely from room temperature up to 180 ºC.

In a second stage, fire resistance tests were performed in GFRP beams and columns in order to obtain comprehensive and significant experimental data about their thermal and mechanical responses, fire resistance and failure modes. The effects of (i) applying different fire protection systems, (ii) exposing the GFRP profiles to fire in either one or three sides, and (iii) varying the service load level were evaluated. Different materials were used as passive fire protection, namely rock wool (RW), calcium silicate (CS) and agglomerated cork (AC) boards, intumescent mat (IM) and intumescent coating (IC). Additionally, different water-cooling fire protection systems were tested, with either flowing or stagnant water. This stage of the experimental programme involved a total of 22 tests, 12 in GFRP beams and 10 in GFRP columns.

Alongside the experimental study, numerical and analytical models of the thermal and structural responses of pultruded GFRP beams and columns were developed and later validated using the experimental data previously obtained. Firstly, two- and three-dimensional finite volume numerical models were developed in *ANSYS Fluent* commercial code to simulate the thermal response of GFRP profiles exposed to fire. In this thermal analysis, the whole cross-section was modelled and the heat exchanges by means of conduction, internal radiation and convection of the air inside the cavity of the GFRP tubular profiles were considered.

Then, three-dimensional finite element models were developed in *ABAQUS Standard* commercial code to simulate the mechanical response of GFRP beams and columns, previously investigated in the fire resistance tests. These numerical models used as input the temperature distributions obtained from the thermal models; considered different thermal degradation curves for compressive, tensile and shear behaviour; took into account thermal expansion effects; and included a failure initiation criterion. This numerical study comprised the investigation of the thermal (temperature distribution) and mechanical (out-of-plane/axial deformations) responses of GFRP profiles, including a stress analysis in both transversal and longitudinal directions. This numerical investigation included also a comprehensive study on the failure behaviour of GFRP beams and columns, in which both Tsai-Hill and Hashin damage initiation criteria were considered. A preliminary investigation on damage propagation was also performed for a particular case (a reference unprotected GFRP column).

Complementing numerical study, analytical models were developed to simulate the mechanical response of GFRP beams exposed to fire, based on beam theory. In these models, flexural, shear and thermal deformation contributions to the overall deflection were estimated. Results of these simpler models were assessed through comparison with both experiments and numerical models.

1.4. Main scientific contributions

This research was funded by the Fundação para a Ciência e a Tecnologia (FCT, Portuguese National Science Foundation) through a doctoral scholarship (SFRH/BD/94907/2013) and the FIRE-FRP (PTDC/ECM/100779/2008) and FIRE-COMPOSITE (PTDC/ECM-EST/1882/2014) FCT-funded projects.

The work developed in the framework of the present thesis provided further knowledge about the mechanical behaviour at elevated temperature of pultruded GFRP material, namely under compressive and shear loads, and about the structural behaviour of pultruded GFRP beams and columns exposed to fire. The experimental and numerical investigations performed in this thesis delivered comprehensive and significant test data and reliable simulation tools, which together provide a deeper understanding about the behaviour of GFRP pultruded structures under elevated temperature and fire exposure. In this section, the main scientific contributions are highlighted.

In the first stage of the test programme, experimental and analytical investigations were performed to characterize the compressive and shear behaviour of pultruded GFRP material from room temperature up to 180 ºC. The compressive tests allowed determining the evolution with temperature of compressive strength, for which relatively few data was available. On the other hand, the shear tests allowed evaluating the variation of shear strength and modulus with temperature. In this last study, the thermal degradation of shear strength (determined based on Iosipescu tests) was compared to other results reported in the literature (obtained from 10º off-axis tensile tests); and the evolution of shear modulus with temperature was assessed, and this specific property (quite relevant to assess the overall deformations of members in bending) was not yet available in the literature. The study about the shear response of pultruded GFRP material at elevated temperatures resulted in the following publication:

1. I. Rosa, T. Morgado, J.R. Correia, J. Firmo, N. Silvestre, Shear behaviour of FRP composite materials at elevated temperature, *Journal of Composites for Construction* 22(3), 2008.

The fire resistance tests on pultruded beams confirmed the effectiveness of fire protections systems in delaying the heating of the GFRP material and, consequently, in increasing significantly the fire resistance of GFRP beams. The tests allowed to assess and quantify the influence of the number of sides exposed to fire on the fire resistance behaviour, namely through the direct comparison between three-side exposure and one-side fire exposure. Likewise, it was also possible to determine the influence of increasing the service load level on the fire resistance of GFRP beams, due to the temperature-dependency of GFRP strength. This particular work resulted in the following publication:

2. T. Morgado, J.R. Correia, N. Silvestre, F.A. Branco, Experimental study on the fire resistance of GFRP pultruded tubular beams, *Composites Part B: Engineering*, 139, 106-116, 2018.

The fire resistance tests on pultruded GFRP columns also provided significant results. First of all, it was possible to compare the fire behaviour of GFRP columns to "equivalent" GFRP beams, *i.e.* for similar types of exposure and protection. As for the beams, the fire resistance tests also allowed to investigate the effectiveness of different passive and active fire protection systems in providing thermal insulation to GFRP columns and extending their fire endurance. These experiments also enabled assessing the influence of the number of sides exposed to fire (either one or three) and of the service load level in the fire resistance behaviour of GFRP columns. The fire resistance tests performed on columns resulted in the following publication:

3. T. Morgado, J.R. Correia, A. Moreira, F.A. Branco, C. Tiago, Experimental study on the fire resistance of GFRP pultruded tubular columns, *Composites Part B: Engineering*, 69, 201-211, 2015.

With the purpose of simulating the thermal response of GFRP tubular profiles exposed to fire, two- and three-dimensional models were developed using a commercial software based on the finite volume method. In these models, the whole cross-section and the air inside the tubular profiles were modelled. Various cases tested in the experimental programme were simulated. The numerical results confirmed that the consideration of the heat exchanges due to internal radiation and convection not only influences considerably the thermal responses of the GFRP profiles, but also provides more accurate temperature predictions. This numerical study resulted in the following publication:

4. T. Morgado, N. Silvestre, J.R. Correia, F.A. Branco, T. Keller, Numerical modelling of the thermal response of pultruded GFRP tubular profiles subjected to fire, *Composites Part B: Engineering*, 137, 202-216, 2018.

In this thesis, three-dimensional finite element models were developed to simulate the fire resistance tests previously conducted on GFRP beams, in which different degradation curves were considered for compressive, tensile and shear moduli, based on experimental data. This numerical study was divided in two parts. The first part presented the numerical models and focused on the most relevant *kinematic* issues (deflections), while the second part presented the numerical results associated to the *static* issues (stresses and failure initiation). The results obtained provided a deeper understanding of the mechanical response in fire of pultruded GFRP beams. This numerical study resulted in the following two publications:

5. T. Morgado, N. Silvestre, J.R. Correia, Simulation of fire resistance behaviour of pultruded GFRP beams - Part I: Models description and kinematic issues, *Composite Structures*, 187, 269-280, 2018.

6. T. Morgado, N. Silvestre, J.R. Correia, Simulation of fire resistance behaviour of pultruded GFRP beams - Part II: Stress analysis and failure criteria, *Composite Structures*, 188, 519-530, 2018.

Aiming at simulating the mechanical response of pultruded GFRP columns exposed to fire, three-dimensional finite element models were also developed. The main objectives of this numerical study were to (i) investigate the most relevant *kinematic* issues (axial and transversal deformations of columns exposed to fire); (ii) present and discuss some important *static* issues (evolution stresses); and (iii) identify the zones in which failure initiation is first reached, as determined through the Tsai-Hill index. A preliminary assessment of a failure propagation criterion was also performed. This work resulted in the following publication:

7. T. Morgado, N. Silvestre, J.R. Correia, Simulation of fire resistance behaviour of pultruded GFRP columns, *Thin-Walled Structures* (submitted for publication).

In addition to the above-mentioned publications, the work developed in the framework of this thesis resulted also in the following publications:

8. T. Morgado, J.R. Correia, F.A. Branco, F. Nunes, C. López, C. Tiago, Fire behaviour of pultruded GFRP beams (in Portuguese), *Revista Internacional Construlink*, 32(11), 4-17, 2013.
9. T. Morgado, J.R. Correia, A. Moreira, F.A. Branco, C. Tiago, C. López, Fire resistance behaviour of GFRP pultruded tubular columns. Experimental study, in *7th International Conference on FRP Composites in Civil Engineering (CICE 2014)*, Vancouver, Canada, 2014.
10. T. Morgado, J.R. Correia, F.A. Branco, Fire behaviour of pultruded GFRP columns. Experimental study (in Portuguese), in *4as Jornadas de Segurança contra Incêndios Urbanos*, Instituto Politécnico de Bragança, Portugal, 2014.
11. T. Morgado, J.R. Correia, N. Silvestre, F.A. Branco, Fire resistance behaviour of pultruded GFRP profiles for rehabilitation applications: Experimental, numerical and analytical studies (in Portuguese), in *CONPAT 2015*, Lisboa, Portugal, 2015.
12. T. Morgado, N. Silvestre, J.R. Correia, F.A. Branco, Simulation of thermal response of pultruded GFRP profiles exposed to fire (in Portuguese), in *5as Jornadas de Segurança contra Incêndios Urbanos*, LNEC, Lisboa, Portugal, 2016.
13. T. Morgado, J.R. Correia, N. Silvestre, F.A. Branco, Fire resistance of pultruded glass fibre reinforced polymer (GFRP) profiles for rehabilitation applications: Experimental, numerical and analytical studies (in Portuguese), *Revista Alconpat*, 6(2), 74-84, 2016.

1.5. Thesis outline

The present document is organized in nine chapters, which were grouped into four parts:

- Part I: Introduction (chapters 1 and 2);
- Part II: Experimental study (chapters 3, 4 and 5);
- Part III: Numerical and analytical studies (chapters 6, 7 and 8);
- Part IV: Conclusions and future developments (chapter 9).

The first and present chapter introduces the thesis subject, describing its context, motivation, objectives, methodology and the main scientific contributions.

Chapter 2 presents a brief overview concerning pultruded GFRP members, addressing their constituent materials, manufacturing process, structural shapes, physical and mechanical properties, type of connections and main applications in civil engineering. The combustion process and the development of a fire are also briefly introduced. The final part of this chapter addresses the fire behaviour of GFRP materials and structures, and the main research needs in this field.

Chapter 3 refers to the experimental characterization of GFRP material at elevated temperatures. In the first part of this chapter, results obtained from dynamic mechanical analysis (DMA) and differential scanning calorimetry and thermogravimetric experiments (DSC/TGA) are presented. Next, the experimental campaign performed to evaluate the compressive and shear behaviour at elevated temperatures is presented. This experimental characterization allowed complementing the information about the thermal and thermo-mechanical properties of GFRP and fire protection materials.

Chapters 4 and 5 present the results of the experimental research on the fire behaviour of pultruded GFRP beams and columns, respectively. These chapters report the main findings of the experiments about the influence on the fire resistance of GFRP profiles of (i) the number of sides exposed to fire; (ii) the load level; and (iii) using different active and passive fire protection systems. For each type of pultruded GFRP member – beams and columns – the corresponding chapter presents and discusses the thermal and mechanical responses, the failure modes and the fire resistance.

Chapter 6 presents the numerical study about the thermal response of pultruded GFRP tubular profiles exposed to fire. In this chapter, the two- and three-dimensional numerical models developed are described and the numerical temperatures are compared with the experimental data measured in the fire resistance tests presented in the preceding chapters.

Chapters 7 and 8 concern the numerical investigation on the fire resistance behaviour of GFRP beams and columns, respectively. In these chapters, the most relevant *kinematic* issues (axial and/or transversal deformations) are compared with the experimental ones; some important *static* issues (stresses) are presented and discussed; and fire resistances and failure modes are investigated using failure initiation criteria and a damage propagation model (only for a single case of columns).

Chapter 9 presents the main conclusions that can be drawn from the experimental, numerical and analytical investigations performed in this thesis, and provides recommendations for future developments.

Chapter 2:

Pultruded GFRP profiles in civil engineering and fire

2.1. Introduction

Although the concept of composite materials is old (known since the Antiquity), the use of fibre reinforcements in a polymeric matrix is relatively recent, having been enabled by the development of the plastic industry at the beginning of 20^{th} century [23]. The first known application of fibre reinforced polymer (FRP) materials was in the reinforcement of the hull of a boat (in the 1930's), in the context of an experimental project [1]. The first application of FRP composite materials in civil engineering dates back to the 1950's and 1960's, when some prototype houses (with one or two floors) were built [24].

Today, FRP materials are being increasingly used in civil engineering applications as a result of their advantageous properties compared to traditional materials. Pultruded glass fibre reinforced polymer (GFRP) profiles in particular are being more often used as structural elements [3, 25, 26], as a result of their main advantages over traditional solutions (such as steel, aluminium and timber) – *e.g.* low self-weight, high strength, electromagnetic transparency and low maintenance costs.

Similarly to other materials, GFRP profiles also present some drawbacks, namely the relatively high deformability and susceptibility to instability phenomena, the brittle behaviour, the lack of design codes, the relatively high initial costs and the poor fire behaviour.

The lack of design guidelines partly stems from the present limited understanding of some aspects concerned with pultruded GFRP profiles, namely their connection technology [27], fire behaviour [6], creep behaviour [28-30], durability [31, 32], economic and environmental sustainability [2]. The present thesis addresses one of the referred issues – the fire behaviour of pultruded GFRP profiles.

In this chapter, general aspects concerning the structural use of FRP composites in civil engineering are first briefly outlined, namely the constituent materials, the manufacturing processes, the structural shapes, the main properties, the connection technology and typical applications. Next, a brief summary about the fire behaviour of GFRP materials and structures is provided. The final part of the chapter highlights the main research needs in this field.

2.2. Composite materials and structures

2.2.1. Constituent materials

FRP composite materials are basically constituted by alternating layers of fibre reinforcement embedded in a polymeric matrix. The main role of the reinforcing fibres is to provide strength and stiffness along their direction, while the polymeric matrix provides support to the fibres maintaining them in position, distributing stresses uniformly across the composite material and protecting the fibres from environmental agents. In addition to the resin, the polymeric matrix often incorporates fillers and additives to improve the manufacturing process, to achieve specific properties (*e.g.* colour, fire reaction) or to reduce costs [25].

Presently, the fibre reinforcement most widely used in composite structures is made of glass (glass fibre reinforced polymer – GFRP). However, in some cases, other types of fibre reinforcement, such as carbon and aramid fibres, may also be used.

In civil engineering, E-glass (electric glass) fibres are the most often used reinforcement for the production of pultruded GFRP profiles. Although S-glass (structural glass) fibres present higher performance (compared to E-glass), they are not often used in the construction industry due to economic reasons, being mainly used in aerospace applications. Comparing to the other types of fibres, glass fibres are the most economical available in the market [25]. Carbon fibres, used in carbon fibre reinforced polymer (CFRP) strips, sheets and pre-stress tendons, present high tensile strength, high fatigue and creep resistance and chemical resistance [1, 33]. However, this type of fibre reinforcement is much more expensive (than glass) and requires a large amount of energy in the manufacturing process [34]. The main physical, mechanical and thermal properties of E-glass and carbon fibres are presented in Table 1.

Table 1: Typical properties of the most common types fibre reinforcements (adapted from [25, 34]).

Property	E-glass	Carbon
Tensile strength [MPa][(i)]	2350 to 4600	2600 to 3600
Elastic modulus [GPa][(i)]	73 to 88	200 to 400
Strain at failure [%][(i)]	2.5 to 4.5	0.6 to 1.5
Density [g/cm^3][(ii)]	2.6	1.7 to 1.9
Thermal expansion coefficient [10^{-6}/K][(iii)]	5.0 to 6.0	-1.3 to -0.1[*] / 18.0[**]
Fibre diameter [μm][(iv)]	3 to 13	6 to 7
Structure of fibres	Isotropic	Anisotropic

[(i)] ISO 5079, ISO 11566, ASTM C 1557, ASTM D 2343, ASTM D 3379; [(ii)] ISO 1889, ISO 10119, ASTM D 1577; [(iii)] ISO 7991; [(iv)] ISO 1880, ISO 11567.

[*] Axial direction; [**] Radial direction.

The above mentioned fibre reinforcements are available in two different general forms: rovings and mats. While rovings correspond to unidirectional continuous fibre filaments and provide almost all of the axial strength and stiffness of pultruded profiles, mats can be oriented (0º/90º and +45º/-45º) or randomly disposed (*cf*. Figure 1) and, together with the polymer matrix, they contribute to the shear stiffness and strength of the composite material. In addition to rovings and mats, the fibre architecture of pultruded FRP laminates can also comprise surfacing veils (thin fibre mats) used next to the surface, which create a superficial resin-rich layer with enhanced durability. Figure 2 shows the typical fibre architecture exhibited by pultruded GFRP profiles.

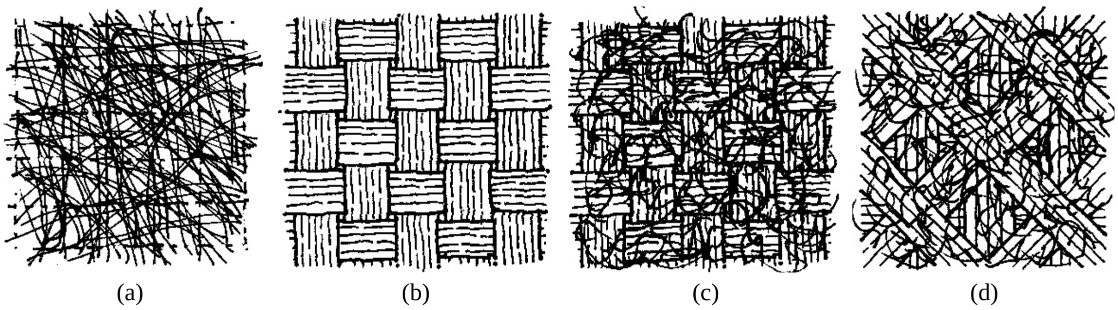

Figure 1: Types of fibre mats: (a) randomly disposed, (b) 0º/90º bidirectional weaves, (c) bidirectional weaves and randomly disposed fibres and (d) 0º/90º and +45º/-45º aligned and randomly disposed fibres [35].

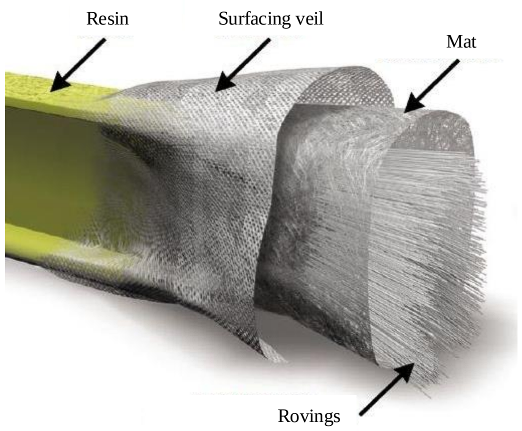

Figure 2: Typical fibre architecture of pultruded GFRP profiles [36].

Regarding the resins used in the polymeric matrixes of pultruded FRP profiles, they can be divided in two main groups: thermoset and thermoplastic resins. Thermoset resins (such as polyester, epoxy and vinylester) are the most used in the production of pultruded composites due to their superior properties and easier processability. In opposition, thermoplastic resins (namely polypropylene and polyethylene) are less used in the construction industry for structural applications [3].

Polyester resins globally present good mechanical, chemical and electrical properties, are easily processed and have the lowest cost among the available resins [3]. Therefore, pultruded GFRP profiles are in general constituted by polyester resins. Epoxy resins on the other hand are the most expensive thermoset resins, being in general used together with carbon fibres [37]. This type of resin presents high mechanical properties, durability and low shrinkage, in particular when compared to polyester resin [25]. Regarding vinylester resins, they combine the best properties of polyester and epoxy resins, as they result from a blend of the two referred resins. Table 2 presents typical values of the main properties of polyester, epoxy and vinylester thermoset resins.

Table 2: Typical properties of the most common thermoset resins (adapted from [34, 37]).

Property	Polyester	Epoxy	Vinylester
Tensile strength [MPa][(i)]	20-70	60-80	68-82
Elastic modulus [GPa][(i)]	2.0-3.0	2.0-4.0	3.5
Strain at failure [%][(i)]	1.0-5.0	1.0-8.0	3.0-4.0
Density [g/cm^3][(ii)]	1.20-1.30	1.20-1.30	1.12-1.16
Glass transition temperature [ºC][(iii)]	70-120	100-270	102-150

[(i)] ISO 527, ASTM D 638; [(ii)] ISO 1183, ASTM D 1505; [(iii)] ISO 11357-2, ISO 11359-2, ASTM E 1356, ASTM E 1640.

2.2.2. Manufacturing process

Composite materials used in civil engineering applications are produced by pultrusion or hand layup in the vast majority of cases. Pultruded elements (such as rebars, laminates and structural profiles) are manufactured in an industrial unit (under controlled conditions) and then applied in the construction site, while the elements produced by hand layup (*e.g.*, sheets for confinement) are generally prepared, applied and cured *in situ*.

In the pultrusion process (illustrated in Figure 3), GFRP profiles with constant section are continuously manufactured and cut with the intended length. This continuous manufacturing process was developed in the decade of 1950 by Brandt Goldsworthy [25], who presented the first pultrusion machine (the Gladstruder), thus allowing to reduce the production cost of FRP materials. This process comprises the following main stages/components:

1. Resin impregnation – rovings and mats are positioned according to the desired fibre architecture and are impregnated by the liquid polymeric matrix, generally in an open bath system.
2. Shaping and curing die – both constituent materials (fibres and polymeric matrix) enter the shaping and curing die guided by plates, which guarantee the proper shape of the

profile's cross-section. The curing of the resin takes place at temperatures varying between 90-180 ºC, depending on the type of resin.

3. Pulling system – the cured part is pulled by the pulling system at an average pultrusion rate of 2 m/min, depending on the shape and complexity of the cross-section.
4. Cutting system – at the end of the pultrusion process, a moving cutting saw cuts the profiles into the intended length.

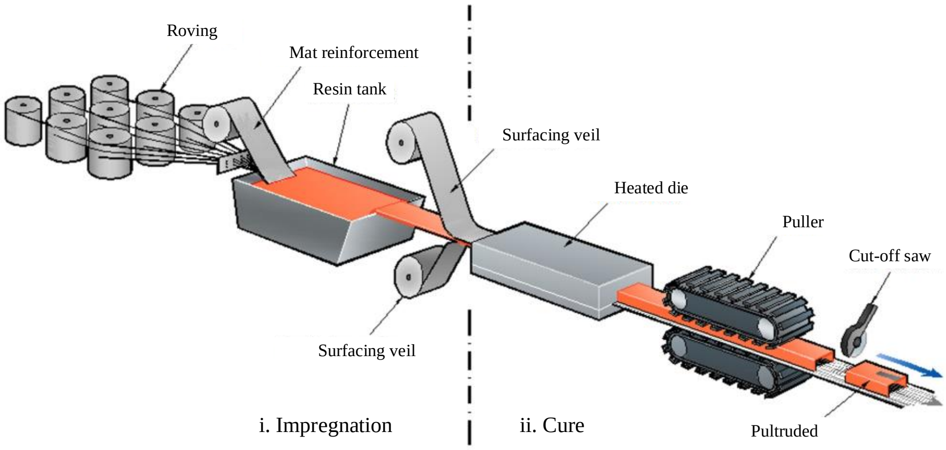

Figure 3: Pultrusion process used for manufacturing GFRP profiles [38].

Although pultrusion only allows producing linear elements with constant cross-section, there are already some adjustments being investigated that can be added to this conventional process with the purpose of manufacturing curved profiles with varying section [25, 39]. Such improvement can promote the widespread application of pultruded GFRP profiles, depending on the respective cost of production.

In this context, it should be mentioned that the composites manufacturing industry is still being developed, in particular, with the purpose of reducing the manufacturing costs and developing specific standardization for the production of FRP materials. The possibility of producing curved pieces and tapered elements with variable cross-section dimensions is being further developed. Also, new types of fibres, resins and additives are being developed, which will likely promote the widespread acceptance of pultruded FRP profiles.

2.2.3. Structural shapes

Presently, different types of FRP materials are produced by pultrusion and used in civil engineering, namely laminates, sheets for confinement, rebars, pre-stress tendons, sandwich panels and pultruded profiles. In terms of pultruded profiles, the first profiles (so called *first generation*) were produced in the 1950s and the definition of their structural shapes was based on steel profiles (thin-walled open sections), which were already being used in construction industry. Due to their thin-walled and generally open cross-section, the *first generation* pultruded GFRP profiles (Figure 4(a)) presented high deformability and susceptibility to instability phenomena [3]. From the 1950s to 1970s, since pultruded GFRP profiles were relatively expensive, they were generally used mainly in buildings requiring electromagnetic transparency and chemical resistance [40].

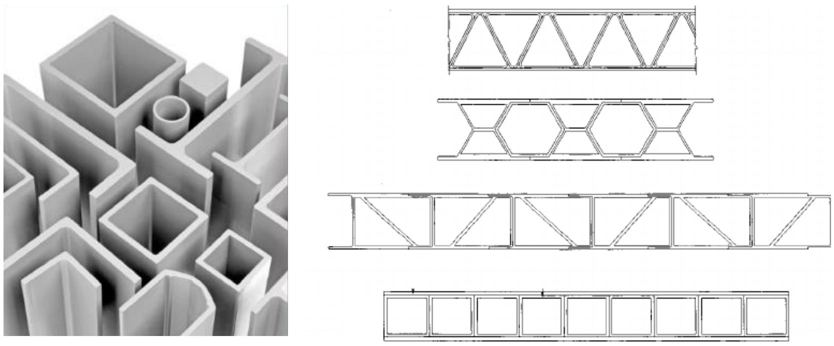

(a) (b)

Figure 4: Typical shapes of (a) the first generation profiles [35] and (b) second generation profiles [41].

Due to the limitations of the *first generation profiles*, a *second generation* of pultruded profiles was developed in order to exploit better the mechanical properties of this composite material. The *second generation profiles* (Figure 4(b)) comprise multicellular panels for floors and decks, thus allowing to mitigate some of the instability phenomena observed in the *first generation profiles*. These pultruded FRP panels, which can be used in both new construction and rehabilitation, usually present lower depths than the *first generation profiles* and, consequently, are more limited in terms of free span between supports. The transversal connection of these panels can be performed by mechanical interlock and/or adhesive bonding [41].

2.2.4. Physical and mechanical properties

The properties of pultruded GFRP profiles depend primarily on the characteristics of their constituent materials (*i.e.* fibre architecture and polymeric matrix) and also on the interaction between the fibres and the polymeric matrix. Despite the different types of constituent materials and manufacturing processes, there are certain aspects that are common to all pultruded elements, namely their orthotropic behaviour, with higher mechanical properties in the longitudinal pultrusion direction (*cf.* Table 3). Comparing to the main competitors (steel profiles), GFRP profiles have relatively high longitudinal strength and low elastic modulus and shear properties.

Table 3: Typical mechanical properties of pultruded GFRP profiles at room temperature (adapted from [25, 27, 34, 37]).

Property	Longitudinal direction	Transverse direction
Tensile strength [MPa]$^{(i)}$	200-400	50-60
Compressive strength [MPa]$^{(ii)}$	200-400	70-140
Shear strength [MPa]$^{(iii)}$	25-30	25-30
Elastic modulus [GPa]$^{(iv)}$	20-40	5-9
Shear modulus [GPa]$^{(v)}$	3-4	3-4

$^{(i)}$ ISO 527, ASTM D 638; $^{(ii)}$ ISO 14126, ASTM D 695; $^{(iii)}$ ISO 14129, ASTM D 3846; $^{(iv)}$ ISO 527, EN 13706-2; $^{(v)}$ ISO 14129, EN 13706-2.

The typical physical properties of pultruded GFRP are presented in Table 4. Compared to conventional steel, the GFRP composite material presents low self-weight, low thermal conductivity coefficient and similar thermal expansion coefficient, namely in the longitudinal direction.

Table 4: Typical physical properties of pultruded GFRP profiles at room temperature (adapted from [27, 34, 37]).

Property	Typical values
Density [g/cm^3]$^{(i)}$	1.5-2.0
Fibre content in weight [%]$^{(ii)}$	50-70
Thermal expansion coefficient [$\times 10^{-6}$ K^{-1}]$^{(iii)}$	8-14* | 16-22**
Thermal conductivity coefficient [W/K.m]$^{(iv)}$	0.20-0.58

$^{(i)}$ ISO 1183, ASTM D 792; $^{(ii)}$ ISO 1172, ASTM D 3171; $^{(iii)}$ ISO 11359-2, ASTM D 696; $^{(iv)}$ ISO 22007, ASTM D 5930.

* Longitudinal direction; ** Transverse direction.

2.2.5. Types of connections

Initially, the connections between pultruded GFRP profiles mimicked those of metallic construction, *i.e.* used bolted connections with the same geometric configurations (Figure 5(a)). However, it was rapidly noted that these connections were not the best solution for GFRP profiles, since they present a distinct material behaviour compared to steel [3]. In fact, the high stress concentrations in the bolt-plate contact surface are critical in the GFRP material, since it does not present a ductile behaviour and it is far more sensitive to stress concentrations in the transverse direction due to its orthotropy.

Although bonded connections (Figure 5(b)) are still scarcely used in the construction industry, this type of connection distributes more efficiently the stresses along the bonded surfaces, thus avoiding the stress concentrations induced by bolted connections. Nevertheless, the widespread use of bonded connections is still being delayed due to uncertainties regarding their long-term behaviour, the performance at elevated temperatures and the lack of design guidance [42].

(a) (b) (c)

Figure 5: Types of connections: (a) bolted connection between GFRP profiles [36], (b) bonded connection between GFRP panels [43], and (c) interlock connection [36].

Other possible solutions are hybrid connections, involving the combination of bolted and bonded connections. Although the stiffness of hybrid connections is provided essentially by the adhesive, the surface-to-surface pressure applied by the bolts may prevent the effect of deficient bonding execution and increase the bonding performance [44].

As an alternative to the mentioned systems, interlock connections (Figure 5(c)) allow connecting pultruded GFRP panels with a grooving and friction mechanism, which can be also complemented with bolting and/or bonding [44]. In fact, this type of connection presents a great potential since it allows a very fast and easy execution at the construction site.

2.2.6. Civil engineering applications

As mentioned, pultruded GFRP profiles were initially used mostly in non-structural elements (Figure 6), such as stairs, grids, benches, gates or fences. This composite material started to be used in these secondary applications mostly due to its lightweight, chemical resistance and electromagnetic transparency.

(a) (b)

Figure 6: Non-structural applications: (a) stairways with grating, handrails and profiles [45] and (b) handrails in a bridge [35].

In 1992, the first all-composite pedestrian bridge, the Aberfeldy bridge (Figure 7(a)), was built in the United Kingdom, including a GFRP deck suspended from GFRP towers by aramid fibre reinforced polymer (AFRP) cables. Then, new bridges were built using this composite material, namely the Pontresina bridge (Switzerland, 1997), the Kolding bridge (Denmark, 1997) and the Lleida bridge (Spain, 2001). The Eyecatcher building (Figure 7(b)), built in Switzerland (1999), constitutes a reference in terms of building construction using FRP materials, being the tallest residential/office building.

(a)

(b)

Figure 7: Structural applications: (a) Aberfeldy bridge [46] and (b) Eyecatcher building [35].

As mentioned, pultruded FRP profiles have more recently started to be used as an alternative to timber, steel and reinforced concrete structures. For instance, they are being used in the rehabilitation of timber building floors (*cf*. Figure 8(a)) and steel structures with durability issues (typically chemical aggressive environments), as well as in the replacement of bridge decks (*cf*. Figure 8(b)). For building applications, fire response is a major issue.

(a)

(b)

Figure 8: Pultruded GFRP elements used in (a) the rehabilitation of a timber floor [35] and (b) the installation of a bridge deck [47].

2.3. Fire behaviour of GFRP materials and structures

2.3.1. Combustion process and development of a fire

Combustion is basically an exothermic chemical reaction between an oxidizing agent and a fuel source, in which thermal energy is released in the form of heat and light. In fact, the fire initiation requires three components: a fuel source, an oxidizing agent and an energy source. When a fuel source (such as the polymeric matrix of FRP materials) is combined with an oxidizing agent (oxygen present in the air) and a source of energy, heating the fuel to its ignition temperature causes the referred exothermic reaction to occur. It should also be noted that the combustion process can be flaming (with flames) or smouldering (without flames) [17].

Regarding the development of a fire (illustrated in Figure 9), although it is a very complex phenomenon that depends on several aspects, it is possible to define the following different stages of fire development [3, 5, 48]:

1. Ignition: corresponds to the ignition of the fuel source, which can be initiated by a burning match or a short-circuit. In this initial period, a significant increase of temperature occurs.
2. Growth: the fire growth and temperature increase depend mainly on the fuel and oxygen available. During this stage, the exothermic reaction occurs very rapidly, releasing elevated rates of energy and generating toxic gases.
3. Flashover: corresponds to a transition period between growth and fully developed fire stages, in which the combustible materials reach their ignition temperature and burst into flame almost simultaneously.
4. Fully developed fire: occurs when the heat release rate and the temperature attain their maxima. In this post-flashover period, peak temperature can vary from 700-1200 ºC.
5. Decay: in this stage, fuel and combustible materials become consumed and, consequently, the energy released is considerably lower (*i.e.*, temperature decreases).

With the purpose of defining the evolution of temperature in the post-flashover development of fires, different time-temperature curves can be considered in the design of structural elements. Figure 9 depicts three different time-temperature curves defined based on Eurocode 1 [49] (red and blue lines, which depend on the degree of ventilation of the room) and ISO 834 [13] (green line). It should be noted that the development of a fire depends on several parameters that are not taken into account in these fire design curves, such as the fire behaviour of the materials used in the buildings.

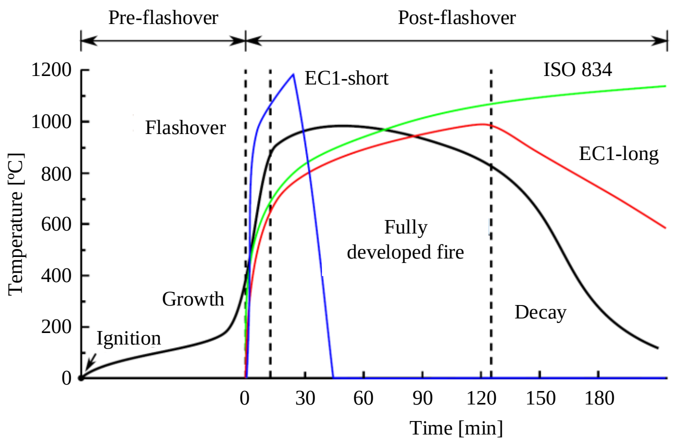

Figure 9: Stages of the fire development (black) and the different fire design curves (red, green and blue) – adapted from [48].

It should also be noted that the combustion process becomes even a more complex phenomenon when it involves FRP materials, since their polymeric matrixes may constitute an important source of fuel. As a result, these composite materials can influence considerably the evolution of temperature, size and spread of flames [5].

2.3.2. Thermal decomposition of GFRP

The thermal decomposition of GFRP material is a complex process, in which thermal, chemical and physical transformations occur. In a first period, the polymeric matrix absorbs the energy radiated from fire, increasing the material temperature up to its decomposition temperature. During the initial heating stage, although GFRP suffers no significant chemical reactions, it changes from a solid to a viscous or rubbery material due to the glass transition process [3]. Then, when the material attains 200-300 ºC, chemical reactions (pyrolysis) begin to occur [50]. As a result of ignition/decomposition of GFRP material, several decomposition products are generated, namely solid residues (char and ash), liquids (partially decomposed polymer) and volatile gases (combustible and incombustible) [5]. It should also be noted that the combustion process of GFRP material generates heat, which promotes the decomposition reaction of the intact parts (*i.e.*, this process constitutes a self-propagating cycle) [51].

Prior to thermal decomposition, the GFRP material softens, creeps and distorts under moderate temperatures (~60-140 ºC), thus presenting a severe reduction of its mechanical properties (strength and stiffness) due to the glass transition of the polymeric matrix [4]. For these temperatures, no relevant chemical reactions occur. Then, at 140-300 ºC, pyrolysis initiates and material starts decomposing, releasing volatiles gases and smoke. When exposed to even more elevated temperatures (~300-500 ºC), the organic matrix of GFRP decomposes, releasing heat, soot and toxic volatiles [5].

Regarding E-glass fibres, typically used in pultruded GFRP profiles, softening and viscous flow starts when temperature reaches roughly 830 ºC, while melting occurs at approximately 1070 ºC [5]. Consequently, E-glass fibre reinforcement suffers no significant changes during the thermal decomposition of the polymeric matrix (*i.e.*, for temperatures below 500 ºC).

2.3.3. Thermo-physical properties of GFRP

In the last decades, many experimental studies were carried out in order to determine the variation of thermo-physical properties of GFRP material with temperature. In fact, such knowledge is crucial to obtain a better understanding about the material behaviour, namely its anisotropic properties and their dependency on temperature. However, the information available still does not provide a comprehensive understanding of the complex variation with temperature of the large set of relevant thermo-physical properties of pultruded GFRP elements.

According to Dimitrienko [52], the typical evolution with temperature of relative density (ρ/ρ_0), heat deformation (ε), gas permeability (K_3) and thermal conductivity (λ) of GFRP material is presented in Figure 10. Regarding these thermo-physical properties, the following main conclusions may be drawn:

- Relative density: suffers a slight reduction for temperatures below the decomposition temperature, due to the vaporization of absorbed water and thermal expansion. Then, when the decomposition temperature is attained, the pyrolysis phenomenon of the polymeric matrix begins, thus causing a drop in density (*cf*. Figure 10). During this period, the density drop is basically dependent on the resin content of the composite material and the heating rate [52].
- Heat deformation: presents a slight increase before the decomposition temperature is attained, as a result of thermal expansion effect. Then, when the material reaches the decomposition temperatures, it presents a decrease due to the development of shrinkage [52].
- Gas permeability: suffers a clear increase when the GFRP material is heated, which is explained by the formation of pores and cracks within the material [52].
- Thermal conductivity: increases up to the polymeric matrix decomposition, with such behaviour being attributed to a growing heat conductivity of the polymer phase [52]. When the decomposition of the polymeric matrix starts, it decreases due to the formation of pores within the matrix and approaches the thermal conductivity of the glass fibres [53].

Regarding the variation of the specific heat capacity with temperature, two curves were proposed by Henderson *et al*. [54], corresponding to theoretical and effective values (*cf*. Figure

11). The theoretical curve was determined using a linear interpolation of the specific heats of both virgin and char materials, corresponding to the energy required to increase the material temperature [55]. In opposition, the effective curve corresponds to the values determined from differential scanning calorimetry (DSC) tests and includes the energy required to increase the material temperature, as well as the energy absorbed or released by the material during the water vaporization and matrix decomposition processes (that are endothermic).

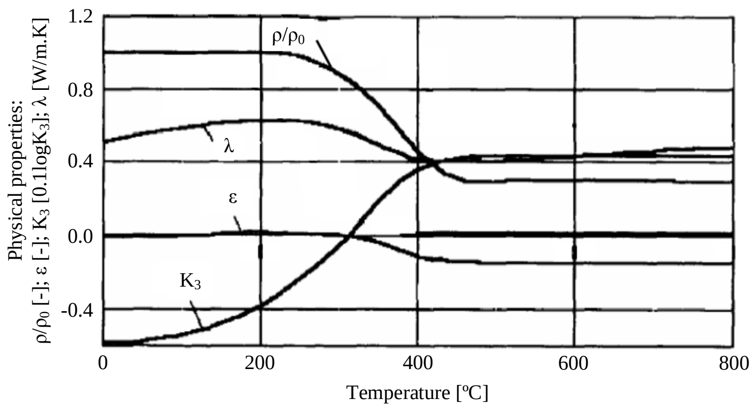

Figure 10: Variation of the thermo-physical properties of GFRP material with temperature (adapted from [52]).

The coefficients of thermal expansion (α) reported in the literature for pultruded GFRP material (all at room temperature) present high variability, with values depending on the materials involved (namely, the volume and type of fibres and the polymeric matrix), and the geometry of the specimens tested. Presently, the experimental data available for this property is very scarce, in particular at elevated temperatures (no results were found). In this topic, Tant *et al*. [56] and Mouritz and Gibson [5] performed numerical and experimental investigations in order to evaluate the thermal expansion of a glass-phenolic composite. In both studies [5, 56], the authors concluded that the thermal expansion coefficient depends significantly on temperature.

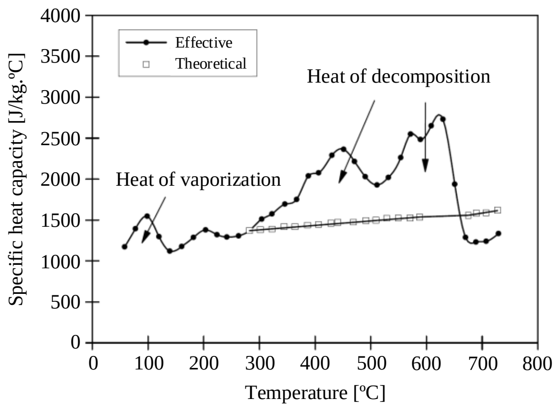

Figure 11: Variation of the specific heat capacity of GFRP material with temperature (adapted from [54]).

Regarding the emissivity of GFRP material, Samanta *et al*. [50] proposed a linear variation between 0.75 and 0.95 for temperatures varying from 20 to 1000 ºC, respectively, while Bai *et al*. [57] suggested to take a constant value of 0.75 (temperature-independent) in thermal analysis of GFRP elements.

2.3.4. Thermo-mechanical properties of GFRP

Similarly to thermo-physical properties, the thermo-mechanical properties of GFRP material are considerably dependent on temperature and orthotropic. When this composite material is exposed to elevated temperatures, the typical variation of a given mechanical property (P) with temperature is illustrated in Figure 12. The mechanical properties of composite materials are maximum (P_U – unrelaxed state) at low temperatures and minimum (P_R – relaxed state) at high temperatures (*cf*. Figure 12). For temperatures below a certain critical value (T_{cr}), the GFRP material retains most of its mechanical properties. Then, a considerable reduction in the mechanical properties is caused by the glass transition of polymeric matrix – the magnitude of such reduction depends considerably of the property at stake (and direction). In Figure 12, the mechanically observed glass transition temperature ($T_{g,mech}$) corresponds to a 50% reduction of the property value and is about 15-20 ºC below glass transition temperature (T_g, determined from thermo-physical tests, such as DSC or DMA) [5]. In other words, when the T_g is reached, the mechanical property presents already a considerable reduction. For instance, the variation with temperature of the Young's modulus, shear modulus and compressive strength are very similar (qualitatively) with the curve plotted in Figure 12.

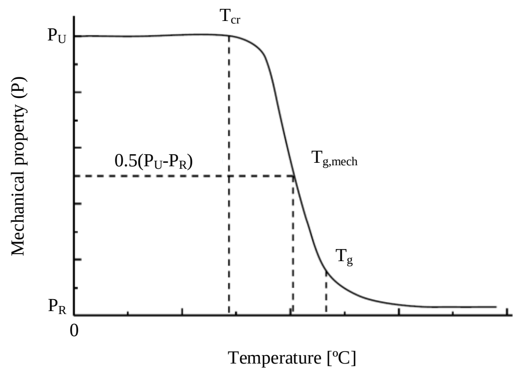

Figure 12: Typical variation of a mechanical property of GFRP material with temperature (adapted from [5]).

The variation with temperature of the tensile and compressive strengths is considerably different. In fact, the compressive strength (and modulus) of GFRP material is clearly more susceptible to temperature increase (*cf*. Figure 13) than the tensile counterparts. According to Mouritz and Gibson [5], the GFRP material presents a drop in the compressive strength already at moderate temperatures (~50-150 ºC). When subjected to compression, the material presents a kinking failure mechanism, which is triggered by excessive local shear deformation. Consequently, compressive failure is strongly dependent on the shear properties of the polymeric matrix. Regarding the thermal degradation of tensile strength, there is also a reduction in the tensile strength at elevated temperatures (~150-250 ºC) due to the softening of the resin, which is no longer able of uniformly distributing the stresses among the fibres. However, compared to compressive strength, the drop in tensile strength is less pronounced and occurs for higher temperatures, which is explained by its lower dependency on the mechanical properties of polymeric matrix.

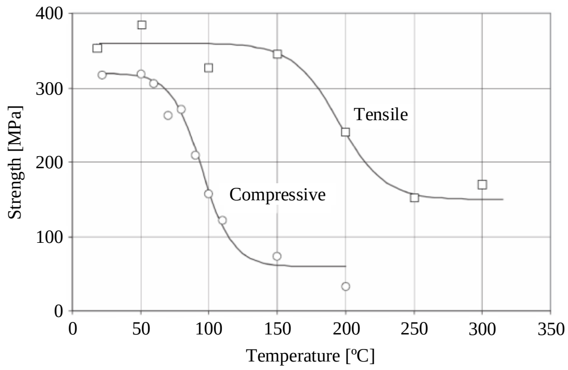

Figure 13: Variation with temperature of the tensile and compressive strength of pultruded GFRP material (adapted from [5]).

In this context, it should be mentioned that the variation with temperature of several matrix-dependent properties of GFRP are still not characterized, namely the compressive and shear moduli. Likewise, very limited information is available about the creep behaviour at elevated temperature [6].

2.3.5. Fire reaction properties of GFRP

The fire reaction properties reflect the contribution of a construction material to the deflagration and propagation of a fire, corresponding to its flammability and combustion properties. In this context, the most relevant characteristics are the time to ignition, the smoke toxicity and density, the oxygen index, the heat release rate and the flame spread rate [5]. These fire reaction properties are described next:

- Time to ignition: corresponds to the period of time required for a material to ignite and sustain flaming combustion. In composite materials, it occurs roughly when the decomposition temperature is attained [5].
- Smoke toxicity and density: these parameters are particularly important in the design of buildings since it has clear influence in the human survival during a fire. For instance,

the decomposition of GFRP materials may release asphyxiants, irritants and carcinogens gases [5].

- Oxygen index: refers to the minimum oxygen content in the air required to maintain the flaming combustion of a material. This parameter allows evaluating the flammability of (composite) materials [17].
- Heat release rate: corresponds to the amount of thermal energy released by a material per unit area when exposed to a fire (*e.g.*, Figure 14). Consequently, materials with low values of peak and average heat release rate are recommended for civil engineering applications. In fact, this parameter is considered the most important fire reaction property since it is the best indicator of fire hazard of a material [58].
- Flame spread rate: refers to the velocity of the flame front propagating in the surface of the combustible material and, therefore, it is intrinsically related to the growth and spread of fire hazard [3].

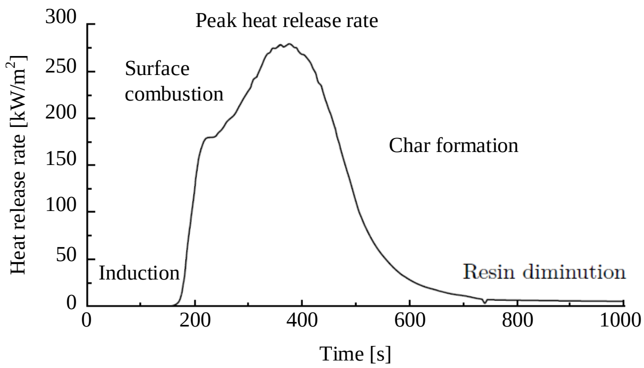

Figure 14: Typical heat release rate curve for GFRP material (adapted from [5, 20]).

2.3.6. Fire resistance behaviour of GFRP structures

As mentioned, the widespread acceptance of pultruded GFRP profiles in civil engineering applications is still hindered due to several issues, including its fire performance. Until presently, only a reduced number of studies addressed the fire behaviour of GFRP beams, columns or slabs; moreover, very limited information is available about the mechanical behaviour of the GFRP material at elevated temperature and the fire behaviour of connections between GFRP members. Consequently, more experimental and numerical works are needed to obtain a better understanding about this critical topic.

In what concerns the fire resistance behaviour of intermediate-to-full scale load bearing pultruded GFRP members in bending, until now very few studies were reported in the literature. In fact, the only experimental data available in the literature concerning one-way slabs was reported by Massot [7] and Keller *et al.* [8]; likewise, for beams, only the data provided by

Ludwig *et al*. [9] and Correia *et al*. [10] are available. Although GFRP material properties in compression are much more susceptible to elevated temperature than those in tension, there are also very few studies in the literature about the response of intermediate- or full-scale pultruded GFRP elements subjected to compression and to fire or elevated temperature [11, 59, 60]. The single study performed for actual fire exposure conditions is the one reported by Bai *et al*. [11], as the tests presented by Wong and Wang [59] and Bai and Keller [60] were performed for temperatures below the glass transition and decomposition temperatures of the GFRP material, respectively.

In the previous studies, with the exception of the beams tested by Ludwig *et al*. [9], all GFRP members were exposed to fire in only one side and subjected to a single load level. The experimental results obtained in the above mentioned experiments showed that passive and active fire protection systems allow increasing significantly the fire resistance of GFRP structural members. A detailed description of these experimental works, performed on slabs, beams and columns is presented in more detail in Part II of the present thesis.

In terms of simulation of the fire behaviour of GFRP members, although some efforts have been reported, many developments are still needed to accurately predict their thermal and mechanical responses in fire. Gibson *et al*. [20] and Bausano *et al*. [21] investigated the mechanical response under compression of GFRP laminates (produced respectively by hand layup and pultrusion) using laminate theory; and Wong *et al*. [22] developed a finite element model to simulate the compressive behaviour of pultruded GFRP profiles. In what concerns the fire behaviour of slabs and beams, Keller *et al*. [8] and Bai and Keller [19] modelled the mechanical response of GFRP multicellular slabs, while Bai *et al*. [15] simulated the fire behaviour of pultruded GFRP beams using an analytical approach. In the numerical investigations carried out in this field, detailed ahead in Part III of this thesis, only part of the cross-section was modelled and only conduction through the solid material was considered. Consequently, these models were not always able to accurately simulate the mechanical response of GFRP members exposed to elevated temperatures, since they departed from relatively simple thermal simulations. The mechanical simulations in fire also presented some limitations, some of which related with the lack of input data on relevant material properties as a function of temperature.

2.4. Main research needs

In terms of material characterization, the variation with temperature of several GFRP material properties is still unknown (*e.g*. compressive modulus, shear modulus, creep coefficients for different stress states, thermal expansion coefficient). It is worth mentioning that, in order to fully understand and simulate the fire behaviour of GFRP profiles, it is not only the thermo-physical properties (specific heat capacity, thermal conductivity, emissivity, thermal expansion and creep), but also the thermo-mechanical properties (tensile, compressive and shear moduli and strengths) that need to be known as a function of temperature. In addition, extensive information about the temperature dependency of thermo-physical properties of materials used as passive fire protection systems is needed in order to simulate accurately the thermal response of GFRP members.

Following the experimental works already reported in the literature, more experimental tests on different types of pultruded GFRP full-scale members - beams, columns and slabs - are needed. In particular, new fire protection systems should be developed and assessed and the influence of applying different types of fire exposure and load levels in the fire resistance of structural elements should be evaluated.

Despite the previous efforts in simulating the thermal and mechanical responses of GFRP structural elements in fire, there are still several topics that require more advanced numerical investigations. The thermal analysis of GFRP profiles is a complex heat transfer problem; it depends on the accurate definition of material thermo-physical properties, some of which are still not well defined. Moreover, the consideration of the different types of heat exchanges in tubular sections is also of paramount importance, namely the radiative exchanges between section walls and the convection of air enclosed in cavities.

In what concerns the mechanical analysis of GFRP structural elements, the main limitations of previous works reported in the literature are as follows: (i) the mechanical simulations were developed based on simple thermal models, which did not always accurately predict the evolution of temperatures in the entire cross-section; (ii) similar reductions of tensile and compressive moduli were assumed, since such information was not available in the literature; (iii) the thermal degradation of shear modulus considered as input was not based on experimental results (also not available in the literature); (iv) there are uncertainties concerning the effects of thermal expansion and creep, which influence significantly the mechanical response; and (v) the influence of using different fire protection systems, types of fire exposure (*e.g*. number of sides exposed to fire) and load levels need to be studied in much further depth.

Taking into account the limitations presented above, the development of models considering the temperature-dependence of all relevant mechanical properties, as well as nonlinear geometrical effects is also very important to accurately determine the structural response of GFRP members, regarding both *kinematic* (displacements, rotations and deformations) and *static* (forces, moments and stresses) issues. In addition, appropriate failure initiation (*e.g.*, Tsai-Hill/Hashin criteria [61, 62]) and damage propagation criteria for composite materials at elevated temperatures should also be implemented in the mechanical simulations in order to reliably predict the collapse of GFRP structural members.

Finally, it should be noted that presently there is no fire design guidance for pultruded GFRP members. Its development strongly relies on additional research efforts responding to the various needs in this area. Consequently, further experimental and numerical investigations on this topic are required to improve the present understanding of this topic and provide the background knowledge and data to develop consensual design codes.

2.5. Concluding remarks

During the last decades, pultruded GFRP profiles have been increasingly used in the construction industry, since they present several advantages compared to traditional materials (such as reinforced concrete, steel and timber). However, there are legitimate concerns about its fire behaviour and the studies available in the literature in this respect are still very scarce.

The literature review, summarized in this chapter, shows that the physical and mechanical properties of GFRP material are considerably dependent on temperature. It shows also that the fire performance of GFRP composite members, for which very few works are available in the literature, is a very complex problem. In this context, more comprehensive experimental investigations at both material and structural levels have to be developed. Additionally, more advanced numerical studies about the fire behaviour of pultruded GFRP members need to be developed in order to include important effects not considered in previous studies.

The main objective of this thesis was to respond to some of these short-comings in the state-of-the-art, providing a better understanding of the fire behaviour of pultruded GFRP profiles, one of the main issues that has been delaying its widespread use in civil structural applications.

Part II:

Experimental study

Chapter 3:

Characterization of GFRP material at elevated temperatures

3.1. Introduction

Fibre-reinforced polymer (FRP) materials in general and pultruded glass-fibre reinforced polymer (GFRP) profiles in particular have been increasingly used in civil engineering applications since the 1960s, due to the advantages they offer over traditional materials [24]. These include lightness, high strength, good insulation properties and durability, even in aggressive environments. In the specific case of pultruded GFRP profiles, in spite of such advantages, the widespread use in structural applications is being delayed due to their susceptibility to instability phenomena, the lack of design codes and the concerns and limited knowledge about their response at elevated temperature and under fire exposure [2, 41].

These concerns about the fire response of GFRP profiles are well-founded, being particularly acute for building applications. Indeed, when exposed to temperatures of about 300 to 500 ºC, the polymeric matrix is decomposed, releasing smoke, soot and toxic volatiles [5]. In addition, at moderately elevated temperatures, especially when approaching and exceeding the glass transition temperature (T_g) of the polymeric matrix [2], which is generally in the range of 60-140 ºC [4], the GFRP material undergoes considerable softening, resulting in severe deterioration of its mechanical properties.

A limited number of studies were already performed to characterize the thermo-mechanical properties of pultruded GFRP profiles. The vast majority of those studies, recently reviewed in [6], were conducted up to temperatures of around 250-300 ºC (*i.e.*, prior to resin decomposition) and focused mainly on the strength of the GFRP material under tension or compression.

Very limited information is available about the variation with temperature of the elastic moduli of the material, namely when subjected to compression. Correia *et al*. [4] performed compressive tests on pultruded GFRP profiles with I-section for temperatures up to 250 ºC. The authors tested short columns (L = 50 mm) and concluded that they exhibited an approximate linear behaviour up to failure, despite presenting an initial nonlinear response (due to test setup adjustments between specimens and loading plates). The results obtained show that the compressive strength is severely reduced by temperature increase – *e.g.*, the reduction of compressive strength measured at 250 ºC was 95%, compared to room temperature strength. Even at moderate temperature (60 ºC), the strength reduction was significant (~30%). In this study, the specimens tested exhibited two different failure modes: (i) at room temperature, material crushing and wrinkling were observed, together with ply delamination; and (ii) at elevated temperature, failure occurred in the central part of specimens, being triggered by resin softening, which consequently led to delamination and kinking of the glass fibres.

In addition to the above mentioned study, Bai and Keller [63] investigated also the compressive behaviour of tubular GFRP columns when exposed to temperatures ranging from room temperature up to 220 ºC. Wong and Wang [59] performed compressive tests on GFRP C-channel columns for temperatures up to 250 ºC. In these three experimental works [4, 59, 63], the variation of compressive strength with temperature and the failure modes were similar, despite the different specimens' geometries tested. The strength reductions measured by Bai and Keller [63] and Wong and Wang [59] were 92% and 90%, respectively, at 250 and 220 ºC, being slightly lower than that reported by Correia *et al*. [4] (95% at 250 ºC).

Despite the above referred experimental works, there are still no studies reported in the literature about the variation with temperature of some relevant mechanical properties of pultruded GFRP material, namely the elasticity modulus, in particular, under compression. With the purpose of investigating the influence of temperature in compressive modulus, compressive tests on pultruded GFRP columns were carried out in the framework of this thesis.

Similarly, the information about the changes with temperature of the shear properties [4, 63], summarized in the next paragraph, is much more limited. However, understanding the influence of elevated temperatures on the shear behaviour of pultruded GFRP material is of paramount importance towards the development of design guidelines for both fire exposure and normal service conditions (namely, for outdoor applications[1]). Indeed, the design of GFRP structures is often governed by deformability requirements and shear deformations generally represent a significant portion of the overall deformations. Moreover, previous tests [6] have shown the susceptibility of pultruded GFRP beams to shear failure under fire exposure. In this context, it is very relevant to determine the variation with temperature of the shear modulus and strength of pultruded GFRP profiles.

Bai and Keller [63] and Correia *et al*. [4] determined the reduction of the shear strength of pultruded GFRP material for temperatures up to 220 and 250 ºC, respectively. In both studies, glass-polyester pultruded laminates were subjected to a 10º off-axis tensile load, *i.e.*, with the load axis making a 10º angle with the pultrusion direction. Despite some differences in the specimens' geometry (350×30×10 mm in the tests of Bai and Keller [63] and 800×20×10 mm in the study by Correia *et al*. [4]), the shear strength variation with temperature was very similar: it

[1] In outdoor applications, the GFRP material may experience relatively high temperatures.

presented a significant reduction with temperature, especially steep across the T_g range (from 90 to 150 ºC), with strength retentions of 13% at 220 ºC ([63]) and 11% at 250 ºC ([4]), compared to the strength at room temperature. In both studies, the load *vs*. cross-head deflection curves were roughly linear up to failure (with only a slight stiffness reduction prior to failure) and in [4] this response was partly attributed to the 10º off-axis test setup, namely the fact that a considerable part of the applied load is carried out in tension and, for this type of loading, the glass fibres present a linear behaviour up to failure and retain a significant fraction of their room temperature modulus. In both experimental programmes, failure was caused by the rupture of the polymeric matrix and the superficial mats, with the longitudinal fibres remaining intact, and the failure surfaces being oriented roughly at 10º with the pultrusion direction. It is worth mentioning that none of these studies reported the variation with temperature of the shear modulus.

In this chapter, experimental and analytical investigations about the shear and compressive behaviour of GFRP pultruded profiles when exposed to elevated temperatures are presented. Firstly, the results obtained from dynamic mechanical analysis (DMA) and differential scanning calorimetry and thermogravimetric analysis (DSC/TGA) performed in GFRP material are shown. Then, experimental studies about the compressive and shear behaviour of GFRP material at elevated temperatures (from room temperature up to 180 ºC) are presented and discussed. These experiments had two main objectives: (i) to determine the mechanical response at elevated temperature of the GFRP material under compression and in-plane shear, thus contributing to the definition of temperature-dependent constitutive relationships and failure criteria; and (ii) to compare the results obtained with those previously reported in the literature. In addition, analytical studies were carried out in order to assess the accuracy of the different models described in the literature to simulate the experimental results.

3.2. DMA and DSC/TGA tests

In order to characterize the thermal and thermo-mechanical properties of the pultruded GFRP material, similar to the one used in the fire resistance tests (chapters 4 and 5), dynamic mechanical analysis (DMA), differential scanning calorimetry (DSC) and thermogravimetric (TGA) tests were performed on GFRP material.

Dynamic mechanical analysis (DMA) experiments were performed to assess the glass transition process undergone by the GFRP material. The DMA tests were performed in a dual cantilever flexural setup, from room temperature (T_{room}) to 250 ºC, at a heating rate of 4 ºC/min. From the results obtained (depicted in Figure 15(a)), the onset glass transition temperature ($T_{g,onset}$) was set as 104 ºC (based on the decay of the storage modulus curve, E’) and the glass transition temperature (T_g) was set at 141 ºC (based on the peak value of the loss modulus curve, E’’). For this particular GFRP material, the $T_{g,onset}$ (determined as illustrated in Figure 15(a)) corresponds to a relatively high reduction of E'; this is most likely due to the occurrence of a secondary relaxation mechanism at relatively low temperatures, visible in both E' and E'' curves.

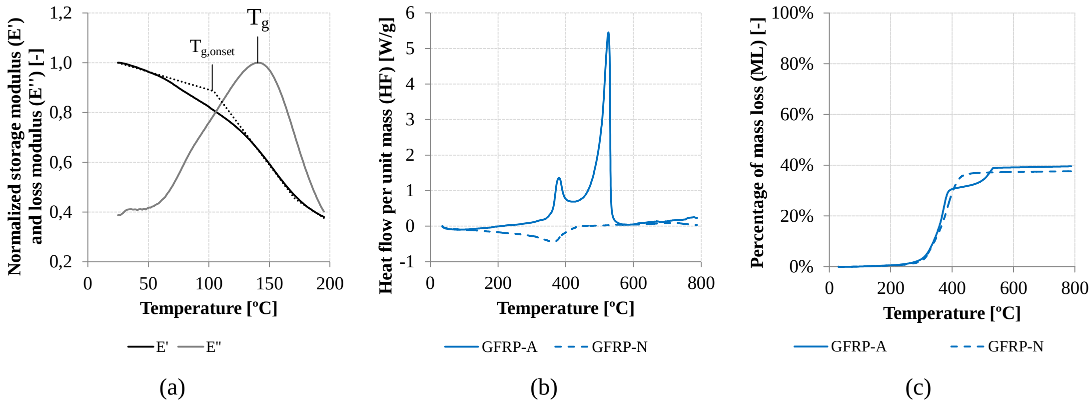

Figure 15: (a) DMA, (b) DSC and (c) TGA results for GFRP material in air (A) and nitrogen (N) atmospheres.

Differential scanning calorimetry and thermogravimetric (DSC/TGA) experiments were also performed to assess the decomposition process of the GFRP material (Figure 15). The DSC/TGA tests were conducted from 30 to 800 ºC, at a heating rate of 10 ºC/min, in two different atmospheres: air and nitrogen (inert) to simulate the thermal decomposition of the material at the outer layers (*i.e.*, in presence of oxygen) and inner layers (where there is low oxygen content), respectively. The decomposition temperature of the GFRP material (T_d) was set at 370 ºC (based on the middle temperature of the sigmoidal mass change – Figure 15(c)), whereas the onset decomposition temperature $T_{d,onset}$ (corresponding to 5% mass reduction) was defined as 315 ºC. As expected, the results of DSC/TGA experiments show that the decomposition process (i) is exothermic in oxygen, with two heat flow peaks related to the onset and end of mass loss, and (ii) endothermic in nitrogen, in this case with a single heat flow peak corresponding to the onset of the mass loss (Figure 15(b)).

3.3. Compressive behaviour at elevated temperature

3.3.1. Experimental programme

Aiming at determining the compressive behaviour of GFRP material at elevated temperatures, compressive tests were carried out on short columns with I-section (120×60 mm, 8 mm thick). Firstly, the 120 mm long columns were heated up to a predefined temperature ranging from room temperature (T_{room}) to 180 ºC (26, 60, 100, 140 and 180 ºC) at a constant heating rate (~4 ºC/min). The short columns were heated up to the intended temperature in a *Tinius Olsen* thermal chamber (with inner dimensions of 605×250×250 mm). Then, at constant temperature, a compression load was applied up to failure [64].

The test setup adopted in these compressive tests is illustrated in Figure 16. The extremities of the test specimens were inserted in grooved steel plates in a length of 30 mm. The compressive tests were performed on an *Inepar* testing machine with a load capacity of 3000 kN and the compressive load was measured with an 800 kN load cell from *Novatech*. The tests were conducted under load control at an average speed of 2.3-2.7 kN/s. The vertical deflection imposed by the hydraulic jack to the test fixture was measured with a displacement transducer from *TML*, positioned outside the thermal chamber (*cf.* Figure 16). Note that such deflection includes the deformability of the test specimen, but also the gaps between the different components of the test setup, as well as the effects of local crushing of the edges of the test specimens.

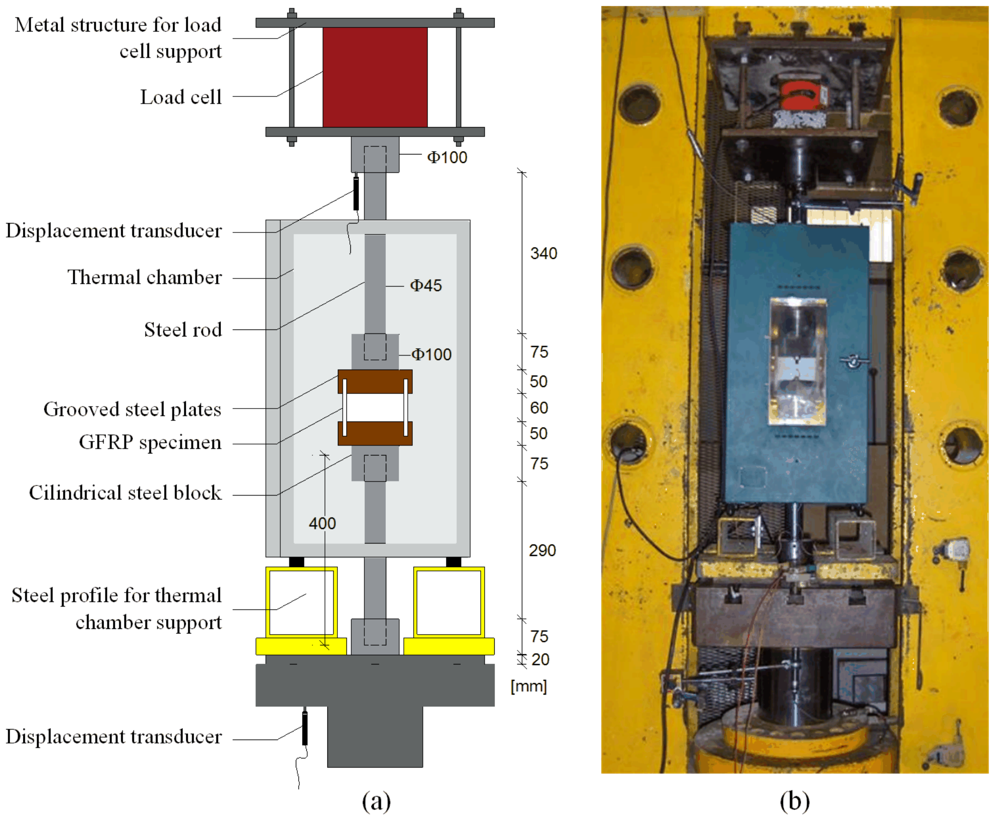

Figure 16: (a) Scheme and (b) general view of test setup and equipment used in compressive tests.

The displacements in different points of the columns' webs (*cf.* Figure 17) were also measured using a videoextensometry technique, with an accuracy of ± 0.005 mm. The equipment used consists of a high definition *Sony* video camera (model *XCG 5005E*, with *Fujinon* lens, model *Fujifilm HF50SA-1*), a tripod, where the camera was fixed, and computer software (*LabView*). This image technique allows to track the position/coordinates (x,y) of targets marked at the surface of the specimen being tested at each instant (and for each load level) and, subsequently, to determine the corresponding strains. It should be noted that the use of videoextensometry allows measuring the displacements at the free height of the columns, thus avoiding errors introduced by the local crushing of the profiles at the grooved steel plates. The temperatures at the central section of the columns (mid-depth and centre of the web) and in the air of the thermal chamber were measured by means of thermocouples type K (Figure 17).

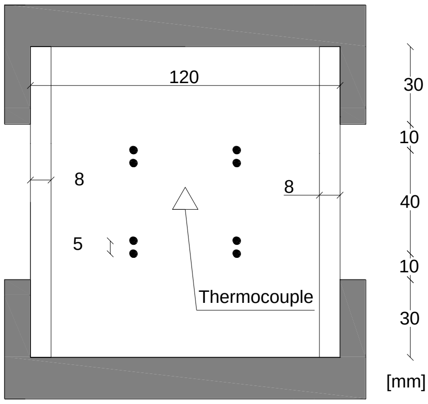

Figure 17: Dimensions and target scheme used in compression specimens.

3.3.2. Experimental results and discussion

Figure 18 presents the load *vs*. displacement curves for one representative specimens of each tested temperature; the displacement corresponds to the total relative displacement between the plates of the testing machine (as measured with the displacement transducer). In all specimens, the curves presented an initial nonlinear branch, as a result of the specimens' adjustment to the grooved steel plates. After that initial period, the GFRP columns presented an approximately linear behaviour up to failure (*cf*. Figure 18). As expected, the composite material exhibited progressive reductions of global stiffness and maximum load with temperature, which can be explained by the glass transition of the polymeric matrix. It should also be highlighted that the global compressive stiffness at 180 ºC corresponds to a residual value of 38%, compared to that at T_{room}.

Figure 19 shows representative axial stress *vs*. axial strain curves obtained for specimens tested at 26, 60 and 100 ºC. These curves, which were plotted only up to the failure of the specimens, exhibit an initial irregular branch caused by test setup adjustments (which caused some disturbance in the tracking of the videoextensometer targets). After that initial stage, the curves presented a relatively linear response, exhibiting a progressive stiffness reduction in the brink of failure. At 100 ºC, the curves presented an irregular branch prior to collapse, which was probably caused by the wrinkling of the material with delamination of its most superficial layers (that characterized the specimens' failure mode). In fact, such phenomenon may have also affected the video extensometer readings. In this experimental campaign, the stress *vs*. strain curves obtained for specimens tested at 140 and 180 ºC presented an erratic behaviour, which may be related to such delamination of the material's superficial layer, which was more pronounced at these temperatures.

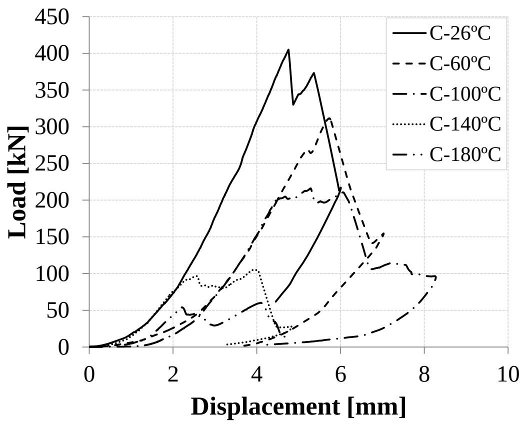

Figure 18: Load *vs*. displacement curves in compression for representative specimens of all tested temperatures.

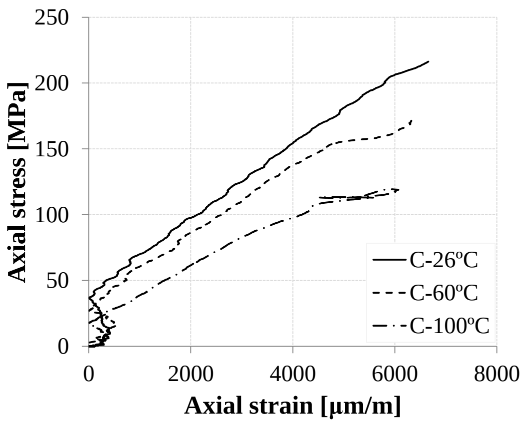

Figure 19: Axial stress *vs*. axial strain curves for representative specimens tested at 26, 60 and 100 ºC.

Figure 20 presents the failure modes observed in the compressive tests. At T_{room} (Figure 20(a)), failure occurred due to GFRP crushing at the grooved steel plates. In some cases, delamination of the outermost glass fibre mats was also observed. For the remaining temperatures, collapse occurred due to crushing at the grooved plates, which seems to have been followed by the wrinkling of the material within the free height of the specimens (Figure 20(b) and Figure 20(c)). The failure modes observed in the present study were consistent with those reported in the literature [4, 59, 63].

Figure 21 presents the variation of longitudinal compressive strength with temperature. The compressive strength exhibited reductions of 55% and 87% at 100 and 180 ºC, respectively, thus confirming the susceptibility/weakness of GFRP material at elevated temperatures when subjected to compression. As shown in Figure 22, the evolution of compressive strength with temperature compares very well with results reported by Bai and Keller [63], Correia *et al*. [4] and Wong and Wang [59], obtained from similar/comparable pultruded GFRP materials.

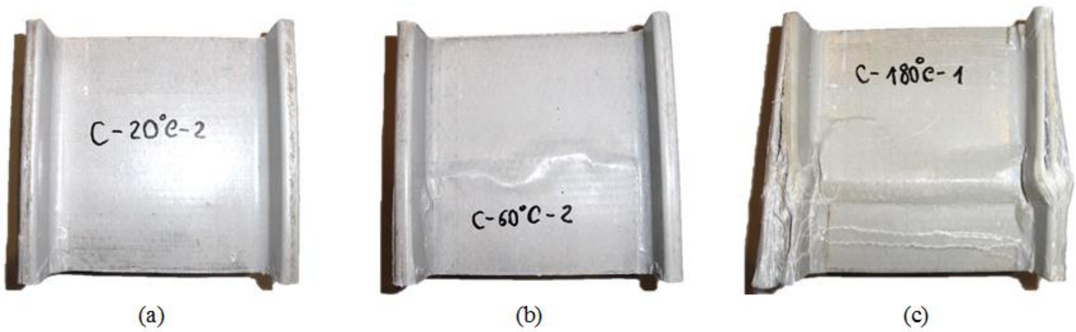

Figure 20: Typical failure modes of specimens tested in compression at (a) 26 ºC, (b) 60-140 ºC and (c) 180 ºC.

Regarding the compressive modulus, reductions of 13% and 19% (compared to T_{room}) were obtained at temperatures of 60 and 100 ºC, respectively. However, these results were not entirely consistent, were determined only up to 100 ºC and there are doubts about the influence of material wrinkling and debonding of the superficial mat layers on the accuracy of the strain measurements. Therefore, the variation of compressive modulus with temperature is not plotted in Figure 21. The determination of the compressive modulus as a function of temperature should be object of further research.

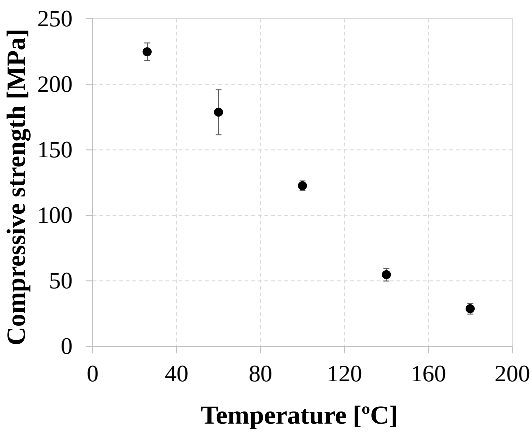

Figure 21: Variation of longitudinal compressive strength with temperature.

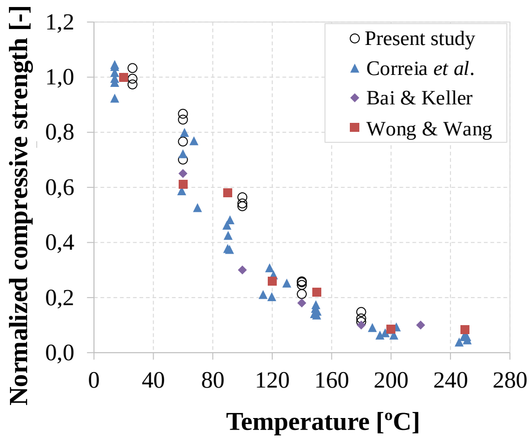

Figure 22: Comparison of the normalized compressive strength reduction with temperature – present study *vs*. other studies reported in literature [4, 59, 63].

3.3.3. Analytical modelling

In previous studies, different models were proposed to simulate/predict the mechanical properties of FRP materials at elevated temperatures. These models include (i) empirical mathematical formulations encompassing curve fitting procedures to the experimental data, namely the models developed by Gibson *et al*. [20], Mahieux *et al*. [65], Wang *et al*. [66] and Correia *et al*. [4], and (ii) semi-empirical approaches, as those proposed by Bai *et al*. [14]. In Correia *et al*. [4], the accuracy of these models to describe the changes with temperature of the tensile, compressive and 10º off-axis shear strength of pultruded GFRP material has been assessed.

In the model of Gibson *et al*. [20], the variation of a generic mechanical property P with temperature T, can be described by the following equation,

$$\mathrm{P(T)} = \mathrm{P_u} - \frac{\mathrm{P_u} - \mathrm{P_r}}{2} \times \left(1 + \tanh\left[\mathrm{k'}\left(\mathrm{T} - \mathrm{T_{g,mech}}\right)\right]\right) \tag{1}$$

where P_u is the property at room temperature and P_r is the property after glass transition (but before decomposition); k' and $T_{g,mech}$ are parameters obtained by fitting the curve to the experimental data.

According to Mahieux *et al*. [65], a mechanical property can be computed as a function of temperature through the following equation, based on Weibull distribution,

$$\mathrm{P(T)} = \mathrm{P_r} + (\mathrm{P_u} - \mathrm{P_r}) \times \exp[-(\mathrm{T}/\mathrm{T_0})^{\mathrm{m}}] \tag{2}$$

in which T_0 is the relaxation temperature and m is the Weibull exponent, with both parameters being numerically fitted to the experimental data.

Wang *et al*. [66] suggested the following model (initially developed for metallic materials) to describe the tensile behaviour of pultruded carbon fibre reinforced polymer (CFRP) laminates at elevated temperature,

$$\mathrm{P(T)} = \mathrm{P_u} \times [\mathrm{A} - (\mathrm{T} - \mathrm{B})^{\mathrm{n}}/\mathrm{C}] \tag{3}$$

where the parameters A, B, C and n, should be fitted to the experimental data and can be estimated for different temperature ranges.

More recently, Correia *et al*. [4] suggested the following model based on Gompertz statistical distribution,

$$\mathrm{P(T)} = \mathrm{P_r} + (\mathrm{P_u} - \mathrm{P_r}) \times \left(1 - \mathrm{e}^{\mathrm{B}\mathrm{e}^{\mathrm{C}\times\mathrm{T}}}\right) \tag{4}$$

where B and C are parameters obtained from fitting the modelling curve to the experimental data.

The rational modelling approach developed by Bai *et al*. [14] for the elasticity modulus of FRP materials was extended to model the strength degradation with temperature of GFRP materials

[67]. According to Bai and Keller [67], the strength value during glass transition stems from the contribution of the material's state before and after the glass transition process. Based on the rule of mixture (Eq. (5)) and the inverse rule of mixture (Eq. (6)), two different models were proposed, providing respectively upper and lower bounds for the effective property of a two-state material,

$$P(T) = P_g \times \left[1 - \alpha_g(T)\right] + P_l \times \alpha_g(T) \times [1 - \alpha_d(T)] + P_d \times \alpha_g(T) \times \alpha_d(T) \qquad (5)$$

$$\frac{1}{P(T)} = \frac{1 - \alpha_g(T)}{P_g} + \frac{\alpha_g(T) \times [1 - \alpha_d(T)]}{P_l} + \frac{\alpha_g(T) \times \alpha_d(T)}{P_d} \qquad (6)$$

in which P_g, P_l and P_d are the materials properties (strength or modulus) in the glassy, leathery and decomposed states, respectively. The parameters α_g and α_d (varying between 0 and 1) correspond to the glass transition and decomposition degrees, respectively. In the present study these parameters were determined from DMA and DSC/TGA measurements (section 3.2.).

Aiming at estimating the compressive strength variation with temperature, the modelling curves presented in this section were fitted to the experimental results obtained in the present study. For the empirical models, the theoretical curves were obtained simply by fitting the experimental data (for all test temperatures) using a standard procedure that minimizes the mean square errors to the experimental results. For the models of Bai and Keller, as they are semi-empirical, the definition of the modelling curve only requires the parameters (experimental data) presented in Eq. (5) and Eq. (6), namely the mechanical properties at two given temperatures (before and after glass transition) and the DMA results.

The parameters obtained for the different models are listed in Table 5, which also includes the value of the absolute mean percentage error (AMPE), used to assess the relative accuracy of the different fitted curves with respect to the experimental data. Figure 23 plots the variation with temperature of the normalized experimental values of compressive strength together with the different modelling curves described above.

Taking into account the analytical models used, it can be concluded that the empirical curves presented relatively accurate predictions of the evolution of compressive strength with temperature. In this case, the model of Mahieux *et al*. provided the most accurate prediction of the thermal degradation of compressive strength, presenting the lowest values of AMPE (*cf*. Table 5). As expected, the models of Bai and Keller (semi-empirical) were less accurate in simulating this mechanical property (they presented the highest AMPE values), especially the model based on the rule of mixtures, which largely overestimated the residual compressive strength.

Table 5: Simulation of GFRP compressive strength – parameter estimation and absolute mean percentage error (AMPE) for the different models.

Model	Parameter	Compressive strength
Gibson *et al*. [20] Eq. (1)	k' [-]	0.2031
	$T_{g,mech}$ [ºC]	94.98
	AMPE [%]	9.0
Mahieux *et al*. [65] Eq. (2)	m [-]	11
	T_0 [K]	384.02
	AMPE [%]	7.7
Wang *et al*. [66] Eq. (3)	A [-]	1.00
	B [-]	26.00
	C [-]	108.99
	n [-]	0.9142
	AMPE [%]	14.7
Correia *et al*. [4] Eq. (4)	B [-]	-8.36
	C [-]	-0.03
	AMPE [%]	13.9
Bai and Keller [67] – Rule of mixtures Eq. (5)	AMPE [%]	53.7
Bai and Keller [67] – Inverse rule of mixtures Eq. (6)	AMPE [%]	18.4

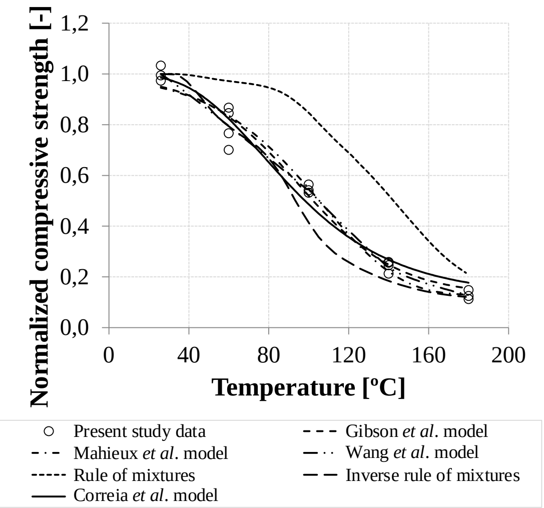

Figure 23: Variation with temperature of normalized compressive strength (compared to T_{room}) – experimental results and modelling curves.

3.4. Shear behaviour at elevated temperatures

3.4.1. Experimental programme

With the purpose of studying the shear behaviour of GFRP material at elevated temperatures, shear tests were performed according to the test method suggested in ASTM 5379/D 5379/M –

05 [68], designated as V-Notched Beam Test. In this experimental campaign, shear tests were performed at eight different temperatures: 18 (T_{room}), 40, 60, 80, 100, 120, 140 and 180 ºC.

GFRP coupons were cut from a pultruded GFRP flat plate with overall geometry of 75×20×10 mm (width × height × thickness), comprising two symmetrical V-notches at their central part (*cf*. Figure 24). Two different coupon geometries were tested, varying only in the thickness at the central part and, consequently, in the shear area of the specimens at the V-notch. Coupons type A (10 mm thick at the V-notch) were tested from T_{room} up to 180 ºC, while coupons type B (8 mm thick at the V-notch) were tested at T_{room}, 120, 140 and 180 ºC. Coupons type B were prepared by removing the superficial layer (1 mm thick) of the material in a length of 12 mm at their central part, as illustrated in Figure 24. The reason for testing coupons type B was concerned with the occurrence of premature failure modes (crushing) at the three highest temperatures in coupons type A, which is discussed in more detail next.

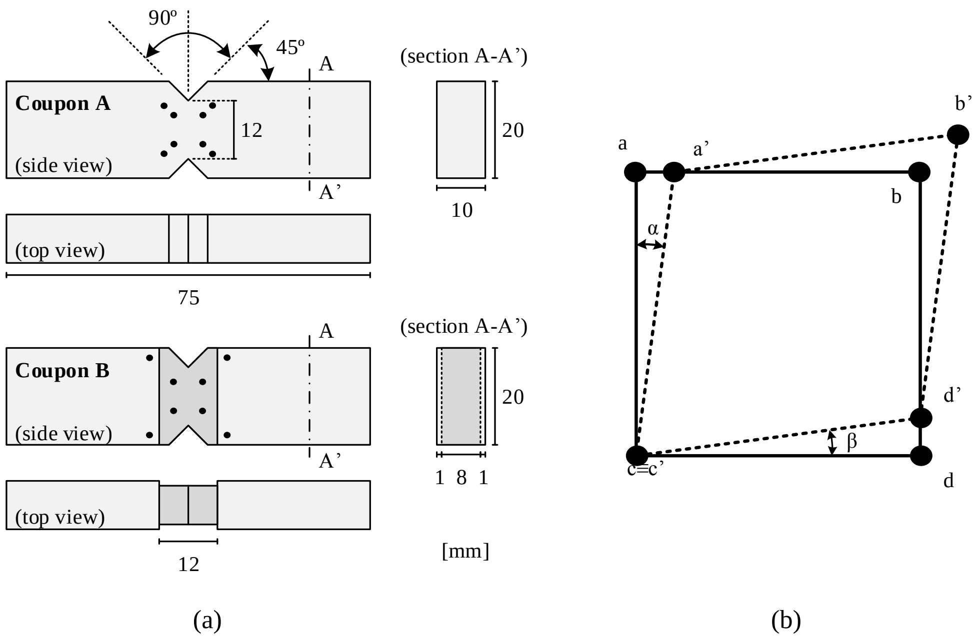

Figure 24: (a) Dimensions and target scheme used in shear coupons; (b) deformation of target dots monitored by video extensometer.

Figure 25 illustrates the test setup used for determining the in-plane shear modulus and strength – Iosipescu tests. The experimental procedure consisted of two stages: in a first stage, the coupons were heated up to the predefined temperature at an average heating rate of about 4 ºC/min, with the same thermal chamber used in the compressive tests; the second stage of the test, in which coupon's temperature remained constant, consisted of loading the test specimens up to failure under displacement control, at an approximate speed of 0.3 mm/min, which was defined in order to produce failure within 1 to 10 min, according to [68]. Load was applied with an *Instron* universal testing machine.

For each temperature and notch geometry, at least three specimens were tested. The following specimen labelling was used: T60-A-2 refers to specimen #2, with notch geometry type A tested at a temperature of 60 ºC.

The temperature in the coupons and in the air of the thermal chamber was measured by means of thermocouples type K. For the coupons, the thermocouples were installed inside a hole, drilled along their length (17.5 mm of depth; 0.25 mm of diameter). The effect of introducing such holes was assessed by means of shear tests performed at T_{room}, allowing to validate this experimental procedure (*i.e.*, no influence in both shear strength and modulus was observed). The applied load and the cross-head displacement of the test machine were also monitored during the tests.

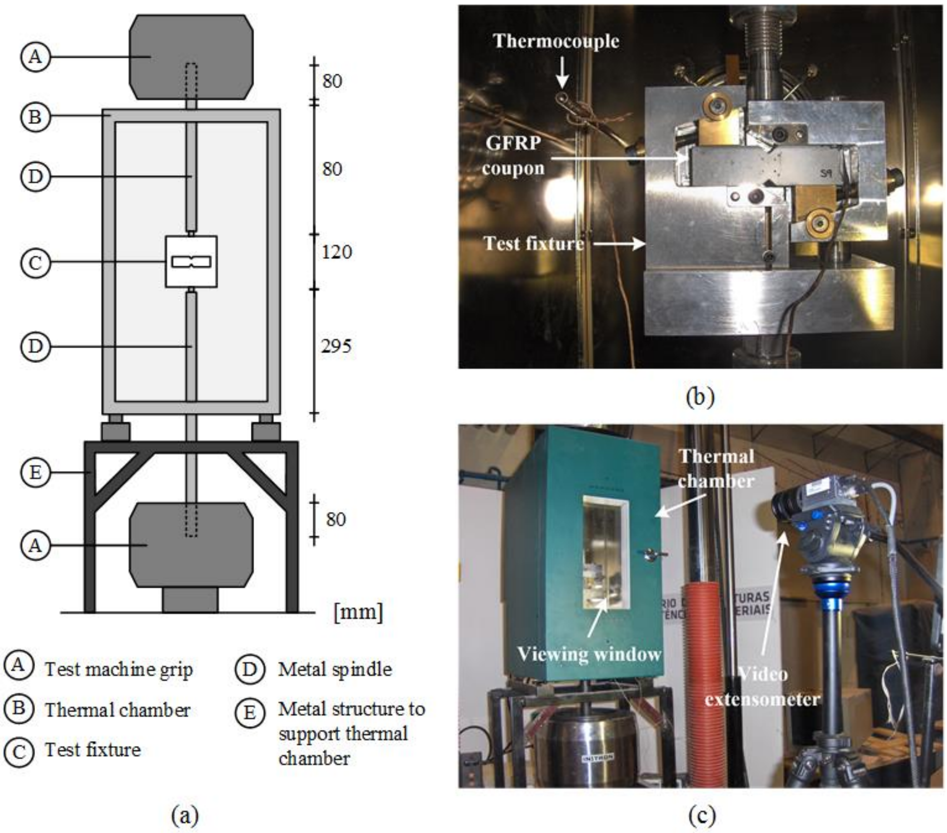

Figure 25: (a) Scheme, (b) general view of test setup and equipment and (c) thermal chamber and video extensometer used in shear tests.

The displacements at different points of the specimens was measured using a video extensometer (Figure 25 (c)), the same equipment previously used in compressive tests (see section 3.3.1.). In this case, target dots were measured at the notched central part of the specimens, as illustrated in Figure 24. The position of these targets was tracked throughout the test and, according to the test standard [68], the shear strains at the notch were estimated based on the variation of their position (*cf.* Figure 24 (b)), considering that the angle distortion is given by $\gamma = \alpha + \beta$, where $\alpha = \overline{aa'}/\overline{ac}$ and $\beta = \overline{dd'}/\overline{cd}$. The standard test method for shear properties of composite materials by the V-notched beam method [68] used in this study recommends determining the shear modulus (G) from the chord modulus over a 4‰ amplitude and for a lower bound of shear strain of 1.5‰ to 2.5‰. Applying this recommendation to the present test data would not allow estimating consistent values for shear modulus, especially at the higher temperatures. Therefore, the shear modulus was determined from the slope of the shear stress *vs*. strain curve (τ-γ) for shear stresses varying between 25% and 50% of the maximum shear stress (τ_{max}), which corresponds to a lower bound of shear strain of 2.8‰ and to an amplitude of 5.3‰ for room temperature results.

3.4.2. Experimental results and discussion

Figure 26 presents, for each target temperature, the load *vs*. displacement curves (cross-head displacement of the test machine) of one representative specimen (corresponding to an intermediate curve obtained within each series). It should be noted that the curves are not represented up to failure (*cf*. Figure 26). Moreover, up to 100 ºC the curves correspond to tests performed in specimens type A, while for temperatures above 100 ºC the results are plotted for specimens type B.

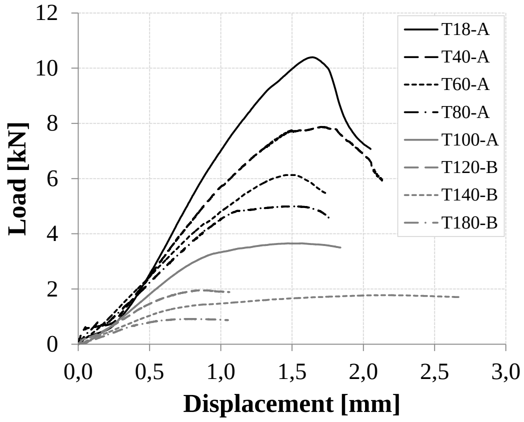

Figure 26: Load *vs*. displacement curves in shear for representative specimens of all tested temperatures.

After the initial adjustments in the test setup, in general the curves then present an approximately linear behaviour during the first stage of the test; this linear branch is shorter and not so marked for specimens tested at 180 ºC. During this linear stage, the overall stiffness presented a considerable reduction with temperature – *e.g.*, at 100 and 180 ºC, the stiffness was reduced to respectively 47% and 15% of that measured at T_{room}. This significant stiffness degradation was naturally due to the matrix softening caused by the glass transition process. For higher load levels, the behaviour then became nonlinear with a progressive (global) stiffness reduction until the maximum load was attained. At T_{room} the load decreased quite steeply;

however, for increasing temperature, in particular above the $T_{g,onset}$ (~104 ºC), the post-peak behaviour of the curves progressively changed, with the load reduction occurring in a much smoother way, even presenting a plateau for temperatures higher than 100 ºC. This post-peak behaviour change should also be related to the glass transition process underwent by the GFRP material, during which the viscosity of the material increases and so does its deformation capacity. It is still worth mentioning that in specimens type A, for the three highest temperatures, there was some local crushing of the GFRP material at the supports (as discussed later), which also influenced the (overall) cross-head displacement measured in the experiments; for this reason only the curves obtained for these highest temperatures and for specimens type B (in which such local crushing was not observed) are shown in Figure 26.

Table 6 lists, for each temperature series, the average and standard deviation values of overall stiffness ($K_{F\text{-}d}$) determined from the slope of the load *vs*. displacement curves in their linear branch. Furthermore, the table also displays the results obtained in terms of maximum load (F_{max}), shear strength (τ_{max}) and shear modulus (G), which will be addressed ahead in this section.

Table 6: Results obtained in the shear tests in terms of overall stiffness ($K_{F\text{-}d}$), maximum load (F_{max}), shear strength (τ_{max}) and shear modulus (G) – average ± standard deviation.

Series	**T [ºC]**	**$K_{F\text{-}d}$ [kN/mm]**	**F_{max} [kN]**	**τ_{max} [MPa]**	**G [GPa]**
T18-A	18 ± 2	9.3 ± 1.2	9.9 ± 0.8	75.7 ± 2.9	3.5 ± 0.3
T40-A	40 ± 2	6.9 ± 0.9	7.6 ± 0.3	59.9 ± 1.7	2.9 ± 0.3
T60-A	60 ± 2	5.7 ± 1.2	6.3 ± 0.3	48.3 ± 2.0	2.4 ± 0.2
T80-A	80 ± 2	4.5 ± 0.9	4.6 ± 0.4	36.2 ± 2.0	1.6 ± 0.3
T100-A	100 ± 2	4.4 ± 0.1	3.7 ± 0.1	28.1 ± 0.9	1.3 ± 0.3
T120-B	120 ± 2	2.8 ± 0.4	2.1 ± 0.1	19.5 ± 0.6	1.1 ± 0.3
T140-B	140 ± 2	2.3 ± 0.5	1.7 ± 0.3	15.6 ± 0.8	0.8 ± 0.1
T180-B	180 ± 2	1.4 ± 0.3	0.9 ± 0.0	8.8 ± 0.4	0.8 ± 0.1

It should also be noted that specimens type B were also tested at T_{room}. The results of such tests were in good agreement with those obtained for coupons type A, in terms of both shear strength and shear modulus, thus validating the experimental procedure adopted. Regarding shear strength, average values of 75.7 ± 2.9 MPa and 72.0 ± 2.5 MPa were obtained respectively for coupons type A and B, whereas the corresponding average values for the shear modulus were 3.5 ± 0.3 GPa and 3.4 ± 0.1 GPa. In both cases, the shear modulus at T_{room} was consistent with experimental data reported in the literature [25, 69]. On the other hand, the shear strength obtained at T_{room} was above the range referred by Bank [25] for similar pultruded GFRP materials; however, the test methods corresponding to such range are not mentioned and it is well known that shear strength can vary considerably with the test method [70]; moreover, the shear strength obtained herein is similar to that of isophthalic polyester resin reported by Barbero [69].

Figure 27 presents, for each target temperature, the shear stress *vs*. shear strain curves of one representative specimen: for temperatures up to 100 ºC, results obtained from specimens type A are plotted, whereas for 120, 140 and 180 ºC, the curves correspond to specimens type B. A representative curve of specimens type B tested at room temperature is also presented in Figure 27. The curves are plotted beyond failure. In this case, unlike the compressive tests, the strain measurements obtained from the video extensometer technique were fairly accurate. This is attributed to the different failure mechanisms observed in the two types of tests.

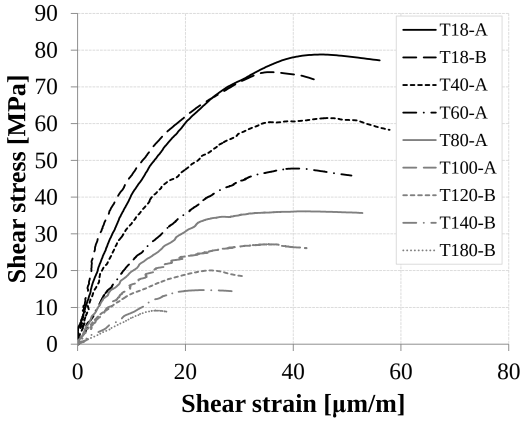

Figure 27: Shear stress *vs*. shear strain curves for representative specimens of all tested temperatures.

Figure 27 shows that in the initial steepest path, the shear stress *vs*. strain curve is approximately linear and then exhibits a nonlinear behaviour up to failure and, consequently, a stiffness reduction. Such nonlinear tendency was also observed in the load *vs*. deflection response, but to a lower extent. At room temperature, it is worth mentioning that the constitutive relation in shear obtained for specimens type B was similar to that obtained for specimens type A; this validated the procedure adopted to derive the shear stress *vs*. shear strain curves at 120, 140 and 180 ºC and to estimate values of τ_{max} and G.

As expected, these results highlight the significant shear strength reduction caused by the temperature increase. Moreover, a noticeable shear modulus (given by the slope of the shear stress *vs*. strain curves) decrease also takes place, mainly due to the softening of the polymeric matrix at higher temperatures.

Figure 28 shows the variation with temperature of the normalized shear strength and modulus of the pultruded GFRP material. It can be seen that both material properties exhibit a considerable reduction with temperature. The shear strength presented a reduction of 36% at only 60 ºC (compared to T_{room}), and that reduction increased to 88% at 180 ºC. Similarly, the shear modulus suffered reductions of 31% at 60 ºC and 78% at 140 ºC. From 140 to 180 ºC the shear strength was further reduced, while the shear modulus remained approximately constant. Overall, the reduction of the shear properties with temperature was particularly steep for temperatures that are considerably lower than the T_g (~141 ºC) and also of the $T_{g,onset}$ (~104 ºC).

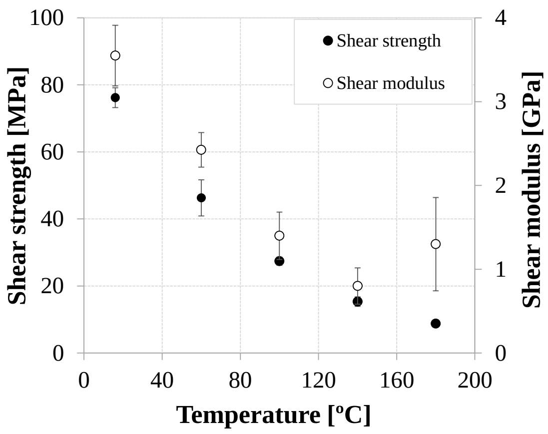

Figure 28: Variation of shear strength and modulus with temperature.

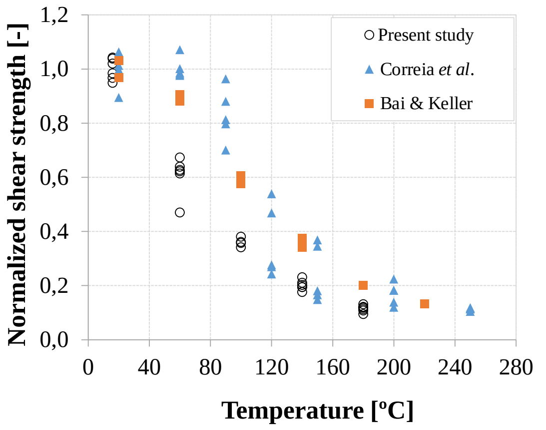

Figure 29: Comparison of the normalized shear strength reduction with temperature – present study *vs*. other studies reported in literature [4, 63].

Figure 29 compares the results obtained in the present study (using the Iosipescu setup) in terms of normalized shear strength (ratio to the strength measured at T_{room}) with the experimental data reported earlier by Bai and Keller [63] and Correia *et al*. [4] (obtained from 10º off-axis tensile tests). It can be seen that the shear strength reduction with temperature obtained in the present study, although presenting the same qualitative pattern to that reported in the literature, occurred much sooner (*i.e.*, for lower temperatures). In this respect, it is relevant to mention that the experiments conducted by Bai and Keller and Correia *et al*. (in this case, using the same material tested herein) comprised 10º off-axis tensile tests; hence, specimens were subjected to both shear and tension. Therefore, the relative difference between such data and the results obtained now should be due to the higher susceptibility of shear strength to elevated temperature when compared to tensile strength.

Regarding the failure modes, coupons type A exhibited two different failure modes. For temperatures up to 100 ºC, failure occurred due to shear in the central section of the specimen, with rupture of the matrix and of the superficial mats and formation of a vertical fracture surface (Figure 30(a)). At 180 ºC and in some specimens tested at 120 and 140 ºC, failure occurred due to ply delamination and crushing of the GFRP material above the fixed support, next to the bottom V-notch (*cf*. Figure 30(b)). In coupons type B, this (premature) failure mode was avoided, since the thickness of the specimens in the central part was reduced. By reducing the shear area in the central part (and keeping the same compressive area in the support), it was possible to promote the intended shear failure mode in the central section, as illustrated in Figure 30(c).

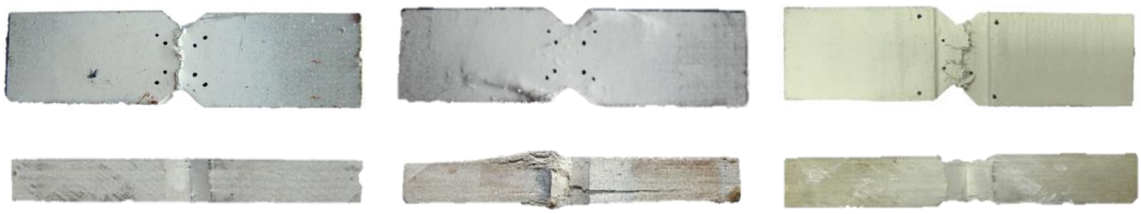

(a) (b) (c)

Figure 30: Typical failure modes of coupons type A tested at (a) T ≤ 100 ºC and (b) T ≥ 120 ºC; and (c) coupons type B tested at T ≥ 120 ºC.

3.4.3. Analytical modelling

As mentioned, empirical mathematical formulations and semi-empirical approaches (presented in section 3.3.3.) were proposed to estimate the variation with temperature of the mechanical properties of FRP materials in previous studies. Using these analytical models, one aimed at simulating the evolution with temperature of shear strength and modulus.

In order to predict the shear strength and modulus variation with temperature, the modelling curves presented in section 3.3.3. were fitted to the experimental results obtained in the present study. Once more, for the empirical models, the theoretical curves were obtained simply by fitting the experimental data (for all test temperatures) using a standard procedure that minimizes the mean square errors to the experimental results. For the models of Bai and Keller, as they are semi-empirical, the definition of the modelling curve only requires the parameters (experimental data) presented in Eq. (5) and Eq. (6), namely the mechanical properties at two given temperatures (before and after glass transition) and the DMA results.

The parameters obtained for the different models are listed in Table 7, which also includes the values of the absolute mean percentage error (AMPE), used to assess the relative accuracy of the different fitted curves with respect to the experimental data. Figure 31 and Figure 32 plot the variation with temperature of the normalized experimental values of shear strength and modulus, respectively, together with the different modelling curves described above.

In general, it is shown that the empirical modelling curves presented a good agreement with the experimental data, indicating that those models are able to provide reasonably accurate estimates of the mechanical properties in shear. The model of Correia *et al*. [4] provided the most accurate estimates for the degradation of the shear strength and modulus with temperature, presenting the lowest values of AMPE (*cf*. Table 7).

Table 7: Simulation of GFRP shear strength and modulus – parameter estimation and absolute mean percentage error (AMPE) for the different models.

Model	Parameter	Shear strength	Shear modulus
Gibson *et al*. [20] Eq. (1)	k' [-]	0.0205	0.0195
	$T_{g,mech}$ [ºC]	74.86	79.08
	AMPE [%]	8.3	17.9
Mahieux *et al*. [65] Eq. (2)	m [-]	9	9
	T_0 [K]	365.41	370.35
	AMPE [%]	9.1	20.7
Wang *et al*. [66] Eq. (3)	A [-]	1.00	1.00
	B [-]	18.00	18.00
	C [-]	29.39	25.94
	n [-]	0.6518	0.6104
	AMPE [%]	10.9	19.3
Correia *et al*. [4] Eq. (4)	B [-]	-5.10	-4.99
	C [-]	-0.03	-0.03
	AMPE [%]	6.2	14.4
Bai and Keller [67] - Rule of mixtures Eq. (5)	AMPE [%]	52.2	49.2
Bai and Keller [67] - Inverse rule of mixtures Eq. (6)	AMPE [%]	15.6	23.9

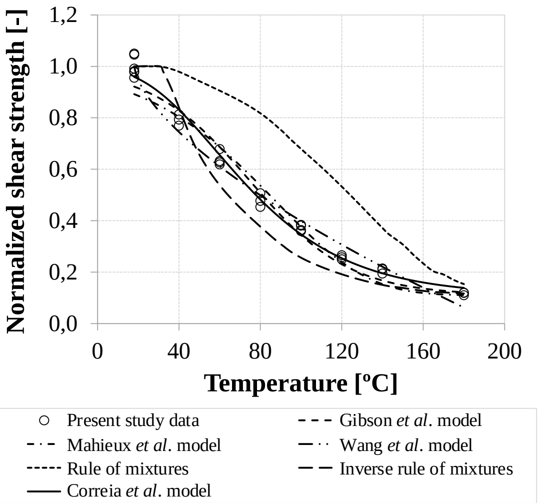

Figure 31: Variation with temperature of normalized shear strength (compared to T_{room}) – experimental results and modelling curves.

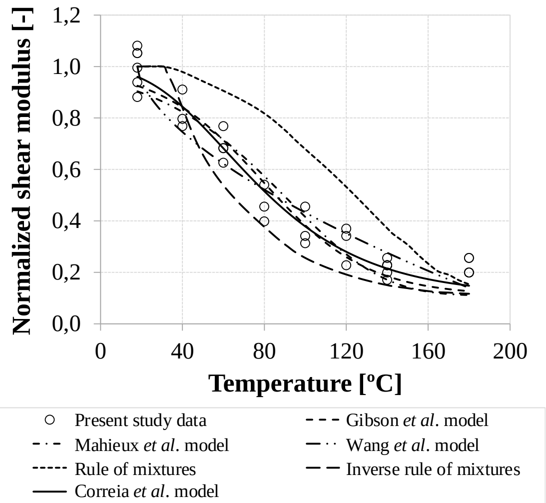

Figure 32: Variation with temperature of normalized shear modulus (compared to T_{room}) – experimental results and modelling curves.

The models of Bai and Keller [67] were less accurate than the various empirical models in simulating the variation with temperature of the GFRP shear properties, exhibiting the highest AMPE values. In this regard, it is worth reminding that these semi-empirical models only require as input the mechanical properties at two temperatures (before and after glass transition) and the DMA and TGA data, *i.e.* they require much less experimental data. As expected, the inverse rule of mixtures (Eq. (6)) provides a much better agreement with the experimental properties in shear than the rule of mixtures (Eq. (5)) – this confirms the findings reported by Bai and Keller [63] when assessing the shear strength from 10º off-axis tensile tests.

3.5. Concluding remarks

Dynamic mechanical analyses (DMA) carried out on the pultruded GFRP material allowed determining its glass transition temperature (T_g), which was set at 141 ºC, based on the peak value of the loss modulus curve. On the other hand, differential scanning calorimetry (DSC) and thermogravimetric analyses (TGA) allowed determining its decomposition temperature (T_d), which was set at 370 ºC, based on the middle temperature of the sigmoidal mass change.

The compressive tests performed on pultruded GFRP material at elevated temperatures (ranging from room temperature to 180 ºC) confirmed the remarkable influence of elevated temperature on its mechanical behaviour in compression. For instance, the compressive strength experienced reductions of 55% and 87% at 100 and 180 ºC, respectively. Failure modes at room temperatures involved material crushing at the loading plates with delamination of the outer strand mat layer; at elevated temperatures (60-180 ºC), material crushing at the end plates was followed by kinking of the longitudinal fibres and wrinkling of the superficial mat layers. All these results are in good agreement with those reported in the literature. In what concerns the longitudinal compressive modulus, results obtained indicate also a considerable reduction with temperature. However, the strain measurements obtained from videoextensometry were not entirely consistent, were determined only up to 100 ºC and there are doubts about the influence of material wrinkling/delamination of the superficial mat layers on the accuracy of those measurements. Future investigations should be pursued to experimentally determine the compressive modulus of pultruded GFRP material.

The characterization of the shear behaviour of GFRP material at elevated temperatures also confirmed its susceptibility to elevated temperatures. The shear strength and modulus presented retentions of 12% and 22%, respectively, at 180 ºC compared to room temperature. Even for a moderately elevated temperature (60 ºC), the shear strength and modulus retentions were 64% and 69%, respectively. The thermal degradation of shear strength obtained in this study was qualitatively similar to that reported in literature. However, the shear strength reduction obtained in this experimental work (from Iosipescu tests) occurred for lower temperatures than that reported earlier (from 10º off-axis tensile tests); these quantitative differences should be related with the influence of tensile stresses in the latter setup, which was avoided in the present study. In these experiments, valid shear failure modes in the central section of the specimens were observed, *i.e.*, rupture of the polymeric matrix and of the superficial reinforcing mats was registered. In this case, strain measurements obtained from videoextensometry were quite consistent.

The models assessed in the analytical study (applicable to the material tested) were able to simulate accurately the variation of the compressive strength and of the shear strength and modulus with increasing temperature, namely their sigmoidal reduction. The most accurate estimates were provided by the different empirical models (curve fitting procedures). The semi-empirical models of Bai and Keller [67] based on the inverse rule of mixtures (requiring much less experimental data than the empirical models), although less accurate, still provided a reasonable agreement for the different properties considered.

Chapter 4:

Fire resistance behaviour of pultruded GFRP beams

4.1. Introduction

Previous studies, recently reviewed in [6], indicate that existing concerns about the fire behaviour of FRP structures are legitimate, especially for building applications. Indeed, when the decomposition temperature of their polymer matrix is approached (T_d, ranging from 300-500 ºC), FRP materials can ignite, spreading flames and releasing heat, smoke and toxic gases. Different approaches have been pursued to improve the fire reaction behaviour of FRP materials, including the use of different types of flame retardants, inherently flame retardant resins (*i.e.*, phenolics) or protective layers [5, 71]. The latter approach has been proved to be very effective in extending the field of application of pultruded GFRP profiles in buildings [23].

From a mechanical point of view, although glass fibres are able to retain a considerable portion of their mechanical properties at elevated temperature (the softening and melting temperatures of E-glass fibres have been reported to be 830 and 1070 ºC, respectively [5]), polymer resins soften and creep when their glass transition temperature (T_g, 100-200 ºC) is approached and exceeded. Consequently, even at moderately elevated temperatures, the mechanical properties of FRP materials can be remarkably reduced, especially the ones that are more matrix-dependent, such as the compressive and shear strengths and moduli [4, 64], addressed in the preceding chapter.

In spite of the above mentioned vulnerability, until now very few studies were conducted about the fire resistance behaviour of intermediate-to-full scale load bearing pultruded GFRP members in bending. The only experimental data available in the literature was reported by Massot [7] and Keller *et al*. [8], concerning one-way slabs, and by Ludwig *et al*. [9] and Correia *et al*. [10], concerning beams. The main findings obtained in these experiments are summarized in the next paragraphs.

In 1994, Massot [7] conducted fire resistance tests on a pultruded deck system used in off-shore platforms. The multicellular cross-section (250 mm of height, with 15 mm thick flanges and 7 mm thick webs), which was made of E-glass fibres and a flame-retarded (ATH) *Modar* acrylic resin, comprised a set of reciprocal protrusions and recessions. The deck system was tested with three 300 mm wide modules placed adjacent to one another in a 4.9 m simply supported span; the deck was loaded in a three-point bending configuration to a mid-span deflection of L/300

(L being the span) and exposed to the hydrocarbon fire [72]. Although the deck did not collapse, the test was stopped after 41 min, because smoke and flames started to propagate between adjacent modules. Due to the relatively low thermal conductivity of GFRP, at the end of the test, the temperature at the cold face of the deck was still below 100 ºC.

Twelve years later, Keller *et al*. [8] performed fire resistance tests on multicellular deck panels (195 mm of height, 15.2-17.4 mm thick flanges, 11 mm thick and inclined webs) made of E-glass fibres and non-retarded isophthalic polyester, for vehicular bridge and building applications. Two 0.914 m wide deck panels were tested in a simply supported 2.75 m span under four-point bending (also up to L/300) and subjected to the ISO 834 fire curve [13]. One of the panels was tested without protection and failed after 57 min; the collapse involved an instability mechanism on the top (colder) flange (under compression), which may have been triggered by exceeding the shear strength at the web-flange junctions [19]. The other panel was protected by means of water-cooling through the cells of the deck (1 m^3/h, full section); it presented much lower increase of deformation during fire exposure and after 120 min it still maintained its structural integrity.

Correia *et al*. [10] investigated the fire behaviour of pultruded square tubular profiles (100×100×8 mm) constituted by E-glass fibre rovings and mats embedded in an isophthalic polyester resin matrix (similar to the ones used in the present study). The 1.5 m span beams were first loaded to L/400 in a simply supported four-point bending configuration and then exposed to the ISO 834 fire only from the bottom side. A total of five beams were tested: one without protection, three with different passive protections applied on the bottom flange (calcium silicate boards, vermiculite/perlite mortar and intumescent coating) and one with a water-cooling system comprising an 8 mm thick layer of water flowing (0.4 m^3/h) over the bottom flange. The unprotected beam failed after about 38 min, the passive fire protections provided a fire resistance between 65-76 min and the water-cooling system prevented the collapse even after 120 min of exposure. The collapse always involved compressive stresses, either at the top flange (axial compression) or at the upper part of the webs under the loaded sections (transverse compression), where shear strength also seems to have been locally exceeded.

Ludwig *et al*. [9] performed the single study reported in the literature on the fire resistance of pultruded GFRP beams with open cross-sections, namely I-section profiles (E-glass and polyester) with 120 mm (IPE120) and 160 mm (IPE160) of height. The 1.5 m long beams were loaded at mid-span with 10 kN (30% of the room temperature capacity of the IPE120 section) and exposed to the ISO 834 fire curve in all sides. Both beams exhibited very low fire resistances, of only 1.45 and 2.25 min for the IPE120 and IPE160 profiles, respectively. The failure mechanism involved the local buckling of the compressed flange, followed by web buckling. In both cases, the average temperature in the GFRP material at failure had already exceeded the $T_{g,onset}$ (100 ºC), being 120 and 155 ºC, respectively in the IPE120 and IPE160 profiles. The authors also tested unloaded IPE120 profiles protected with 50 mm thick mineral wool and 0.25 mm thick water-based intumescent coating; although the profiles were subjected only to their own dead-weight, the passive protections provided fire resistances of only 16 and 12 min, respectively, thus highlighting the very poor performance of open cross-sections exposed to fire in four-sides.

The literature review presented above shows that pultruded GFRP flexural members with tubular cross-section are able to present fire endurances of 30 to 60 min (depending on the wall thickness) even without any type of fire protection, provided that they are exposed to fire only from the bottom side. For this type of exposure, it has been shown that with passive protection the fire resistance can exceed 60 min, while with water-cooling 120 min of fire endurance can be attained. The results reported by Ludwig *et al*. [9] suggest that three-side fire exposure, which is the most common in beams, may be much more severe compared to one-side exposure. However, no results are reported in the literature concerning beams exposed to fire in three-sides. In addition, the influence of the load level in the fire resistance of GFRP flexural members has not been addressed in the literature – in all studies mentioned above, a single load level was adopted.

This chapter presents further experimental investigations about the fire resistance behaviour of pultruded GFRP profiles. The main objectives were to investigate the influence on the thermal and/or mechanical responses of the beams of: (i) the number of sides exposed to fire; (ii) the load level; and (iii) using different fire protection systems (for both one- and three-side fire exposure). To this end, a total of 12 fire resistance tests were performed in GFRP beams with square tubular section. The beams were exposed to the ISO 834 fire curve in either one or three sides and were subjected to two different load levels, causing mid-span deflections of L/400 or L/250, L being the span. Various fire protection systems were compared, namely different insulation materials and water-cooling. The main novelties compared to the previous work of the authors [10] is three-fold: the evaluation of the effects of (i) the number of sides exposed to fire and (ii) the load level on the fire resistance of tubular beams and (iii) the assessment of the efficacy of water cooling when applied to tubular beams under three-side fire exposure.

4.2. Experimental programme

4.2.1. Materials

The pultruded GFRP profiles studied have a square tubular cross-section (100×100×8 mm) and were produced by *Fiberline*. This material is constituted by alternating layers of unidirectional E-glass fibre rovings and strand mats (69% of inorganic content in weight) embedded in an isophthalic polyester resin matrix. The profiles present rovings in the centre of the section walls and mats positioned next to their outer surfaces, with continuity in the web flange junctions. Table 8 lists the mechanical properties of the GFRP material, determined from coupon tests in tension, compression, flexure and shear. Three-point bending tests were performed on simply supported beams according to the test procedure described in EN 13706 [73], providing the full-section longitudinal (E_L = 31.0 GPa) and shear (G_{LT} = 3.6 GPa) moduli of the GFRP profiles.

Table 8: Mechanical properties (at room temperature) of the GFRP profiles – average and standard deviation values.

Test and direction	Strength (σ_u) [MPa]	Elastic modulus (E) [GPa]
Flexural longitudinal$^{(i)}$	352.7 ± 76.1	28.0 ± 6.1
Tensile longitudinal$^{(ii)}$	336.5 ± 87.7	39.9 ± 2.7
Compressive longitudinal$^{(iii)}$	416.4 ± 22.2	25.3 ± 2.5
Compressive transversal$^{(iii)}$	93.1 ± 14.9	8.3 ± 1.8
Interlaminar shear$^{(iv)}$	37.0 ± 2.9	-

$^{(i)}$ ISO 14125; $^{(ii)}$ ISO 527; $^{(iii)}$ ASTM D 695; $^{(iv)}$ ASTM D 2344.

According to dynamic mechanical analysis (DMA) experiments performed on GFRP material (presented in section 3.2.), the glass transition temperature (T_g) was set at 141 ºC, based on the peak value of the loss modulus curve. The decomposition temperature (T_d) of the GFRP material was set at 370 ºC, considering the thermogravimetric and differential scanning calorimetry (DSC/TGA) experiments performed and presented in section 3.2.

In this experimental campaign, the following five different materials were used as passive fire protection systems:

- Agglomerated cork (AC) boards with 25 mm of thickness, density (ρ) of 100-120 kg/m^3 and thermal conductivity (λ) of 0.04 W/mºC [74] (at room temperature); the boards are produced by *Robcork* in a process that involves grinding, heating and pressing the raw material.
- Rock wool (RW) boards with 25 mm of thickness, density of 100 kg/m^3, thermal conductivity of 0.04 W/mºC (at room temperature), and null thermal expansion

coefficient [75]; these boards, produced by *Rockwool* (according to ISO 1182), are made of rock wool fibres (non-combustible material), presenting a melting temperature higher than 1000 ºC.

- Calcium silicate (CS) boards (type H) with thickness of 25 mm, density of 500 kg/m^3, thermal conductivity of 0.09 W/mºC and nominal humidity of 3-5% [76] (at room temperature); these boards, produced by *Promatect*, are also non-combustible.
- Intumescent mat (IM) with 2 mm of thickness, density of 325 kg/m^3 (at room temperature), expansion ratio of 12:1 and activation temperature of 190 ºC [77]; this mat (Technofire 60853A), supplied by *Technical Fibre Products Lda*, is constituted by graphite fibres and suffers an intumescence process as a result of temperature increase, thus providing a fire barrier. These mats can be either bonded to the surface of the members to be protected (the solution used in the present study) or incorporated directly in the pultrusion line.
- Intumescent coating (IC) with thickness of 2 mm (after drying), density of 1320 kg/m^3, solids volume of 69% and volatile organic compound content of 412 g/L [78] (at room temperature). This intumescent material (C-THERM HB), supplied by *CIN*, exhibits also a volume increase when subjected to heat exposure, thus forming a fire protective foam barrier with low density.

DSC/TGA experiments were also carried out on different fire protection materials (also used in the fire resistance tests) – agglomerated cork, rock wool, calcium silicate, intumescent mat and intumescent coating. TGA results are presented in Figure 33.

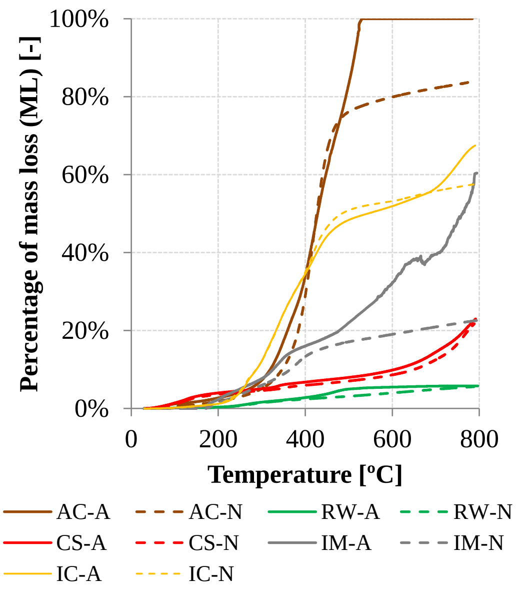

Figure 33: TGA results for all fire protection materials tested in air (A) and nitrogen (N) atmospheres.

DSC/TGA tests performed on the fire protection materials allowed assessing their mass loss as a function of temperature, showing that: (i) the decomposition of agglomerated cork (AC) starts at temperatures above 200 ºC, with mass loss above 500 ºC ranging from 80% (nitrogen) and 100% (air); (ii) rock wool (RW) presents a small percentage of mass loss (about 6% at 800 ºC); (iii) calcium silicate (CS) exhibits also a small mass loss (below 20% at 800 ºC), with such mass loss increasing especially from 600 to 800 ºC; (iv) the mass loss of the intumescent mat (IM) is relatively high, ranging between 20% (nitrogen) and 60% (air); and (v) the intumescent coating (IC) exhibits very significant mass loss for temperatures above 200 ºC, with the mass loss at the end of the test ranging from 55% (nitrogen) and 70% (air).

4.2.2. Test programme

As mentioned, the experimental programme was designed to evaluate the thermal and mechanical responses, the failure modes and the fire resistance of pultruded GFRP beams. The main goals were to study the effects on those responses of (i) applying different fire protection systems, (ii) exposing the GFRP beams to fire in either one or three sides, and (iii) varying the load level. To that end, the test programme included a total of 12 fire resistance tests in 1.6 m long pultruded GFRP beams, divided in three series, as summarized in Table 9.

Table 9: Overview of the fire resistance tests performed on pultruded GFRP beams.

Series	Specimen	Fire protection	Fire exposure	Load level
Series S1	U-S1	-	E1S (one-side exposure)	L/400 (11.7 kN)
	AC-S1	Agglomerated cork		
	RW-S1	Rock wool		
	CS-S1	Calcium silicate		
	IM-S1	Intumescent mat		
	IC-S1	Intumescent coating		
	WC-S1	Water-cooling		
Series S2	U-S2	-	E3S (three-side exposure)	L/400 (11.7 kN)
	CS-S2	Calcium silicate		
	WC-S2	Water-cooling		
Series S3	U-S3	-	E1S	L/250 (18.7 kN)
	CS-S3	Calcium silicate		

Series S1 comprised seven specimens, one unprotected and six with different fire protection systems, five passive (agglomerated cork, rock wool, calcium silicate, intumescent mat and intumescent coating) and an active water-cooling system (described in section 4.2.3.). In this series, the beams were exposed to fire only in one side (the bottom one) and were subjected to a total load of 11.7 kN, corresponding to the serviceability load for a mid-span deflection of

L/400 (L being the span). The applied load corresponds to about 7.6% of the flexural strength determined from full-scale beam tests carried out at room temperature.

Series S2 included three beams, all exposed to fire in three sides (the bottom and lateral ones) and subjected to the same service load used in series S1. In addition to an unprotected beam, a single passive system was tested (calcium silicate), as well as the active water-cooling system. As mentioned, the performance of these fire protection systems under this type of fire exposure had not yet been assessed.

Finally, in series S3 two beams were exposed to fire in one side and subjected to a total load of 18.7 kN (about 12.2% of room temperature strength), corresponding to the serviceability load for a mid-span deflection of L/250. One beam was tested without any protection and the other was protected with calcium silicate.

4.2.3. Test setup, instrumentation and procedure

Regarding the test setup used, the fire resistance tests were conducted using a vertical oven, with external dimensions of 1.35×1.20×2.10 m (long × wide × high), as illustrated in Figure 34. The oven is fired by six gas burners and is controlled by a computer, which allows adjusting the burners' intensity in order to follow, as close as possible, a predefined time-temperature curve. In the present study, the time-temperature curve defined in ISO 834 [13] was adopted. As illustrated in Figure 35 the furnace has two different top cover sets, one causing fire exposure in only one side (the bottom one) of the test specimen (positioned on the top of the furnace) and the other allowing for three side fire exposure (the bottom and lateral sides).

The tubular profiles were tested in four-point bending, in a simply supported span of 1.30 m. The total length of the span directly exposed to fire was 0.95 m. The load was applied by means of concrete blocks (with known weight), suspended by a load transmission steel beam with pulley blocks, as illustrated in Figure 34. To allow for the free vertical deformation of the GFRP beams along their span during the fire experiments, the specimens were positioned keeping a vertical distance of 50 mm between their bottom surfaces and the oven's lateral walls.

As mentioned, some of the tubular beams were protected against fire using a water-cooling system. The active fire protection system used in these experiments, similar to the one adopted in [8, 10], is constituted by two flexible rubber hoses, a flow-rate meter, a flow valve control and two metallic covers, as schematized in Figure 36. In these experiments, a water flow of 0.4 m^3/h was adopted (as in [8, 10]), provided by the laboratory building's water supply network. As shown in Figure 36, only the bottom flange was protected with an 8 mm thick layer of flowing water.

In terms of instrumentation, the thermal response of the GFRP beams was monitored at mid-span section using thermocouples type K, which were inserted into holes drilled at predefined depths and bonded with polyester resin. The number and position of the thermocouples varied according to the type of fire protection system used and the number of sides exposed to fire, as presented in Figure 34. In general, three thermocouples (T1-T3) were installed in the top flange (at depths of about 2.0, 4.0 and 6.0 mm, respectively), three (T4-T6) were placed along the height of the web (all at mid-depth), and five (T7-T11) were positioned in the bottom flange (at depths of 0.5, 2.0, 4.0, 6.0 and 7.5 mm, respectively).

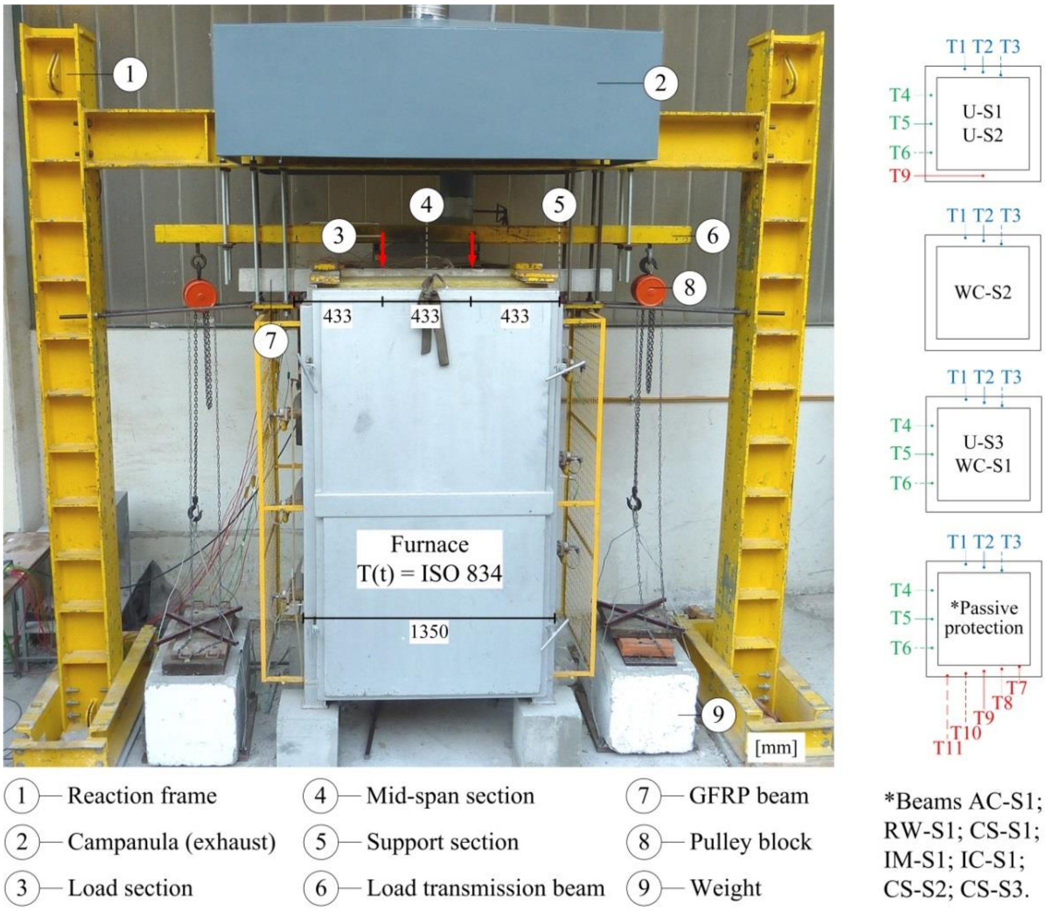

Figure 34: Frontal view of test setup (left) and thermocouples position at mid-span section (right).

To measure the mechanical response of the beams, one wire displacement transducer from *TML* (model CDP-500) was used to measure deflections at mid-span section; the transducer was positioned at the centre of the top surface of the beams.

Concerning the experimental procedure adopted, the fire resistance tests started with the application of the structural load, either 11.7 kN (series S1 and S2) or 18.7 kN (series S3). After a period of about 10 min, set in order to guarantee the stabilization of deformations, the furnace’s burners were turned on and the specimens were thermally loaded up to failure or until 120 min of fire exposure (the maximum duration predefined for the experiments). In the beams protected with water-cooling, prior to the application of the structural load, the water circuit was opened and the water flow was adjusted to the predefined value. During the fire resistance tests, which were performed at initial temperatures ranging from 15 to 25 ºC, the mid-span deflections and temperatures were recorded using built-in data loggers from *HBM*.

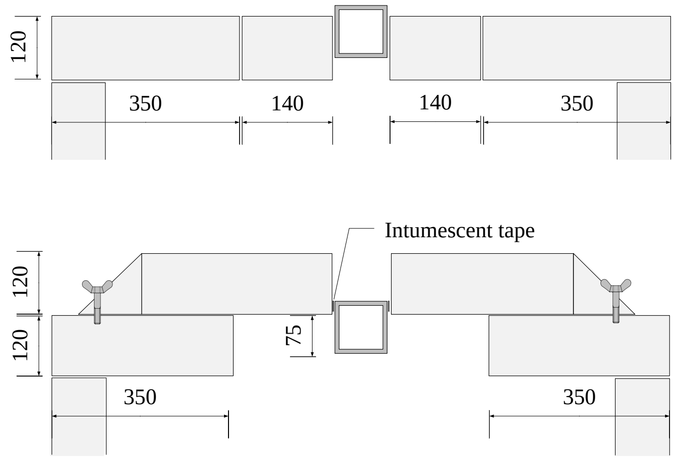

Figure 35: Cross-section of test setup for one side (top) and three sides (bottom) exposure.

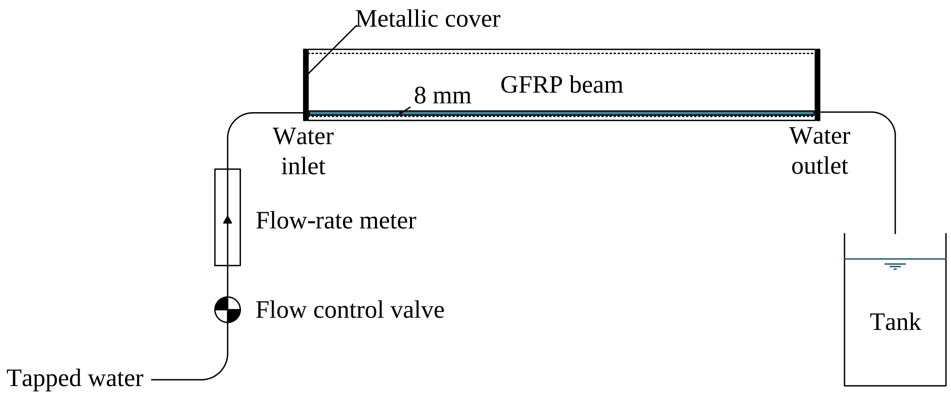

Figure 36: Scheme of the water-cooling system used.

Figure 37 shows the evolution of the furnace temperatures in the different tests, together with the ISO 834 [13] standard curve. It can be seen that all experimental curves are in (very) close agreement with the time-temperature curve defined in ISO 834. The highest deviation was recorded during the first 20 min of the test AC-S1, with the furnace temperature quickly approaching the standard curve after that initial period.

4.3. Results and discussion

4.3.1. Thermal response

Figure 38 presents the temperature profile measured in the reference beam U-S1 (one-side exposed to fire); the glass transition (T_g) and decomposition (T_d) temperatures of the GFRP material are also plotted as a reference. In beam U-S1, the average temperature at the bottom flange reached the T_g after about 3 min and attained the T_d after about 17 min. At the end of the test (failure instant), elevated ($T \geq T_g$) and moderate ($T \approx T_g$) temperatures were registered in (most of) the web and top flange, respectively, while the temperature at the centre of the bottom flange had largely exceeded T_d.

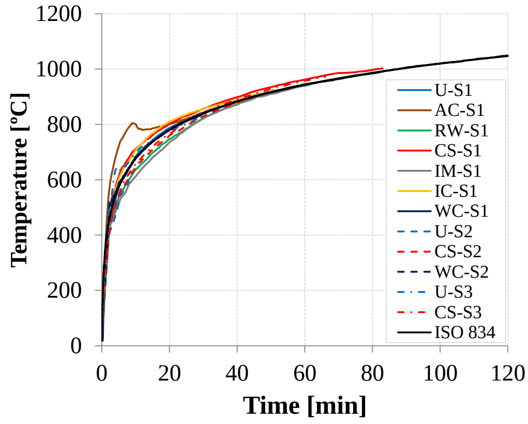

Figure 37: Evolution of furnace temperature in all tests.

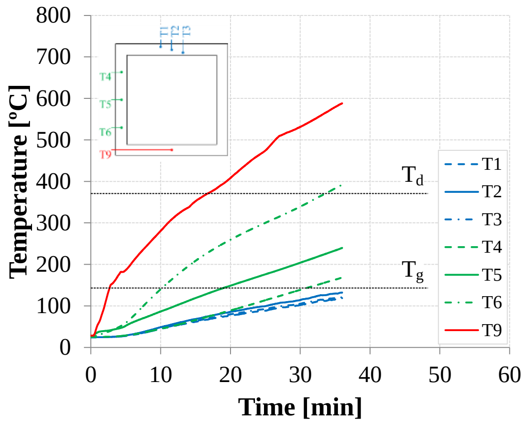

Figure 38: Temperature profile measured in beam U-S1.

Figure 39 presents the temperatures profiles measured in the beams from series S1 (exposed to fire in one side) at different section walls, namely at (i) the centre of the top flange (T2), (ii) the middle of the web (T5) and (iii) the centre bottom flange (T9). As expected, for similar exposure durations, the unprotected beam (U-S1) exhibited the highest temperatures in the different section walls.

Taking beam U-S1 as reference, a significant temperature reduction was achieved with the various passive fire protections, especially with CS, RW and AC thick boards, which presented comparable performance; for these beams, the T_g was attained at the centre of the bottom flange after respectively 32, 26 and 27 min (*vs*. 3 min in beam U-S1), *i.e.*, those systems provided 23 (RW) to 29 (CS) min of thermal insulation to the bottom flange (considering the time to attain T_g as an insulation criterion). In the case of beam CS-S1, after 60 min of fire exposure, the temperatures at the different monitoring points were lower than those measured in beam U-S1 after 30 min.

The intumescent fire protections (the IM and especially the IC) were (much) less effective than the thicker passive fire protection systems, extending the period of time for the centre of the bottom flange to attain T_g in about 2 min (using protection IM). The limited effectiveness of these passive systems in providing fire protection to the GFRP profiles (especially to the bottom flange) is attributed to its very low thickness (compared to the much thicker AC, CS and RW boards) and relatively high activation temperature. As mentioned, the activation temperature of the IC is higher than 190 ºC, already well above the T_g of the GFRP material.

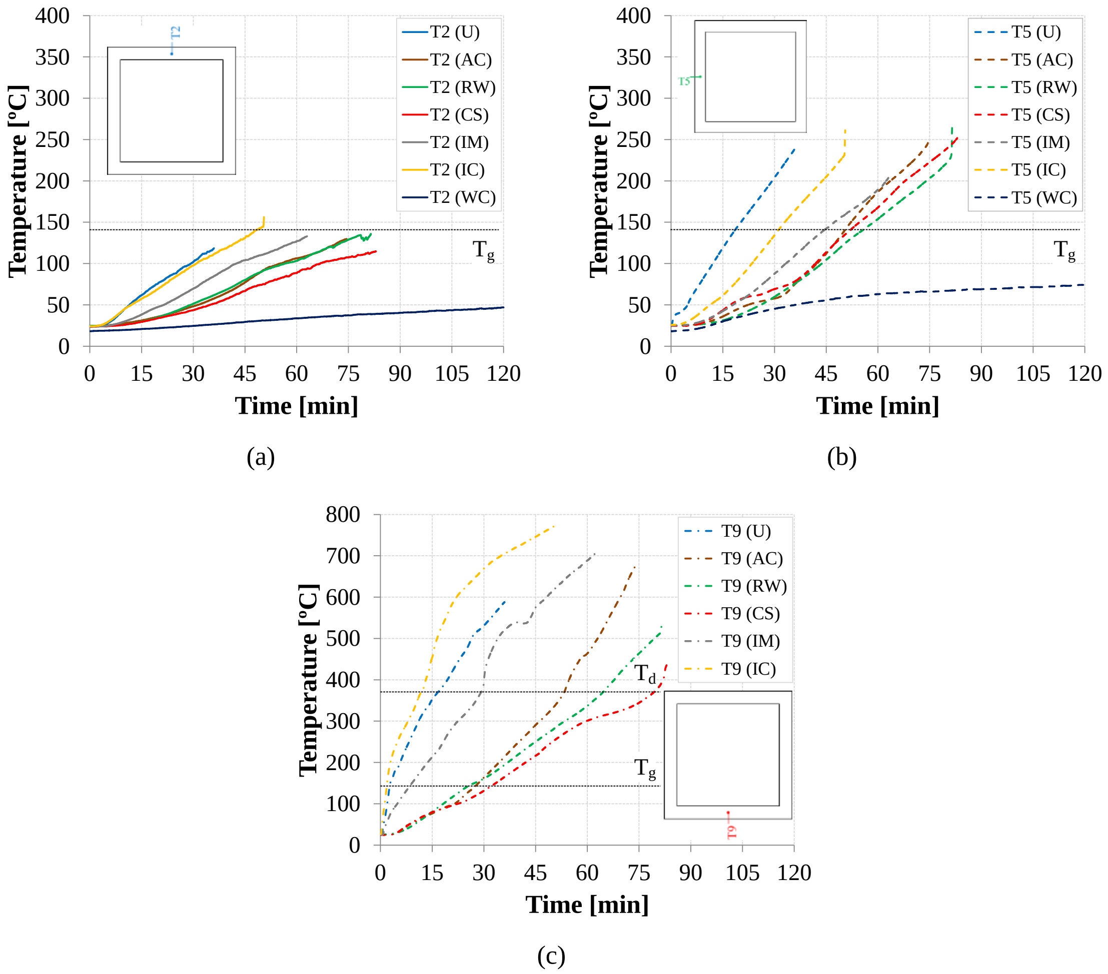

Figure 39: Temperature profiles for beams from series S1 (a) at centre of top flange, (b) mid-height and depth of web and (c) centre of bottom flange.

The active fire protection system provided considerable reduction of the temperatures at the top flange and webs, with temperatures in those walls remaining lower than T_g during 120 min. In fact, at the end of the test, temperatures at the centre of the top flange and mid-height of the web were only 47 and 74 ºC, respectively. This explains the good mechanical performance of beam WC-S1 (*cf.* section 4.3.2.). Although the temperatures at the bottom flange were not monitored in this specific beam (due to concerns associated with drilling holes in the GFRP material and the possible consequent leakages), previous experiments conducted by Correia *et al.* [10] and numerical studies developed in the framework of this thesis indicate that the water-cooling system should have been much less effective in protecting this section wall than the CS, RW and AC boards.

As expected, very similar thermal responses were registered in equivalent beams from series S1 and S3, as they were subjected to the same type of fire exposure.

Figure 40 compares the temperatures measured in beams from series S1 and S2 (one- and three-side fire exposure, respectively), both unprotected and protected with CS boards. These thermal responses agree well with the measurements performed in GFRP columns (chapter 5).

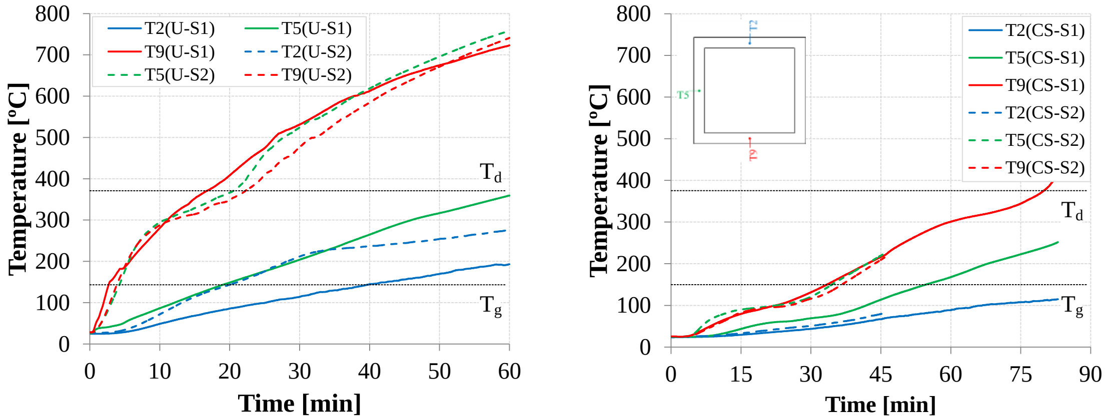

(a) (b)

Figure 40: Temperature profiles for series S1 (one-side exposure) and S2 (three-side exposure) in (a) unprotected beams and (b) beams with CS protection.

As for one-side exposure, the passive fire protection with CS boards provided very significant reduction of the temperatures at the different section walls, compared to the unprotected profile. In the unprotected beam (U-S2), the glass transition temperature (T_g) was attained at the web (T5) and top flange (T2) after respectively 4 and 19 min, thus explaining its poor fire resistance (*cf.* section 4.3.2.). By using the passive fire protection (CS-S2), the web was afforded 29 min of thermal insulation (once again, considering the time to attain T_g as an insulation criterion). At collapse (46 min), the temperature at the top flange was 82 ºC (relatively high, but still below T_g), which attests the effectiveness of this fire protection in retarding considerably the heating of the top flange for three-side fire exposure.

The following additional aspects are highlighted regarding the influence of three-side fire exposure: (i) as expected, the evolution of temperatures at the bottom flange was basically analogous to that observed for one-side exposure, since the heat exposure of that specific wall was also the same; (ii) for a given beam under three-side exposure, the evolution of temperatures at the bottom flange and web was very similar, since those walls were both directly exposed to fire; (iii) without fire protection, as expected, temperatures at the top flange were significantly higher for three-side exposure than for one-side exposure – although the GFRP material exhibits relatively low thermal conductivity, for the former type of exposure the webs are directly exposed to fire; and (iv) with CS protection, temperatures at the top flange remained below T_g for both one- and three-side exposure, being only slightly higher for the latter type of fire exposure – this is attributed mostly to the effectiveness of the fire protection provided by the CS boards.

4.3.2. Mechanical response

Figure 41(a) presents the mid-span deflection measured in the beams tested from series S1, *i.e.* under fire exposure from the bottom side and loaded to a mid-span deflection of L/400. In beams U-S1 and WC-S1, vertical displacements suffered a rapid increase during the first 5-10 min of fire exposure, due to relatively fast heating of the bottom flange, which causes (i) a thermal gradient throughout the depth of the cross-section and (ii) a stiffness loss. The beams protected with intumescent materials also presented relatively fast deformation increase at the early stages of the test (beam IM-S1 and especially beam IC-S1); this is explained by the fact that these materials, as mentioned, were not fully effective in providing thermal barrier to the bottom flange during that initial period. In the beams protected with thick board systems (AC-S1, RW-S1 and CS-S1) the deformation increase during the initial stage of the test was relatively low; this is associated to the effective thermal insulation provided to the bottom flange by those fire protection systems. After that initial period, with the exception of beam WC-S1, mid-span deflection continued to increase, at progressively increasing rates up to failure. Regarding beam WC-S1, the vertical displacements stabilised and remained almost constant after 30 min, in line with the temperatures measured in the webs and top flange, which presented very limited increase after that period. In other words, the deformation increase presented by this beam was caused mostly by the stiffness loss experienced by the bottom flange (and the corresponding thermal gradient). These results are very consistent with previous investigations reported by Correia *et al.* [10].

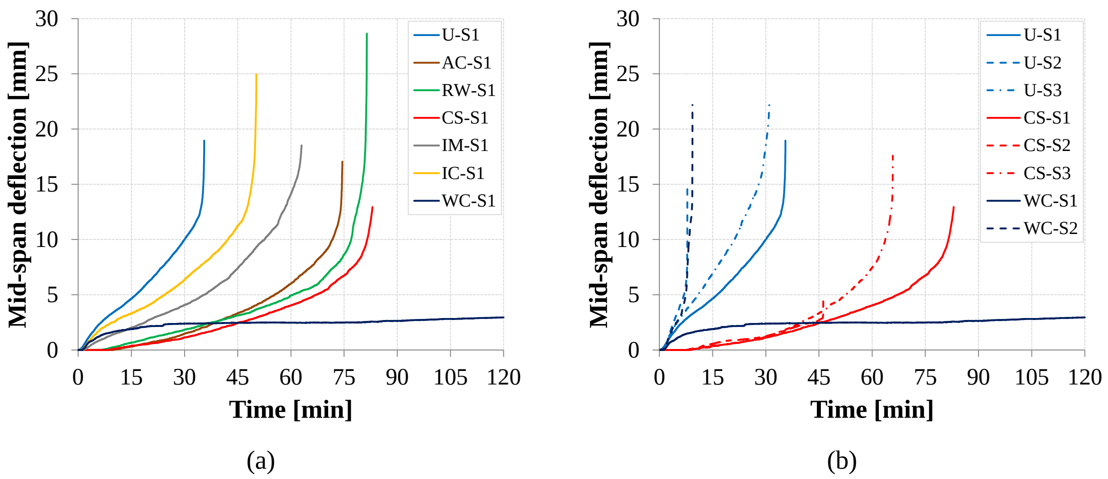

Figure 41: Comparison between mid-span deflection measured in (a) beams from series S1 and (b) beams from series S1, S2 and S3.

Figure 41(b) compares the mechanical responses of equivalent beams from series S1, S2 and S3, allowing to assess the influence of the number of sides exposed to fire (S1 and S2, respectively one and three sides) and the load level (S1 and S3, mid-span deflections of respectively L/400 and L/250) on the evolution of vertical displacements.

As for one-side exposure, the beams without passive protection exposed to fire in three sides exhibited a rapid increase of vertical displacements; compared to equivalent beams of series S1, beams U-S2 and WC-S2 presented much faster increase of vertical displacements at the early stages of the tests. This is basically due to the fact that now it was not only the bottom flange but also most of the webs' depth that were directly exposed to heat and hence contributed to the stiffness reduction of the cross-section. In these beams, the three-side fire exposure involved such a severe thermal load that the specimens collapsed very prematurely, presenting fire resistances lower than 10 min, which compares with 36 min and more than 120 min in beams U-S1 and WC-S1, respectively. In fact, as illustrated in Figure 42 at a certain point the bottom flange and the webs provided only a residual contribution to the flexural strength of the cross-section, which basically stemmed from the top flange.

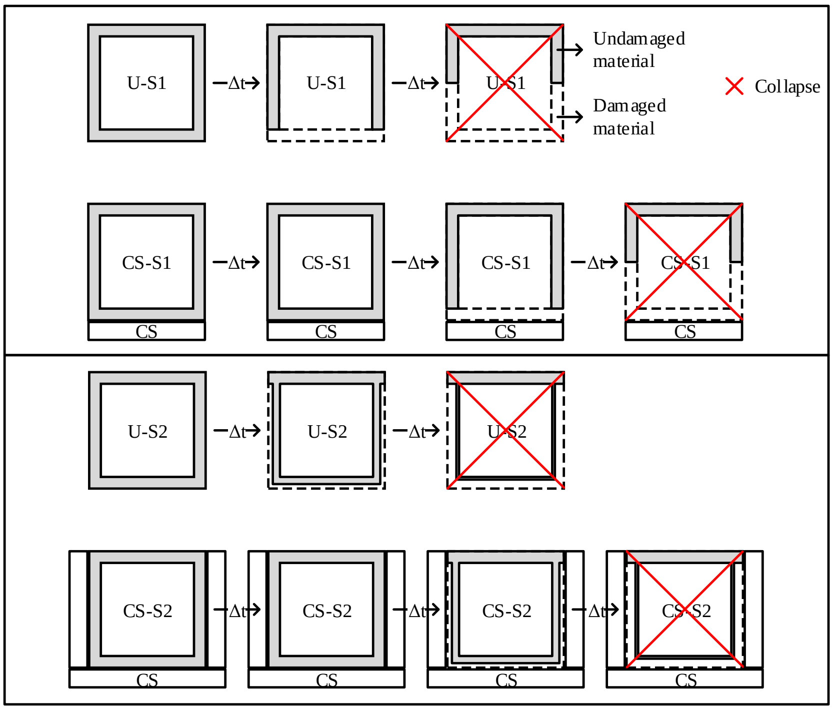

Figure 42: Illustrative scheme of the evolution of the residual cross-section of the beams under one- (U-S1 and CS-S1) and three-side (U-S2 and CS-S2) fire exposure.

Now comparing the mechanical behaviour in fire of the beams protected with CS boards exposed to fire in either one (CS-S1) or three sides (CS-S3), roughly similar mechanical responses were observed during the first 30 min of fire exposure (Figure 41(b)). Subsequently (and up to failure), the mid-span deflections of beam CS-S2 started to increase at a faster rate than those of beam CS-S1. This is consistent with the thermal insulation provided by the CS boards measured in the fire resistance tests – based on temperature measurements, it was concluded that they provided about 30 min of thermal insulation (considering the time to attain T_g as an insulation criterion). In beam CS-S2, after that period, the stiffness of both the bottom flange and the webs were significantly affected, while in beam CS-S1 most of the webs' depth was still well below T_g and therefore these walls mechanically contributed to the overall stiffness (and strength) of the cross-section (Figure 42).

Finally, regarding the influence of the load level, in both unprotected beams and beams protected with CS boards the mechanical behaviour was qualitatively similar for the two different load levels. The initial deformation increase was very similar and at some point mid-span deflections of beams subjected to higher load levels increased at a faster rate, especially in the unprotected beam. In the same way, as expected, the fire resistance was lower for the beams subjected to higher load levels. This is basically explained by the fact that in those beams equivalent section walls were subjected to higher stress levels and the GFRP resistance is strongly dependent on temperature [4, 19, 79].

4.3.3. Failure modes

In general, the GFRP beams collapsed without any prior warnings signs, presenting brittle failure behaviour, with the exception of the water cooled beam exposed to fire in one side (WC-S1) that did not collapse during the 120 min of fire exposure.

In series S1, the unprotected beam (Figure 43) collapsed due to the compressive failure of the top flange (TF) at mid-span section, which seems to have been followed by shear failure of the webs (W). In all the beams with passive protection (*cf*. Figure 44), the collapse occurred in one of the loaded sections and seems to have been caused by a combination of horizontal (longitudinal) compressive stresses in the top flange and vertical (transverse) compressive and shear stresses in the upper part of the webs.

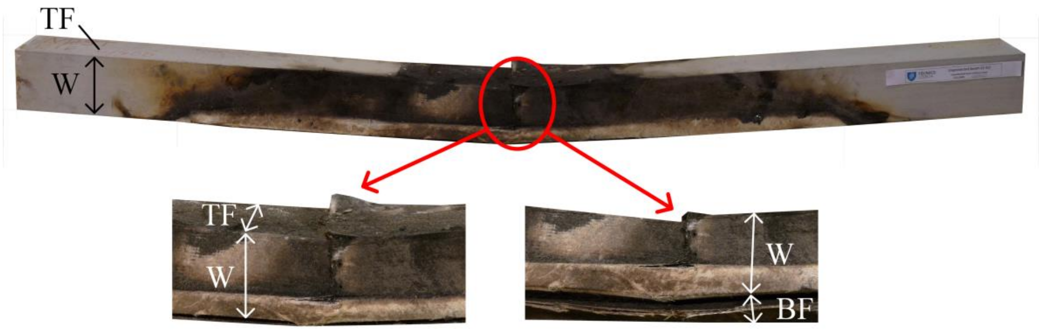

Figure 43: Post-fire observations in beam U-S1.

Although the temperatures measured in the bottom flange (BF) of the GFRP beams were much higher than those measured in the top flange, tensile failure never occurred. In fact, when these beams failed the average temperatures at the top flange had just attained T_g (roughly 140 ºC), while the temperature at mid-depth of the bottom flange was already higher than T_d (in average 620 ºC). The explanation for this result is two-fold: (i) at elevated temperature, the reduction of tensile strength (compared to room temperature) is much lower than that experienced by the compressive and shear strengths; and (ii) the fibres in the bottom flange, although being subjected to a temperature (well) above T_d, were anchored in the unheated sections of the beam and, therefore, were able to keep part of their mechanical contribution to the beam through a catenary action. This behaviour, already reported in [10], was also found and exploited in CFRP strengthened reinforced concrete [80, 81] and GFRP-reinforced concrete [82, 83] members in bending.

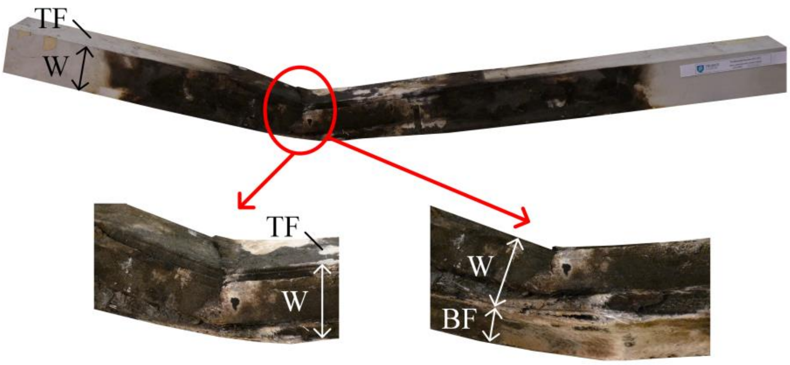

Figure 44: Post-fire observations in beam CS-S1 (after removal of the CS board).

Now regarding the beams exposed to fire in three-sides (series S2), the collapse of the unprotected beam (U-S2) seems to have been caused by the softening of the resin matrix of the webs, which led to a shear failure mechanism involving the sinking of those section walls along the entire length directly exposed to fire (note that this failure mode was different from that observed in the beams from series S1, which was localized in the upper part of the loaded sections); as shown in Figure 45, at mid-span section a crack also developed along the width of the top flange, but this seems to correspond to a secondary mechanism. This difference in failure mechanisms is supported by the temperature measurements: when beam U-S2 collapsed (8 min), the average temperatures at the top flange was still well below T_g (51 ºC, about $T_g/3$), while the average temperature of the web was already well above T_g (about 267 ºC); temperatures at the upper part of the web (thermocouple T4) were also well above T_g (206 ºC), *i.e.*, there was no residual section able to resist/transmit shear stresses.

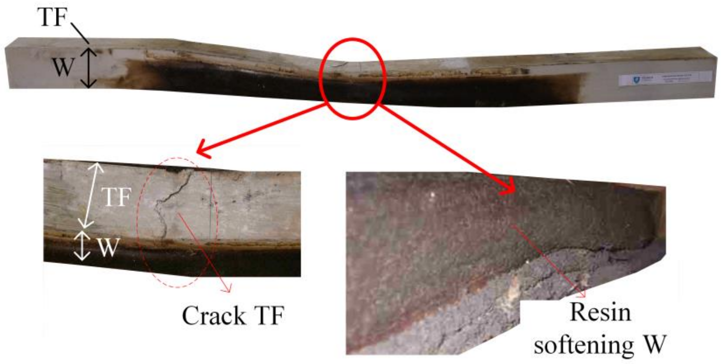

Figure 45: Post-fire observations in beam U-S2.

Regarding the beam with passive protection (CS-S2), the failure mode was very similar to that observed in specimen CS-S1 – compressive failure of the top flange (*cf*. Figure 46). This attests the effectiveness of the thermal insulation provided the CS boards to the webs of the GFRP profile, preventing their shear failure. The water cooled beam (WC-S2), whose webs were now directly exposed to fire, presented a similar failure mode to that of the unprotected beam (U-S2) – *i.e.*, shear failure of the webs along the length directly exposed to heat (with the top flange also exhibiting a crack at mid-span section).

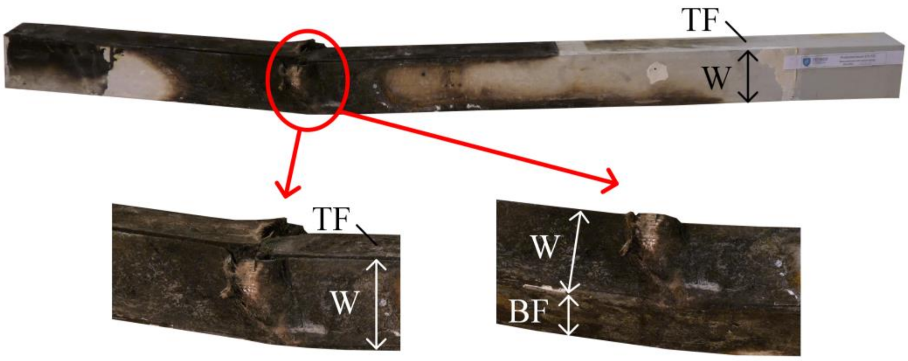

Figure 46: Post-fire observations in beam CS-S2.

Finally, in series S3, when the GFRP profiles were subjected to an increased load level, the beams presented a brittle failure mode similar to the one observed in series S1: compressive failure of the top flange and shear failure of the webs at one of the loaded sections. As discussed in section 4.3.4., at the collapse instant, the temperatures measured in the beams from series S3 were lower than those from series S1. This is explained by the fact that the stresses in the different section walls were higher in beams from series S3 due to the higher load level (the mechanical properties of the pultruded GFRP material are strongly dependent on temperature).

4.3.4. Fire resistance

Figure 47 compares the fire resistance (in minutes) of the pultruded GFRP beams tested in this experimental programme, for the different series. This information is presented also in Table 10, together with the average temperatures at failure (or at the end of the fire exposure) in the various section walls: bottom and top flanges and webs. Figure 48 illustrates the average temperatures in the top (TF) and bottom (BF) flanges at failure. Aiming at determining the fire resistance of GFRP beams tested, the following criteria were considered: maximum (δ_{max} $[m]$) and maximum increase rate $\left(\left(\frac{\partial\delta}{\partial t}\right)_{max}\ [mm/min]\right)$ of mid-span deflection during the fire resistance tests, which were defined according to Portuguese standard [84] and European classification system [13].

In series S1, the reference unprotected beam presented a relatively modest fire resistance of 36 min, only slightly higher than the 30 min (minimum) threshold set in several building codes. For instance, in Portugal, for residential buildings, this threshold only allows GFRP profiles to be used in floors of buildings up to 3 storeys (9 m high); for buildings up to 9 storeys (28 m high) a fire resistance of 60 min is required ([85]). Compared to this reference beam, the fire behaviour of the GFRP beams was considerably improved when the fire protections were installed. The best performance was achieved using the water-cooling system, which prevented collapse from occurring even after 120 min of fire exposure. The best performing passive fire protections were the CS and RW boards, presenting fire resistances slightly higher than 80 min, which were followed closely by the AC boards that provided a fire resistance of 75 min (more than the double of the unprotected beam). As mentioned, the intumescent protections provided considerably lower fire resistances (51-63 min), with the intumescent coating not even attaining the 60 min threshold.

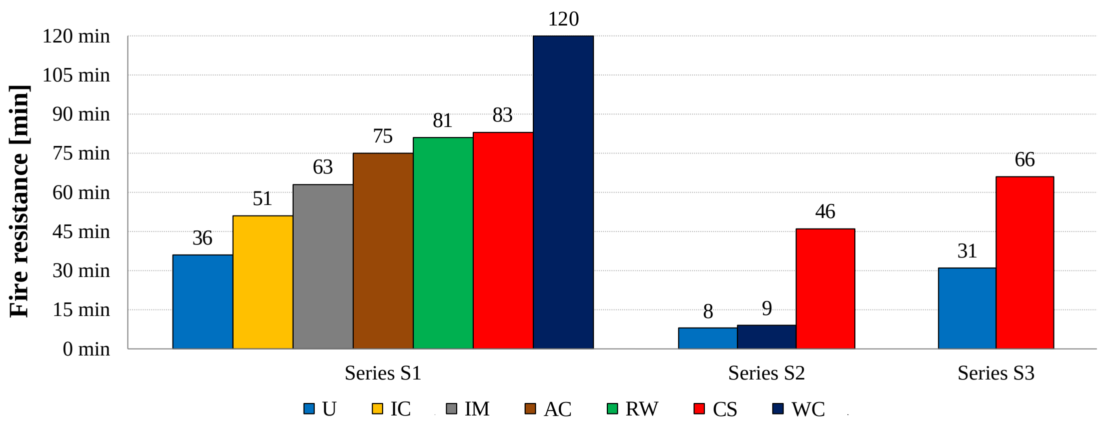

Figure 47: Fire resistance of the beams tested.

In this series, the beams' collapse seems to have occurred when the top flange average temperature approached/exceeded the glass transition temperature of the GFRP material ($T_{g,onset}$ = 104 ºC; T_g = 141 ºC); maximum temperatures in that section wall varied between 118-145 ºC (*cf*. Table 10), being very similar among the different beams. Regarding the remaining section walls, the average temperatures at the webs were significantly higher than T_g, while at the bottom flange they were already considerably higher than the decomposition temperature ($T_d \approx 370$ ºC), presenting a considerable variation (452-727 ºC). These temperature data are consistent with the post-fire assessment, namely the occurrence of compressive failure of the top flange and/or compressive and shear failure of the upper part of the webs and the non-occurrence of tensile failure in the bottom flange (in spite of the very high temperatures attained in that section wall).

Three-side fire exposure (series S2) caused a remarkable reduction of fire resistance. Without fire protection, the fire resistance decreased from 36 min for one-side exposure (beam U-S1) to about 8 min for three-side exposure (beam U-S2, about 78% reduction). Likewise, for beams with CS protection, the fire resistance decreased from 83 min (beam CS-S1) to 46 min (beam CS-S2, approximately 45%). For three-side exposure, although the CS boards provided a significant fire resistance increase *w.r.t.* the unprotected beam (~575%, from 8 to 46 min), the 60 min threshold now was not achieved. Regarding the beam with WC protection, three-side exposure caused a drastic drop of effectiveness (for this particular WC system): the fire resistance decreased from more than 120 min (WC-S1) to less than 10 min (WC-S2); in fact, for three-side exposure the fire resistance of the water cooled beam almost matched that of the unprotected beam. This (very relevant) result indicates that the water-cooling system used in the tests is only effective for structural members in bending under one-side exposure, *i.e.* for slabs or for beams integrated in the floors. In this respect, it is worth referring that an alternative WC system with the entire cavity filled with water could potentially provide better fire performance; however, we would not expect such performance increase to be very significant. In fact, for GFRP columns (webs under compression) exposed to fire in three sides, the effectiveness of such a fire protection system (entire cavity filled with water) was very low (*cf*. chapter 5); moreover, the webs of GFRP beams are mainly exposed to shear and it has been shown in [6] that the shear and compressive properties are affected by elevated temperature in pretty much the same way.

Overall, this reduction of fire resistance from one- to three-side exposure is consistent with the almost negligible fire resistance reported by Ludwig *et al*. [9] for I-section beams exposed to fire in four-sides. The average temperatures at collapse in the different section walls (*cf*. Table 10) seem to explain the differences in the failure modes of beams U-S2/WC-S2 (shear failure of the webs) and beam CS-S2 (top flange compression failure). In fact, in the former beams the maximum temperatures in the top flange (around 55 ºC) were much lower than those in beam CS-S2 (82 ºC); in addition the maximum temperature in the web of beam U-S2 (expected to be relatively uniform across the height, at least in the exposed area) was also considerably higher compared to beam CS-S2. The maximum temperature in the top flange of beam CS-S2 was below the $T_{g,onset}$ and was also lower compared to the other beams of series S1 (which presented a similar failure mode); this may be related with the higher temperatures in the upper part of the webs (that support the top flange) of beam CS-S2 (due to three-side exposure) compared to the beams of series S1.

Table 10: Fire resistance and average temperatures at failure (or at the end of the fire exposure) at the bottom flange (BF), webs (W) and top flange (TF) of all beams tested.

Specimen		**Average temperature**			**Fire resistance**
		BF	**W**	**TF**	
(E1S; L/400)	U-S1	588 ºC	267 ºC	124 ºC	36 min
	AC-S1	695 ºC	259 ºC	128 ºC	75 min
	RW-S1	557 ºC	217 ºC	136 ºC	81 min
	CS-S1	452 ºC	302 ºC	118 ºC	83 min
	IM-S1	697 ºC	284 ºC	131 ºC	63 min
	IC-S1	727 ºC	272 ºC	145 ºC	51 min
	WC-S1	-	84 ºC	49 ºC	> 120 min
(E3S; L/400)	U-S2	263 ºC	268 ºC	55 ºC	8 min
	CS-S2	217 ºC	226 ºC	82 ºC	46 min
	WC-S2	-	-	56 ºC	9 min
(E1S; L/250)	U-S3	540 ºC	234 ºC	110 ºC	31 min
	CS-S3	351 ºC	230 ºC	102 ºC	66 min

Finally, the results obtained show that increasing the load level (series S3) caused a moderated reduction of fire resistance. For the unprotected beams, when the load level was increased 60% (mid-span deflections of L/400 and L/250 in series S1 and S3, respectively, L being the span), the fire resistance decreased from 36 to 31 min (5 min, 14%). For the beams protected with CS boards, the magnitude of the fire resistance reduction was similar, from 83 to 66 min (17 min, 20%). As mentioned, this reduction is basically due to the fact that the stress levels in the different section walls of beams from series S3 were increased compared to those of series S1 and the mechanical strength of the GFRP material strongly depends on temperature. Concerning the average temperatures at the beams' collapse, for similar protection, lower temperatures were observed in series S3, compared to series S1, which is consistent with the variation of the mechanical properties with temperature. In particular, maximum temperatures in the top flange (where failure occurred) range from 102 and 110 ºC in series S3 (once more, very similar within the series), which compares with 118 and 145 ºC in series S1.

In spite of the differences in terms of failure modes described above, Figure 48(a) shows that there is a good correlation between the average temperature at TF and the fire resistance for both the U (blue dots and dashed line) and CS (red dots and dashed line); the same applies to the BF (Figure 48(b)). As expected, the slope of the straight line (average temperature-to-fire resistance ratio) of U series is higher than that of CS series for both TF and BF, which indicated the efficacy of this fire protection. However, it is also clear that the difference between slopes is much more evident for TF (where failure in general occurs) than for BF. In Figure 48, the dots (yellow, grey, brown, green) corresponding to the other protections (series S1) are located well inside the cone formed by these straight lines, meaning that these protections are not so effective as the CS protection (red) but behave better than the unprotected case (blue).

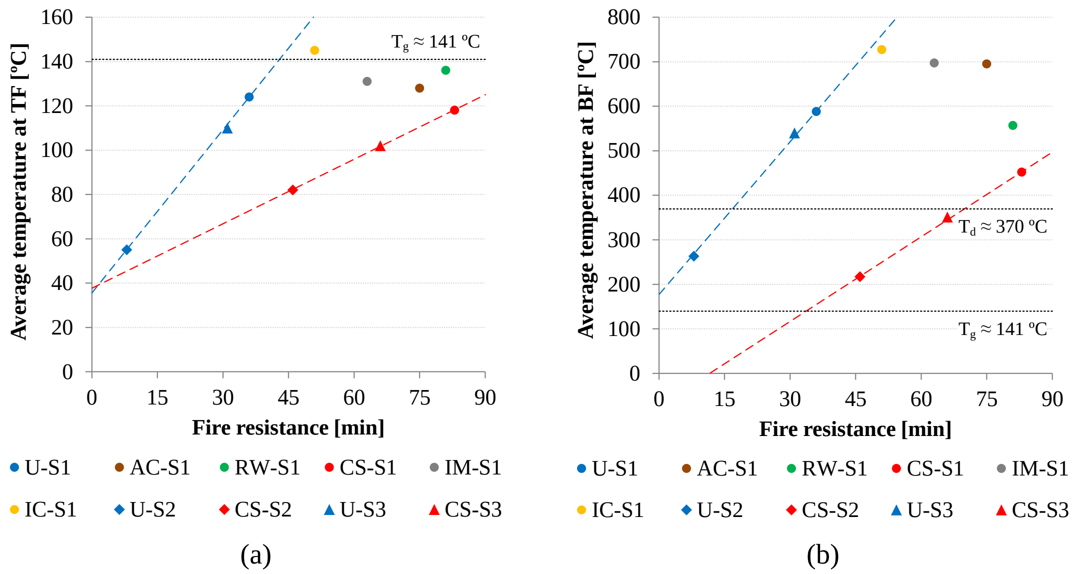

Figure 48: Average temperature in (a) top and (b) bottom flanges at failure for the different series.

4.4. Conclusions

This chapter presented an experimental study about the fire behaviour of pultruded GFRP beams with square tubular cross-section, investigating their thermal and mechanical responses. The experiments addressed (i) the effectiveness of different passive and active fire protection systems, (ii) the influence on the fire resistance response of the number of sides exposed to fire, and (iii) the effect of the load level in the fire resistance of the beams. Based on the results obtained, the following main conclusions may be drawn:

- For one-side exposure, the thick fire protection systems tested (agglomerated cork, rockwool and calcium silicate) were effective in reducing temperatures throughout the cross-section of the tubular beams; therefore, the fire performance was considerably improved after applying those passive fire protections, with fire resistance increasing from 36 min (unprotected beam) to 75-83 min (protected beams). The intumescent protections were not so effective (51-63 min) and this was attributed to their relative high activation temperature when compared to the glass transition temperature (T_g) of the GFRP material. The active fire protection system tested proved to be the most effective solution – the water cooled beam attained a fire resistance of at least 120 min, which is consistent with previous works reported in the literature.

- The influence of the number of sides exposed to fire on the fire resistance behaviour was remarkable. When the unprotected beam was exposed to fire in three-sides, the fire resistance suffered a drastic reduction (to only 8 min), compared to the corresponding profile under one-side exposure. With CS protection, it was possible to increase significantly the fire endurance compared to the unprotected beam (from 8 to 46 min), but the 60 min threshold was not attained. For three-side exposure, the efficacy of the water-cooling system used in the tests (applied only to the bottom flange) was drastically affected, with the fire resistance being as low as 9 min; in this case, although water-cooling allowed retarding the temperature increase at the inner part surface of the bottom flange, such protection was not provided to the webs, which now became directly exposed to fire.

- Increasing the load level caused a moderate reduction of fire resistance of the GFRP beams: for a load level increase of 60%, the fire resistance decreased between 14% (unprotected beams) and 20% (CS protected beams). This was naturally attributed to the increased stress level in the section walls and the temperature dependency of the GFRP strength.

- In general, the beams failed due to one or more of the following modes: (i) compression (flexural) failure of the top flange, with laminate wrinkling; (ii) compressive (vertical) and shear failure of the upper part of the webs (under applied loads), in some cases with material wrinkling; and (iii) shear failure (sinking) of the webs. Although the bottom flanges were always submitted to temperatures higher than the resin's decomposition temperature (T_d), tensile failure of the bottom flange never occurred, because the rovings were anchored at the support sections (kept at much lower temperatures). This result confirms the much higher vulnerability of the GFRP material under compression and shear stress than under tension stresses. Temperature measurements in the different section walls at failure also confirm that the limiting criterion for fire resistance seems to be approaching or exceeding the T_g in parts under axial/transversal compression and/or shear.

Chapter 5:

Fire resistance behaviour of pultruded GFRP columns

5.1. Introduction

Modern codes specify requirements for the fire reaction and fire resistance behaviour of construction materials used in different parts of a building. In particular, materials must present adequate fire reaction behaviour, avoiding fire deflagration, flame spreading and excessive smoke production and spreading. Additionally, structural elements are also expected to present sufficient fire resistance, depending on the building type and geometry, in order to prevent structural collapse under fire and allow for the safe evacuation of occupants [86].

The fire behaviour of pultruded GFRP profiles is critical for their widespread acceptance. Despite all the accomplished advances in the last decades on the numerical simulation of structural models, the study of this problem still remains a considerable challenge, involving heat transfer, fluid dynamics, radiation between the walls of closed cavities and physically and geometrically nonlinear structural analysis. Moreover, the thermal and mechanical material properties are anisotropic and nonlinearly dependent on the temperature. Therefore, at the present stage, it is natural to resort to experimental tests. Even so, there are only a few experimental studies at a full-scale level reported in the literature about this issue, most of which addressing the response of horizontal members, either floor/deck panels [7, 8, 24] or beams [10]. These studies have shown that GFRP horizontal members, when exposed to fire from the bottom, are able to sustain service loads for relatively long periods, even without any fire protection (30-60 min of fire resistance were reported). This is basically due to (i) the high residual strength in tension (the stress state in the side exposed to fire for members in bending), provided that the glass fibres remain anchored/unexposed at the support sections, and (ii) the low thermal conductivity of GFRP. In fact, failure of such members was generally seen to be triggered in their upper side, due to compressive stresses. With passive (coatings, boards) [10] and active (water-cooling) [8, 10, 24] protections, fire resistance increased considerably, with ratings of 60-120 min being attained.

Although GFRP material properties in compression are much more susceptible to elevated temperature than those in tension, there are only a few studies in the literature about the response of intermediate- or full-scale pultruded GFRP columns subjected to fire or elevated temperature [11, 59, 60]. These studies are described next.

Wong and Wang [59] performed compressive tests on pultruded GFRP channel (100×40×4 mm) columns with different lengths (500, 900 and 1350 mm) and rotational restraints (around the minor and major axis) at temperatures varying from 20-120 ºC. At the maximum tested temperature (120 ºC), the strength of the shorter columns was significantly reduced (40% retention for minor axis tests), whereas that of the medium length and longer columns was either moderately affected (strength retentions of 62% and 66%, respectively) or remarkably affected (26% and 38%), for minor axis and major axis tests, respectively. For minor axis tests, all columns failed due to global buckling. For major axis tests, the longer columns failed due to buckling, while the shorter columns collapsed due to a combination of buckling and material crushing. The authors attributed the different rates of strength reduction with temperature to the different failure modes for varying column lengths, arguing that the reduction in compressive strength of the GFRP material with temperature should be faster than that experienced by the compressive stiffness.

Bai and Keller [60] studied the efficacy of using internal water-cooling to provide thermal protection to 300 mm long pultruded GFRP tubes (outer diameter of 40 mm, wall thickness of 3 mm). Water-flow rates of 8 and 20 cm/s (average speed in the cross-section cavity) were used (slightly higher than those used in the mentioned deck panels ([8, 24]). Specimens were loaded up to different fractions of the serviceability load (50%, 75%, and 100%) and then exposed to elevated temperature using a thermal chamber set to a target temperature of 220 ºC and heated at a rate of 5 ºC/min. For the test conditions used in this study, it was shown that water-cooling system was very effective in improving the fire endurance of GFRP columns. The authors also concluded that, differently from what had been observed in deck panels with higher wall thickness (15 mm, [8]), the efficacy of water-cooling in GFRP columns with low thickness walls is highly dependent on the water flow. In fact, for the columns subjected to the full service load, the following times to failure were obtained: 7 min without protection, 72 min with the lower flow-rate, and 164 min with the higher water-flow rates.

Bai *et al*. [11] then investigated this water-cooling concept on full-scale GFRP columns, loaded and exposed to fire from one side. Two columns with multicellular cross-section (195 mm high, flange thickness varying between 15.2-17.4 mm), 2805 mm of length and 609 mm of width, were subjected to an axial load of 145 kN (causing a relatively low axial stress of about 5 MPa) and then exposed to the ISO 834 fire curve [13]. One column was tested without protection and the other was protected with water-cooling (2.5 cm/s). The unprotected column failed after 49 min due to a global buckling mechanism, which, according to the authors, was most like caused by a series of preceding local failures. The protected column was able to sustain the applied load for 120 min without collapsing. The authors acknowledged the contribution of the multicellular cross-section for these positive results: in fact, since it comprised four cells, the three inner webs were prevented to heat more rapidly, as they were not directly exposed to heat.

The pioneering studies reviewed above, although providing very relevant information, do not allow for a complete understanding about the fire response of pultruded GFRP columns. Only the study of Bai *et al*. [11] was performed for actual fire exposure conditions (the maximum temperatures in the preceding works of Wong and Wang [59] and Bai and Keller [60] were below the glass transition and decomposition temperatures of GFRP, respectively). In addition, in the study of Bai *et al*. [11] the exposure conditions were relatively favourable, not only due to the multicellular geometry, but also because the columns were exposed to fire only in one surface. Finally, none of the studies reported above investigated the effect of using passive fire protection, which was seen to be effective in extending the fire endurance of pultruded GFRP beams [10].

This chapter presents results of an experimental study about the fire resistance behaviour of pultruded GFRP columns with square tubular cross-section. The main objective was to study the viability of their structural use in buildings. The efficacy of (i) applying calcium silicate boards, and (ii) using water-cooling systems, with either stagnant or flowing water, in providing fire protection to GFRP columns was investigated. The effect of exposing the columns to fire in either one or three faces was also assessed, as well as the effect of varying the service load.

5.2. Experimental programme

5.2.1. Materials

The pultruded GFRP profiles used in these fire resistance tests had a square tubular cross-section (100×100×8 mm) and were produced by *Fiberline* – the same profiles previously used in the fire resistance tests on GFRP beams (*cf*. section 4.2.1.). The most relevant mechanical properties of the GFRP material in tension, compression, flexure and shear were determined by means of coupon tests and are summarized in Table 8. The full-section longitudinal (E_L = 31.0 GPa) and shear (G_{LT} = 3.6 GPa) moduli of the GFRP profiles were determined from three-point bending tests (EN 13706) performed on 1.5 m long beams. Full-scale compressive tests up to failure (caused by material crushing) were also carried out on 1.5 m long non-braced tubular columns, which allowed determining the longitudinal elasticity modulus (E_L = 30.6 ± 0.4 GPa, in agreement with that obtained from flexural tests) and the full-section axial compressive strength ($\sigma_{L,comp}$ = 280.6 ± 24.0 MPa). The glass transition (T_g) and decomposition (T_d) temperatures of the GFRP material used were set at 141 and 370 ºC, respectively, as presented in section 3.2.

In this experimental campaign, calcium silicate (CS) boards with a thickness of 25 mm produced by *Promatec* (type H) were used as passive fire protection system. The boards are made of agglomerate CS, presenting the following thermo-physical properties at room temperature: dry density of $\rho = 450$ kg/m^3, thermal conductivity of $\lambda = 0.090$ W/mK and specific heat capacity of $C_p = 810$ J/kgºC. The CS boards were bonded to the GFRP with a thin layer of fire resistant mastic. Thin metal handles were applied at two cross-sections as a redundant connection system.

5.2.2. Test programme

As mentioned, the main goal of this study was to evaluate the thermal and mechanical responses, the failure modes and the fire resistance of pultruded GFRP columns. In particular, one aimed at evaluating the effects of (i) applying different fire protection systems, (ii) exposing the GFRP columns to fire in either one or three sides, and (iii) varying the service load level. Accordingly, the test programme included 10 fire resistance tests in 1.5 m long columns, divided in three series (S1, S2 and S3), as summarized in Table 11.

Table 11: Overview of the fire resistance tests performed on pultruded GFRP columns.

Series	Specimen	Fire protection	Fire exposure	Load level
Series S1	U-S1	-	E1S (one-side exposure)	L/1500 (55 kN)
	CS-S1	Calcium silicate		
	WC_s-S1	Water-cooling standing (WC_s)		
	WC_f-S1	Water-cooling flowing (WC_f)		
Series S2	U-S2	-	E3S (three-side exposure)	L/1500 (55 kN)
	CS-S2	Calcium silicate		
	WC_s-S2	Water-cooling standing (WC_s)		
	WC_f-S2	Water-cooling flowing (WC_f)		
Series S3	U-S3	-	E1S	L/750 (110 kN)
	CS-S3	Calcium silicate		

In series S1, four specimens were tested, one unprotected (U) and three with the following types of fire protection: CS boards (CS), and water-cooling, either standing (WC_s) or flowing (WC_f). In both water cooled specimens, the cavity of the cross-section was completely filled with water, which either remained standing (WC_s) or was renewed (WC_f) at a rate of 0.4 m^3/h (7.2 cm/s the same flow used in a previous study on GFRP tubular beams [10]), by means of two small orifices opened at the top flange (wall unexposed to fire) of the GFRP column (at both extremities). The columns of this series were exposed to fire only in one side (the bottom one, *cf.* section 5.2.3.) and were subjected to a compressive load of 55 kN, corresponding to an axial shortening of L/1500 (defined in [25] for service limit states design), L being the column length. This load caused an average longitudinal compressive stress of 18.7 MPa, about 6.7% of the compressive strength determined from the full-scale column tests performed at room temperature.

Series S2 comprised also four specimens, with the same type of fire protection used in series S1. In this case, the CS boards were applied in the bottom flange (wall directly exposed to fire) and the webs. The columns were subjected to the same load as in series S1, but were exposed to fire in three sides (the bottom and the lateral ones).

Series S3 included two specimens, one unprotected and the other with CS board protection. The columns were exposed to fire only in the bottom surface (as in series S1), and subjected to a compressive load of 110 kN, corresponding to an axial shortening of L/750, *i.e.* the double of that applied in series S1 and S2. In this case, the axial compressive stress was 37.4 MPa (13.4% of the room temperature strength). In this experimental study, the following nomenclature was adopted: U-S1 (unprotected column, series S1); WC_f-S2 (column protected with flowing water-cooling, series S2).

5.2.3. Test setup, instrumentation and procedure

The experiments were conducted on a vertical oven, with external dimensions of 1.35×1.20×2.10 m, that presents an opening on the top (Figure 49) – the same previously used in the fire resistance tests on GFRP beams (presented in section 4.2.3.). Once again, two different top cover sets (Figure 35), composed by a metallic structure lined with ceramic wool, were used at the top of the oven. One of the cover sets (used in series S1 and S3) allows exposing to fire only one side of the GFRP profiles (the bottom one), while the other cover set (used in series S2) allows exposing to fire three sides of the GFRP profiles (the bottom and lateral ones). The oven is fired by six gas burners and is controlled by a computer, which reads the oven temperature from three internal thermocouples and is able to adjust the burners' intensity in order to follow, as close as possible, a predefined time-temperature curve. In the present study, the time-temperature curve defined in ISO 834 [13] was adopted. The interested reader should refer to M.Sc. dissertation of Moreira [87] for more detailed information on the test setup and instrumentation.

The specimens were positioned on top of the oven keeping a vertical distance of 4 cm between their bottom surface and the oven's lateral walls, in order to enable the free vertical (transverse or out-of-plane) deformation of the GFRP profiles during the test. The axial (horizontal) load was applied by means of a hydraulic jack (Figure 50(b)), fixed to a closed steel reaction frame and connected to a hydraulic pressure system (Figure 50(a)). Two load transmission steel beams (HEB100 profiles), suspended from the steel reaction frame, were used to transmit the load from the hydraulic jack to the GFRP columns (Figure 50(d)). At both support sections of the

GFRP profiles two machined steel blocks (diameter of 140 mm, thickness of 50 mm), with 30 mm deep grooves mimicking the tubular cross-section's walls (Figure 50(c)), were used in order (i) to restrain any relative displacement or rotation of the end sections, and (ii) to guarantee a uniform compressive load. In the left support section, only the longitudinal displacement was allowed. At the right support section, a spherical hinge was positioned between the steel block and the loading system. The compressive load was measured with a load cell placed between the reaction frame and the right load transmission steel beam (Figure 50(g)). Vertical (out-of-plane) displacements of the top flange were measured at the central section using a displacement transducer (Figure 50(e)), and horizontal displacements (longitudinal direction) were measured at the columns' extremities using four displacement transducers (two on each extremity, Figure 50(d)).

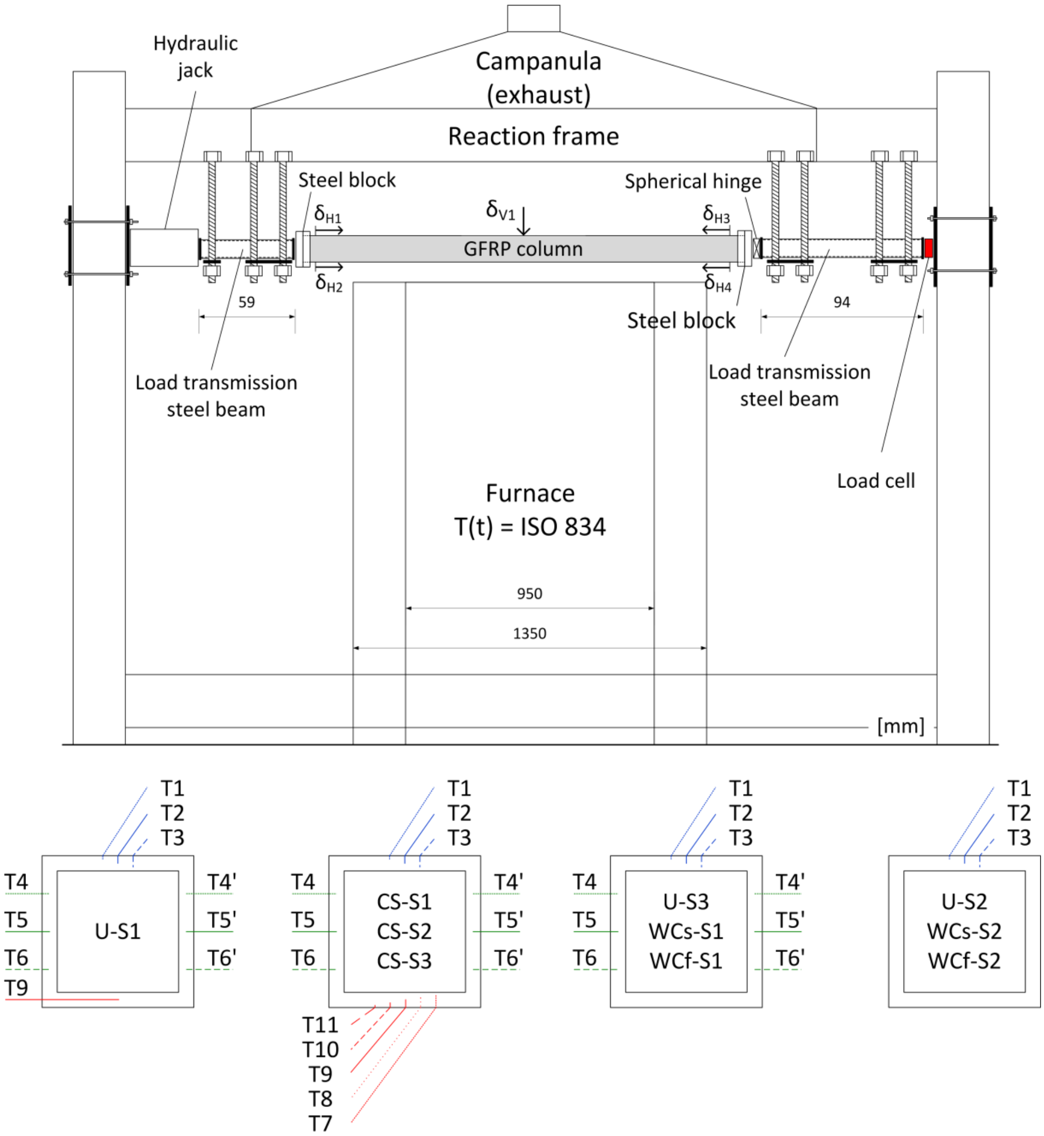

Figure 49: Frontal view of test setup (top) and thermocouples position at mid-span section (bottom).

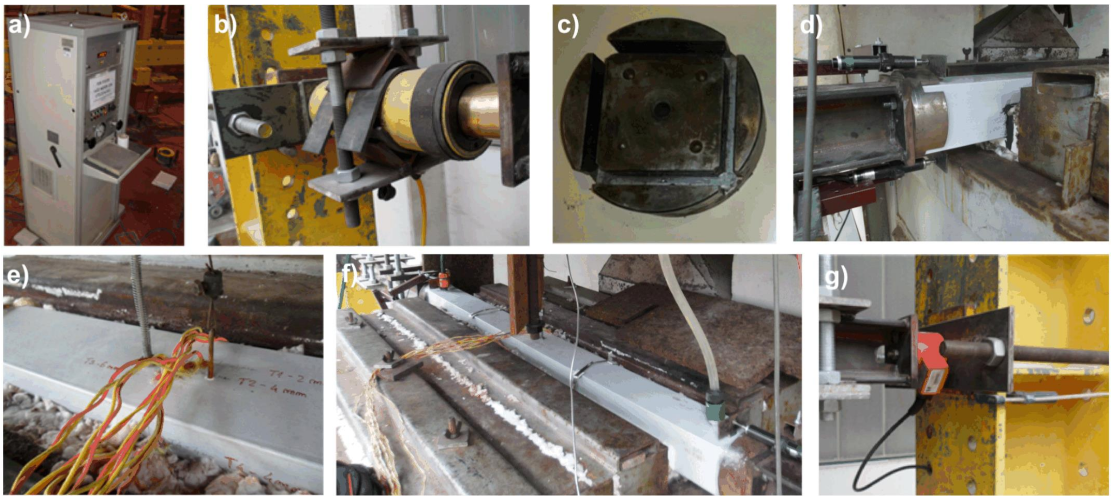

Figure 50: Components of the test setup - (a) pressure unit; (b) hydraulic jack; (c) steel blocks of the supports; (d) load transmission beam and horizontal displacement transducers; (e) thermocouples and vertical displacement transducer at central section; (f) hoses of the WC_f system; (g) load cell.

The temperatures in different positions of the central section (*cf*. Figure 49) were measured with thermocouples type K (Figure 50(e)), which were inserted on holes drilled at predefined depths and bonded with polyester resin. Thermocouples T1 to T3 were installed in the top flange (at depths of about 2, 4 and 6 mm, respectively), thermocouples T4 to T6 were placed in the web (all at the mid-depth), and thermocouples T7 to T11 were applied in the bottom flange (at depths of about 0.5, 2, 4, 6 and 7.5 mm, respectively). As indicated in Figure 49, the number of section walls instrumented was different depending on the type of fire protection and number of sides exposed to fire. This aimed at preventing the thermocouples from being directly exposed to fire, thus causing their detachment. In order to determine the complete thermal response of unprotected specimens from series S1 and S2, two additional unprotected columns were tested, exposed to fire in one or three sides, respectively, but without any mechanical load (referred to as U-S1-T and U-S2-T). In these specimens, unlike those subjected to mechanical load, thermocouples were also installed in the bottom flange (S1), and in the web and bottom flange (S2), allowing to measure the thermal response in the entire cross-section. To this end, quadrangular openings (approximately 8×8 cm^2) were saw-cut in the top flange and web in order to allow for the installation of the thermocouples from the interior of the tubular section (thus preventing the thermocouples from being exposed to fire). Those opening were then sealed with epoxy adhesive according to the procedure adopted in [24].

The flowing water-cooling system comprised (i) custom flexible rubber hoses, (ii) a flow-rate meter (with a measuring range from 0.3 to 3.0 m^3/h), and (iii) a flow control valve. The water was provided by the laboratory building's water supply network, entering and exiting the GFRP columns through orifices opened at their top flange (Figure 50(f)). For the columns protected with the stagnant water-cooling system, the cavity of the tubular section was simply filled with water, applied through one of those two orifices, which were sealed in order to avoid the water evaporation during the tests.

The fire resistance tests were performed at initial temperatures ranging from 15 to 25 ºC. For columns with water-cooling protection, prior to the application of the compressive load, the tubular cavity of the GFRP section was filled with water. In columns protected with flowing water, the water circuit was opened and the water-flow was adjusted to 0.4 m^3/h. The next step, which was the first for all the other specimens, involved the application of the compressive load, either 55 kN (series S1 and S2) or 110 kN (series S3). After a period of 10 min, set in order to guarantee the stabilization of deformations, the furnace burners were started. Specimens were thermally loaded up to structural collapse or until 120 min of exposure (the maximum duration set for the experiments). During this period, due to the progressive loss of stiffness of the specimens, the pressure in the hydraulic jack had to be adjusted in order to guarantee a constant load. Load, deflection and temperature measurements were recorded in a PC using built-in data loggers from *HBM*.

5.3. Results and discussion

5.3.1. Thermal response

Figure 51 plots the evolution of the furnace temperatures measured in all fire resistance tests. It can be seen that all experimental curves are in very close agreement with the time-temperature curve defined in ISO 834 [13]. The highest deviations were observed during the first 30 min of the test CS-S1; however, even in this test the relative differences to the standard curve were lower than 60 ºC.

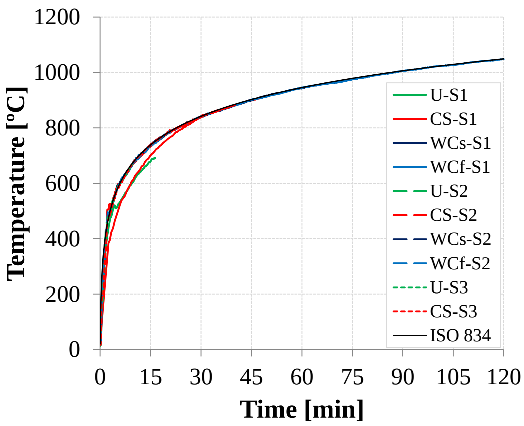

Figure 51: Furnace temperatures measured in all tests.

Figure 52 presents the temperature profiles of all columns from series S1. In these curves, the glass transition (T_g) and onset decomposition ($T_{d,onset}$) temperatures of the GFRP material are also plotted as a reference. In general, the thermal responses of columns from series S3 were very similar to those of series S1.

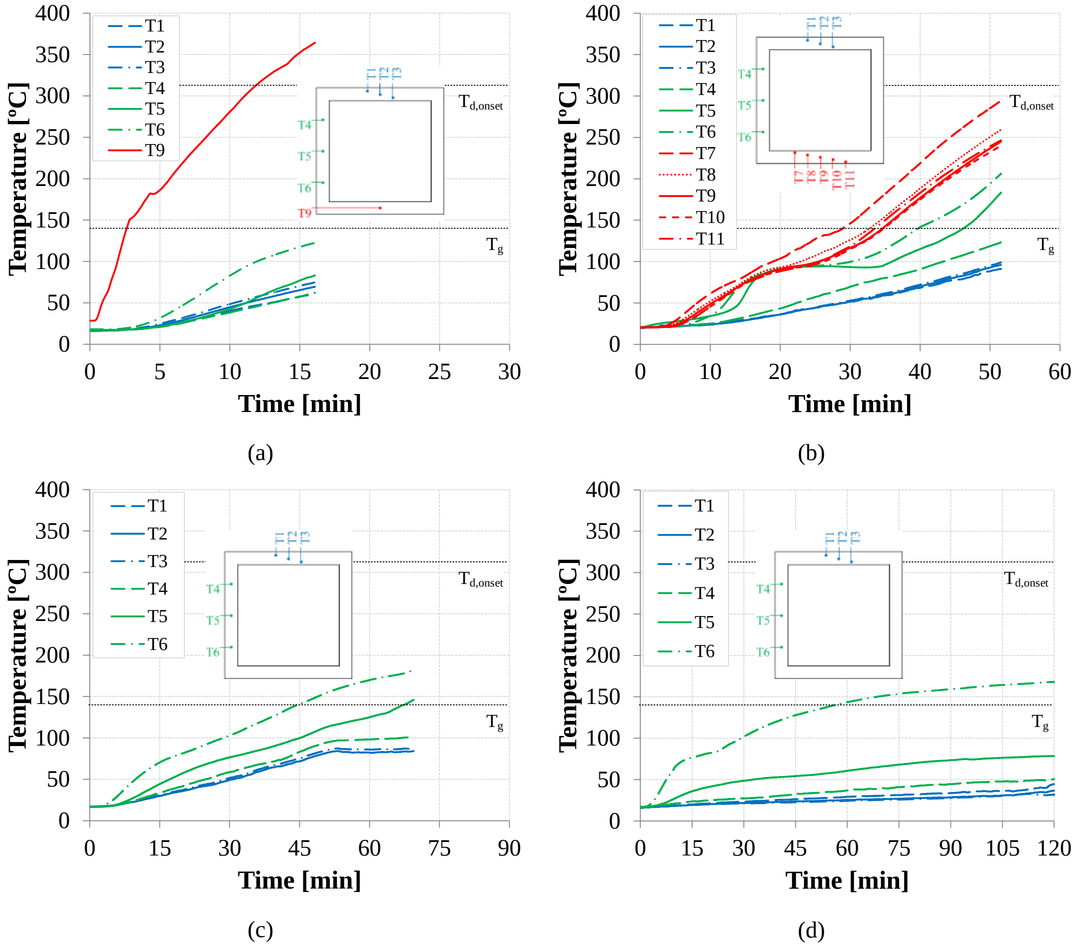

Figure 52: Temperature profiles for columns from series S1 - (a) U-S1; (b) CS-S1; (c) WC_s-S1; and (d) WC_f-S1.

It can be seen that, for similar exposure durations, as expected, the unprotected profile U-S1 (Figure 52(a)) exhibited the highest temperatures, with the average temperature at the bottom flange reaching the T_g and the $T_{d,onset}$ after respectively 3 and 12 min. As expected, the CS board provided considerable temperature reduction in all cross-section's walls (Figure 52(b)); in this case, it took 33 and 46 min for the average temperature in the bottom flange and webs, respectively, to reach the T_g of the GFRP material. Compared to column U-S1, and taking into account the time for the bottom flange to attain the T_g (as a reference), this means approximately 30 min of thermal insulation. In what regards the water-cooling protection systems (Figure 52(c) and Figure 52(d)), they both provided considerable temperature reductions in the webs and top flange, particularly when flowing water was used. In fact, with stagnant water it took 63 min for the average temperature in the webs to attain T_g, whereas with flowing water such temperature remained well below the T_g during the entire duration of the test. In both cases, the temperatures at the top flange always remained below the T_g, although it is worth noting that in column WC_s-S1, the average temperature at the top flange had already surpassed the $T_{d,onset}$ at the end of the test. Although the temperatures at the bottom flange were not monitored when water-cooling protection was used, it is very likely that these systems were much less effective than the CS boards in protecting the bottom flange [10].

Figure 53 plots the evolution of the average temperatures in the top flange (TF) and web (W) of columns from series S1 and S2 protected with the stagnant and flowing water-cooling systems, thus allowing to compare the effect of streaming on the thermal response of the GFRP material. Curves plotted in Figure 53 for similar section walls attest the higher thermal insulation provided by the flowing water, which naturally stems from its improved liquid cooling capacity [8]. It can also be seen that the relative magnitude of such improved protection is higher in the top flange than in the webs. Naturally, this should be related with the position of the water inlet and outlet (top flange, *cf*. Figure 50(f)), as well as with the horizontal position of the columns, leading to higher water flow at the upper part of the tubular cavity. In fact, in column WC_f-S1 (unlike in column WC_s-S1) temperatures were always lower in the bottom part of the top flange (in contact with the flowing water) than in its upper part, as illustrated in Figure 54. The flowing water also had considerable influence in the temperature profiles across the webs' depth: comparing to stagnant water (WC_s-S1, Figure 55(a)), flowing water (WC_f-S1, Figure 55(b)) led to much lower average temperatures (as mentioned), particularly at the upper part of the web (closer to the water flow), where temperature remained considerably below $T_{g,onset}$ even after 120 min of fire exposure.

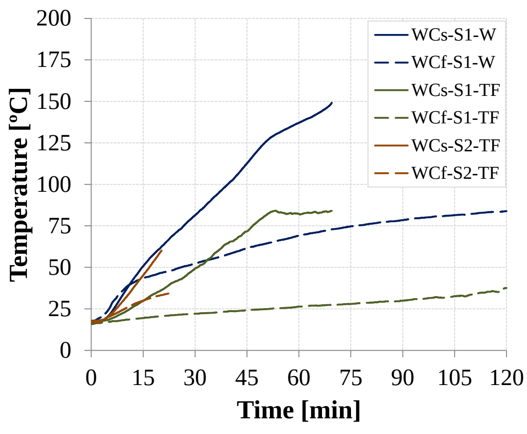

Figure 53: Evolution of average temperatures in the top flange (TF) and web (W) of columns with stagnant or flowing water-cooling protection from series S1 and S2.

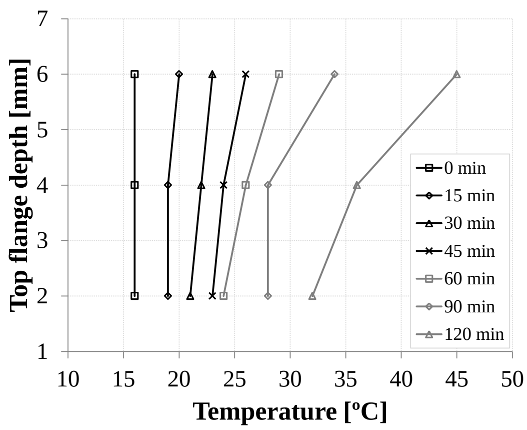

Figure 54: Temperatures across the top flange depth of column WC_f-S1 for different fire exposure periods.

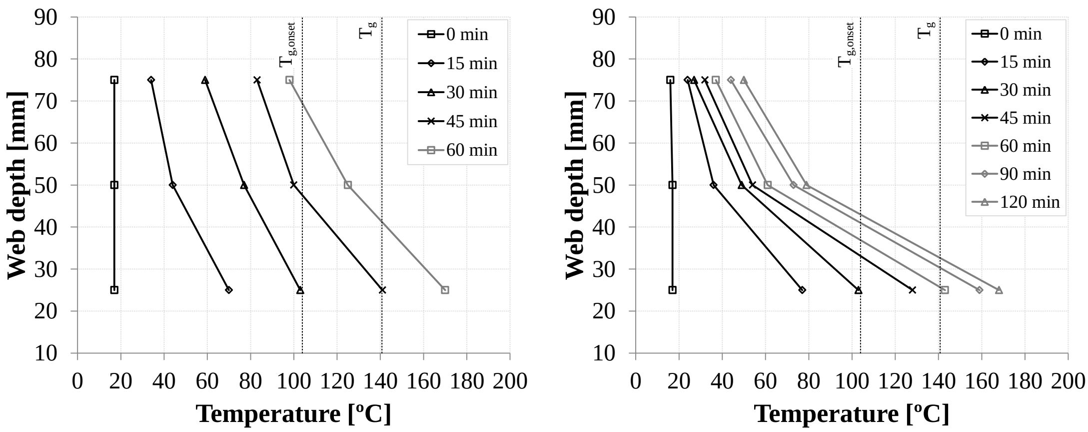

(a)

(b)

Figure 55: Temperatures across the webs' depth for different fire exposure periods – (a) column WC_s-S1; (b) column WC_f-S1.

Figure 56 illustrates the evolution of the average temperatures in the top flange (TF), web (W) and bottom flange (BF) of unprotected (and unloaded) columns from series S1 and S2, thus allowing to compare the effect of exposing the GFRP profile to fire in either one or three sides.

The results plotted in Figure 56 prompt the following comments regarding the effect of fire exposure at three sides: (i) the temperature evolution in the bottom flange is basically analogous to that corresponding to one-side exposure, since the heat exposure of that wall is also similar; (ii) the temperature evolution in the bottom flange and webs becomes very similar, which stems from the fact that they are now both directly exposed to fire; (iii) compared to one-side exposure, the temperature increase in the top flange and particularly in the webs (now exposed to fire) suffers a substantial augment; as an example, the time for the average temperature of the web to attain T_g is reduced from 16 min (S1) to only 5 min (S2). It is interesting to note that those exposure durations correspond precisely to the fire resistance of such columns (*cf*. section 5.3.4.).

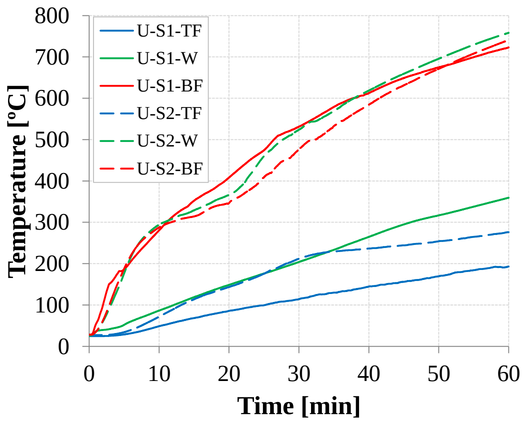

Figure 56: Evolution of average temperatures in the top flange (TF), web (W) and bottom flange (BF) of unprotected columns U-S1-T and U-S2-T.

5.3.2. Mechanical response

Figure 57 presents the evolution of the axial load (measured by the load cell) as a function of the fire exposure duration for all tests. It can be seen that despite some (limited) fluctuations in the axial load level, for all test series the predefined loads (55 and 110 kN) were maintained up to failure, which corresponded to an abrupt reduction of the applied load.

Figure 58 depicts the variation of the average axial shortening as a function of the fire exposure duration. In general, the GFRP columns exhibited a progressive axial shortening, which increased roughly linearly with the fire exposure duration. This axial shortening was naturally due to the progressive stiffness decrease as the average temperature in the cross-section increased, thus causing a reduction of the GFRP elasticity (and shear) modulus. The axial shortening measured in the columns protected with CS boards was lower than that registered in the other specimens, due to the thermal protection conferred by the calcium silicate. Compared to water-cooling, such passive protection layer was able to slow down the stiffness reduction of the wall(s) covered by the CS panel(s). It is interesting to note that during the initial instants of the test, both the unprotected columns and those protected with flowing water exhibited a slight axial elongation (more significant in column U-S2), which must be attributed to the thermal expansion of the material due to the temperature increase; this effect was soon counterbalanced by the above mentioned stiffness decrease. Such initial elongation was not observed in the CS board protected columns, most likely due to the lower relative magnitude of the thermal expansion effect, compared to the stiffness reduction.

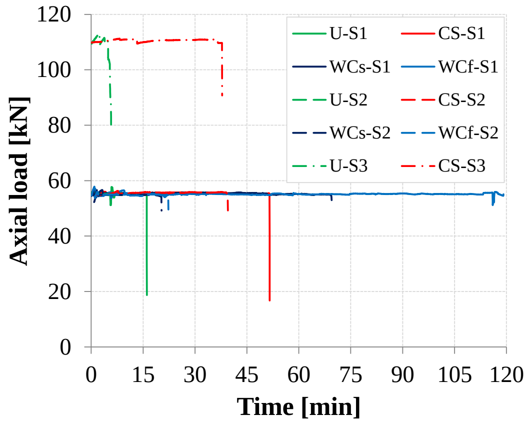

Figure 57: Axial load *vs*. duration of fire exposure.

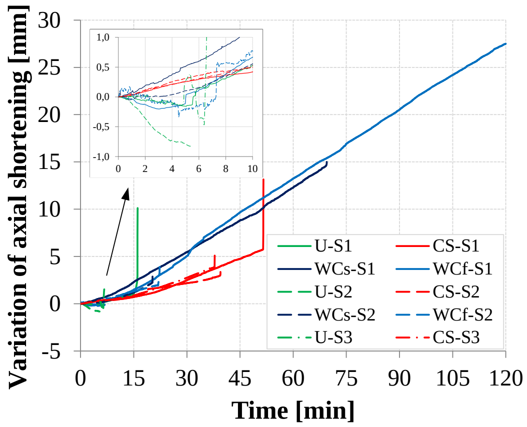

Figure 58: Variation of axial shortening *vs*. duration of fire exposure.

Figure 59 presents the variation of the central section vertical (out-of-plane) displacements of the columns (measured at the top flange) as a function of the fire exposure duration (upwards deflections are presented with a positive sign). Some of the curves plotted in Figure 59 (*e.g.*, WC_s-S1 and WC_f-S1) present sudden variations of vertical deflection (marked with an arrow in the figure and that could be matched with slight changes in the applied load, *cf*. Figure 57); those variations are deemed to be due to adjustments of the test setup (rotation at the right support) caused by the minute changes in the applied load. It is also worth noting that the vertical deflections plotted in Figure 59 were measured in the top flange, so they incorporate not only the average deflection of the columns, but also the influence of local effects, namely the relative deformations of the top flange *w.r.t.* the other cross-section's walls.

In general, when the columns started to be exposed to fire, the vertical displacements measured at the central section became negative, *i.e.* the GFRP columns (top flange) started to move downwards (towards the heating source). This descending movement must have been caused by the differential thermal expansion component of the cross-section, as the bottom surface (exposed to heat) became much hotter than the top surface. During this first stage (and also during the remainder of the tests), the vertical displacements exhibited by the columns protected with CS boards were lower than those of the other columns, which is consistent with the thermal insulation conferred by the CS board, which reduced the thermal gradient across the cross-sections' depth. After certain duration of fire exposure, all columns started deflecting upwards. As a consequence of the fire exposure, the cross-section's walls progressively started to lose their stiffness and, due to the thermal boundary conditions, such reduction occurred at different rates in the different section walls (*e.g.* for one-side exposure, those rates were maximum at the bottom flange, intermediate at the webs and minimum at the top flange). This "differential" loss of stiffness caused a progressive change in the position of the stiffness centre. Since the position of the load application system remained constant (due to the test setup), a negative bending moment developed in the columns, explaining this progressive ascending movement which, at some point, counterbalanced the descending movement caused by the thermal gradient (a similar response had been reported earlier by Bai *et al*. [11] and Kardomateas *et al*. [88], the latter based on numerical modelling). In general, such ascending movement was continuous up to failure, which occurred in a brittle manner (*cf*. section 5.3.3.), with a very steep and abrupt vertical (ascending) movement.

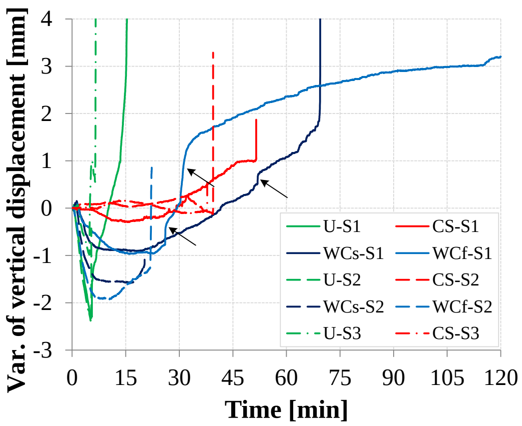

Figure 59: Variation of vertical (out-of-plane) displacement *vs*. duration of fire exposure.

5.3.3. Failure modes

With the exception of column WC_f-S1, which did not fail after 120 min of fire exposure, all GFRP columns collapsed without any prior warning signs. As mentioned, failure occurred in a brittle manner, in the vicinity of a single section, located within a maximum distance of 300 mm from the centre of the columns. The compressive failure involved the formation of a hinge at this cross-section.

The collapse of columns from series S1 and S3 (Figure 60 and Figure 61) seems to have been triggered at the bottom flange (only the top surface was visible during the tests), which exhibited a wrinkling type of failure with material crushing and delamination (kink-band failure). The webs and in most cases the top flange were also damaged, exhibiting either cracking (transverse to the cross-section, Figure 60) or wrinkling (Figure 61). At failure, the average temperature at the bottom flange of all columns from series S1 and S3 was well above the T_g of the GFRP material. In most columns, the average temperature of the webs was also above T_g or at least above the $T_{g,onset}$. In series S1, the average temperature of the top flange had also attained the $T_{g,onset}$. These figures and the considerable reduction of GFRP compressive strength with temperature [4] explain the collapse of those columns. In opposition, after 120 min of exposure, the average temperatures at the top flange and the entire upper half of the webs of column WC_f-S1 were well below the $T_{g,onset}$. This justifies why the flowing water cooled cross-section was still able to support the compressive load after 120 min of fire exposure.

Figure 60: Post-fire observations in column U-S3.

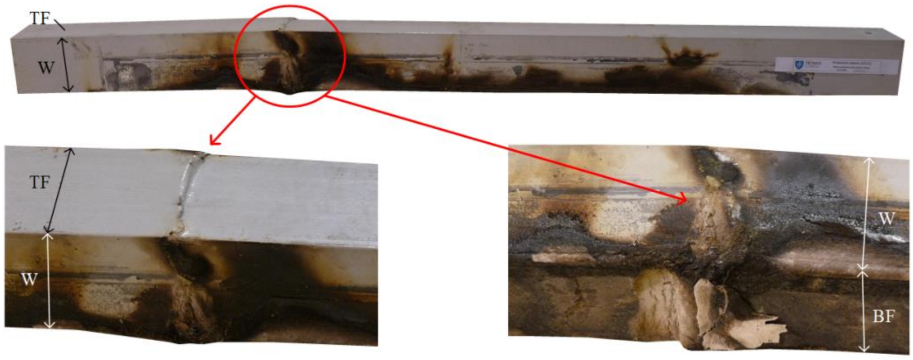

Figure 61: Post-fire observations in column CS-S1 (after removal of the CS board).

The collapse of the columns from series S2 apparently started with the failure of both the bottom flange and the webs (Figure 62 and Figure 63), which exhibited material crushing and delamination; as a consequence of a hinge formation, the top flange finally cracked. In some cases, the cross-section became completely sectioned, *i.e.* along the entire depth. At failure, the average temperature at the bottom flange and webs of columns U-S2 and CS-S2 (in columns with water-cooling those measurements were not performed) was already higher than the T_g of the GFRP material, explaining why failure was apparently triggered both at the bottom flange and the webs.

Figure 62: Post-fire observations in column U-S2.

Figure 63: Post-fire observations in column WC_f-S2.

5.3.4. Fire resistance

Figure 64 presents a comparison between the fire resistances of the pultruded GFRP columns from the different test series. This information is also available in Table 12, complemented with the average temperatures at failure (or at the end of the fire exposure) at the bottom flange (BF), webs (W) and top flange (TF) of all the tested columns.

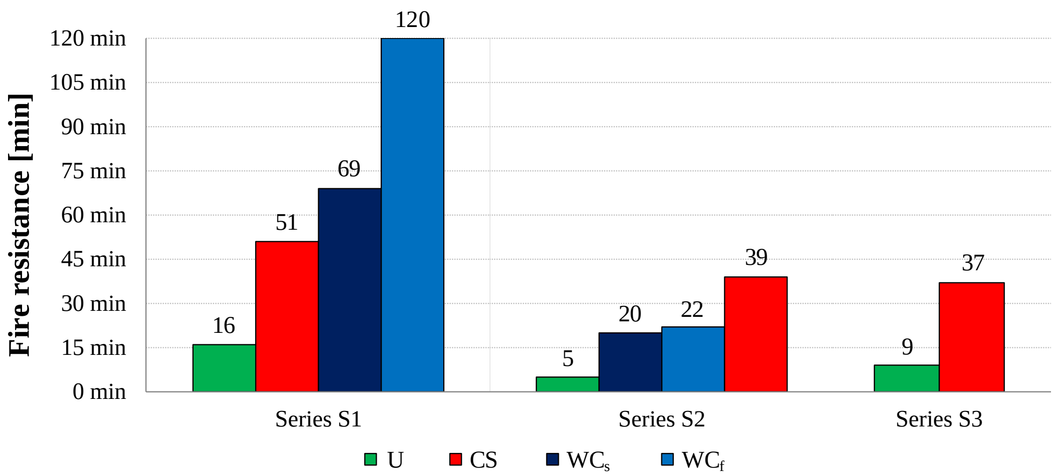

Figure 64: Fire resistance of all columns tested.

Regarding series S1, the unprotected column achieved a very low fire resistance of only 16 min, taking into account the requirements often defined in building fire safety codes. As an example, the Portuguese fire safety code [85] specifies the following minimum fire resistance ratings of

30, 60 and 90 min for standard residential houses with heights up to respectively 9, 28 and 50 m. The CS board protection would enable fulfilling the first requirement but not the second one, as it provided a fire resistance of 51 min (more than the triple of the unprotected column). The stagnant water-cooling, with a fire resistance of 69 min, would allow fulfilling the second requirement. Finally, the flowing water-cooling system (WC_f-S1), which provided the best fire protection, even preventing collapse after 120 min of fire exposure, would allow fulfilling the most stringent requirement.

Table 12: Fire resistance and average temperatures at failure (or at the end of the fire exposure) at the bottom flange (BF), webs (W) and top flange (TF) of all columns tested.

Specimen		**Average temperature**			**Fire resistance**
		BF	**W**	**TF**	
(E1S; L/1500)	U-S1	359 ºC	94 ºC	82 ºC	16 min
	CS-S1	254 ºC	166 ºC	94 ºC	51 min
	WC_s-S1	-	149 ºC	84 ºC	69 min
	WC_f-S1	-	94 ºC	38 ºC	> 120 min
(E3S; L/1500)	U-S2	190 ºC	160 ºC	34 ºC	5 min
	CS-S2	202 ºC	153 ºC	67 ºC	39 min
	WC_s-S2	-	-	60 ºC	20 min
	WC_f-S2	-	-	34 ºC	22 min
(E1S; L/750)	U-S3	263 ºC	82 ºC	42 ºC	9 min
	CS-S3	171 ºC	98 ºC	60 ºC	37 min

Results obtained for series S2, compared to those of series S1, indicate that GFRP columns experience a noticeable decrease of fire resistance when exposed to fire in three sides. The unprotected column from series S2 failed after only 5 min, *i.e.* about three times less than the corresponding column of series S1. In the CS board protected column, the fire resistance (39 min) was also lower compared to the corresponding column of series S1, although the relative magnitude of such reduction (about 24%) was very much attenuated. It is worth mentioning that in this series, the CS protection provided a remarkable fire resistance increase, compared to the unprotected column (about 8 times). In opposition, the efficacy of both types of water-cooling systems for three-side exposure was much lower compared to one-side exposure – the fire resistances with stagnant and flowing water were respectively 20 and 22 min, about half of the fire resistance attained with the CS board protection. These results prompt the following additional comments regarding the effect of three-side exposure: (i) the performance of flowing water is only slightly better than that of stagnant water; (ii) the efficacy of water-cooling systems is low (for the test setup used in this study); and (iii) the fire resistance performance of pultruded GFRP columns is severely reduced compared to one-side exposure. This latter result brings the attention to the importance of adopting a building layout in which the GFRP columns are embedded in the partition/external walls. If this type of architecture is not adopted, even with fire protection systems, building fire ratings will very hardly be fulfilled.

As expected, increasing the load level (series S3) caused a moderate to high reduction of the fire resistance. The unprotected GFRP column failed after about 9 min, roughly half of the fire resistance exhibited in series S1. The CS board-protected column from series S3 failed after about 37 min, which represents a 27% decrease compared to the corresponding column of series S1. This performance reduction naturally stems from the dependency of the GFRP compressive strength with temperature.

5.4. Conclusions

This chapter presented an experimental study about the thermal and mechanical responses of pultruded GFRP columns subjected to fire, investigating the effects of (i) different passive and active fire protection systems, (ii) the number of sides exposed to fire, and (iii) the load level. The results obtained allow drawing the following main conclusions:

- For one-side fire exposure, all fire protection systems were effective in providing thermal insulation to the GFRP columns: the CS board was more effective in protecting the bottom flange, whereas the water-cooling systems, particularly the one with flowing water, were more effective in insulating the webs and top flange. Accordingly, for one-side fire exposure, all fire protection systems were very effective in extending the fire endurance of GFRP columns, with fire resistances above 50 min (CS board and stagnant water) and 120 min (flowing water).
- For three-side fire exposure, the temperatures in the top flange and particularly in the webs (if directly exposed to fire, *i.e.* in unprotected and water cooled protected columns) suffered a substantial increase compared to one-side exposure. Consequently, for three-side exposure, the fire resistance of the different solutions tested was severely reduced: the efficacy of the water-cooling systems remarkably decreased to about 20 min and did not improve much when flowing water was used; in this case, the best performance was provided by the CS board protection, with about 40 min of fire resistance.
- As expected, the increase in the load level caused decrease in fire resistance, due to the higher stresses developed in the sections’ walls and to the GFRP compressive strength reduction with temperature.
- During fire exposure, columns without CS board protection exhibited a slight axial elongation (due to the material thermal expansion); subsequently, all columns presented a progressive axial shortening (caused by the compressive stiffness decrease) up to

failure. Regarding the out-of-plane deformations, during the initial stage of the tests, in general, the columns presented a descending movement due to the thermal gradient throughout the depth of the cross-section; then, all columns started presenting an ascending movement, which was attributed to the increasing eccentricity of the applied load.

- All GFRP columns collapsed in a brittle manner, without any prior warning signs. The failure mode, which involved the formation of a hinge at a cross-section located in the central part of the columns, seemed to have been triggered either at the bottom flange or at the bottom flange and webs (depending on the number of sides exposed to fire), with those walls exhibiting a wrinkling type of failure with material crushing and delamination. In most cases, damage also propagated to the top flange, in the form of either cracking or wrinkling.
- In general, the average temperature of the section walls in which failure was triggered had already attained the T_g or at least the $T_{g,onset}$ of the GFRP material.

Part III:

Numerical and analytical studies

Chapter 6:

Thermal response of GFRP profiles exposed to fire

6.1. Introduction

Pultruded GFRP profiles are being increasingly used for civil engineering applications, in both new construction and structural rehabilitation, being connected by means of bolting or bonding [89, 90]. When compared to traditional materials, such as reinforced concrete and steel, the main advantages of GFRP profiles are lightness, high strength, ease of installation, good thermal and electro-magnetic insulation properties, durability and reduced maintenance [91]. On the other hand, the widespread acceptance of GFRP profiles is being hampered by their initial costs, relatively low stiffness and concerns about the behaviour at elevated temperature and under fire exposure [5].

These well-founded concerns, which are particularly acute for building applications, are due to the poor fire reaction and fire resistance behaviour of fibre reinforced polymer (FRP) materials in general [83, 92-97], and of pultruded GFRP profiles in particular [5, 98]. Moreover, the available guidelines do not provide any specific procedures for the fire design of GFRP profiles. The development of such guidance depends on obtaining a better understanding of the thermal and mechanical responses of GFRP profiles under fire exposure and also on the development of accurate modelling tools.

The mechanical properties of GFRP profiles considerably depend on temperature, with considerable changes taking place during the glass transition and decomposition processes, in which the material respectively changes from a glassy state to a rubbery solid state and then undergoes thermal decomposition. For instance, when the glass transition temperature (T_g, ~100-200 ºC) is approached and exceeded, the GFRP material softens, creeps and distorts, and its strength and stiffness decrease significantly, particularly under compression and/or shear [82, 99]. For higher temperatures (300-500 ºC), the polymeric matrix starts decomposing, releasing heat, smoke, soot and toxic volatiles [5], and further degradation of mechanical properties occurs.

The thermo-physical properties of the GFRP material, namely its density, thermal conductivity and specific heat, are also largely affected by the increase of temperature. When the decomposition temperature (T_d) is approached density suffers a substantial reduction due to pyrolysis of the polymeric matrix; after all the resin is consumed, density reaches a constant value, which is function of the inorganic content of the material [53]. The specific heat also exhibits considerable changes with temperature, due to the endothermic processes of water vaporization and especially of resin decomposition. The thermal conductivity also presents significant changes with temperature, presenting a considerable reduction during the decomposition process due to the porosity increase; once the pyrolysis process is completed, the thermal conductivity approaches that of the glass fibres [57], which present a progressive increase with temperature.

Regarding the modelling of the thermal responses of GFRP profiles in fire, previous analytical simulations were performed considering one-dimensional (in the through-thickness direction) or two-dimensional (cross-section) simplifications. For more complex problems, involving two- and three-dimensional geometries, computational simulations were done using the finite element (FE) method [6]. Such modelling efforts are summarized next.

Bai *et al*. [14] presented a one-dimensional heat transfer model to predict the thermal responses of pultruded GFRP multicellular deck panels. The authors considered the mechanism-based thermo-physical property models developed in [57] and assumed that heat transfer occurs only in the through-thickness direction of the bottom flange. In this study, the bottom flange was discretized into eight layers (1 mm thick) and a uniform through-thickness temperature distribution in each layer was assumed. The model was validated from the comparison between numerical results and experimental data obtained from fire endurance tests on full-scale GFRP multicellular decks [8], both unprotected and protected by means of water-cooling in the cells. This active protection was modelled as a convective boundary at the top face of the bottom flange of the deck panels (*i.e.*, the water flow was not explicitly modelled). A similar one-dimensional heat transfer approach was used by Bai *et al*. [15] to simulate the thermal responses of GFRP tubular sections exposed to fire from the bottom and protected with either different insulation materials or an active water-cooling system. Again, only the bottom flange of the cross-sections was explicitly modelled in these simulations.

Keller *et al*. [16] presented a two-dimensional thermal model of the above mentioned fire resistance tests on GFRP multicellular decks [8]. The model was developed using the commercial FE package *ANSYS Fluent* and provided accurate predictions of the temperatures in the bottom face of the panels, *i.e.*, the one exposed to fire. In these models, although convection and radiation boundary conditions were modelled at the hot surface, only conduction through the solid material was considered in the heat transfer process – the heat exchanges due to (i) internal radiation between the inner surface of the section walls of the cavity and (ii) convection of the air enclosed were not considered. As for the models of Bai *et al*. [15], only part of the cross-section was modelled (the bottom half) and the air inside the cells was not considered.

Very recently, López *et al*. [100] developed a model to simulate the thermal response of GFRP tubular profiles exposed to fire from the bottom, which was validated with the experimental data obtained from the fire resistance tests performed in the present thesis. An in-house two-dimensional FE code was developed in MATLAB, which considered the whole cross-section and also the air enclosed in the cavity by means of computational fluid dynamics (CFD). The main novelties of this work were (i) the consideration of the radiative heat exchanges between the faces of the cavity and (ii) the natural convection of the air enclosed in the section. The model was deemed valid as long as the fluid flow remains laminar. Furthermore, it was assumed that thermal properties of the air were temperature-independent. The results obtained highlighted the significant dependence of the temperatures in the GFRP material on both the radiative heat exchange between the faces of the cavity and the natural convection due to the air. However, at high temperatures, to obtain converged solutions very small time steps were required and this strongly increased the CPU time.

This chapter presents further numerical investigations about the thermal response of pultruded GFRP profiles subjected to fire. In order to overcome some of the limitations involved in the FE code presented by López *et al*. [100], namely the limited computational efficiency of the numerical algorithm and some of the simplifying assumptions (*e.g.*, the temperature-independent properties of the air), numerical models of the thermal response of GFRP profiles were developed using the commercial software *ANSYS Fluent* [18]. In particular, the thermal models were used to simulate the thermal responses measured in the fire tests conducted in the present thesis and Tracy's [24] in GFRP square tubular profiles and multicellular decks, respectively.

The remainder of the chapter is organized as follows. Section 6.2. describes the numerical thermal models of those tests, including the thermal properties considered for the materials involved. Section 6.3. presents the results of those models and the comparison with the corresponding test data. In order to further validate the thermal model, section 6.4. presents the numerical simulation of the fire tests performed by Tracy [24]. Finally, section 6.5. presents the main conclusions drawn from this study.

6.2. Numerical models

6.2.1. Introduction

The numerical thermal models of the fire resistance tests performed on this thesis were developed using the commercial software *ANSYS Fluent* [101], which allows solving heat transfer problems considering conduction, convection and radiation. Numerical models involving conduction and/or convection heat transfer are the simplest ones, while buoyancy-driven flow or natural convection and radiation models are more complex. Depending on the type of problem, the software solves the variation of energy equation, given by,

$$\underbrace{\frac{\partial(\rho E)}{\partial t}}_{Unsteady} + \underbrace{\nabla\cdot\left(\vec{v}(\rho E + p)\right)}_{Convection} = \nabla\cdot\left(\underbrace{k_{eff}\nabla T}_{Conduction} - \sum_j \underbrace{H_j \vec{J}_j}_{\substack{Species\\ diffusion}} + \underbrace{\left(\overline{\overline{\tau}}\cdot\vec{v}\right)}_{\substack{Viscous\\ dissipation}}\right) + \underbrace{S_H}_{\substack{Enthalpy\\ source}} \tag{7}$$

where t is time, ρ is density, E corresponds to equation $E = H - p/\rho + v^2/2$, H is sensible enthalpy, $\vec{v}$ is velocity, p is static pressure, k_{eff} is effective thermal conductivity, T is temperature, $\vec{J}$ is diffusion flux, $\overline{\overline{\tau}}$ is stress tensor and S_H is heat of chemical reaction.

Regardless of the type of flow considered, the software solves conservation equations for mass and momentum, and considers the solution of an additional equation for energy conservation when flows involve heat transfer or compressibility [101]. These equations are based on Navier-Stokes theory and govern the time-dependent laminar flow of viscous, incompressible and Newtonian fluids. The expressions for the conservation of mass or continuity equation (Eq. (8)) and for the conservation of momentum (Eq. 9) are as follows,

$$\frac{\partial\rho}{\partial t} + \nabla\cdot\left(\rho\vec{v}\right) = S_m \tag{8}$$

$$\frac{\partial}{\partial t}\left(\rho\vec{v}\right) + \nabla\cdot\left(\rho\vec{v}\vec{v}\right) = -\nabla p + \nabla\cdot\left(\overline{\overline{\tau}}\right) + \rho\vec{g} + \vec{F} \tag{9}$$

where S_m is the mass added to continuous phase from dispersed phase, $\rho\vec{g}$ is gravitational body force, and $\vec{F}$ are external body forces.

In the numerical models developed, natural convection and buoyancy-driven flows were considered since the tubular profile's cavity is filled with a fluid (air and/or water). In fact, a flow can be induced into a fluid volume due to the force of gravity acting on density variations of a heated fluid. Such buoyancy-driven flows are named as natural convection flows and can be modelled using *ANSYS Fluent*, which calculates buoyancy forces depending on the ratio between Grashof and Reynolds (Re) numbers and the value of the Rayleigh number (Ra), given by

$$Ra = \frac{g\beta(T_s - T_\infty)L^3}{\upsilon\alpha} \tag{10}$$

where g is acceleration due to gravity, β is thermal expansion coefficient of the fluid, T_s is surface temperature, T_∞ is fluid temperature far from the surface of the object, L is characteristic length, υ is kinematic viscosity and α is thermal diffusivity.

Regarding cavity radiation, as mentioned, the GFRP profiles' cavities were filled with air or water in the experiments carried out in this thesis. Among the different radiation models available in *ANSYS Fluent*, the surface-to-surface (S2S) radiation model allows accounting for the radiation exchange in an enclosure of gray-diffuse surfaces [101] and, therefore, this option was selected to simulate the enclosure radiative heat transfer, assuming non-participating media (air and/or water). In that radiation model, energy exchange between two surfaces depends on their size, separation distance and orientation. These parameters are taken into account through the use of a "view factor" (a calculated geometric function). This radiation model assumes the surfaces to be gray and diffuse, and the emissivity is considered equal to the absorptivity, according to Kirchoff's law [102]. The S2S model equations used for calculating the energy flux leaving from a surface and the energy flux incident on the surface are as follows,

$$q_{out,s} = \varepsilon_s \sigma T_s^4 + (1-\varepsilon_s) q_{in,s} \tag{11}$$

$$q_{in,s} = \left(\sum_{n=1}^{N} A_n q_{out,s} F_{ns} \right) \Big/ A_s \tag{12}$$

where $q_{out,s}$ is energy flux leaving surface s, ε_s is emissivity, σ is Stefan-Boltzmann constant ($5.699 \times 10^{-8} W/(m^2K^4)$), $q_{in,s}$ is energy flux incident on the surface that is reflected, A_s is area of surface s and F_{ns} is view factor between surface s and surface n.

The heat exchanges by radiation and convection with the furnace and with the laboratory environment are imposed at the external boundaries.

Finally, it is worth mentioning that this software is based on the finite volume method – the domain is discretized into a finite set of control volumes, for which general conservation equations for mass, momentum and energy are solved.

6.2.2. Description of numerical models

Overview and geometry of the models

Table 13 lists the numerical models that were developed in this study, indicating the type of fire protection (unprotected, CS boards or water-cooling, stagnant or flowing – illustrated in Figure 65), the type of exposure (one- or three-side) and the geometry of the model (two- or three-dimensional). As mentioned, in the fire tests temperatures were recorded only in the central part of the GFRP profiles (*cf*. “$T_{section}$” in Figure 66) and therefore this was the focus of the numerical simulations.

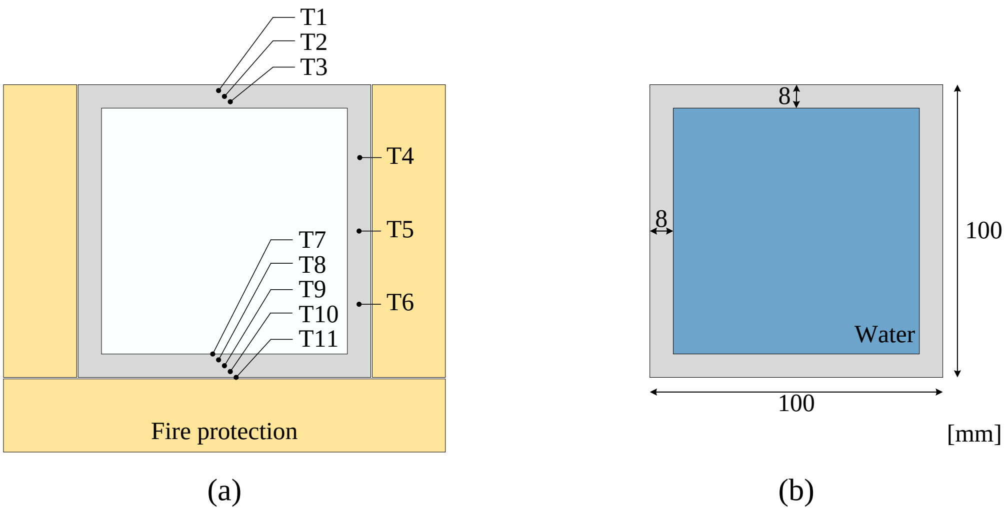

Figure 65: Scheme of the fire protection systems: (a) passive fire protection (for three-side exposure) and position of thermocouples, and (b) active fire protection for columns (WC_s/WC_f – water filled cavity, stagnant/flowing).

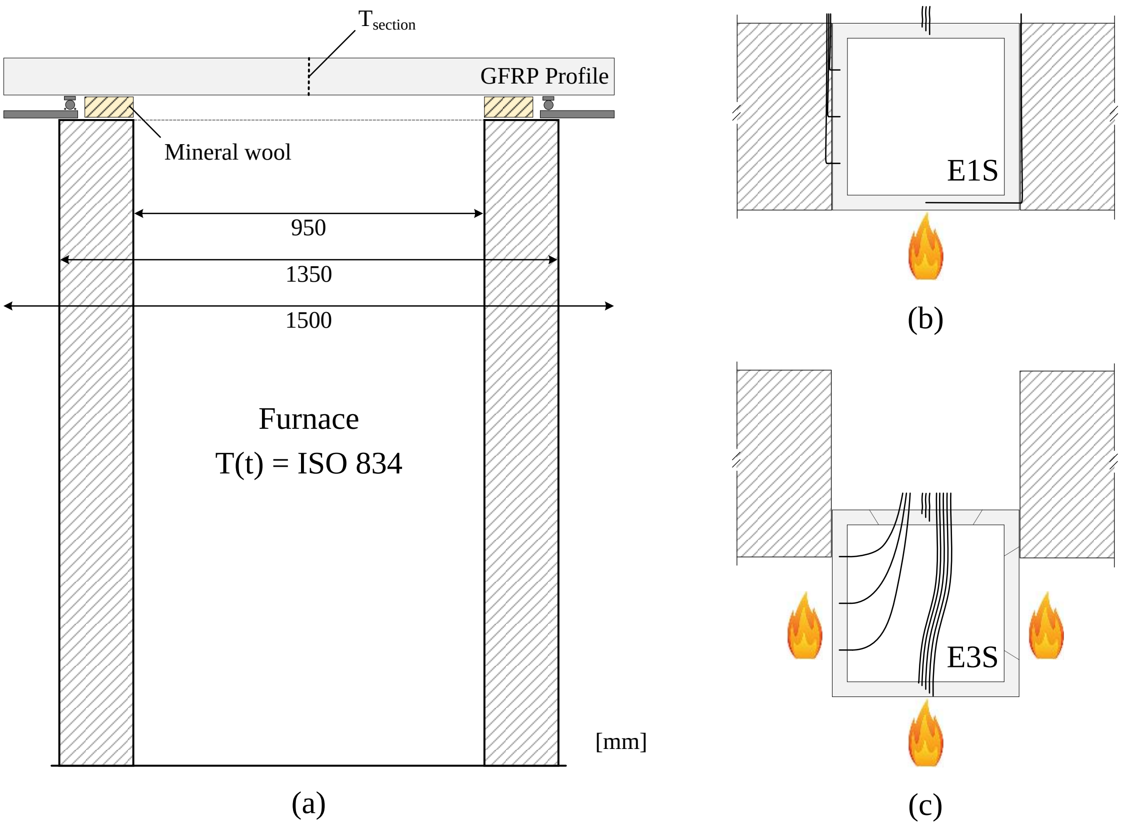

Figure 66: (a) Frontal view of test setup and fire exposure in (b) one-side (E1S) or (c) three-side (E3S).

Regarding the geometry of the models, with the exception of the cases involving flowing water (for which 3D models were developed, as described below), two-dimensional models were deemed as sufficiently accurate to simulate the thermal response of the GFRP profiles (namely, of their central section). This assumption was assessed for the unprotected profile exposed to fire from the bottom side (U-E1S – the reference profile), for which 3D models with two different lengths (200 and 400 mm, corresponding respectively to the double and the quadruple of the profile's height) were also developed and provided similar results to those obtained using 2D models. These two geometries were chosen to assess the influence of length on the temperature distributions at the mid-span section (where measurements were made) of both unprotected and protected specimens. It is worth mentioning that when natural convection inside the cavity of the tubular section is considered and the CFD analysis is performed, the CPU time necessary to solve the numerical problem significantly increases (for 3D, such increase is high). For example, in the reference profile (U-E1S), the CPU time required to complete the simulation of the 3D model was about 12 times higher than that needed to perform the 2D analysis. Although less refined mesh, higher time step and only a central part of the profile have been considered in the 3D simulations (as described in next sections), the computational effort required to solve this heat transfer problem was significantly higher when compared to the 2D analysis.

Table 13: Numerical thermal models developed.

Model	**Fire protection**	**Geometry**	**Fire exposure**	**Duration**
U-E1S	-	2D and 3D	One-side (E1S)	120 min
SC-E1S	Calcium silicate	2D		120 min
WC_s-E1S	Water-cooling (stagnant)	2D		60 min
WC_f-E1S	Water-cooling (flowing)	3D		120 min
U-E3S	-	2D	Three-side (E3S)	60 min
CS-E3S	Calcium silicate	2D		60 min
WC_s-E3S	Water-cooling (stagnant)	2D		60 min
WC_f-E3S	Water-cooling (flowing)	3D		120 min

For profiles protected with flowing water (WC_f-E1S and WC_f-E3S), three-dimensional (3D) models were developed due to the 3D nature of this particular problem – note that the water flows transversely to the cross-section. Since the main goal was to simulate the temperatures at mid-span section, to reduce the computational cost, a length of 200 mm was adopted for these models based on the marginal temperature increase obtained from the experiments at the water inlet and outlet (similarly to [3, 24]).

Boundary conditions

The following boundary conditions, illustrated in Figure 67, were considered in the computational models: (i) the bottom flanges (one-side exposure) and part of the webs (three-side exposure) are heated through radiation (ε_{GFRP} = 0.75 or ε_{CS} = 0.70) and convection (h = 25 W/m^{2}K) due to the ISO 834 fire curve; (ii) heat transfer occurs through conduction and also through internal radiation (ε = 0.75) between the cavity walls; (iii) the webs are considered as adiabatic surfaces for one-side exposure (E1S models); and (iv) the top flanges are cooled by radiation (ε = 0.75) and convection (h = 10 W/m^{2}K).

Due to the lack of specific information concerning the furnace used in the tests, the convection and emissivity coefficients were considered constant with temperature. The convection coefficient for the hot surface (h = 25 W/m^{2}K) was taken from Eurocode 1 [103]. With exception of the profiles with CS protection, the emissivity (ε_{GFRP}) for the hot surface was assumed constant and equal to 0.75, according to Bai *et al*. [57]. The emissivity of CS (ε_{CS}) was set as constant and equal to 0.70, according to Mimoso [104].

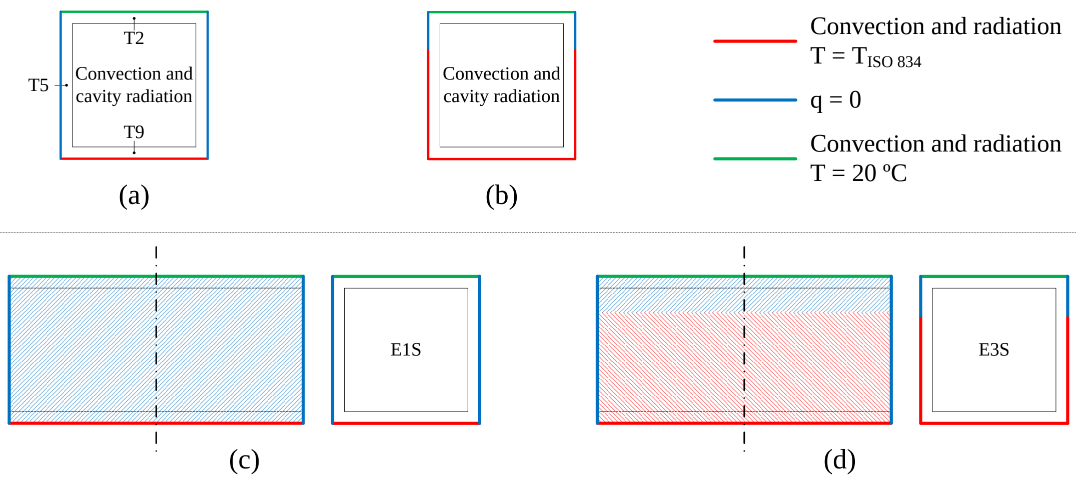

Figure 67: Boundary conditions for profiles under (a) one-side and (b) three-side fire exposure (2D model); for flowing water cooled profiles under (c) one-side (E1S) and (d) three-side (E3S) fire exposure (3D model).

Material properties

The thermo-physical properties of the materials at 20 ºC are listed in Table 14 and their variation with temperature is illustrated in Figure 68. Regarding these properties, the following assumptions were adopted: (i) for GFRP and CS materials, the density, specific heat and thermal conductivity were considered temperature-dependent, according respectively to Bai *et al*. [57] and to the information provided by the CS boards manufacturer (described in [80]); (ii) for air and water, the density, specific heat, thermal conductivity and dynamic viscosity were also considered temperature-dependent and were taken from [105, 106]. Regarding the thermal expansion of the fluid inside the cavity, the coefficient β is automatically computed by the software based on the variation of density and temperature [101].

Table 14: Thermal properties at 20 °C (reference values).

Material	**ρ_0 [kg/m^3]**	**c_{p0} [J/kg·°C]**	**k_0 [W/m·°C]**	**μ_0 [kg/m·s]**
GFRP [57]	1890.0	1053.0	3.5×10^{-1}	-
Air [105]	1.2	1004.6	2.6×10^{-2}	1.8×10^{-5}
Water [105]	998.0	4183.0	6.0×10^{-1}	1.0×10^{-3}
SC [76]	450.0	815.0	9.0×10^{-2}	-

ρ – density; c_p – specific heat; k – thermal conductivity; μ – dynamic viscosity.

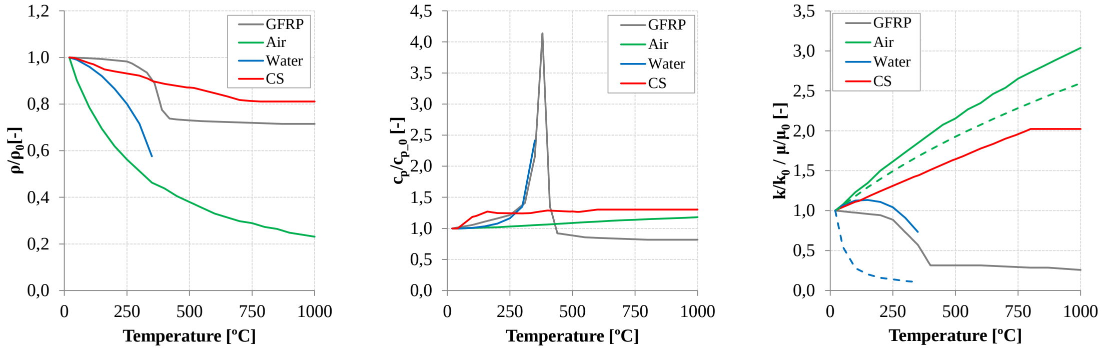

(a) (b) (c)

Figure 68: Normalized thermal properties as a function of temperature: (a) density, (b) specific heat and (c) thermal conductivity and kinematic viscosity (dashed).

Mesh

The 2D models of the unprotected profiles (models U-E1S and U-E3S) and of the profiles protected with CS boards (CS-E1S and CS-E3S) and stagnant water (WC_s-E1S and WC_s-E3S) were discretized using a regular mesh of quadrilateral elements (*Quad4*) with 1 mm of size, in both the solid and fluid parts. For the unprotected profiles, this mesh size involved 10,000 elements and 10,201 nodes. For the 3D models of the unprotected profile (U-E1S) and of the profiles protected with flowing water (WC_f-E1S and WC_f-E3S) a regular mesh of hexahedral elements (*Hex8*) with 2 mm of size was adopted. For the model of the unprotected profile with 200 mm of length, this involved 262,701 nodes and 250,000 elements.

Type of analysis

ANSYS Fluent has two options for the type of regime of fluid flows: laminar or turbulent, the latter being far more complex and computationally demanding. In order to define the type of fluid flow inside the section cavity to be considered in the thermal analyses, the dimensionless Rayleigh number (Ra) was calculated. Note that if Ra is below a critical value ($Ra_c = 1708$) heat transfer in the fluid enclosed in the section cavity occurs through conduction, while if Ra exceeds this critical value heat exchanges should be considerably affected by convection. In this case, a laminar regime is generally observed for $10^3 < Ra < 10^5$, while a turbulent regime is expected to occur for $Ra > 10^9$ [107]. Taking into account the experimental temperatures measured in the reference specimen (U-E1S), the maximum value of Ra calculated using

Eq. (10) varied between 5×10^5 and 3×10^6 and, therefore, a laminar-to-transitional regime would be expected in this heat transfer problem. Thus, given the complexity (and CPU time) involved in three-dimensional turbulent analysis, the fluid flow was considered laminar in all thermal analyses performed in this study. For water-cooling, laminar flow was also considered. The validity of this assumption was confirmed based on results obtained (max Re = 1341 < 2100, upper bound of laminar flow [108]).

Transient analyses were carried out considering a total time of 60 or 120 minutes (Table 13). Time steps of 1 and 2 seconds were used in the 2D models and 3D models, respectively. In all models, the initial temperature was set equal to 20 ºC. For the profiles protected with flowing water, measurements made during the tests indicated that the water temperature at the outlet section remained between 20 and 30 ºC. Thus, the following assumptions were considered in these numerical simulations: (i) at the inlet surface, temperature was considered as 20 ºC and the velocity was set constant at 1.6 cm/s; (ii) at the outlet surface, pressure was set as 0 Pa, since the outlet orifice was open.

6.3. Numerical results and discussion

6.3.1. Unprotected profiles

As mentioned, in the 2D models of the unprotected profile exposed to fire in one-side (U-E1S) different options were tested regarding the heat transfer inside the cavity of the tubular section. Figure 69 illustrates the temperature profiles obtained for 2D models MC (only solid part), MCR and MCRV (solid and fluid parts) after 60 min of fire exposure. Figure 70 presents the comparison between numerical and experimental temperatures at thermocouples T2, T5 and T9, located respectively at the top flange (half-thickness), web (half-height) and bottom flange (half-thickness), as illustrated in Figure 65(a).

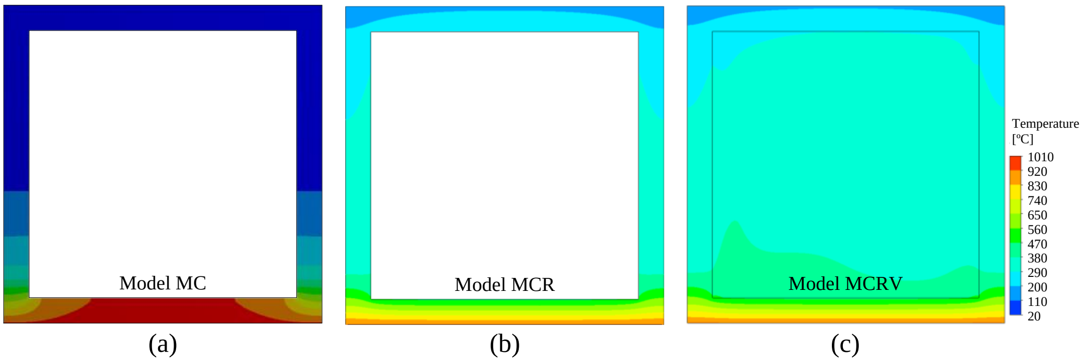

Figure 69: Temperature distributions obtained from numerical models (a) MC, (b) MCR and (c) MCRV (time = 60 min).

By considering only heat exchanges by conduction in the solid part – model MC – temperatures calculated in the bottom and top flanges are respectively much higher and much lower than their experimental counterparts (Figure 70(a)). It is also worth mentioning the non-uniform temperature distribution across the width of the bottom flange in this model (Figure 69(a)). By considering cavity radiation – model MCR – a better agreement between numerical temperatures and experimental data is obtained, namely in the top flange (*cf*. Figure 70(b)); nevertheless, numerical temperatures in the bottom flange (now, more uniform across the width, Figure 69(b)) still remain considerably higher than the experimental ones, and temperatures in the webs and top flange also present significant differences to the corresponding experimental data. If natural convection and radiative heat exchange inside the cavity are considered simultaneously – model MCRV – the numerical temperatures generally agree much better with test data (Figure 70(c)). Although similar temperature distribution (shown in Figure 69(c)) had been observed in models MCR and MCRV, the second model provided the best agreement with test data. Based on these results, which confirm the previous findings of López *et al*. [100], it was decided to consider the convection and radiative heat exchanges inside the cavity in the remaining thermal simulations. It can also be seen that the influence of internal radiation seems to be more relevant than that of the convection inside the cavity. Figure 70(c) also highlights the agreement between temperatures obtained from 2D and 3D models.

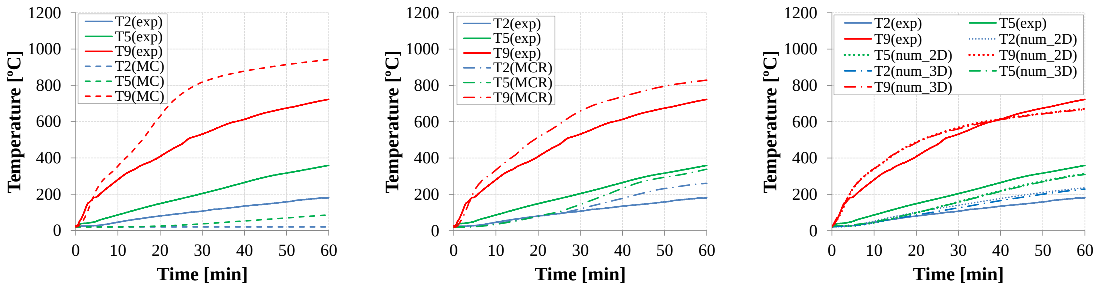

(a) (b) (c)

Figure 70: Comparison between experimental and numerical temperatures for reference profile (U-E1S) using (a) model MC (2D), (b) model MCR (2D) and (c) model MCRV (2D and 3D models).

Figure 71 shows the velocity fields obtained from model MCRV at different exposure periods. During the initial stages of fire exposure, two convective cells are formed almost symmetrically (Bénard cells), corresponding to a steady laminar regime – note that very limited vortices emerge in this stage but with residual rotational velocity. At some point, the flow becomes unsteady, with the formation of vortices of very small dimension at the bottom corners of the cavity. Beyond this point, the vortices tend to grow slightly in dimension and move the convective cells upwards, becoming asymmetrical and irregular. The highest velocities occur during the first 30 min of exposure, a fact that is consistent with the maximum temperature differences found between the inner surfaces of bottom and top flanges. The above-mentioned changes in the fluid flow are also consistent with the Ra number – according to Pallares *et al*. [109], for Ra higher than 10^6, unsteady laminar flows may develop with formation of vortices.

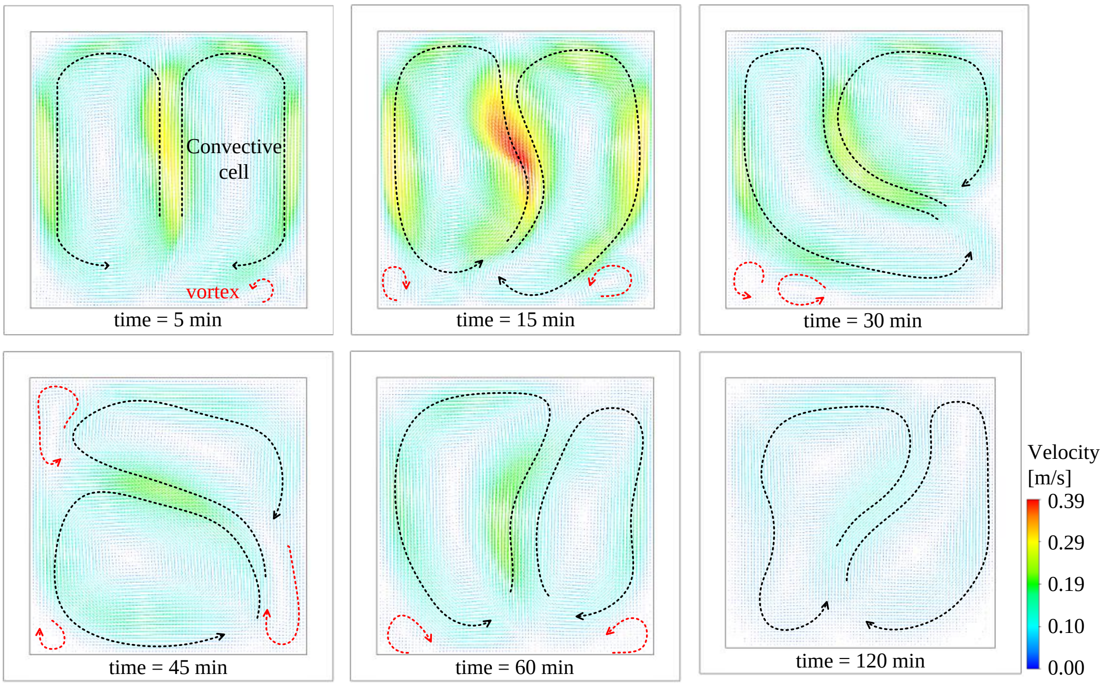

Figure 71: Velocity field (model MCRV) in the reference profile (U-E1S) after 5, 15, 30, 45, 60 and 120 min.

Table 15 presents a comparison between numerical and experimental temperatures after 30 and 60 min obtained using the different 2D models tested for the reference profile U-E1S. Two parameters were determined for comparison purposes, one based on temperature differences (ΔT) and the other considering the differences between the areas defined by the time-temperature curves (GE),

$$\Delta T = \left(T_{num} - T_{\exp}\right) / T_{\exp} \tag{13}$$

$$GE = \left(A_{num} - A_{\exp}\right) / A_{\exp} \tag{14}$$

where T_{num} and T_{exp} are respectively the numerical and experimental temperatures, and A_{num} and A_{exp} are respectively the areas below the numerical and experimental time *vs.* temperature curves.

Once more, results listed in Table 15 confirm the higher accuracy of model MCRV, highlighting the need to simultaneously consider conduction, radiation and convection heat transfer inside the cavity. In MCRV model, numerical temperatures in the top flange were about +20% higher than those measured experimentally. In the web, calculated temperatures were -20% to -35% lower than the measured ones. For the bottom flange, the numerical and experimental temperatures were similar, with relative differences below 10%.

Table 15: Numerical *vs*. experimental results for the profiles U-E1S and CS-E1S.

			Top flange (T2)		**Web (T5)**		**Bottom flange (T9)**	
Profile	**Time**	**Model**	ΔT	GE	ΔT	GE	ΔT	GE
U-E1S	30 min	MC	-81%	-69%	-82%	-75%	+53%	+43%
		MCR	+10%	+6%	-31%	-45%	+23%	+22%
		MCRV	+22%	+15%	-30%	-37%	+4%	+11%
	60 min	MC	-89%	-79%	-76%	-78%	+30%	+41%
		MCR	+43%	+26%	-6%	-19%	+15%	+21%
		MCRV	+20%	+20%	-20%	-28%	-8%	+1%
CS-E1S	30 min	MCRV	-9%	-18%	-46%	-42%	+11%	+10%
	60 min		+2%	-5%	-34%	-38%	-5%	+9%
	75 min		+4%	-3%	-33%	-44%	-10%	+4%

As mentioned, 3D models with two different lengths (200 and 400 mm) were also developed for the reference profile (U-E1S) to compare results from 2D and 3D analyses. The numerical results obtained for the 3D models with the two different lengths were virtually similar. Figure 72 shows the distribution of temperatures obtained from the 3D model with 200 mm of length in the transversal (for plane z = 0.10 m, 0.00 ≤ x ≤ 0.10 m and 0.00 ≤ y ≤ 0.10 m) and longitudinal (for plane x = 0.05 m, 0.00 ≤ y ≤ 0.10 m and 0.00 ≤ z ≤ 0.20 m) directions. In the longitudinal section, it can be seen that temperature distributions are roughly constant along the length, which confirms the suitability of using 2D models for unprotected profiles (and also for profiles with passive protection). Expectedly, as shown in Figure 70(c), the results obtained from the 2D MCRV model were very similar to those provided by the 3D model (200 mm long).

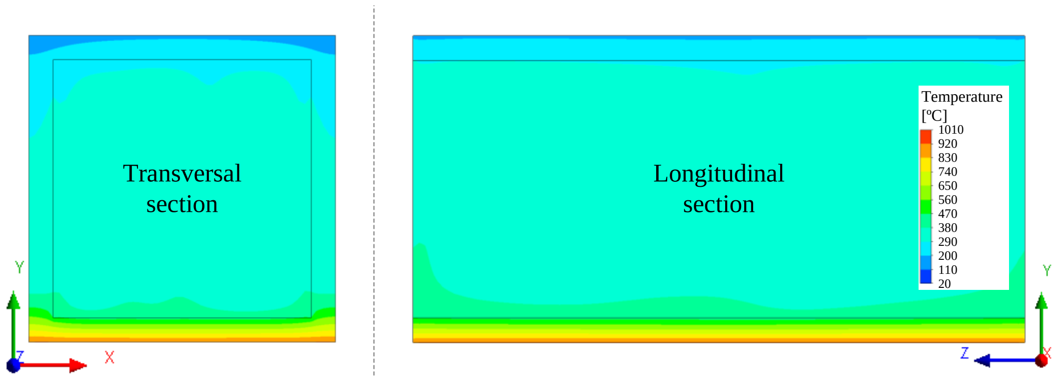

Figure 72: Temperature distribution for profile U-E1S using 3D model (time = 60 min).

Regarding the unprotected profile exposed to fire in three sides, Figure 73(a) presents the temperature distribution after 60 min of exposure and Figure 74(b) presents a comparison between the calculated temperature profiles at the positions of thermocouples T2, T5 and T9 (*cf.* Figure 65(a)) for one- and three-side exposure. For three-side exposure, temperatures in the bottom flange and web were very similar (due to the similarity of their thermal exposure). In addition, those temperatures were much higher than those corresponding to one-side exposure, particularly at the webs. Figure 74(b) shows also that top flange temperatures were of similar magnitude for one- and three-side exposures.

6.3.2. Profiles with CS passive protection

Figure 73(b) and Figure 73(c) show the temperature distribution after 60 min of exposure for profiles CS-E1S and CS-E3S, subjected respectively to one- and three-side fire exposure. Figure 74(a) presents a comparison between the numerical and experimental temperature evolutions for profile CS-E1S.

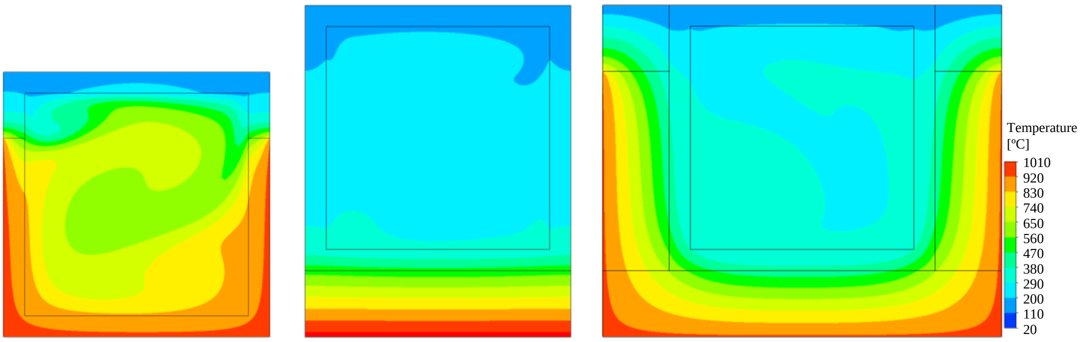

(a) (b) (c)

Figure 73: Temperature distribution for profiles (a) U-E3S, (b) CS-E1S and (c) CS-E3S (time = 60 min).

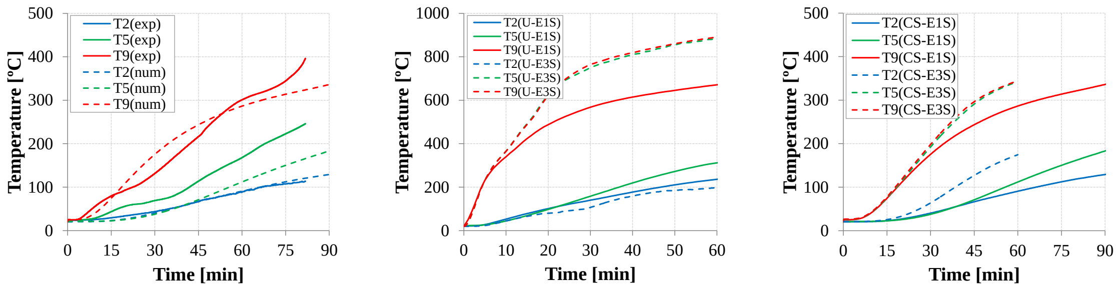

(a) (b) (c)

Figure 74: (a) Experimental and numerical temperature evolutions for profile CS-E1S; and numerical temperature evolutions for profiles (b) U-E1S/E3S and (c) CS-E1S/E3S.

For both CS board protected profiles, numerical and experimental results, although presenting some differences (namely in the bottom flange and web), are in general good agreement, in particular for one-side fire exposure. Those differences probably stem from the thermal properties considered for the CS material (for instance, there may be differences in the moisture content of the CS panels used in the fire tests and those used in the characterization tests made by the manufacturer). In these simulations, once again at some point multiple vortices were observed in the velocity fields, as in the reference profile.

Figure 74(c) compares the numerical temperature evolutions obtained for profiles CS-E1S and CS-E3S, highlighting the effects of three-side exposure in CS-protected profiles. As expected, the temperatures in the different section walls of profile CS-E3S are higher than those of profile CS-E1S, with the highest relative differences occurring in the top flange and especially the webs. For both types of exposure, taking as a reference the temperatures reported above for the unprotected profiles, Figure 74 confirms the efficacy of the CS passive fire protection in delaying the heating of the GFRP profile's section walls, for both one- and three-side fire exposure.

Table 15 compares the numerical and experimental results for the protected profile CS-E1S. According to the ratios calculated for profile CS-E1S, similar temperature differences were measured not only at the top flange (in general, lower than 10%), but also at the bottom flange (lower than 11%). As for the unprotected profile, in the web the numerical temperatures were lower than measured, with relative differences varying from -33% to -46%. It is likely that such differences are due to a non-fully effective lateral insulation of the webs during the fire experiments. Indeed, although one aimed at guaranteeing that the lateral insulation was tight enough to avoid the heat from flowing along the outer faces of the webs, at the same time it was also necessary to allow for the free deformation of the profiles during the tests. Because the cover sets used as lateral insulation could not be fully tightened against the GFRP profile, the assumption of adiabatic lateral faces is not entirely true.

6.3.3. Profiles with water-cooling protection

To simulate the thermal responses of water cooled profiles and to further assess the efficacy of this type of active fire protection, 3D models had to be developed for flowing water protection (WC_f), while 2D models were used for the stagnant water-cooling protection (WC_s). Figure 75 shows the temperature distribution for profiles WC_s-E1S and WC_s-E3S (stagnant water) after 60 min of fire exposure and for profiles WC_f-E1S and WC_f-E3S (flowing water) after 60 and 120 min of exposure, illustrating the influence of the number of sides exposed to fire and also of the water flow. The results show (i) the remarkable influence of flowing water in reducing the temperatures in both solid and fluid parts of the section (with standing water, the evaporation temperature of water is largely exceeded), (ii) the much higher temperatures reached in the GFRP material under three-side exposure, and (iii) the temperature stabilization after 60 min with flowing water.

Figure 76(a) presents a comparison between experimental and numerical temperatures for profile WC_s-E1S and Figure 76(b) compares the numerical temperatures for one- and three-side exposure in profiles WC_s. Although the numerical temperatures were slightly higher in the top flange and lower in the webs compared to the experimental ones, given the complexity of the problem, it is fair to claim that the thermal simulations provided consistent and relatively accurate results (*cf.* Figure 76(a)). Now comparing numerical temperatures for one- and three-side exposure, as expected, the heating rates in profile WC_s-E3S are much higher than those in profile WC_s-E1S.

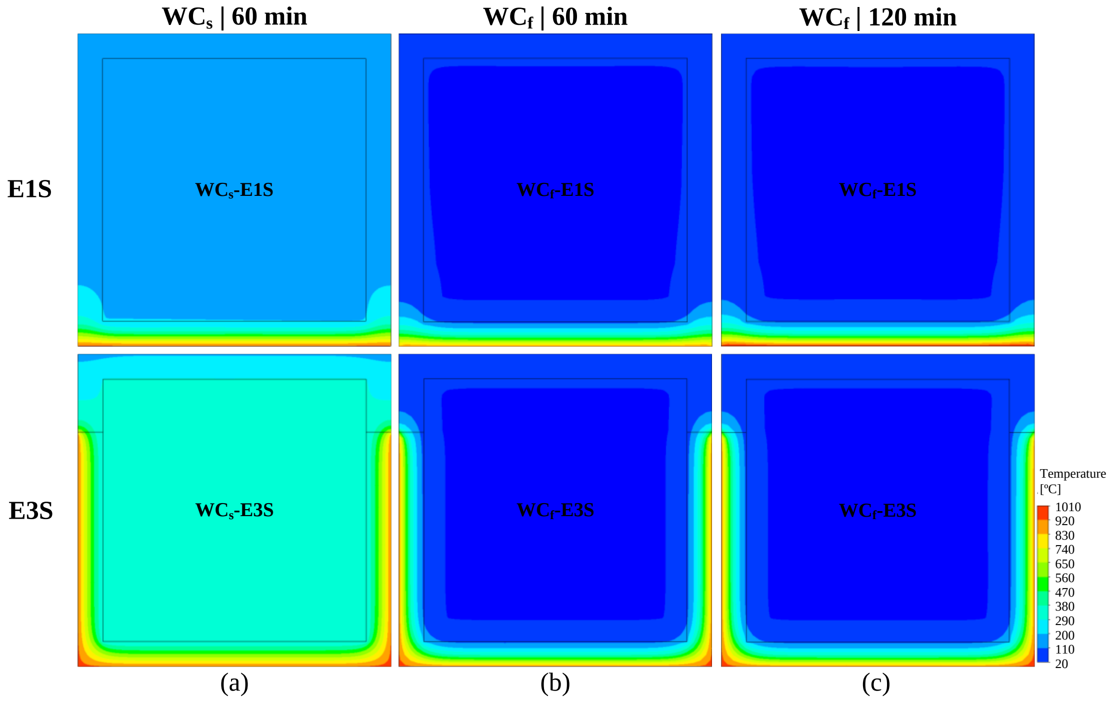

Figure 75: Temperature distribution for (a) profiles WC_s-E1S and WC_s-E3S after 60 min, and profiles WC_f-E1S and WC_f-E3S after (b) 60 min and (c) 120 min.

Figure 76(c) plots the evolution of temperatures at the centre of the top flange (T2), web (T5) and bottom flange (T9) of profile WC_f-E1S (cavity filled with flowing water, one-side exposure) obtained from the numerical model, together with the experimental measurements in the webs and top flange. According to the numerical results, after 120 min of fire exposure, the temperatures in the webs and top flange of profile WC_f-E1S presented a marginal increase (from 20 to 21 ºC). In the experiments, such temperature increase was much higher, especially in the web. Once again, it is very likely that these differences stem from the lateral insulation used in the experiments; as mentioned, such insulation was not fully effective and, for one-side exposure, the outer surface of the webs were not completely adiabatic.

Figure 76(d) plots the (numerical) evolution of temperatures at the centre of the section walls for both one- and three-side exposure. For three-side exposure, similar temperature increase occurs in the bottom flange and webs (note that the curves coincide), while temperatures in the top flange remain approximately constant (similar to the one-side exposure).

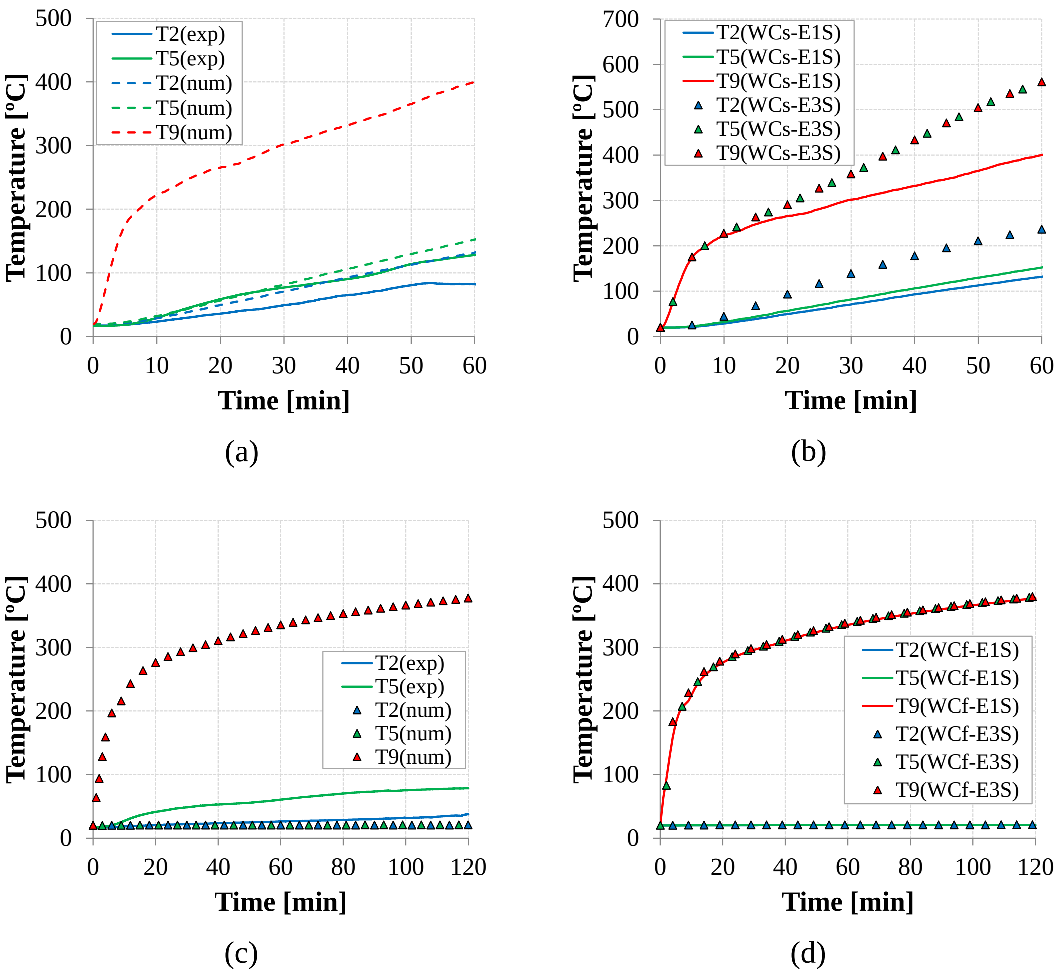

Figure 76: Experimental and numerical temperature evolutions for profiles (a) WC_s-E1S and (c) WC_f-E1S; and numerical temperature evolutions for profiles (b) WC_s-E1S/E3S and (d) WC_f-E1S/E3S.

6.3.4. Effectiveness of fire protection systems

As discussed in the preceding sections, the passive and active fire protection systems allowed delaying the temperature increase in the GFRP profile. As shown in Figure 77, and in comparison with the unprotected profiles, a considerable reduction of temperatures took place in the different section walls. This temperature decrease between the unprotected and protected profiles leads naturally to an improvement of the mechanical behaviour of GFRP profiles in fire because their mechanical properties significantly decrease with increasing temperatures. In case of one-side exposure (Figure 77(a)) the water-cooling system provided the most effective protection for the webs and top flange, while the passive fire protection was more effective in reducing the temperatures at the bottom flange. In case of three-side fire exposure (Figure 77(b)), the water-cooling system was also the most effective in protecting the top flange, while the CS boards were the most efficient in protecting the webs and the bottom flange.

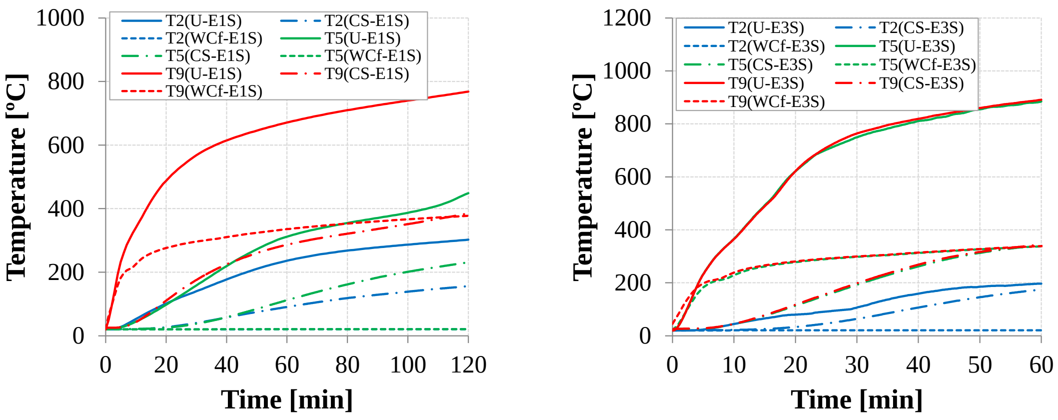

(a) (b)

Figure 77: Numerical temperature evolutions in the unprotected and protected profiles when exposed to fire in (a) one side and (b) three sides.

The numerical study described above provided the evolution of temperatures throughout the cross-section of the GFRP profiles, for different protection schemes and types of exposure. Aiming to perform mechanical calculations and following Gibson *et al*. [110, 111], these temperatures can be used to define a “residual section” based on a “critical” temperature. This residual section, is defined as the ratio between the area of material with temperature below $T_{g,onset}$ (82 ºC), set as an indicative critical temperature, and the total area of the wall (webs, bottom and top flanges). For both types of fire exposure, Figure 78 presents the evolution of such residual section, given in percentage (%), for the different walls.

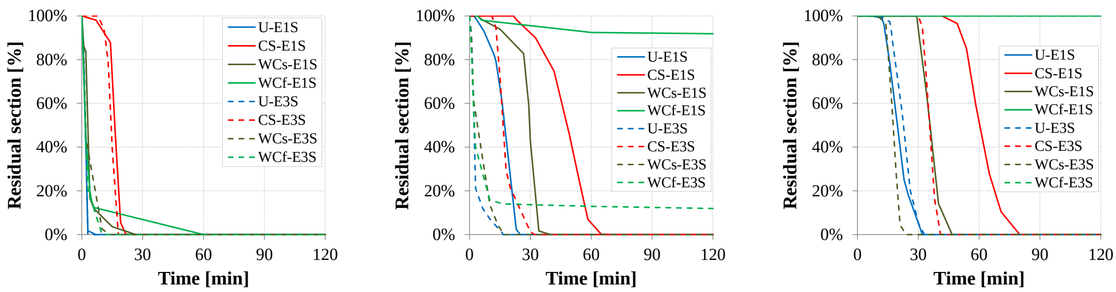

(a) (b) (c)

Figure 78: Evolution of residual section of walls for one- and three-side exposure: (a) bottom flange, (b) web and (c) top flange.

Figure 78(a) shows that the reduction of the residual section of the bottom flange is very similar (and sudden) for the unprotected profiles and the water cooled (WC_s/WC_f) profiles – here, the only effective protection is provided by the CS boards: for the protection thickness used, the residual section is reduced to 50% after about 16 and 14 min respectively for one- and three-side exposure. For one-side exposure and for the webs (Figure 78(b)), the CS boards are more effective than flowing water-cooling (WC_f) during the first 25 min of exposure (where both protections are very effective); subsequently, the residual section is kept roughly constant for flowing water-cooling (WC_f) while it suffers a considerable reduction for CS protection, dropping to less than 50% after 48 min. For three-side exposure, the effectiveness of flowing water-cooling is very quickly reduced – the residual section drops to 50% after only 3 min and then tends to about 33%; in this case, the CS boards are more effective in protecting the webs (for the first 11 min of exposure), but the residual section of the webs becomes null after 32 min. Concerning the top flange (Figure 78(c)) and regardless of the type of exposure, the most effective protection method is flowing water-cooling (WC_f), which is able to keep the temperature of the entire section wall below $T_{g,onset}$ during (at least) 120 min of exposure. For CS protection, the residual section starts to decrease after about 42 and 30 min respectively for one- and three-side exposure (for the indicative "critical" temperature considered herein). Results obtained highlight the much less efficacy of standing water-cooling (WC_s) compared to both flowing water-cooling and CS boards – with the former protection the overall residual section is reduced to 50% after about 30 and 3 min for one- and three-side exposure, respectively.

6.4. Numerical simulation of tests by Tracy

6.4.1. Introduction

In order to extend the numerical models developed in this study to other configurations of cross-sections and further validate them, the tests conducted by Tracy [24] were also simulated. These experiments comprised two fire resistance tests on GFRP multicellular slabs (Figure 79(a)), one unprotected and the other protected with a water-cooling system. The slabs were first subjected to a serviceability load in a four-point bending simply supported configuration and then exposed to the ISO 834 [13] fire from the bottom surface.

The full-scale slab specimens, with a six-cell cross-section, had 914 mm of width, 195 mm of depth and 3500 mm of length, and were tested in a 2750 mm span. In the protected specimen, three 7 m long circuits of water flowing in the six cells of each slab were prepared (two cells for each circuit). To allow the water to flow the length of one interior cell and then return in the adjacent one, notches were cut into the webs separating the cells at the far ends of the slab. Notches were also cut in the top flange in order to install the water-cooling system (for water inlet and outlet). Tracy measured the thermal (and mechanical) responses of the slabs during the tests and reported the temperature measurements made in the bottom flange [24].

6.4.2. Description of numerical model

Like in the previously shown models, the simulations of the thermal response of the slabs in fire were also performed using *ANSYS Fluent*. The effect of considering the different heat transfer processes, not only conduction through the solid material, but also internal radiation and convection inside the cavities, was studied. As for the tubular profiles tested in this thesis, it was concluded that reliable results can only be found if all these phenomena are taken into account in the thermal analyses. Likewise, laminar fluid flow was also considered in this simulation.

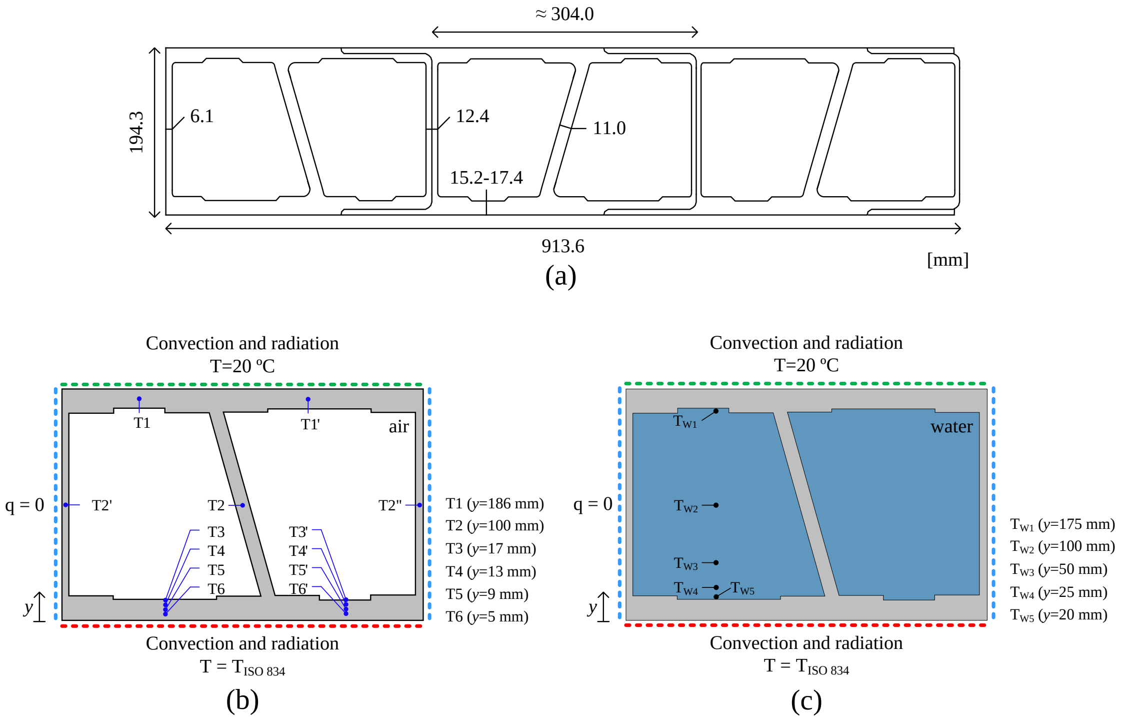

Figure 79: (a) Cross-section of GFRP multicellular slabs tested by Tracy [24]; and boundary conditions considered for the (b) unprotected and (c) protected slabs and location of points where temperature was monitored.

In terms of geometry, only a central part of the water cooled slab was modelled because the simulation of the entire slab would be much more cumbersome in terms of the amount of degrees-of-freedom and would require a significant CPU time. This central part corresponds to the two-cell profile illustrated in Figure 79(b) and Figure 79(c). As for the two-cell profile, a 2D model was developed for the unprotected slab, while a 3D model was used to simulate the protected slab. Based on the 3D thermal analyses performed for the two-cell profile, a length of 608 mm was adopted in the 3D models of the protected slab, corresponding to the double of the maximum dimension of the cross-section (in this case, the width, 304 mm). During the fire resistance tests, the inlet and outlet temperatures of the flowing water were recorded experimentally and were reported to have increased between 5 and 11 ºC [24], which further justifies the option for modelling only the central part of the GFRP multicellular slab.

The following boundary conditions were considered: (i) the bottom flanges were heated through radiation (emissivity ε varying linearly from 0.75 to 0.95 for temperatures of 20 and 1000 ºC, respectively, according to the information provided by Tracy [24]) and convection (h varying linearly from 5 to 50 W/m^2K for those same temperatures, also according to Tracy [24]); (ii) heat transfer occurred through conduction and also through internal radiation ($\varepsilon = 0.75$, as defined by Bai *et al*. [57]) between the cavity walls; (iii) the lateral webs were considered as adiabatic surfaces; and (iv) the top flanges were cooled by radiation ($\varepsilon = 0.75$) and convection ($h_c = 10$ W/m^2K), as shown in Figure 79(b) and Figure 79(c).

The GFRP material used in Tracy's experiments was very similar to that tested in the present thesis – alternating layers of E-glass fibre rovings and mats embedded in a polyester matrix and, therefore, the same thermal properties (presented in Table 14) were considered. The variation with temperature of the thermal properties of the different materials (air, water and GFRP) was considered (see Figure 68).

For the discretization of the unprotected slab (2D model), with dimensions of 194×304 mm, quadrilateral and triangular elements (*Quad4* and *Tri3*) with a size of approximately 2 mm were used for both solid and fluid parts. The mesh adopted had 15,362 nodes and 15,124 elements. To simulate the water cooled slab (3D model), a mesh of hexahedral and wedge elements (*Hex8* and *Wed6*) with about 4 mm of size was used, comprising a total of 612,153 nodes and 589,760 elements. The following initial conditions were set: (i) initial temperature of 20 ºC, (ii) water temperature of 20 ºC and constant velocity (2.5 cm/s) for the inlet surfaces, and (iii) pressure equal to 0 Pa for the outlet surfaces. For both slabs, transient analyses were carried out for a total time of 60 minutes, with time steps of respectively 1 second (unprotected slab – 2D model) and 2 seconds (water cooled slab – 3D model).

6.4.3. Numerical results

Figure 80 shows the temperature distributions obtained numerically for the unprotected (2D model) and protected (3D model) slabs after 60 min of fire exposure. The two-dimensional (x-y plane) distribution of temperatures depicted in Figure 80(b) corresponds to the mid-span cross-section (for plane $z = 0.304$ m, $0.000 \leq z \leq 0.608$ m) of the water cooled slab obtained from the 3D model. In this case (3D model), the temperature distributions in x-y plane along the length of the slab (variation with z) were similar to the one obtained at the mid-span cross-section and presented in Figure 80(b).

Figure 81 plots the numerical temperatures at different positions of the top flange (T1), web (T2) and bottom flange (T3, T4, T5 and T6) of the unprotected and protected slabs (see Figure 79(b)), together with experimental results at some of those positions, namely in the bottom flange (measurements were made at mid-span cross-section). It is worth mentioning that the time-temperature curves were similar in both cells of the cross-section (T1-T1', T2'-T2''and T3-T3').

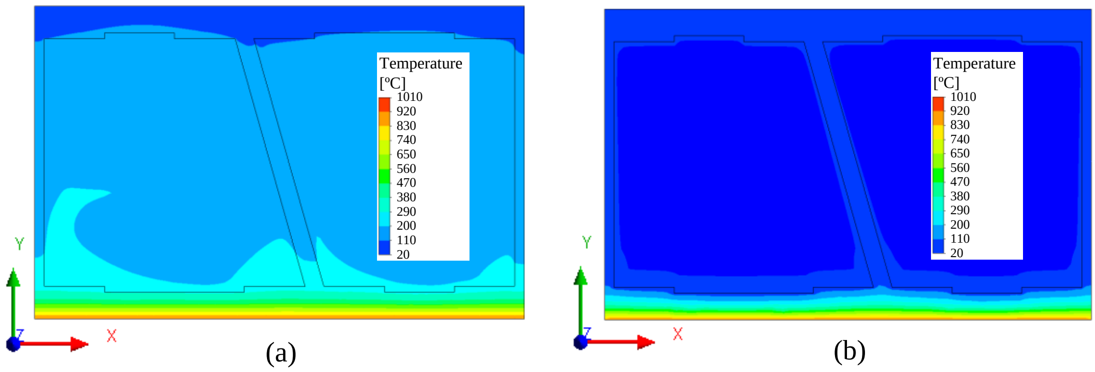

(a) (b)

Figure 80: Temperature distribution for (a) unprotected (b) protected slabs (after 60 min).

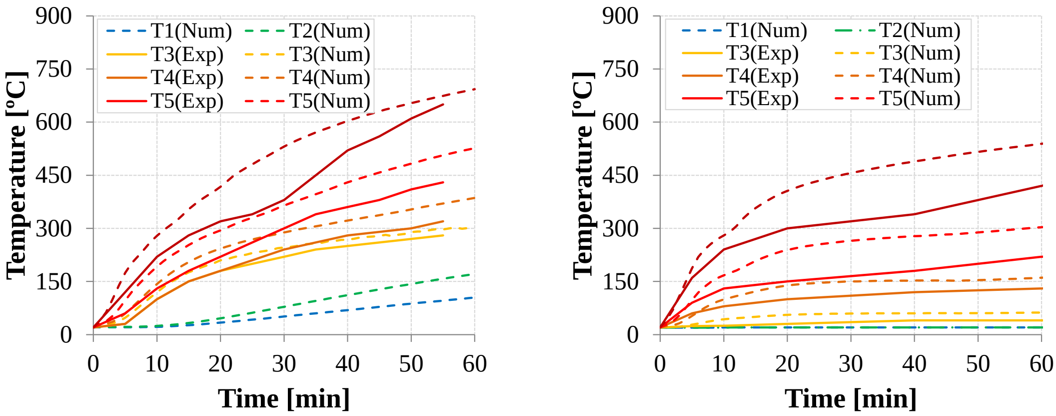

(a) (b)

Figure 81: Numerical temperature evolutions for the (a) unprotected and (b) protected slabs.

The results presented in Figure 81 show that the variations of temperatures determined numerically with time are qualitatively similar to those measured experimentally. Despite some relative differences (Table 16), particularly close to the hot face (position T6), the temperatures obtained numerically are in fairly good agreement with the experimental ones. These differences may stem from different sources, including the thermal properties considered for the GFRP material. Taking into account the comparison between the experimental and numerical results, a better agreement was obtained in case of the unprotected slab. The results also confirm the effectiveness of the active protection in delaying the temperature increase (measured in the experiments) (i) in the bottom flange (particularly in its inner part, positions T3 and T4) and especially (ii) in the webs and top flange, whose temperatures exhibited minor changes with the exposure period. Figure 82 illustrates the efficacy of the fire protection system, by plotting the temperature profiles in the unprotected and protected slabs at different exposure periods.

Table 16: Comparison between numerical and experimental results from Tracy's experiments [24].

Simulation	Time	Bottom flange (T3)		Bottom flange (T6)	
		ΔT	*GE*	ΔT	*GE*
Unprotected slab	30 min	+12%	+18%	+40%	+11%
	55 min	+8%	+33%	+7%	+22%
Protected slab	30 min	+69%	+66%	+43%	+68%
	60 min	+55%	+10%	+27%	+35%

Figure 83(a) plots the evolution of water temperature at different positions throughout the section height of the protected slab (*cf.* Figure 79(c)). As expected, the temperature increase in water is much higher next to the GFRP bottom flange. Indeed, water temperature increases only in a thin layer next to the bottom flange (T_{W4} and T_{W5}), with temperatures remaining approximately constant (~20 ºC) in most of the thickness of the water-cooling layer (~97%).

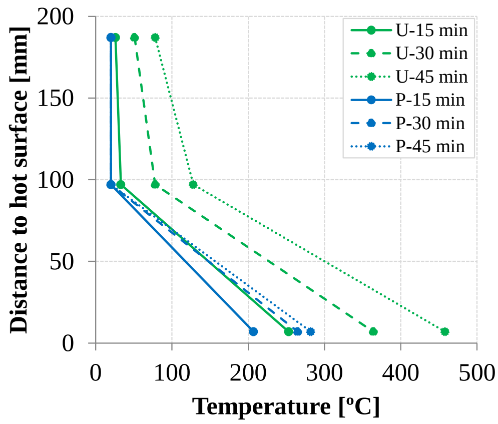

Figure 82: Temperatures across the GFRP cross-section depth for different fire exposure periods (15, 30 and 45 min) for the unprotected (U) and protected (P) slabs.

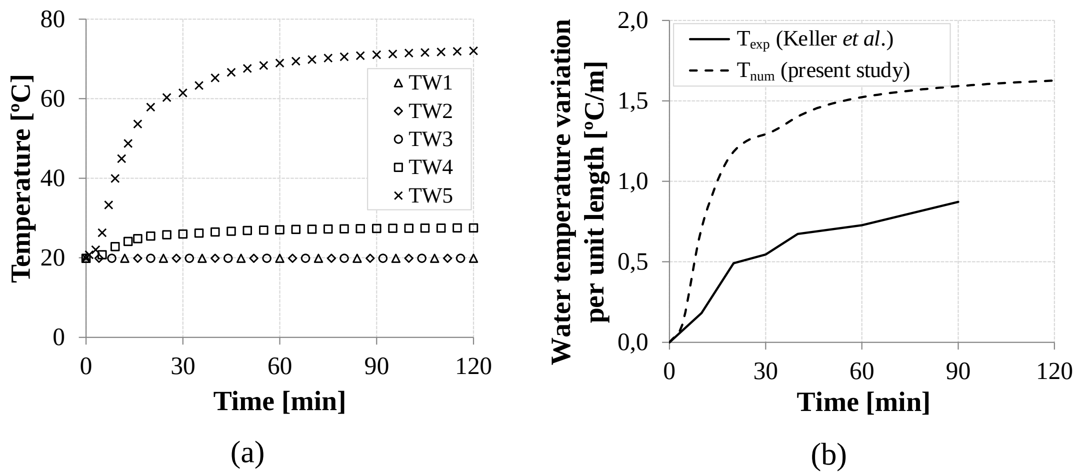

Figure 83: Water temperature variation: (a) numerical temperatures in different positions as function of time and (b) comparison of numerical and experimental results from [8] (normalized values, per unit length).

Figure 83(b) plots the average temperature increase per unit length of the multicellular slab, comparing the results obtained from the numerical model with the experimental measurements presented by Keller *et al.* in [8]. The average temperature increase in water after 90 min of fire exposure obtained from the numerical model (in a slab length of 608 mm) was 0.97 ºC (~1.60 ºC/m). This compares with a water temperature increase of 4.80 ºC measured in the test, but in a length of 5500 mm (~0.87 ºC/m). Given the complexity of the phenomena involved, this consistency between numerical and experimental results provides further validation to the model.

6.5. Conclusions

This chapter presented a numerical study about the thermal response of pultruded GFRP profiles subjected to fire, aiming to analyse the effects of different fire protection systems and the number of sides exposed to fire. From this study, the following main conclusions can be drawn:

- When GFRP tubular profiles or multicellular slabs are exposed to fire, the heat transfer process occurs not only through conduction (via the webs), but also through radiation and convection inside the cavities/cells of the cross-section. In fact, the consideration of the heat exchanges due to internal radiation and convection not only influences significantly the thermal responses of the GFRP material but also provides more accurate temperature predictions.

- Despite the complexity involved in the heat transfer problems and the need to define several assumptions, the numerical results obtained with the thermal models were in general good agreement with experimental results of fire resistance tests conducted in this thesis and Tracy's [24], for both unprotected and protected profiles/slabs. In particular, the assumptions made on the temperature dependent thermo-physical properties of the materials and especially on the boundary conditions (including the lateral insulation of the tubular profiles) might play a key role in the differences found.

- The computational simulation of the thermo-mechanical problems has always been a major challenge for engineers, not only because of its inherent complexity (interactive behaviour) but also due to the very large number of parameters (variables) involved. In the particular case of the present work, the differences found may be attributed to two major sources: (i) some uncertainty of temperature measurements in tests and (ii) several assumptions undertaken by the numerical models. First, it should be highlighted that the performed tests were not purely thermal, but thermo-mechanical (the members were subjected to simultaneous thermal and mechanical loadings [112]). While the thermal action involves degradation of material properties, the mechanical loading induces deformation, cracking, delamination (and, possibly ablation). This thermo-mechanical interaction (occurring in tests) requires a renewed update of boundary conditions in time, which is very complex and extremely difficult to model. Bearing in mind that the current models are purely thermal (they exclude any type of mechanical dependence), the quantitative differences found between experiments and numerical results may also be partly explained on the basis of this interactive behaviour.

- Given the practical difficulties involved in performing temperature measurements in GFRP profiles/slabs exposed to fire, the numerical simulations also provided further insights about the efficacy of the different fire protection systems. For members under one-side fire exposure, the results obtained confirmed the much higher efficiency of water-cooling in insulating the webs and top flange, while the passive protection provided by CS boards is more beneficial in protecting the bottom flange. For three-side exposure, the efficacy of water-cooling is remarkably reduced and, in this case, passive protection is by far more advantageous.

- The results obtained from the numerical simulations of the tubular profiles highlighted the remarkable influence of the number of sides exposed to fire in the thermal response of GFRP profiles. Compared to one-side exposure, three-side exposure involves a much faster temperature increase in the webs and top flange, causing a much faster reduction of their residual section. This also highlights the better performance of multicellular sections under fire, as the internal webs are protected from direct heat exposure.

Chapter 7:

Mechanical response of GFRP beams exposed to fire

7.1. Introduction

The numerical simulation of pultruded GFRP materials and structures at elevated temperatures is still at present in an early stage of development. Most of current studies have been developed for marine and aerospace applications [5]; only a few works concerning civil engineering applications were reported in the literature. In this context, two thermo-mechanical simulations were performed on GFRP slabs: a numerical study presented by Keller *et al*. [16] and an analytical investigation conducted by Bai and Keller [19]. Also, a thermo-mechanical (analytical) model was developed by Bai *et al*. [15] to predict the mechanical response of GFRP beams under fire. The main features of these studies are reviewed next.

The first modelling effort in this field was made by Keller *et al*. [16]. The authors used the commercial software *ANSYS Multiphysics* [18] to simulate the mechanical response of full-scale pultruded GFRP multicellular deck panels exposed to fire, according to ISO 834 [13], both unprotected and protected with a water-cooling system [8]. Three-dimensional models were developed considering the temperature-dependent properties of the GFRP material in order to estimate the deformation of the panels under elevated temperatures. For the water cooled panels, the models fairly accurately predicted the deformation (both mid-span deflections and axial strains) during the 120 min of fire exposure, although the evolution of mid-span deflections was slightly overestimated. The authors attributed those differences to the simplifying assumption of assigning single compressive/tensile modulus *vs*. temperature curves; in fact, the reduction with temperature of axial stiffness in compression is considerably lower than that in tension [6]. The mid-span deflections were also determined considering the separate effect of mechanical load and thermal effects. According to the values calculated, the relative contributions of these two effects to the total deflections remained approximately constant for different instants, about 15% resulting from thermal expansion and 85% from mechanical load. In this respect, it is worth referring that the authors considered a constant thermal expansion coefficient (*i.e.*, no change with temperature). Regarding the unprotected slab, the numerical deformations significantly overestimated the experimental ones. The authors argued that the numerical model did not allow for a proper simulation of the thermo-mechanical behaviour of the upper face of the panels; indeed, due to the limitations of the thermal model, it was to possible not reproduce the considerable heating of the top face of the unprotected slab (in contrast to the liquid-cooled conditions, which allowed the top face to remain close to room temperature as in the experiments).

Bai and Keller [19] presented a further effort to simulate the mechanical responses in fire of the above mentioned pultruded GFRP multicellular slabs (tested by Keller *et al*. [8]), with and without fire protection. In this study, based on kinetic models proposed by Bai *et al*. [57], a one-dimensional thermo-chemical model was developed to estimate the thermal responses of the GFRP slabs, which allowed predicting the variation of temperature in the bottom face sheet of the specimens – the heating of webs/top face sheet due to convection and radiation was not explicitly modelled. Based on these simplifying assumptions, the authors used beam theory to investigate the mechanical behaviour of the GFRP slabs with and without fire protection systems. With this analytical approach, the authors assessed the influence in the mid-span deflection increase of three different effects: (i) the degradation in material stiffness, (ii) the thermal expansion, and (iii) the viscoelastic behaviour of the GFRP material. The variation of the mechanical properties with temperature was obtained from the rule of mixtures, assuming the same variation of tensile and compressive moduli with temperature. The thermal expansion coefficient was considered temperature-dependent and its variation with temperature was assumed to follow that of the storage modulus curves obtained from DMA tests (no specific thermal expansion experiments were performed in this respect). The variation of material viscosity with temperature was determined using a rule of mixtures (similarly to temperature-dependent mechanical properties), in which the parameters were calculated based on creep tests at room temperature and DMA tests. The results obtained confirmed the remarkable influence of material stiffness degradation in the deflection increase. The influence of material thermal expansion on deflection increase changed during the fire exposure period (due to the above mentioned assumption), with a maximum contribution of 30% in the unprotected slab after 10 min. Regarding the influence of the material viscoelasticity, which was also variable during the fire exposure period, its contribution to the deflection increase of the panels was very low, ranging between 3% and 6%. An overall good agreement between simulations (using both numerical and analytical theories) and experimental data was reported.

Bai *et al*. [15] extended the previous analytical approach to study the mechanical response of pultruded GFRP beams (tested by Correia *et al*. [10]) exposed to fire in one-side and comprising various fire protection systems: different fire protection materials and a water-cooling system. The step forward in this study was the consideration of the temperature-dependence of the thermo-physical properties of the fire protection materials (in addition to those of the GFRP). In this study, the evolution of temperatures across the tubular section of the GFRP profiles was modelled considering the following assumptions: (i) the bottom flange (hot face) was heated by the furnace, with the time-temperature curve defined in ISO 834 [13] being directly imposed at this boundary (to obtain a better agreement with the experimental data); (ii) for the top flange (cold face), radiative and convective heat exchanges were considered (with the air temperature) and the coefficient of heat convection was determined based on the minimization of the differences between experimental and modelling temperatures at the top flange. Once again, natural convection and radiative heat exchanges in the cavity were not considered in the thermal simulation. Regarding the mechanical properties used in the modelling of the mechanical response, its variation with temperature was also obtained considering the rule of mixtures, neglecting the different behaviour of GFRP material in compression and tension. The analytical model underestimated the mid-span deflections of beams U (unprotected), CS (protected with calcium silicate) and VP (protected with vermiculite/perlite-based mortar), particularly at the beginning of fire exposure (where relative differences of 16-20% were observed). According to the authors, this difference was explained by (i) the high heating rate of the oven and (ii) the absence of thermal expansion effects in the model. On the other hand, when simulating the behaviour of the water cooled beam (beam WC), an overestimation of the time-temperature displacements (24% maximum) was obtained. In this work, it was assumed that the entire span was exposed to fire (and, therefore, exhibited the same stiffness degradation), while in the experiments the extremity sections of the beams were not directly exposed to fire – this may have also contributed to the above mentioned differences.

The previous efforts in simulating the mechanical response in fire of pultruded GFRP beams and slabs reflect the complexity of the problem. In the previous works, the main limitations regarding the modelling of the mechanical behaviour of the GFRP structural elements were the following: (i) the mechanical simulations departed from relatively simple thermal models (neglecting the heat exchanges in the cavities by radiation and convection), which prevented the accurate simulation of the temperatures throughout the entire depth of the cross-section, namely in its upper part; (ii) similar reductions of tensile and compressive elastic moduli were considered (when their reduction with temperature is very different); (iii) the shear modulus variation with temperature considered as input was not based on experimental data (not available at that time); (iv) there is some uncertainty about the definition and influence of the thermal expansion coefficient; (v) only one type of fire exposure (in one-side) and a single load level were considered.

In what concerns the stress analysis, aiming at studying the fire behaviour of GFRP composites, Gibson *et al*. [20] and Bausano *et al*. [21] simulated the mechanical response of GFRP laminates exposed to one sided heat flux. Gibson *et al*. [20] presented analytical models to simulate the thermal degradation of tensile and flexural stiffness and to predict the evolution with temperature of tensile and compressive strengths after heat exposure. Bausano *et al*. [21] predicted the variation of axial strains with temperature using classical laminate theory and developing a finite element model. In this study, the time to failure of GFRP laminates was predicted and a good agreement was obtained between simulation results and experimental data; however, the models were not able to accurately predict the evolution of strains with temperature.

Keller *et al*. [16] numerically simulated the mechanical response of full-scale pultruded GFRP decks, developing three-dimensional models in software *ANSYS*. The thermo-mechanical models developed by these authors allowed simulating the evolution of mid-span deflection, as well as the axial strains. In the corresponding experiments, liquid-cooled and non-cooled specimens were tested and the variation of axial strains on the upper and lower face sheets and mid-span deflections was monitored. In what concerns axial strains, the numerical results obtained for the liquid-cooled specimens were consistent in the upper face sheet, while for the lower face sheet they slightly overestimated the experimental data. In the non-cooled specimen, the numerical results were less accurate, in particular at the lower face sheet. Later, Bai and Keller [19] used Timoshenko beam theory to estimate de mechanical response of liquid-cooled and non-cooled GFRP multicellular deck panels; the authors studied the influence of thermal expansion and viscoelastic behaviour on the deformability of the panels. In all these studies, only the *kinematic* issues (namely, the evolution of deflections or strains) were investigated; *i.e.*, no stress analysis was reported concerning the mechanical response of GFRP structural members under fire and no predictions of their failure responses were provided.

Besides the above mentioned works, in what concerns the modelling of *static* issues, only numerical studies at room temperature were found in the literature. The scarce number of works on the *static* response of composite structural members under fire exposure truly emerges the need for further research. In this study, the *static* issues (stress distributions and failure criteria) of the numerical simulation of GFRP structures under fire action are presented and discussed.

To clarify some of the issues reported above and obtain a better understanding of the fire response of GFRP members, the thermal and mechanical behaviour of pultruded GFRP tubular beams tested in the present thesis was numerically simulated. A first effort consisted of modelling the thermal response in fire of the GFRP profiles – two-dimensional thermal analyses (presented in chapter 6), were performed using a commercial software based on the finite volume method. As mentioned, the main innovation in this work was the consideration of the radiative and convective heat exchanges inside the cavity of the GFRP tubular profiles, which were seen to considerably influence the temperature profiles in the cross-section. The thermal models developed provided consistent and accurate results compared to experimental data, and allowed predicting the temperature distributions along the entire depth of the cross-section.

Departing from the thermal simulation performed in this thesis (chapter 6), the second effort, comprised the numerical and analytical simulation of the mechanical response in fire of the pultruded GFRP beams. In the three-dimensional FE models developed, the thermo-mechanical properties of the GFRP material were considered temperature-dependent based on experimental data and different values and degradation curves were used for compressive ($E_C(T)$), tensile ($E_T(T)$) and shear ($G_{LT}(T)$) moduli. Moreover, the effect of varying the assignment of material properties as a function of the neutral axis position, as well as the effect of using different thermal expansion coefficients were assessed, namely their influence on the evolution of mid-span deflection with temperature. Alongside the numerical study, one-dimensional analytical models based on Timoshenko beam theory were also developed to predict the evolution of the mid-span deflection of the GFRP beams during the fire exposure. The same physical-mechanical properties were considered in both numerical and analytical models. The numerical and analytical models enabled studying also the effects (i) of exposing the GFRP beams to fire in either one or three sides, and (ii) of applying different load levels.

The present chapter describes both the numerical (finite element, FE) and analytical (Timoshenko beam theory) models. Some relevant *kinematic* issues are presented, in particular the evolution of beam deflection and position of neutral axis as a function of temperature increase. The effects of using different fire protection systems, types of fire exposures and load levels are also investigated in this thesis. Additionally, further insights are discussed regarding the *static* issues, such as the evolution of stress distributions (in both longitudinal and transverse directions) and failure (Tsai-Hill failure criterion) with fire exposure time.

The remainder of this chapter is organized as follows: sections 7.2. and 7.3. describe respectively the numerical models and results; then, sections 7.4. presents analytical models and results; finally, the main conclusions are presented in section 7.5.

7.2. Numerical models

7.2.1. Introduction

The main objective of this investigation was to simulate the mechanical responses of pultruded GFRP beams exposed to fire. As mentioned, prior to this study, the thermal simulation of the profiles was carried out using the software *ANSYS Fluent* [18]; two-dimensional (finite volume element) models were developed considering the heat exchanges in the cavity due to convection of the enclosed air and radiation between the inner faces of the section walls. In that numerical study thermal analyses of unprotected and protected profiles were performed, allowing simulating both one- and three-side fire exposure. The numerical temperature distributions compared reasonably well with the experimental ones, in particular considering the complexity involved in this heat transfer problem.

Departing from those thermal simulations (presented in chapter 6) and aiming at modelling the mid-span deflection evolution of the GFRP beams when exposed to elevated temperature, three-dimensional FE models were developed using the software *ABAQUS Standard* [113][2]. The effects of considering different types of fire exposure and load levels were studied in these simulations. The description of numerical models and the comparison between numerical and experimental results are presented in the next two sections.

Table 17 summarizes the numerical models developed, indicating the type of fire protection, the type of fire exposure and the respective duration (defined as function of the experimental results), and the labelling adopted for the six series, where (i) U means “unprotected” and CS denotes “CS protected”; (ii) E1S means “one-side exposure” and E3S denotes “three-side exposure”. Note also that the load level (causing the mid-span deflection indicated in Table 17) and duration of fire exposure depend on each series.

Table 17: Numerical mechanical models developed.

Model	**Fire protection**	**Fire exposure**	**Load level**	**Duration**
U-S1	-	One-side (E1S)	L/400	60 min
CS-S1	Calcium silicate			90 min
U-S2	-	Three-sides (E3S)	L/400	22 min[3]
CS-S2	Calcium silicate			60 min
U-S3	-	One-side (E1S)	L/250	60 min
CS-S3	Calcium silicate			90 min

7.2.2. Description of numerical models

Geometry and FE mesh

As mentioned, 3D FE models of the beams tested were developed. Figure 84 illustrates the geometry, mesh and boundary conditions of one of the models. Eight-node solid elements with reduced integration (C3D8R) were used. The profile’s section was meshed uniformly, with 4 and 50 elements across the thickness and height, respectively, and 187 elements were used along the length, resulting in an FE aspect ratio of 2:1. In order to reduce the computational effort required by the numerical solution, only a quarter of the profile was modelled by

[2] This software did not allow performing two-dimensional thermal analysis considering simultaneously conduction and radiation and convection inside the cavity. Therefore, it was decided to perform the thermal (2D) and mechanical (3D) analyses using software *ANSYS Fluent* and *ABAQUS Standard*, respectively.

[3] Due to convergence issues, only the indicated duration was successfully achieved (although the intended one was 30 min).

assuming conditions of double-symmetry in both transversal and longitudinal directions, as illustrated in Figure 84. Globally, a mesh with a total of 70,094 FEs and 89,304 nodes was used. In this mechanical simulation, only the GFRP material was modelled (*i.e.*, the mechanical contribution of CS boards to deflection was neglected, as discussed in this section).

Boundary conditions and loading

The mechanical response of the GFRP beams was simulated assuming symmetric conditions with respect to y-z and x-y planes (planes of symmetry) and, therefore, displacements in x- and z-axes, respectively, were fully restrained. As illustrated in Figure 84, the load was applied through a steel bearing plate by means of a pressure force and the support restrained the vertical displacement ($\delta_y = 0$). In order to study the influence of load level on the mechanical response of GFRP beams under fire, pressures of 975 kPa (series S1/S2, mid-span deflection of L/400) and 1558 kPa (series S3, mid-span deflection of L/250) were applied to the beams. These values correspond to a quarter of the total load, 11.7 kN (S1/S2) and 18.7 kN (S3), applied directly to the steel plate. The interface between GFRP and steel parts was modelled assuming tie constraints.

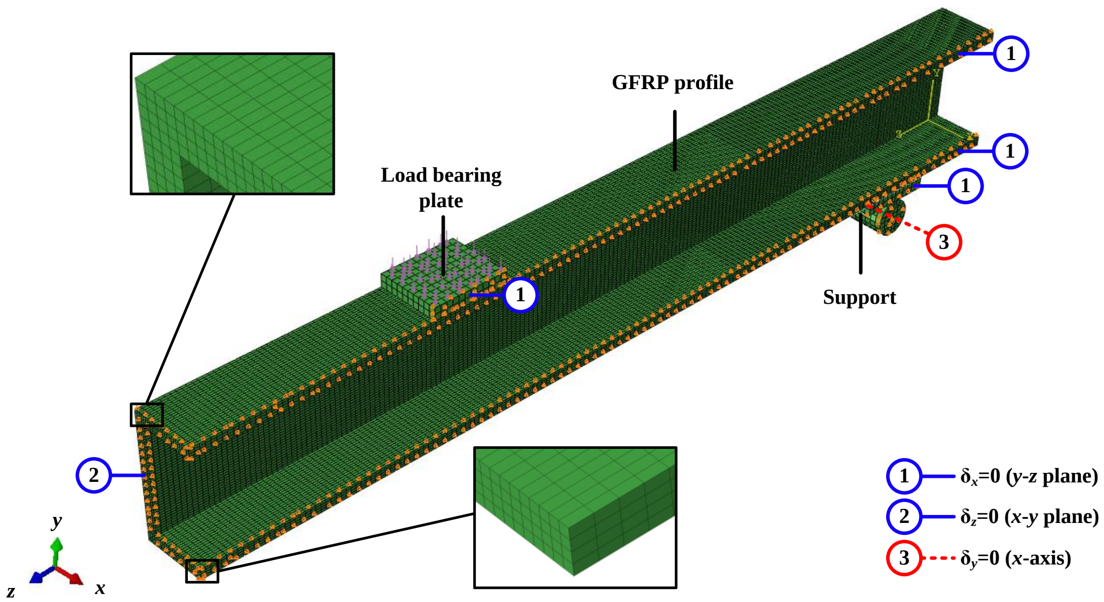

Figure 84: Geometry, mesh and boundary conditions of FE model.

Regarding the thermal boundary conditions, the evolution with time of nodal temperatures was imposed based on the results obtained from the two-dimensional thermal analysis previously performed (chapter 6). Figure 85 presents the variation of temperature with the time of fire exposure at the middle of top flange (TF), web (W) and bottom flange (BF) for beams U-S1, CS-S1 and U-S2.

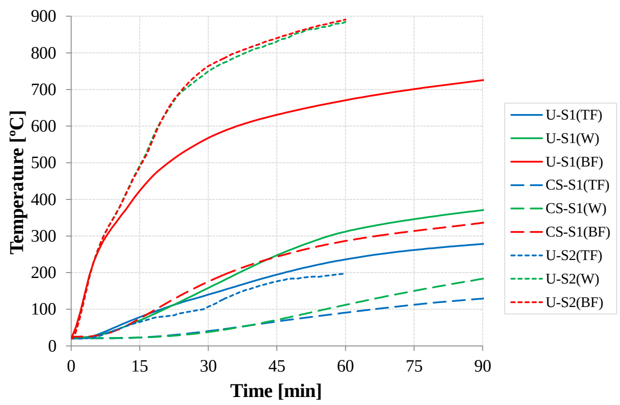

Figure 85: Numerical temperatures obtained from two-dimensional thermal analysis performed.

Taking into account the test setup used (*cf*. chapter 4), the temperature variation along the length of the profile was not constant. However, neither the experimental nor the numerical distribution of temperatures along the longitudinal direction (z-axis) were known and, therefore, simplifying assumptions had to be made. To take this into account, as illustrated in Figure 86, the beam was discretized in the following three parts, where the following uniform temperature distributions (along the length) were assumed: (i) 2D numerical temperatures (directly exposed part); (ii) half of 2D numerical temperatures (unexposed part); and (iii) initial temperature set equal to 20 ºC (exterior part).

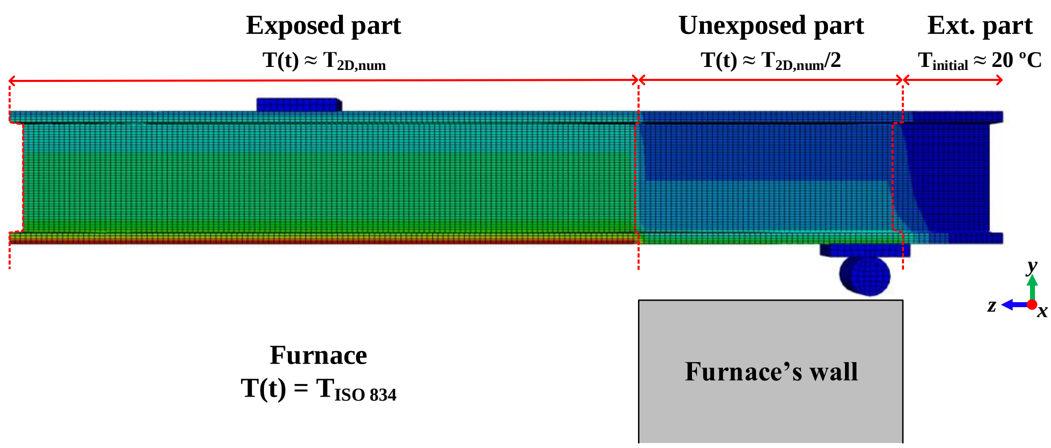

Figure 86: Temperature distribution assumed along the length GFRP beams.

Material properties

The GFRP material was modelled considering an orthotropic behaviour defined using the “engineering constants” option of *ABAQUS Standard*, which allows assigning three elastic moduli, Poisson’s ratios and shear moduli associated with the material’s principal directions.

The following properties were considered at room temperature (the corresponding source is indicated in brackets): in-plane longitudinal modulus, $E_L = 31.0$ GPa (full-section elastic modulus); in-plane transverse modulus, $E_T = 8.3$ GPa (compressive transverse modulus); out-of-plane modulus, $E_Z = 3.5$ GPa (compressive modulus of polymeric matrix); in-plane shear modulus, $G_{LT} = 3.6$ GPa (full-section and material shear modulus), in the other shear planes a similar value was assumed; $\nu_{LT} = 0.27$ (coupon tests), in the other planes a value of 0.11 was assumed, based on [25]. All moduli were assumed to vary with temperature, while the Poisson's ratios were considered constant. The variation with temperature of the elastic properties of the GFRP material was based on experimental tests performed and data reported in the literature, as explained next.

Figure 87 depicts the variation with temperature of the longitudinal tensile and compressive moduli and in-plane shear modulus considered as input. The thermal degradation of the in-plane shear modulus ($G_{LT}(T)$) with temperature was assessed through experimental tests conducted in the framework of this thesis on V-notched small-scale coupons (*cf.* chapter 3). However, due to difficulties in measuring accurately the longitudinal strains at elevated temperature in coupons under compression, it was assumed that the mechanical degradation of $E_{L,comp}(T)$ would be similar to that of the longitudinal compressive strength ($\sigma_C(T)$) measured in compressive tests carried out on short pultruded GFRP columns (*cf.* chapter 3). According to the measurements performed, both $E_{L,comp}(T)$ and $G_{LT}(T)$ are significantly and quite similarly reduced with temperature, as shown in Figure 87. Regarding the variation of the longitudinal tensile modulus ($E_{L,tens}(T)$) with temperature, the curve proposed by Wang *et al*. [114] was assumed in the present study (Figure 87); such data was obtained from tensile tests on pultruded GFRP bars (comparable fibre content) for temperatures between 20-500 ºC; for temperatures above 500 ºC, a linear reduction was considered up to a temperature of 800 ºC (fibres softening [115]), for which the tensile modulus was assumed to be negligible. As shown in Figure 87, the reduction with temperature of the longitudinal tensile modulus (more fibre dependent) is much lower than that of the compressive and shear moduli (more matrix dependent).

Based on the experimental data reported above, two different GFRP materials were defined, with similar room temperature properties, but different degradation of in-plane longitudinal modulus due to temperature: (i) $GFRP_{comp}$ ($E_L(T) = E_{L,comp}(T)$) for elements in compression; and (ii) $GFRP_{tens}$ ($E_L(T) = E_{L,tens}(T)$) for elements in tension. In other words, the reduction with temperature of the in-plane longitudinal modulus (E_L) in materials $GFRP_{comp}$ and $GFRP_{tens}$ reproduced the curves $E_{L,comp}(T)$ and $E_{L,tens}(T)$, respectively. Regarding the variation with temperature of the elastic moduli in the other directions, for both GFRP materials it was assumed to be similar to that of the curve $E_{L,comp}(T)$, as those properties are matrix-dependent (especially the out-of-plane modulus) and no specific data was found in the literature. As mentioned, for both materials the reduction with temperature of the shear modulus in all planes was assumed to follow the curve $G_{LT}(T)$ and the Poisson's coefficients were considered temperature-independent (due to the lack of data in the literature).

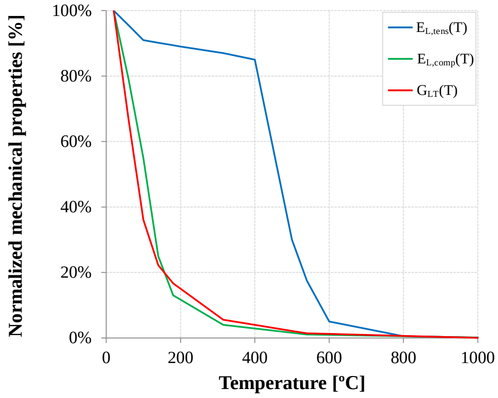

Figure 87: Variation with temperature of the longitudinal compressive ($E_{L,comp}(T)$) and tensile ($E_{L,tens}(T)$) moduli and of the shear modulus ($G_{LT}(T)$).

The thermal expansion coefficient of the GFRP material was also taken into account, due to its potential influence on the mechanical response of GFRP beams, as reported in the literature [19]. In fact, thermal expansion seems to be particularly relevant at the beginning of fire exposure, when temperature gradients in the profiles' cross-section are high.

The coefficients of thermal expansion (α) reported in the literature for pultruded GFRP material (all at room temperature) present high variability, with values depending on the materials involved (namely, the volume and type of fibres and the polymeric matrix), and the geometry of the specimens tested. Since the experimental data available for this property is still scarce, particularly concerning its variation with temperature (no results were found), the following options were tested: (i) thermal expansion coefficients constant with temperature and equal in both longitudinal and transverse directions ($\alpha_{long} = \alpha_{trans}$); (ii) temperature-dependent thermal expansion coefficients equal in both longitudinal and transverse directions ($\alpha_{long}(T) = \alpha_{trans}(T)$); and (iii) thermal expansion coefficients constant with temperature, but different in the longitudinal and transverse directions ($\alpha_{long} \neq \alpha_{trans}$). These options are summarized in Table 18. Because no experimental data was available for this specific profile, the values of the thermal expansion coefficients (at room temperature) used in the simulations were based on the results reported by Tracy [24] and Bank [25] for comparable GFRP materials. As suggested by Bai and Keller [19], the temperature dependence of the thermal expansion coefficient was considered to follow the variation with temperature of the storage modulus of the GFRP material (obtained from DMA tests [4]).

Table 18: Thermal expansion coefficients tested.

$\alpha_{long/trans}$	$\alpha_{long}(T)$ [ºC^{-1}]	$\alpha_{trans}(T)$ [ºC^{-1}]	Temperature-
$\alpha_{0/0}$	0	0	Independent
$\alpha_{6/6}$	6×10^{-6}	6×10^{-6}	
$\alpha_{8/8}$	8×10^{-6}	8×10^{-6}	
$\alpha_{12/12}$	12×10^{-6}	12×10^{-6}	
$\alpha_{6/6}(T)$	6×10^{-6} (20 ºC)	6×10^{-6} (20 ºC)	Dependent
$\alpha_{12/12}(T)$	12×10^{-6} (20 ºC)	12×10^{-6} (20 ºC)	
$\alpha_{6/12}$	6×10^{-6}	12×10^{-6}	Independent
$\alpha_{6/18}$	6×10^{-6}	18×10^{-6}	
$\alpha_{6/24}$	6×10^{-6}	24×10^{-6}	

Note: α_{long} and α_{trans} correspond to longitudinal and transversal directions, respectively.

Regarding the CS material, although it was considered in the thermal model (to obtain the temperature distributions), it was not taken into account in the mechanical model. It is therefore worth noting that the mechanical contribution of this passive protection material to the beams' stiffness (deflections and stresses) was neglected in the numerical simulations. This contribution is generally negligible, but may be non-marginal with stiffer fire protections, as is the case of calcium silicate. Calculating the cross-section equivalent inertia (homogenized in GFRP material), it can be seen that the CS protection provides a flexural stiffness increase at room temperature of nearly 10% (one-side exposure) and 19% (three-side exposure) compared to the flexural stiffness of the GFRP beam determined. This simplifying assumption was due to the limited magnitude of those figures, but especially to the lack of information in the literature regarding both (i) the mechanical behaviour of GFRP-CS interfaces (including at high temperature) and (ii) the thermo-mechanical properties of CS.

The steel material parts, corresponding to the blocks used for the load bearing and reaction supports, were defined with temperature-independent isotropic properties (E_{steel} = 210 GPa, ν_{steel} = 0.3).

Methodology and analysis

Transient linear analyses were carried out considering different total times, from 30 to 90 min (Table 17). In these simulations, as mentioned, different longitudinal elastic moduli were considered for compression and tension; moreover, the effect of varying the mechanical properties of the elements as function of the position of the neutral axis (y_{LN}) was also assessed. To investigate the influence of this latter effect in the mechanical simulation of the GFRP beams, two different types of analysis were performed – *preliminary* and *incremental* –, which are described in detail in the following paragraphs.

The *preliminary-analysis* was performed by considering a constant assignment of the materials $GFRP_{comp}$ and $GFRP_{tens}$, *i.e.* regardless of the variation of the neutral axis position with the fire duration exposure. Taking into account the applied load and support conditions (illustrated in Figure 84), materials $GFRP_{tens}$ and $GFRP_{comp}$ were assigned to the bottom ($0 < y < 50$ mm) and top parts ($50 < y < 100$ mm) of the section, respectively. To simulate the fire resistance tests, three steps were then defined: (i) an initial step to impose the boundary conditions and initial nodal temperatures (20 ºC); (ii) a mechanical load step (general, static) to apply the pressure; and (iii) a thermal load step (with a time step of 1 min) to impose the nodal temperatures as a function of time.

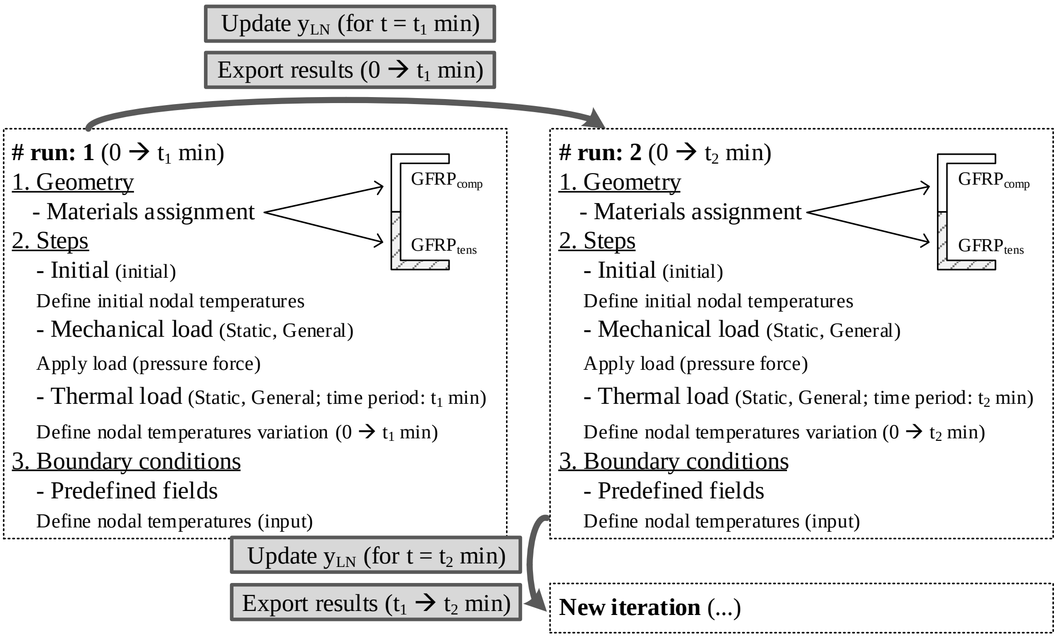

Figure 88: Scheme of the incremental analysis performed.

Because the effect of varying the assignment of materials was expected to be potentially significant (given the differences between compressive and tensile modulus reduction at elevated temperature), *incremental-analysis* was carried out to update the material properties. In the first time increment (0 → t_1 min), the previously described procedure was employed. After completing the first analysis, the new position of neutral axis (in the mid-span section) was determined according to the numerical results and, subsequently, a new assignment of material properties was performed. Besides this modification, also the duration of the thermal load step was changed (0 → t_2 min). Once these adjustments have been done, the second analysis was carried out. With the exception of beam U-S2, the time increment between analyses (t_i → t_{i+1}) was 5 min. In the simulation of beam U-S2, it was necessary to reduce the time increment to 2 min since the position of neutral axis showed a considerable variation during the first 5 min. Figure 88 schematizes the incremental procedure used for completing the analysis and determining the mechanical response of the GFRP beams, which was obtained from each increment process.

7.3. Numerical results and discussion

7.3.1. Deformation

Effect of thermal expansion

Figure 89 presents the results of the parametric study about the effect of the thermal expansion coefficient (α) in the mechanical response of the reference beam (U-S1), exposed to fire in one-side and subjected to the lowest load level (L/400). As mentioned, different (i) constant (temperature-independent) values of α (in both longitudinal and transverse directions) and (ii) temperature-dependent values of α were tested.

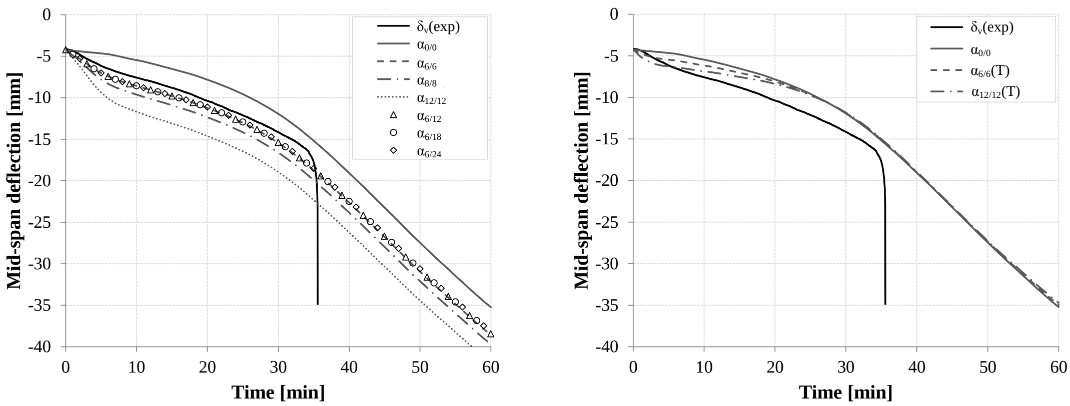

(a) **(b)**

Figure 89: Influence of the variation of the thermal expansion coefficient for beam U-S1: (a) temperature-independent and (b) temperature-dependent coefficients – *preliminary-analysis* models.

At first, no thermal expansion effect was taken into account (curve $\alpha_{0/0}$) and the numerical results obtained were not in good agreement with the experimental ones, particularly for short durations of fire exposure (*cf.* Figure 89) - it was not possible to capture the rapid increase of experimental mid-span deflections during the first 10 min due to the fast heating of the bottom flange (which caused a stiffness loss, as well as a temperature gradient in the cross-section). Due to some uncertainty about the longitudinal tensile modulus (E_{Ltens}) variations for temperatures above 500 ºC (as mentioned, no experimental results were found in the literature for similar GFRP material), different values from those depicted in Figure 87 were tested. However, for all variations of $E_{L,tens}(T)$ tested in the model, the quick deflection increase observed in the tests could not be simulated by the model. Consequently, those initial differences between numerical and experimental results were attributed to the thermal expansion of the material (and not to an inaccurate simulation of the tensile modulus at very high temperatures).

Regarding the numerical tests with constant values of α, as shown in Figure 89(a), the best fit to the experimental results was obtained for $\alpha_{long} = 6\times10^{-6}$, regardless of the α_{trans} used; the latter parameter proved to have little influence on the evolution of mid-span deflections. For the temperature-dependent thermal expansion coefficients ($\alpha_{6/6}(T)$ and $\alpha_{12/12}(T)$), although the models were able to reproduce the rapid increase of vertical displacements during the first 5 min, the overall tendency of the numerical results was not consistent with the experimental data, with the increase of numerical deflections progressively "slowing down" (*cf.* Figure 89(b)). As a result of this parametric study, it was decided to use constant thermal expansion coefficients in the numerical models, *i.e.* temperature-independent coefficients, in both longitudinal and transverse directions ($\alpha_{long} = 6.7\times10^{-6}$; $\alpha_{trans} = 22.0\times10^{-6}$), according to the values reported in the literature (at room temperature) [25].

Evolution of mid-span deflection

Figure 90(a) presents the numerical and experimental variation of the mid-span deflection of the beams from series S1 (one-side exposure) – unprotected (U-S1) and protected (CS-S1). For the unprotected beam, the numerical results obtained from the two types of analysis are shown, *preliminary-analysis* (num_PA) and *incremental-analysis* (num_IA).

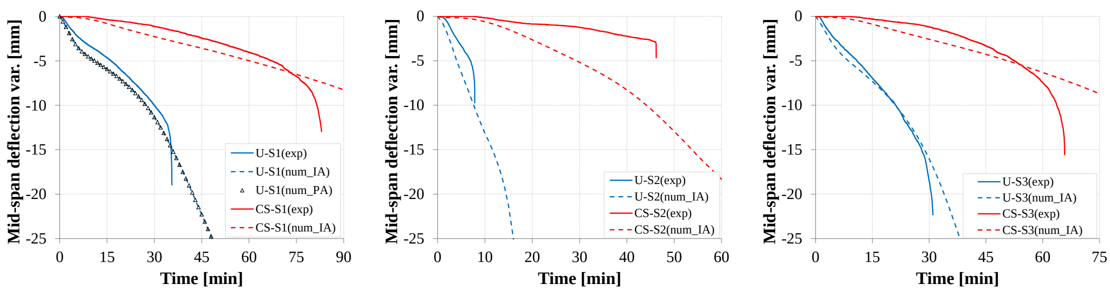

(a) **(b)** **(c)**

Figure 90: Variation of mid-span deflections (both experimental and numerical) with time for series (a) S1, (b) S2 and (c) S3.

Figure 90(a) shows that, in general, regardless of the numerical procedure (*preliminary* or *incremental*), a good agreement between numerical and experimental curves was achieved. As mentioned, no failure criterion was implemented in the models and, therefore, the differences in terms of vertical displacements that occur in the brink of collapse were expected *a priori*. To some extent these differences may also be related to uncertainties regarding the thermo-mechanical properties of the GFRP material, as well as the (thermal) boundary conditions used, for which some (simplifying) assumptions had to be considered. Regarding the comparison between the two types of numerical analyses performed, very similar results were obtained for the reference beam (U-S1), *i.e.*, modifying (or not) the assignment of the materials and their dependence on the neutral axis position did not influence significantly the numerical results (as shown ahead, the same does not occur when the same beam is subjected to negative bending). Although not shown in Figure 90, the same qualitative trend was observed in the simulations of the other beams.

Figure 90(b) and Figure 90(c) show respectively the mid-span deflection variation obtained from the numerical simulations of beams from series S2 (three-side exposure) and S3 (increased load level), together with the corresponding experimental data. With the exception of beam CS-S2, the numerical and experimental results are in quite good agreement. Given this overall good agreement between numerical and experimental curves, it is very likely that some experimental problem might have occurred related to the data acquisition/measurement of the mid-span deflections of beam CS-S2. To some extent, differences can also be due to the mechanical contribution of the CS boards to the overall flexural stiffness of the beams (not considered in the models). This explanation seems to be consistent with two aspects: (i) the numerical simulations of protected beams consistently overestimated mid-span deflections, and (ii) the magnitude of such overestimation was higher in beam CS-S2 (where CS boards were applied in three walls).

Aiming at checking the influence of varying the assignment of GFRP materials as a function of time, a distinct numerical model was developed, in which the load was applied in the opposite direction (*i.e.*, upwards), causing compressive stresses on the bottom flange, the section wall directly exposed to fire. In this case, as shown in Figure 91, the results obtained from *preliminary-analysis* (num_PA) and *incremental-analysis* (num_IA) were now noticeably different, confirming the importance of varying the “assignment” of GFRP materials in fire simulations. In this numerical simulation, for the sake of simplicity no thermal expansion effect (α) was considered.

In the *preliminary-analysis* (num_PA), when the temperature at the bottom part of the profile (under compression and assigned with material $GFRP_{comp}$) starts increasing, the position of neutral axis starts moving upwards (*i.e.*, y_{LN} increases). Consequently, there will be elements in compression assigned with material $GFRP_{tens}$ (which is severely less affected by temperature increase, compared to material $GFRP_{comp}$); note that in this case the assignment of materials is not changed during the simulation. In opposition, in the *incremental-analysis* (num_IA) the materials assignment was changed every 5 min depending on the longitudinal stresses at the elements. As a result, a considerable overall flexural stiffness reduction occurs in the *incremental-analysis*, compared to the *preliminary-analysis*, which explains the differences (δ_v(num_IA) > δ_v(num_PA)) between both simulations (particularly, after the first 20 min).

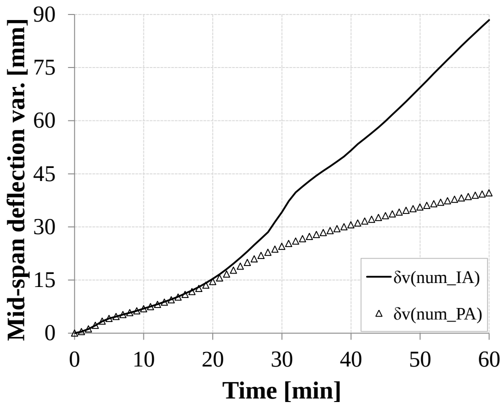

Figure 91: Influence of varying the assignment of materials for a beam similar to U-S1 but exposed to negative bending.

Variation of axis position

Besides the evolution of mid-span deflection, the present study also focused on the variation of the neutral axis position (y_{LN}) with the fire exposure time – these results are depicted in Figure 92.

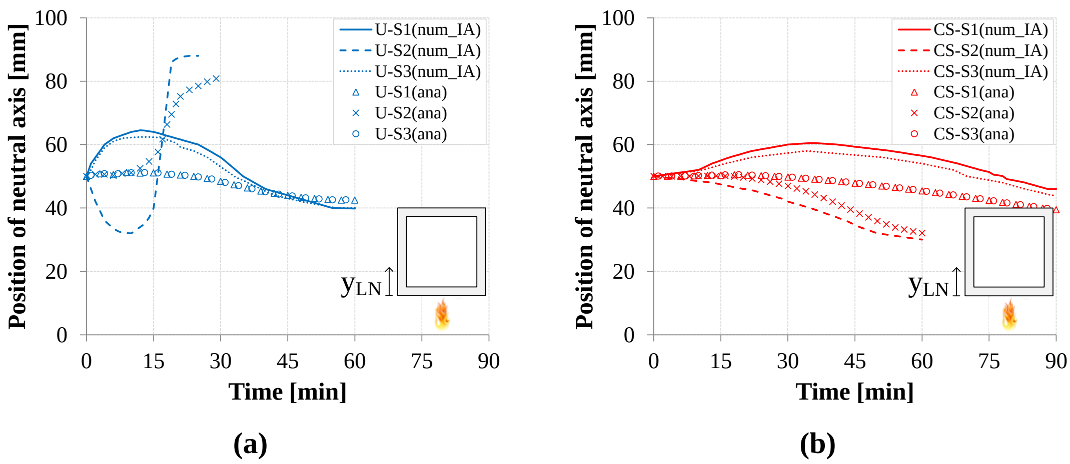

Figure 92: Neutral axis position as a function of time according to numerical (num) and analytical (ana) simulations for beams (a) U and (b) CS (series S1-S3).

In case of unprotected beams with one-side exposed to fire (U-S1/S3), Figure 92(a) shows that y_{LN} increases significantly during the first 7-13 min, due to (i) the reduction of tensile modulus at the bottom flange and (ii) the thermal expansion of the material. After that initial period, the temperature at the top flange also increases (causing a reduction of the compressive modulus) and, therefore, y_{LN} starts decreasing. On the contrary, for three-side exposure (U-S2), the position of neutral axis moves towards the bottom side (y_{LN} decreases) during the first 10 min, as a result of the thermal expansion effect, and then it rapidly moves upwards (y_{LN} increases) due to the high temperatures at the lower part of the profile (bottom flange and web).

Regarding the protected beams (Figure 92(b)), the variation of the neutral axis position as a function of time was different from that exhibited by the unprotected beams. In all the protected beams, y_{LN} remained approximately constant during an initial period since the temperatures in the GFRP profiles remained close to the initial temperature (20 ºC). After that period, for fire exposure in three-sides (CS-S2), neutral axis gradually started moving towards the bottom flange (*i.e.*, y_{LN} decreased). Considering the mechanical properties of the GFRP material[4] and the low temperature gradient in the cross-section, it may be concluded that the upper part of the cross-section (in compression) was more susceptible to temperature than its bottom part (in tension), thus justifying the y_{LN} decrease. In beams CS-S1 and CS-S3, the y_{LN} presented an increase during the first 35 min and then progressively started decreasing, similarly to beams U-S1/U-S3.

7.3.2. Stress distribution

Unprotected beam with one-side fire exposure

The finite element models developed in this numerical study also allowed determining the evolution of longitudinal (σ_{11}), transversal (σ_{22}) and shear (σ_{12}) stresses with fire exposure time. Aiming at evaluating and comparing the evolution of stress patterns in both longitudinal and transversal directions, some representative sections were selected and the numerical results shown hereafter. In the longitudinal direction (beam axis), four heated sections were selected (*cf*. Figure 93): S_A, section with maximum bending moment (mid-span, away from load bearings); S_B and S_C, sections with maximum stress concentrations (underneath load bearings); S_D, section with maximum shear force (away from load/reaction bearings). Concerning the location in the cross-section plane, fifteen elements were selected (*cf*. Figure 93): P1-P4, four elements at the centre of top flange (through the thickness); P5-P11, seven elements along the web height (P5 at the top flange; P11 at the bottom flange); P12-P15, four elements at the centre of the bottom flange (through the thickness).

In this section, the evolution of stress distributions in the reference beam (U-S1) will be analysed. Then, the effect of using a fire protection system (CS-S1) and exposing the GFRP beams to fire in three sides (U-S2) will also be reported and discussed in this section.

[4] GFRP profiles are much more vulnerable under compression than under tension.

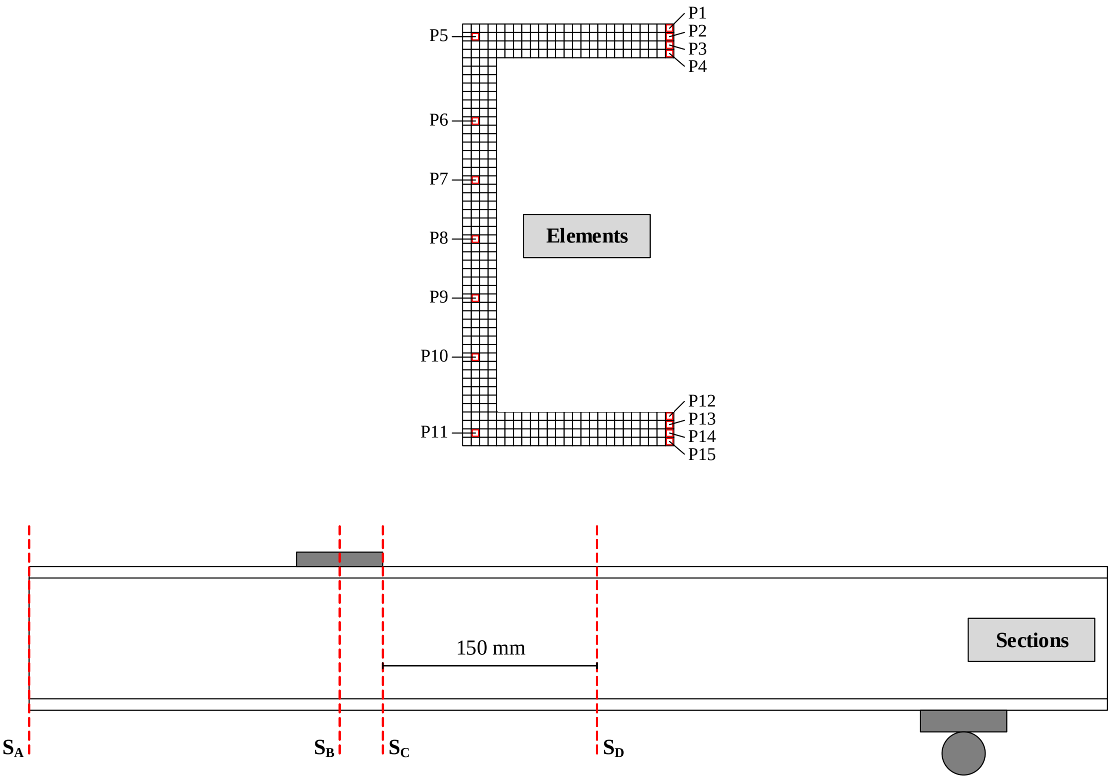

Figure 93: Finite elements (P1-P15) and sections (S_A-S_D) considered in the analysis of stress distributions.

Longitudinal stresses

Figure 94 presents the variation, with time, of longitudinal stresses (σ_{11}) in beam U-S1 (unprotected beam under one-side fire exposure) for different cross-sections (S_A, S_B, S_C, S_D) and section walls, namely (i) the top flange (points P1-P4, Figure 94(a)), (ii) the web (points P5-P11, Figure 94(b)), and (iii) the bottom flange (points P12-P15, Figure 94(c)).

In the top flange (P1-P4, Figure 94(a)), as expected, compressive stresses ($\sigma_{11} < 0$) were computed, higher at mid-span section (S_A) and approximately uniform between sections S_B and S_D. Nevertheless, it should be noted that a high stress gradient develops at the top flange due to the sharp edge corner of the steel plate (load bearing). In fact, the high longitudinal stresses registered in the upper part of top flange (P1-S_C, element P1 at section S_C) are consistent with the experiments, in which specimens collapsed due to compressive failure of the top flange combined with wrinkling. The numerical results show that longitudinal stresses increased during the first minutes, as a result of the rapid stiffness reduction (in tensile modulus) at the bottom flange, and then decreased due to the heating of top flange, as a consequence of the decrease in compressive modulus.

Regarding the compressive stresses in the top part of web (P5-P7, blue curves in Figure 94(b)), no significant variation was observed, with the exception of P5, where stresses increased significantly most likely as a result of temperature increase at the bottom flange/bottom part of web and, then, decreased due to the heating of the top part of web (particularly, in sections S_A and S_C). In the bottom part of the web (P9-P11, red curves in Figure 94(b)), similar tensile stress *vs*. time curves were obtained for sections S_A, S_B and S_C, while for section S_D a slight decrease was observed (due to the lower bending moment). It should be mentioned that the stiffness reduction of the bottom flange (including also P11) led to an increase of σ_{11} values at the bottom part of the web (P8-P10), where high tensile stresses are observed during the fire exposure time (*cf*. Figure 94(b)).

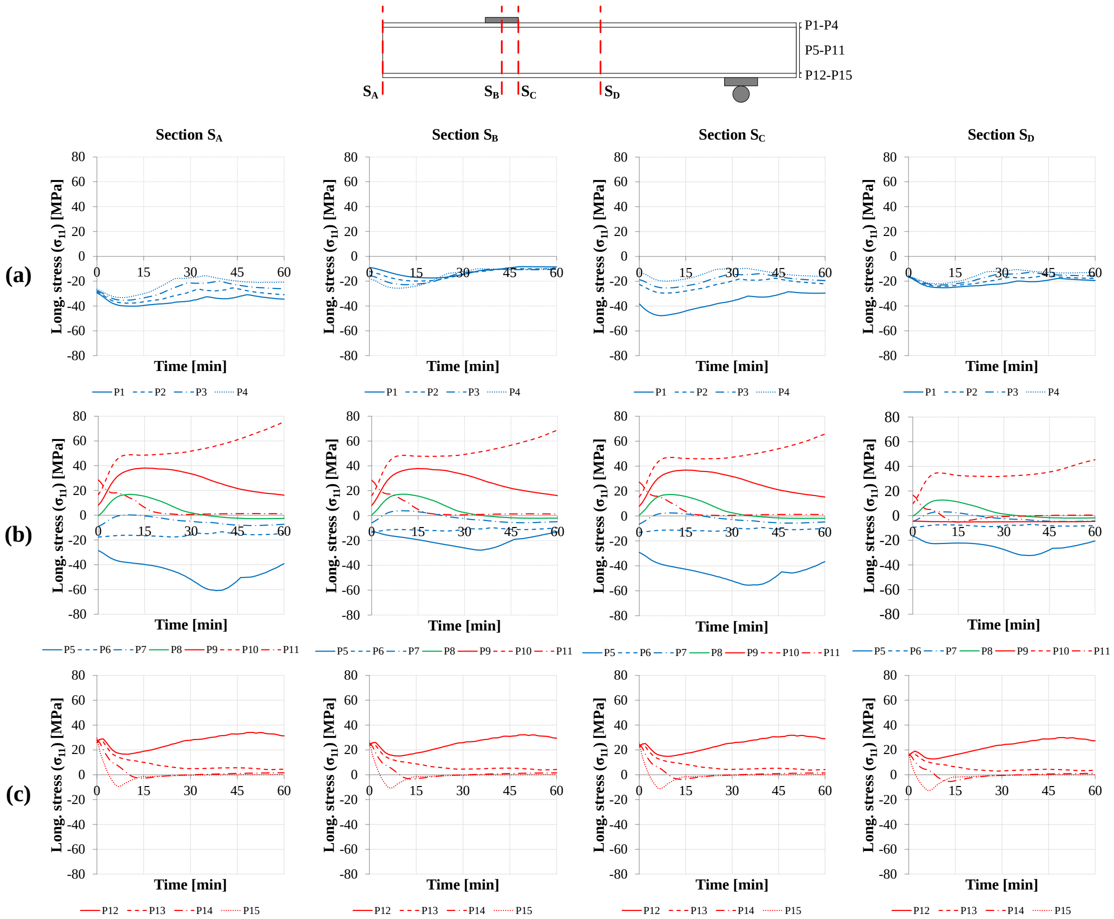

Figure 94: Longitudinal stresses (σ_{11}) in beam U-S1 at (a) top flange (P1-P4), (b) web (P5-P11) and (c) bottom flange (P12-P15) – sections S_A, S_B, S_C and S_D.

In the bottom flange (P12-P15, Figure 94(c)), a rapid drop of tensile stresses occurs at the exterior layers (P15 and P14) due to the prompt drop of stiffness associated with the quick temperature increase. The same occurred in P13, but to a slighter extent. In opposition, a tensile stress increase in the interior layer (P12) was registered, which means that this layer was responsible for keeping the structural performance of the bottom flange. This phenomenon also took place in the bottom part of the web, where a stress migration occurred from P11 to P9-P10.

Transversal stresses

Figure 95 (similar to Figure 94) now presents the variation of transversal stresses (σ_{22}) in beam U-S1. In the top flange (P1-P4, Figure 95(a)) the transversal stresses were residual (almost null) at sections S_A and S_D. Nevertheless, higher compressive stresses ($\sigma_{22} < 0$) were obtained in sections S_B and S_C due to load application through the bearing plates, which originated much localized stress patterns (more evident in P1-S_C, *i.e.* the upper part of the top flange). In the web (P5-P11, Figure 95(b)), the transversal stress values were also negligible ($|\sigma_{22}| < 3$ MPa), with slightly higher stresses in sections S_B and S_C due to load application (similarly to the top flange).

In the bottom flange (P12-P15, Figure 95(c)) and regardless of the cross-section, transversal stresses (considerably lower than the longitudinal ones – $\sigma_{22} << \sigma_{11}$) emerged due to the thermal expansion effects. During the first 2 min of fire exposure, tensile stresses developed in the internal layers (P12-P13), while high compressive stresses arose in the external layers (P14-P15). After this initial period, the transversal stresses decreased (as a result of temperature increase and, consequently, of transversal modulus reduction) and tended to stabilize (*cf.* Figure 95(c)).

Shear stresses

Figure 96 shows the variation of shear stresses (σ_{12}) in beam U-S1, but only for the web (regardless of the section, nearly zero shear stresses occur in both top and bottom flanges). As expected, σ_{12} were null in the web at mid-span section (S_A). In section S_D, prior to fire exposure, the shear stresses decreased from the web mid-point (P8) to the web-flange nodes (P5 and P11); these results are in agreement with the typical shear stress diagram for this type of cross-section and load configuration. The numerical results obtained (Figure 96) show that, during fire exposure, shear stresses varied marginally with time and the shear stress distribution became slightly asymmetric due to the (also asymmetric) heating of the profiles, more significant in the bottom part of the cross-section. Noting that S_B is a transitional section between the beam zones with null (*e.g.* S_A) and non-null (*e.g.* S_D) shear forces, the shear stresses in section S_B were almost uniform along the web height (P6-P10) and approximately zero at web-flange nodes (P5 and P11) – this distribution remained almost unchangeable with time.

The shear stresses at the loaded section S_C were somewhat between those of sections S_B and S_D (*cf.* Figure 96), noting that significant shear stresses were developed at the top part of the web (P5-S_C). The time variation of σ_{12} at P5-S_C (blue curve) is explained by the stress concentration induced by both heating and load bearing (induced by the sharp corner of the steel plate. This evidence was consistent with the failure modes observed in the experimental tests, in which combined compressive and shear failure at the upper part of the webs was most often recorded.

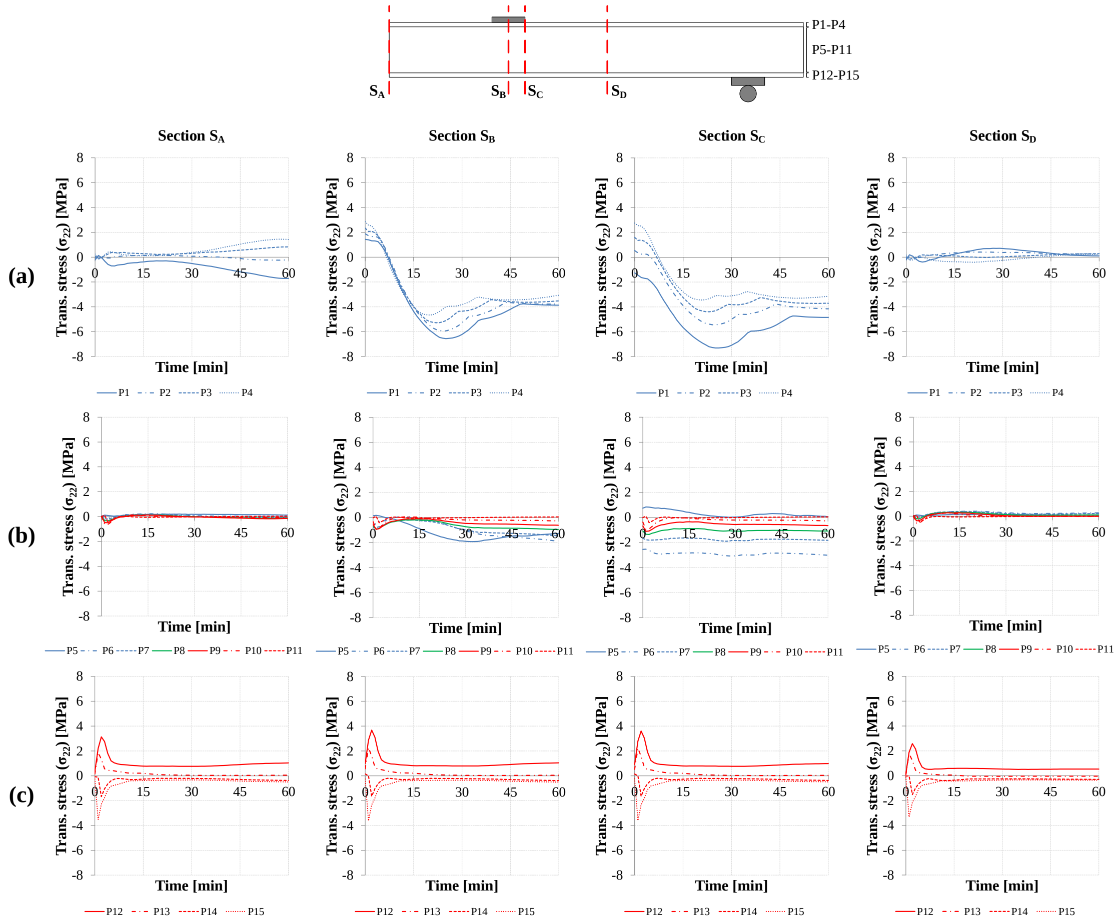

Figure 95: Transversal stresses (σ_{22}) in beam U-S1 at (a) top flange (P1-P4), (b) web (P5-P11) and (c) bottom flange (P12-P15) – sections S_A, S_B, S_C and S_D.

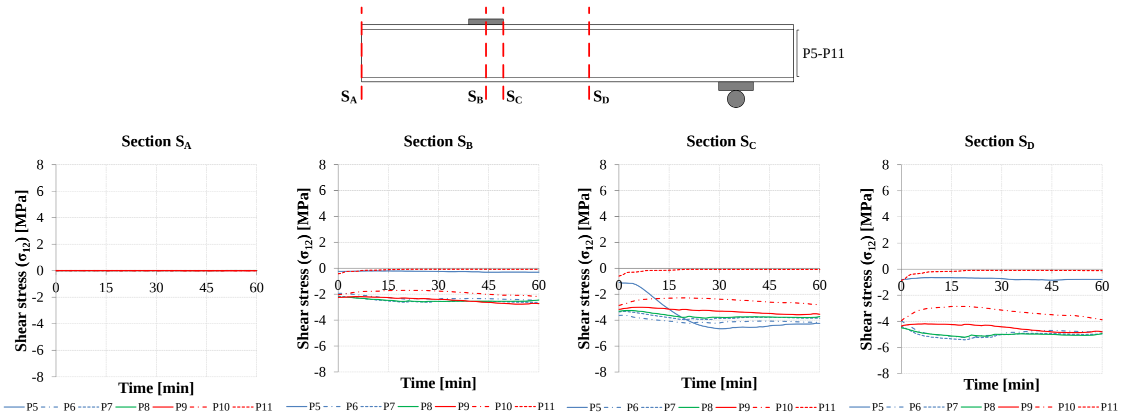

Figure 96: Shear stresses (σ_{12}) in beam U-S1 at web (P5-P11) – sections S_A, S_B, S_C and S_D.

Effect of fire protection system

In order to evaluate the effect of fire protection, beams under one-side fire exposure U-S1 and CS-S1 (unprotected and protected with calcium silicate, respectively) are now compared. Figure 97(a) depicts the variation of longitudinal stresses (σ_{11}) along the web's height (y) in section S_C, where higher stresses were observed. Initially, the variation of σ_{11} stresses was almost linear in both cases, presenting a slight nonlinearity (at the upper part of the web) due to load application.

When profiles started being exposed to fire, an increase in the longitudinal stresses was observed at the lower part of the web (particularly in P10), which is likely to be due to the thermal degradation of mechanical properties in the bottom flange and the thermal expansion effects. This was clearly more evident in the unprotected beam (*cf.* Figure 97(a) at “U-S1” row). Simultaneously, an increase of σ_{11} stresses was also observed at the upper part of the web, also due to the tensile modulus reduction in the bottom flange. Then, as a consequence of the temperature increase at the top flange (which causes a compressive modulus decrease), a reduction of σ_{11} stresses occurred, which was again more evident in the unprotected profile. Taking into account the numerical results, it may be concluded that the longitudinal stress distribution in the unprotected beam (U-S1) became highly nonlinear and presented higher σ_{11} values, compared to the protected beam (CS-S1) – see Figure 97(a) at “U-S1 *vs*. CS-S1” row. This is explained by the much faster temperature increase registered in beam U-S1, which affects significantly the material stiffness degradation and increases the thermal deformation effects.

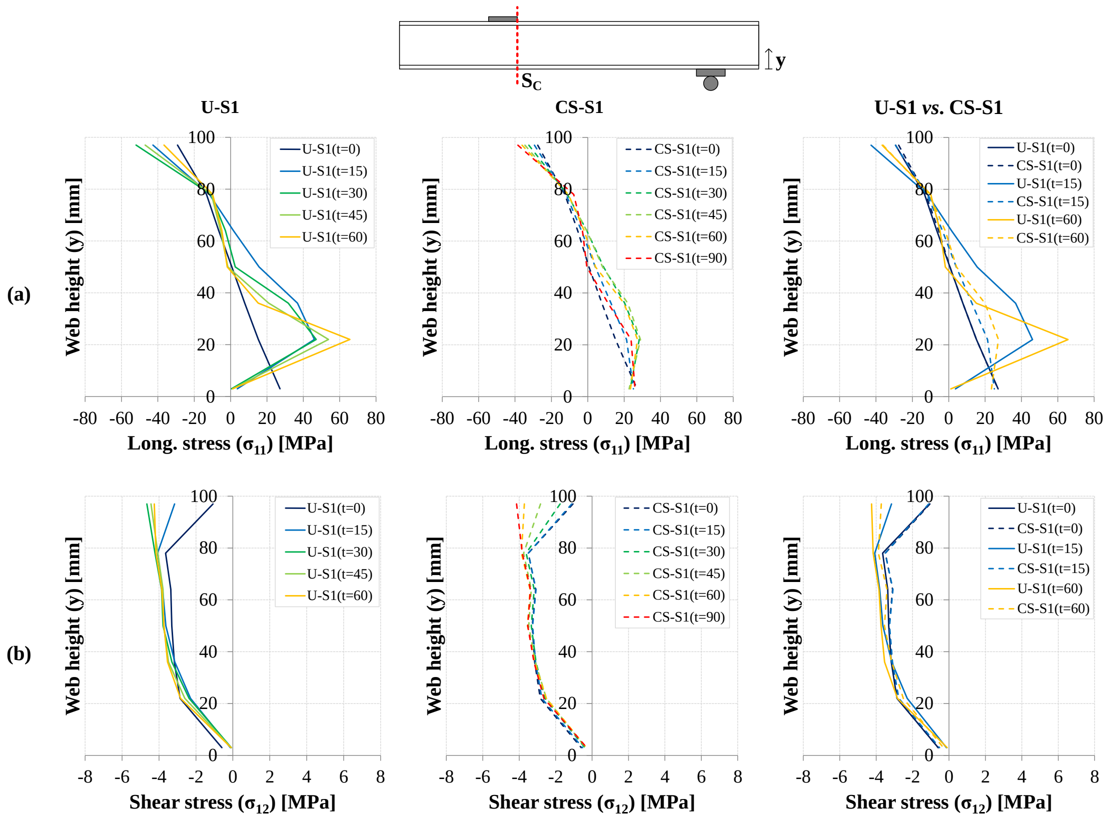

Figure 97: Comparison of (a) longitudinal (σ_{11}) and (b) shear (σ_{12}) stresses evolution for beams U-S1 and CS-S1 after 0, 15, 30, 45, 60 and 90 min – section S_C.

The variation of shear stresses (σ_{12}) along the web’s height (y) for these two beams is also compared in Figure 97(b). It can be observed that before fire exposure started the shear stress diagram in section S_C was not symmetric, as a result of the stress concentrations induced by the sharp corner of the steel plate (load application). In opposition, prior to fire exposure, the shear stress diagrams were symmetric in section S_D (located between load and support sections), which are not presented in Figure 97(b). In fact, the referred non-symmetry of the diagrams (for t = 0 min) was caused by the contact between the sharp corner of the bearing plate with the GFRP profile, which induced a stress concentration. After the beginning of fire exposure, a significant increase in shear stresses occurs at the upper part of the web (Figure 97(b)), where temperatures were lower (namely, for y = 96 mm). By comparing the σ_{12} stresses for both beams, higher stresses were observed in the unprotected beam, compared to those presented by the protected one, in particular at the upper part of the web and during the first minutes of fire exposure (*e.g.*, for t = 15 min).

Effect of the number of sides exposed to fire

To evaluate the effect of the type of fire exposure, the unprotected beams U-S1 and U-S2 (respectively under one- and three-side fire exposure) were considered. The evolution of longitudinal stresses (σ_{11}) along the web's height (y) at section S_C of those beams is presented in Figure 98. After only 10 min of fire exposure, σ_{11} stresses in beam U-S2 became approximately null, except in the upper part of the section. The rapid decrease in longitudinal stresses was caused by tensile modulus reduction at both the bottom flange and webs, as a result of exposing the profile to fire in three sides. Consequently, longitudinal stresses increased considerably at the top flange. After that period (*e.g.*, at 20 min), temperature started increasing at the top flange and, subsequently, a reduction in compressive modulus occurred. Therefore, a slight increase in the longitudinal stresses was registered at the lower part of the profile, with a stress redistribution being observed. The results shown in Figure 98 indicate that the evolution of stresses in both beams presented a similar overall tendency at the upper part of their section (in compression) and a completely different one at their lower part (in tension), which is explained by the different types of fire exposure they were subjected to. It should also be underlined that these differences are consistent with the different failures modes observed in the corresponding experiments. Indeed, beam U-S1 collapsed due to a combination of compressive failure of the top flange and shear failure at the upper part of the webs, while beam U-S2 failed by shear as a consequence of resin softening along the entire depth of the webs.

By comparing the evolution of shear stresses (σ_{12}) in the webs of these beams (see Figure 98), a reduction of σ_{12} values was observed after 10 min, which is explained by the temperature increase at the bottom flange and webs (causing a significant decrease in shear modulus). Then, an increase in the shear stresses was observed, most likely due to the heating of the top flange and the consequent reduction of the compressive modulus. Once again, significant differences were observed between the shear stress diagrams of beams U-S1 and U-S2. As expected, it may also be concluded that the fire exposure in three sides (U-S2) also affects the evolution of σ_{12} stresses, compared to fire exposure in one side (U-S1).

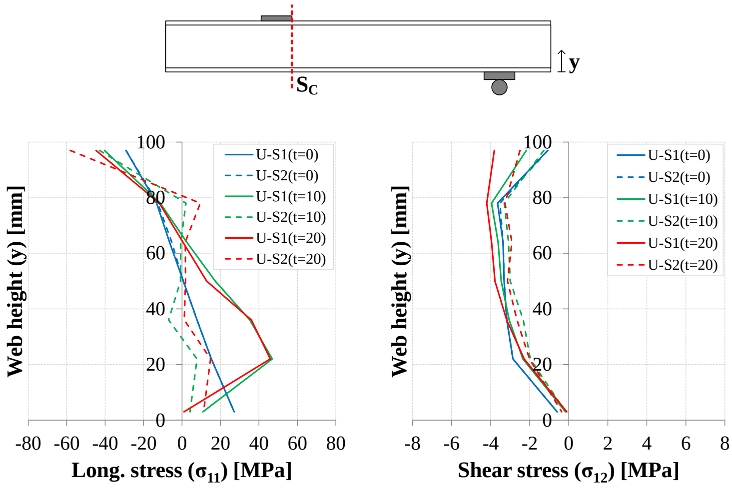

Figure 98: Comparison of longitudinal (σ_{11}) and shear (σ_{12}) stresses evolution for beams U-S1 and U-S2 at 0, 10 and 20 min – section S_C.

7.3.3. Failure prediction

Stress ratios and Tsai-Hill index

In order to estimate the load carrying capacity of GFRP beams under fire exposure and to predict their collapse, the Tsai-Hill failure criterion [62] was used. In this criterion, the interaction between acting stresses and material strength components was considered according to the following equation,

$$I_F = \frac{\sigma_{11}^{\;2}}{\sigma_{u,11}^{\;2}} - \frac{\sigma_{11}\sigma_{22}}{\sigma_{u,11}^{\;2}} + \frac{\sigma_{22}^{\;2}}{\sigma_{u,22}^{\;2}} + \frac{\sigma_{12}^{\;2}}{\sigma_{u,12}^{\;2}} < 1.0 \tag{15}$$

where I_F is Tsai-Hill failure index, σ_{11}, σ_{22} and σ_{12} are respectively the longitudinal, transversal and shear stresses in a given point of the beam and $\sigma_{u,11}$, $\sigma_{u,22}$ and σ_{12} are respectively the ultimate longitudinal, transversal and shear stresses of the GFRP material. When Tsai-Hill index reaches the unit value ($I_F = 1.0$) at a given point, it indicates that such point achieved the onset of failure. For a given (calculated) stress state, this criterion allows the distinction between the damaged ($I_F > 1.0$) and undamaged ($I_F < 1.0$) state of the beam. However, it should be emphasized that this failure criterion has no influence on the stiffness degradation and strength of the GFRP beams: it only identifies the zones that are more susceptible to present failure, but this "failure" does not introduce any type of reduction in the mechanical properties of the material.

To simulate the first failure of GFRP beams under elevated temperatures, the variation of the strength-related mechanical properties (tensile, compressive and shear strengths) with temperature is needed. Because the failure index associated to the Tsai-Hill failure criterion depends on the GFRP strength for different stress states ($\sigma_{u,11}$, $\sigma_{u,22}$ and $\sigma_{u,12}$), the variation of these properties with temperature (T) must now be provided. It should also be highlighted that the GFRP material exhibits different strength properties in compression (σ_{comp}) and tension (σ_{tens}), and that those properties are also different in the longitudinal and transversal directions, and so is their degradation with temperature.

Figure 99 presents the degradation with temperature of tensile ($\sigma_{L,tens}$(T)) and compressive ($\sigma_{L,comp}$(T)) strengths in the longitudinal direction and shear strength (τ_{LT}(T)) considered as input, as well as the strengths considered at room temperature, namely, tensile/compressive strengths in longitudinal ($\sigma_{L,tens}$/$\sigma_{L,comp}$) and transversal ($\sigma_{T,tens}$/$\sigma_{T,comp}$) directions.

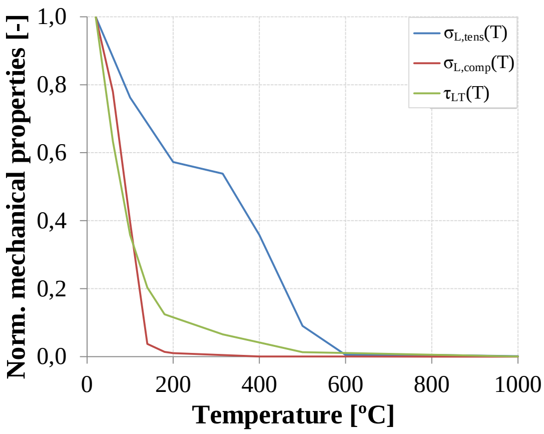

Strengths at 20ºC	
$\sigma_{L,tens}$	336.5 [MPa]
$\sigma_{T,tens}$	60.0 [MPa]
$\sigma_{L,comp}$	416.4 [MPa]
$\sigma_{T,comp}$	93.1 [MPa]
τ_{LT}	37.0 [MPa]

Figure 99: Temperature-dependent variation of longitudinal tensile and compressive strengths and shear strength used in numerical models and room temperature strengths (reference values).

The variation of longitudinal tensile strength with temperature for T < 500 ºC was based on the experimental results presented by Wang *et al*. [114] (9% retention at 500 ºC); for T > 500 ºC, it was assumed that the (high) reduction experimentally observed between 300 and 500 ºC was associated to the decomposition of the GFRP material (a phenomenon expected to be completed at ~600ºC) and that longitudinal tensile strength would be approximately zero at 800 ºC, the fibres softening temperature [115].

The reduction of the shear strength with temperature was based on an experimental campaign carried out in V-notched pultruded GFRP specimens (presented in chapter 3), which allowed determining the strength reduction between 20 and 180 ºC (88% reduction, *cf*. Figure 99); for higher temperatures, the shear strength was reduced to 5% at 370 ºC[5] as a result of material decomposition.

The variation of compressive strength with temperature was defined according to the experimental data reported by Sun [116] obtained from compressive tests on GFRP laminates from 20 to 125 ºC (84% reduction); at elevated temperature, the author reported kinking failure mechanisms, associated to laminate wrinkling, similar to the ones observed in the top compressed flange of the GFRP beams subjected to fire – the latter test results are the bases of the present study; similarly to the shear strength, the residual longitudinal compressive strength was considered to be almost null (0.1%) at 370 ºC as a result of material decomposition.

Note that both longitudinal compressive and shear strengths (matrix-dependent) assumed in this study show very steep descending paths up to 200 ºC due to the softening (glass transition) of the polymer matrix, followed by smooth descending branches for increasing temperatures; while the longitudinal tensile strength (fibre-dependent) considered as input shows a less steep degradation up to 600 ºC, followed by a horizontal (residual) plateau beyond this temperature. For the tensile and compressive strengths in the transversal direction and since no experimental data are available in the literature, thermal degradation was assumed to be that of the longitudinal tensile and compressive strengths, respectively.

The main goal of this section is to identify the stresses that most influence the failure of GFRP beams under fire action. In order to achieve this goal, let us observe that the expression of Tsai-Hill index (Eq. (15)) comprises four terms, hereafter designated by quadratic stress ratios $(\sigma/\sigma_u)^2$ for (i) longitudinal stresses $(\sigma_{11}/\sigma_{u,11})^2$, (ii) transversal stresses $(\sigma_{22}/\sigma_{u,22})^2$, (iii) shear stresses $(\sigma_{12}/\sigma_{u,12})^2$, and (iv) combined longitudinal-transversal stresses $\sigma_{11}\sigma_{22}/(\sigma_{u,11})^2$. Next, the evolution of these stresses/ratios as a function of time are analysed for different beams, *w.r.t.* the type of fire exposure, fire protection and load level.

Unprotected beam with one-side fire exposure

Figure 100 (top and bottom flanges) and Figure 101 (web) depict the variation of the above mentioned ratios and the Tsai-Hill index (I_F) with fire exposure time for section S_C of beam U-S1.

In the top (P1 and P4) and bottom (P12 and P15) flanges, longitudinal (σ_{11}) and transversal (σ_{22}) stresses were the most influential to the failure index, while the shear stresses (σ_{12}) were the less influential (as expected). Considering the evolution of I_F at the bottom flange (*cf.* Figure 100), it can be seen that failure (as mentioned, the term “failure” means failure initiation) of the external

[5] According to DSC/TGA experiments performed, the decomposition temperature of the GFRP material was set at 370 ºC, based on the middle temperature of the sigmoidal mass change.

layer (P15) occurred after 14 min (I_F = 1.0), while the internal layer (P12) did not present failure even after 60 min (I_F < 1.0). According to these results, the bottom flange was able to retain part of its structural integrity. In opposition, the failure of the top flange (P1 and P4) occurred between 25 and 27 min – in the experiments, beam U-S1 collapsed after 36 min of fire exposure; failure was not governed by the bottom flange but rather by the top flange (and upper part of web), a fact that is in agreement with the results of this analysis.

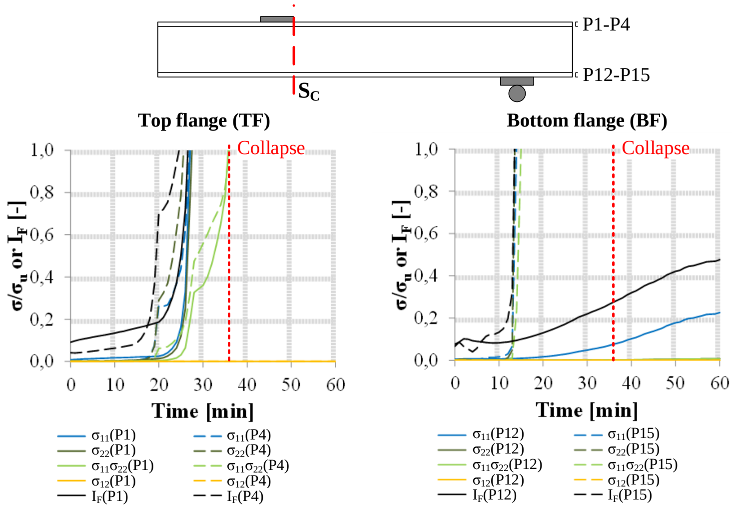

Figure 100: Stress ratios (σ/σ_u) and Tsai-Hill index (I_F) evolution in beam U-S1 at top (P1 and P4) and bottom (P12 and P15) flanges – section S_C.

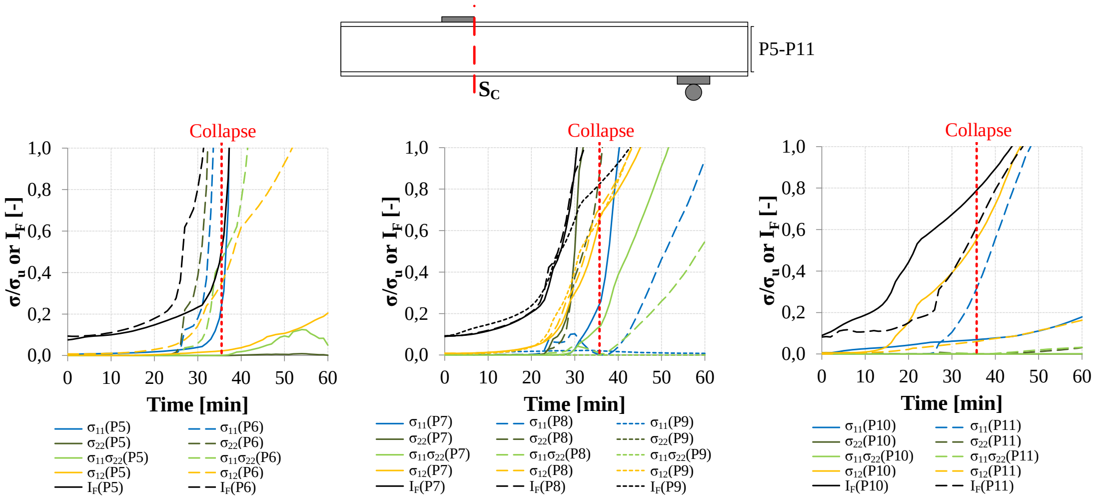

Figure 101: Stress ratios (σ/σ_u) and Tsai-Hill index (I_F) evolution in beam U-S1 at web (P5-P11) – section S_C.

Regarding the evolution of stress ratios at the upper part of web, longitudinal stresses were the most influential to the Tsai-Hill index in element P5, while both longitudinal and transversal stresses were meaningful in element P6, as shown in Figure 101. In the central part of the web (P7-P9), transversal and shear stresses were the most influential to the failure index, despite the high longitudinal stresses registered in element P7. In the lower part of the web, shear and longitudinal stresses were the most influential to the considered failure index in elements P10 and P11, respectively. Considering the failure index evolution, the web failure at its upper part (P5-P7) occurred after 31-38 min, which is consistent with the experimental observations.

Taking into account the results of fire resistance tests performed in this thesis, the failure mode (after 38 min) of the reference beam (U-S1) involved compressive failure at the top flange, which seemed to have been almost immediately followed by shear failure of the webs. Considering the Tsai-Hill index evolution, the top flange failure occurred between 25-27 min, while failure of the upper part of the web occurred after 31-38 min; *i.e.*, the top flange was more susceptible to collapse. Therefore, the Tsai-Hill failure criterion seems to provide a reasonably good agreement with experimental results of beam U-S1, confirming its failure mode and indicating an estimate of its fire resistance which, although conservative, is of the same order of magnitude of that observed in the experiments.

Effects of fire protection, fire exposure and load level

Figure 102 shows the variation of Tsai-Hill index (I_F) with the fire exposure time for all beams (U-S1/S2/S3 and CS-S1/S2/S3), highlighting the effect of the type of fire protection (U *vs*. CS), fire exposure (S1 *vs*. S2) and load level (S1 *vs*. S3). In this comparison, the evolution of I_F in different elements of section S_C – middle of the top (P2-P3) and bottom (P13-P14) flanges and web (P8) – is presented.

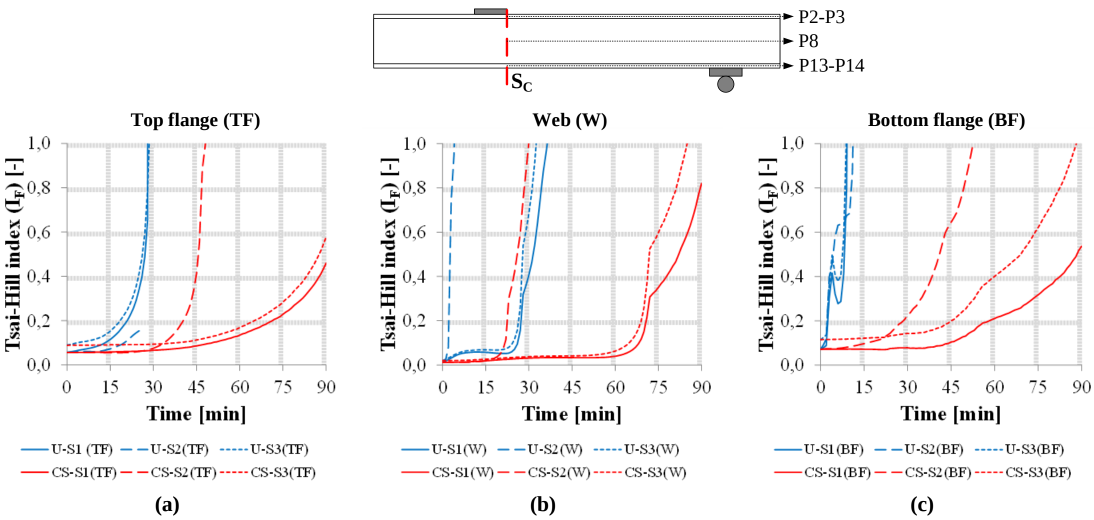

Figure 102: Comparison of Tsai-Hill index (I_F) evolution at (a) top flange (TF), (b) web (W) and (c) bottom flange (BF) for all beams – section S_C.

Regarding the top flange (*cf*. Figure 102(a)), in the unprotected beams, as expected, the failure instant ($I_F = 1.0$) associated to that section wall is considerably shorter than in the protected beams. Also in line with the experiments, the fire exposure in three sides has a clear influence on Tsai-Hill index variation, but such influence is distinct in beams U-S2 and CS-S2: in the former it leads to lower values of I_F, whereas in the latter it causes much higher values (compared to one-side exposure). These differences may be due to the temperature increase at the bottom flange and web of the unprotected beam, which was significantly higher than that observed in the protected profile (which also explains the different failure modes experimentally registered in those beams). Fire protection considerably extended the instant when $I_F = 1.0$. The load level increase caused initial higher values of I_F at the top flange, which is expected; however, for both unprotected and protected beams the instant when $I_F = 1.0$ at the top flange did not seem to be much affected by the load level.

The overall tendency of the results in the web (*cf*. Figure 102(b)) follows that of the top flange. Once more, the effect of fire protection in delaying the instant when $I_F = 1$ is quite clear. Similarly, different $I_F(t)$ curves were obtained for fire exposure in three sides (series S2), compared to one-side fire exposure (series S1), which was also expected, since the webs are severely affected by fire exposure in three sides, causing much more significant temperature increase in these walls. As for the top flange, quite similar $I_F(t)$ curves were obtained in series S3 (L/250) compared to series S1 (L/400); in other words, the load level increase in the models caused only a slight reduction of fire resistance, as indicated by the failure instant ($I_F = 1$) in the web (and top flange); reductions of fire resistance observed in the experiments (associated to those section walls) were more relevant and these differences are likely to be due to: (i) inaccuracy in modelling the thermo-mechanical properties of the GFRP material (assumption made), (ii) the small difference between the two load levels tested (8% *vs*. 12% of strength at room temperature) and (iii) the fact that the Tsai-Hill criterion does not take into account the damage progression.

In the bottom flange (*cf*. Figure 102(c)), two distinct behaviours were observed: the Tsai-Hill index in the unprotected beams reaches the limit (unit) value after about 9 min (regardless of the load level), while it attains 1.0 in the protected beams after only 53 min, which is explained by the thermal insulation provided by the passive fire protection system. Again, very similar $I_F(t)$ curves are observed in the unprotected beams subjected to different load levels. Now the same applies for beams subjected to different types of fire exposure – note that this result is logical as the bottom flange is always exposed to fire for both of one- and three-side fire exposure. Likewise, and similarly to what was observed in the other section walls, fire protection leads to significant reductions of I_F.

It should also be noted that the unprotected beam under three-side exposure (U-S2) presented web and bottom flange failure for very short durations of fire exposure – I_F attained 1.0 in those walls after respectively 5 and 12 min –, while the Tsai-Hill index at the top flange remained well below 1.0 during that period. Thus, both web and bottom flange contribute the most to the failure of beam U-S2. This fact is also consistent with the distinct failure mode experimentally observed in this beam, which took place after only 8 min.

Figure 103 presents the Tsai-Hill index distributions for the reference beam (U-S1) and the unprotected beam exposed to fire in three sides (U-S2), for three different instants. The grey colour in Figure 103 corresponds to the damaged zones, *i.e.* where $I_F > 1.0$.

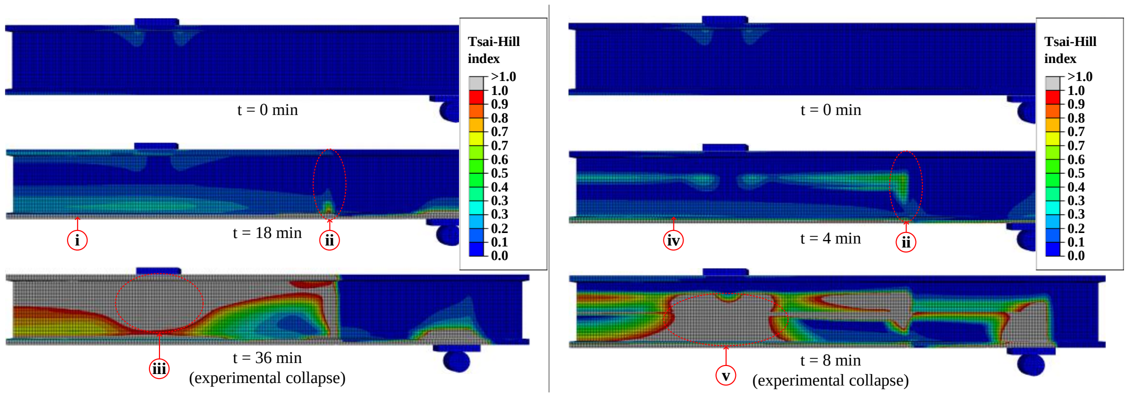

(a) **(b)**

Figure 103: Tsai-Hill index evolution in beams (a) U-S1 and (b) U-S2 for different time steps.

Considering the numerical results obtained for beam U-S1 (Figure 103(a)), it may be observed that $I_F > 1.0$ at a significant portion of the bottom flange after 18 min, corresponding to “zone i” in Figure 103(a). For this instant, a discontinuity (“zone ii”) in the longitudinal evolution of Tsai-Hill index was also observed, as a result of the (non-uniform) temperature distribution assumed in the longitudinal direction of the profiles (*cf.* Figure 86). Effectively, such discontinuity was also observed in the longitudinal and transversal stresses. Additionally, an increase in the value of I_F was registered in the top flange and web close to the loaded section (particularly at the sharp corners of the bearing plate), indicating a section where failure would be expected to occur. At 36 min (experimental collapse instant), failure was observed at the top flange and web (“zone iii”). Thus, the Tsai-Hill index has reached the referred limit value in a significant part of the tubular cross-section.

A similar analysis was performed for beam U-S2 (Figure 103(b)). After 4 min, the value of I_F attained 1.0 only in a portion of the bottom flange – “zone iv” in Figure 103(b). Once again (and due to the same reasons), a longitudinal discontinuity (“zone ii”) was registered. At the instant of the beam’s experimental collapse (8 min), both bottom flange and web (“zone v”) were severely degraded, while the Tsai-Hill index at the top flange remained well below 1.0, as shown in Figure 103(b). As discussed, these results are consistent with the experimental ones, namely the different failure modes observed in these two beams.

Figure 104 illustrates the deformation of beams U-S1 and U-S2 (section S_C) at the instant of experimental collapse. In the one-side exposed beam (U-S1), although slight in-plane deformation of cross-section was observed after 36 min of fire exposure, failure was triggered by the local buckling of the top flange/upper part of web (*cf*. Figure 102) – in this case, the degradation of stiffness due to compression in the upper zone of the beam supersedes the degradation of stiffness associated to heating of the lower zone of the beam. In opposition, the collapse of the three-side exposed beam (U-S2) occurred due to excessive local deformation of the web and bottom flange (as previously discussed – Figure 102) – in this case, the effect of stiffness degradation related to heating of the lower zone of the beam is more relevant than the stiffness degradation due to compression in the upper zone of the beam. This failure mode is also consistent with the experimental observations – beam U-S2 presented shear failure of the web, which seemed to buckle along its entire length exposed to fire due to matrix softening (Figure 105).

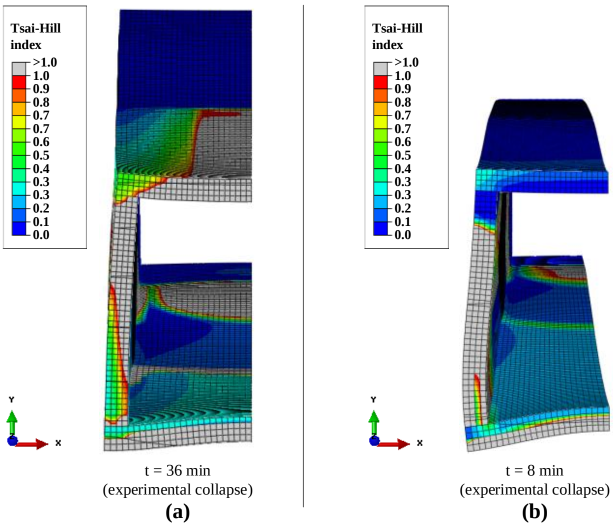

Figure 104: Tsai-Hill index at experimental failure of beams (a) U-S1 and (b) U-S2 – section S_C (deformation scale factor: 10).

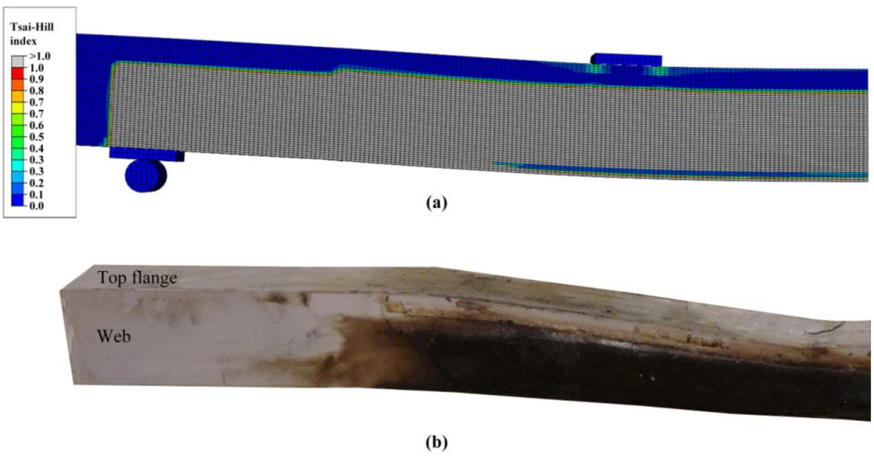

Figure 105: Comparison between (a) numerical and (b) experimental failure modes for beam U-S2 (deformation scale factor: 2).

Evolution of residual section index

In this section, the residual section index (I_R) is defined, which corresponds to the ratio between the area of each section wall (top flange, web, bottom flange) of the tubular profile that remains with the Tsai-Hill index below the unit value ($I_F < 1.0$) and the total area of that wall. It is given by,

$$I_R = \frac{A_i - A_{F,i}}{A_i} < 1.0 \qquad (16)$$

where A_i is the total area of the section wall *i* (the subscript *i* refers to either the top flange, the web or the bottom flange), and $A_{F,i}$ is the area of the section wall *i* that has failed ($I_F > 1.0$).

Figure 106 shows the evolution of I_R with time, evaluated for the different unprotected (Figure 106(a)) and protected (Figure 106(b)) beams at section S_C and for the three section walls – top flange (TF), web (W) and bottom flange (BF).

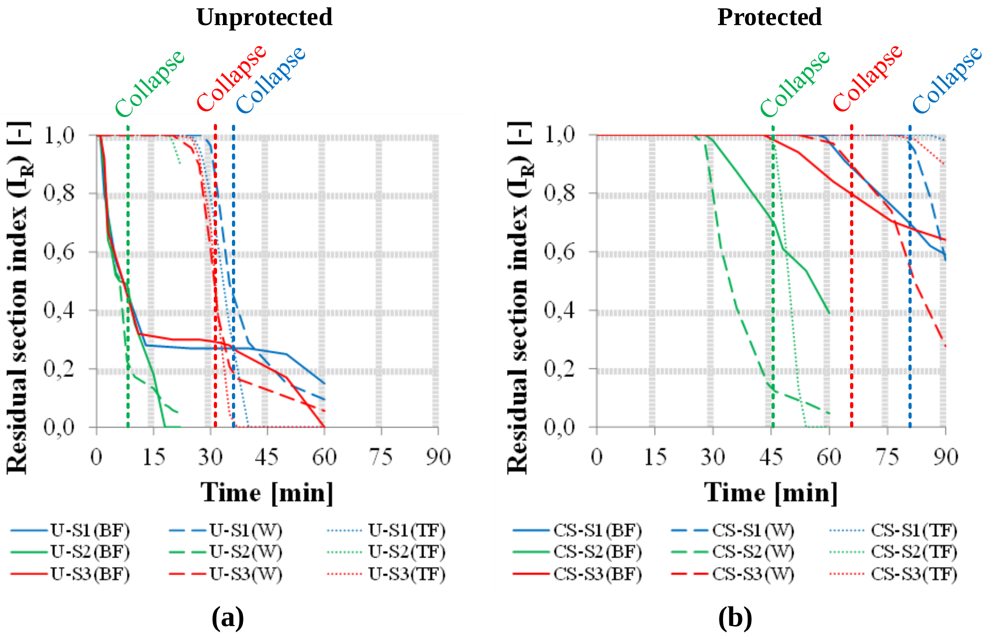

Figure 106: Evolution of residual section index (I_R) with time at top flange, web and bottom flange of (a) unprotected and (b) protected beams – section S_C.

Without protection, the collapse of one-side exposed beams (U-S1 and U-S3) occurred after a sudden drop of I_R at the top flange and web, when the bottom flange was already completely damaged ($I_F > 1.0$). In opposition, for three-side exposure (beam U-S2), both bottom flange and web were partially damaged at the failure instant, while the entire top flange remained undamaged ($I_F < 1.0$), as shown in Figure 106(a). This indicates that most likely the failure of beam U-S2 occurred mainly due to the reduction of I_R at the web (which is consistent with the test results).

Concerning the collapse of protected profiles, unlike the unprotected beams the Tsai-Hill index now did not reach 1.0 in a significant part of the bottom flange (*cf*. Figure 106(b)). The evolution of I_R was similar for both beams under one-side exposure, CS-S1 and CS-S3. According to the residual section index determined, the collapse of these beams seemed to occur when I_R started decreasing at the web. For the protected beam under three-side exposure (CS-S2), failure seems to have occurred as a result of an abrupt drop of I_R at top flange, which is in agreement with the failure mode observed in the tests. It is also interesting to note that, compared to this beam, the failure of beam U-S2 (also under three-side exposure) seems to have been caused by I_R decrease at the web. In fact, these results are consistent with the experimental tests, namely with the different failure modes of beams U-S2 and CS-S2.

The evolution of Tsai-Hill index presented in Figure 102 showed similar $I_F(t)$ curves for series S1 (L/400) and S3 (L/250). Figure 106 shows now, especially for the protected beams, the dependence of fire resistances of GFRP beams on the load level, a fact that is consistent with the test results.

The above-mentioned analysis provided relevant insights on the failure mechanisms of pultruded GFRP beams under fire exposure and, for most parameters tested, it identified correctly its influence on the fire endurance of the beams; however, it was not possible to obtain precise estimates of the failure resistance of the beams. In other words, although the Tsai-Hill criterion allows investigating the initiation of damage in the GFRP beams (providing conservative estimates of the failure instant), it does not take into account the material stiffness degradation when $I_F > 1$ nor the associated stress redistributions. In order to accurately simulate the failure modes of the GFRP beams, it thus seems necessary to develop models in which material stiffness degradation is considered. Since such models require more input data, it is crucial to perform further experiments to determine the evolution of several properties with temperature increase (which in some cases are still not available even at room temperature).

7.4. Analytical study

7.4.1. Description of analytical models

To simulate the mechanical response of GFRP beams under fire exposure, analytical models were also developed on the basis of the previous work presented by Mouritz [111]. The main goal was to predict the evolution of the mid-span deflection using a simple analytical model based on Timoshenko beam theory; in particular, one aimed at assessing if it is possible to obtain accurate predictions of experimental deflections using a much more straightforward simulation tool than the numerical models presented in the preceding section.

In these models, the tubular cross-section was divided into 28 horizontal slices (*cf*. Figure 107(a)) and both physical and mechanical properties of the GFRP material were considered temperature-dependent (as in the numerical models). In each time increment, the mechanical properties of each slice were calculated according to the slice's temperature (determined from the numerical thermal model developed in this thesis). Based on Timoshenko beam theory [117], both flexural and shear deformation contributions to the overall deflection were estimated, which correspond to the first two parts of the expression (17). In these models, it was assumed that the beams were simply supported and loaded in two sections (*cf*. chapter 4). The evolution of elastic mid-span deflection (δ_E) with time (t) was calculated according to the following expression,

$$\delta_E(t) = \int \frac{M\bar{M}}{EI_{eq}(t)}dz + \int \frac{V\bar{V}}{G_m(t)A_v}dz + \int \bar{M}\alpha_{long}\frac{\Delta T(t)}{h}dz \tag{17}$$

where M is bending moment, EI_{eq} is flexural stiffness of the section, V is shear force, G_m is average shear modulus of the section, A_v is shear area, α_{long} is thermal expansion coefficient, ΔT is temperature gradient through the depth of the cross-section and h is the depth of the cross-section.

For each time step, the position of neutral axis (y_{LN}) was determined and the section's equivalent flexural stiffness (EI_{eq}) was calculated. Analogously, shear stiffness (G_mA_v) was estimated, in which shear area ($A_v = k \times A$)[6] was set as constant and the average shear modulus calculation was dependent on the temperatures at webs' slices, as illustrated in Figure 107(b).

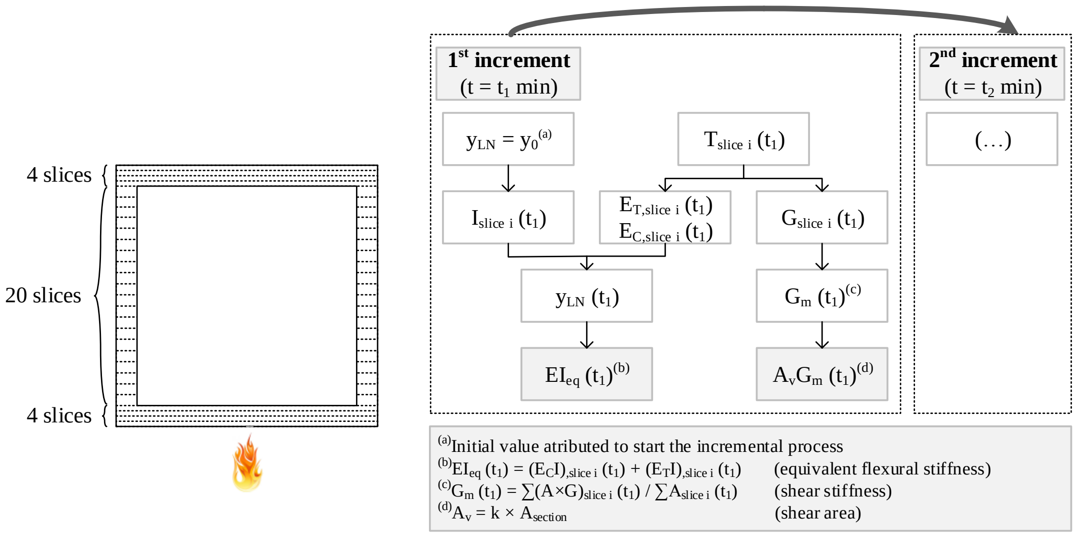

(a) **(b)**

Figure 107: (a) Cross-section discretization considered and (b) scheme of procedure used for calculating analytical results.

[6] k and A denote the shear correction factor (0.42) and cross-section area, respectively.

Since the specimens were subjected to thermal loading, the temperature gradient between the top and bottom surfaces caused an additional deflection in the downwards direction, contributing to the increase of the total deflection – see the third component of Eq. (17). Therefore, the thermal expansion of GFRP material was also considered in the analytical models using the same thermal expansion coefficient ($\alpha_{long} = 6.7\times10^{-6}$) and the same longitudinal temperature distribution (Figure 86) adopted in the numerical FE models.

7.4.2. Analytical results and discussion

Figure 108 presents the analytical results obtained – variation of mid-span deflections as a function of time for series S1, S2 and S3 – and the comparison with the numerical and experimental results. Despite the limitations of the analytical models (based on beam theory), the analytical results were fairly similar to those obtained from the numerical simulations. Accordingly, with the exception of beam CS-S2 (most likely due to the reasons already stated, *cf.* section 7.3.1.), the analytical models provided fairly accurate predictions of the mid-span deflections (*cf.* Figure 108).

As mentioned above, very similar results were provided by the analytical and numerical models, in particular for the fire exposure in one-side (series S1 and S3). Thus, it may be stated that the simple analytical models developed for determining the mid-span deflection provided a good approximation not only to the experimental data, but also to numerical results. For three-side exposure (series S2), significant differences between analytical and numerical results were expected, taking into account the cross-section discretization used in the analytical approach (*cf.* Figure 107). Yet, the overall trends of the analytical curves were in close agreement to the numerical ones and so were the magnitudes of the predicted deflections.

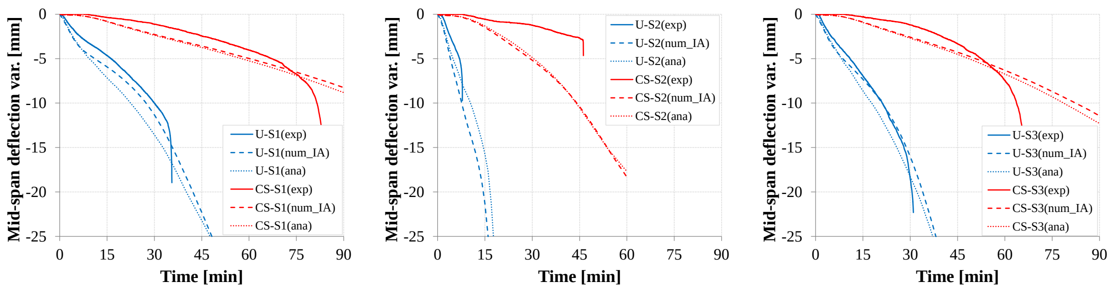

(a) **(b)** **(c)**

Figure 108: Experimental, numerical and analytical mid-span deflections variation for series (a) S1, (b) S2 and (c) S3.

The analytical model was also used to determine the variation of neutral axis position (y_{LN}) as a function of time – Figure 92. Although numerical and analytical curves of y_{LN} have a qualitatively similar behaviour, it can be seen that the magnitude of the variations is significantly different, in particular during an initial period. As mentioned, the temperature gradient (ΔT) between the top and bottom surfaces, as well as the consideration of material thermal expansion, caused an additional deformation/deflection (considered in Eq. (17)). Aiming at determining the referred temperature gradient, some assumptions had to be taken into account in the analytical model, thus explaining the differences between analytical and numerical results during the initial period (where the temperature distribution across the section is highly nonlinear). This also explains the more consistent results obtained for the protected beams, where the temperature gradients were considerably lower than those observed in the unprotected beams.

7.5. Conclusions

This part of the thesis presents an in-depth study on the fire behaviour of GFRP beams. In this chapter, some relevant *kinematic* (deflections and strains) and *static* (stresses and failure) issues about the fire behaviour of pultruded GFRP beams were investigated by means of numerical (finite element) and analytical (beam theory) models. The effects of using fire protection systems were evaluated, different types of fire exposure were tested and distinct load levels were considered. According to the results obtained, the following main conclusions were drawn:

- The thermal expansion coefficient strongly influenced the mechanical response of GFRP beams, particularly in the unprotected profiles and for the initial period. This was due to the high thermal gradient in the cross-section.

- The numerical and analytical models were reasonably accurate in estimating the fire behaviour of the GFRP beams, *i.e.*, the mechanical responses obtained were consistent with the experimental data. Despite the differences observed between numerical and experimental results for the unprotected beam exposed to fire in three-sides, both models presented accurate predictions of the evolution of mid-span deflection with time, when compared to the experimental data.

- Despite the various simplifying assumptions of the analytical models, in general, they provided good agreement with experimental data and numerical simulations, particularly considering the complexity of the phenomena involved.

- According to the numerical and analytical models, the position of neutral axis depends significantly on (i) the temperature field (unprotected and protected beams) and (ii) the consideration (or absence) of the thermal expansion coefficient together with the load level increase.

- The heating process changed the linear longitudinal stress diagram (initial instant) to highly nonlinear diagrams with stress concentration at both top and bottom parts of the web (unprotected beam under one-side exposure) and stress concentration at the top part of the cross-section (unprotected beam under three-side exposure). Fire protection did not change significantly this behaviour, although it attenuated the above mentioned nonlinearity.

- The shear stress diagrams are not symmetric with respect to the web centre due to stress concentration at the top of the profile (close to the load bearing plates) and also shear deformation effects. Its shape does not vary qualitatively with time of fire exposure. The fire protection had little effect on this behaviour. In opposition, the exposure to fire in three sides significantly changed the shear stresses evolution: (i) the shear stresses decreased in the web as a consequence of temperature increase in both bottom flange and web (initial period of fire exposure) and (ii) the shear stresses increased in the web due to the heating of top flange rather than the web material softening (remaining period of fire exposure).

- The transversal stresses were less meaningful than longitudinal and shear stresses. With the exception of the sections below the bearing plates, low (marginal) values of transversal stress were computed in the top flange and web of the unprotected beam, and such stresses were not much affected by the increase of temperature. In the sections below the bearing plates, the contact between the sharp corner of the plates and the top flange led to a concentration of transversal stresses. As a result of thermal expansion effects, transversal stresses were also developed in the bottom flange along the exposed length.

- The collapse of unprotected beams under one-side fire exposure was triggered by failure of the upper zone of the beam. The Tsai-Hill failure index exceeded the unit value in a significant part of upper zone of the beam and this corresponded to a significant drop of the residual section index, being in close agreement with experimental results. For the protected beams under one-side exposure, failure occurred when the Tsai-Hill index exceeded the unit value at the upper part of the web and top flange – in the latter case, the unit failure index was exceeded only to a minor extent at the instant of experimental collapse.

- The collapse of unprotected beams under three-side fire exposure was achieved by failure of the web (experimentally) and failure of bottom flange and web (numerically). In opposition, the collapse of protected beams occurred due to top flange failure (both experimentally and numerically). A sudden drop of the residual section index was observed in the top flange, when the bottom flange and web failed partially. The numerical models also indicated that collapse of the GFRP beams was triggered by the failure of sections below the load bearing plates. With a single exception (failure at the central span), all beams collapsed experimentally in these loaded sections.

The Tsai-Hill failure criterion was not able to accurately capture the influence of load level on the beam fire resistance, as observed in the experiments. The magnitude of the fire resistance reduction measured in the tests was higher than that suggested by the evolution of either stresses or residual section index. A possible explanation might be related to the assumptions undertaken in the modelling of the thermo-mechanical properties of the GFRP material. Nevertheless, the application of the Tsai-Hill criterion provided interesting insights about the failure mechanisms of pultruded GFRP beams subjected to fire and the failure predicted by numerical simulations was generally consistent with experimental results. However, it was not possible to obtain accurate estimates of the fire endurance of the different beams. Future research should address more advanced failure criteria that consider damage propagation and stress redistribution.

As discussed, there are several uncertainties regarding numerical/analytical simulations of the GFRP beams, such as (i) the variation of physical-mechanical properties with temperature (namely, the thermal expansion coefficient); (ii) the thermal and mechanical boundary conditions used in the experiments; and (iii) creep, which is not considered in these simulations. Despite these uncertainties, the complexity of the problem and the assumptions undertaken, it may be concluded that the mechanical response of GFRP beams exposed to elevated temperatures was successfully simulated.

Chapter 8:

Mechanical response of GFRP columns exposed to fire

8.1. Introduction

Although several investigations have been reported in the last decade, further studies are still needed to better understand the fire behaviour of pultruded GFRP structures [6]. In particular, it is known that (i) the action of compressive stresses in structural members always leads to undesired nonlinearities and buckling, and (ii) the thermo-mechanical behaviour of GFRP in compression is poorer than in tension. These evidences make the current experimental and numerical research on the fire resistance of pultruded GFRP members under compression (columns) of utmost relevance. The few numerical works reported in the literature about the structural response of pultruded GFRP columns subjected to elevated temperatures are summarized next.

Regarding the numerical studies, and besides the works presented by Gibson *et al*. [20] and Bausano *et al*. [21] at the GFRP laminate level, not much has been done in the modelling and simulation of GFRP profiles under fire exposure. In this scope, the works reported by Wong *et al*. [114] and Bai *et al*. [11, 14] deserve to be credited. Wong *et al*. [22] studied the compressive behaviour of pultruded GFRP columns with C-section for different temperatures (20-250 ºC) using finite element (FE) models developed within the framework of *ABAQUS* software. Although their models included local buckling effects and the influence of geometrical imperfections, they concluded that the modelling approach overestimated the experimental failure loads. Bai *et al*. [11] also simulated the fire behaviour of GFRP multicellular columns based on one-dimensional thermal analysis and using their own models [14], in which the variation of thermo-physical properties with time and temperature was considered. The evolution of lateral deformation with time was determined by considering the second-order deflections due to both thermal expansion and load eccentricity. In addition, the variation of Euler buckling load and ultimate load with time was estimated using second-order bending theory. The authors concluded that the fire resistance of GFRP multicellular columns may be well predicted through the calculation of the Euler buckling load.

While the structural response of pultruded GFRP members exposed to elevated temperature has been modelled by assuming perfect elasticity, it is known that moderate to high temperatures always lead to viscoelastic effects that may be significant for moderate to long durations [6].

Despite the absence of comprehensive studies on the creep behaviour of pultruded GFRP profiles under high temperatures, there are a few works on GFRP laminates. Dutta and Hui [118] modelled the short-term (30 min) creep response of GFRP coupons at low to moderate temperatures (25-80 ºC) using a modified version of Findley's power law calibrated through experimental values (time-dependent thermal deformation and failure stresses). Boyd *et al.* [119] also performed creep failure tests on one-side fire exposed GFRP laminates subjected to compression. In this study, an analytical model was developed to simulate the creep behaviour and compressive strength, which included thermo-viscoelasticity and was based on Budiansky and Fleck model [120].

In resume, the interaction between different and complex phenomena involving mechanical and thermal anisotropy, heat transfer, fluid dynamics, viscosity and delamination, still hinders the development of full and rigorous simulations of GFRP structures under fire. These effects added to the deteriorating influence of compressive stresses, lead to an extremely complex behaviour of pultruded GFRP columns that is still far from being correctly captured through numerical models.

Aiming at determining the mechanical response of pultruded GFRP tubular columns exposed to elevated temperatures and simulating as rigorously as possible fire resistance tests previously carried out and described in chapter 5, three-dimensional FE models were developed using *ABAQUS Standard* [113] software. In this numerical study, different complex phenomena are considered, such as thermo-mechanical anisotropy, heat transfer and fluid dynamics, while the creep behaviour and delamination effects are neglected. The thermo-mechanical properties are assumed temperature-dependent and different curves are considered for the degradation of compressive ($E_C(T)$) and shear ($G_{LT}(T)$) moduli. Heat transfer is considered through conduction, radiation and convection of air inside the tube using fluid dynamics. The numerical results presented include: (i) the evolution of axial and flexural deformations of the GFRP columns (compared to the experimental data); (ii) the variation with time of stress distributions in both longitudinal and transversal directions of the unprotected column under one-side fire exposure (reference column); (iii) the effects of fire protection system; and (iv) the influence of different fire exposure conditions (one- *vs.* three-side) and load levels. Moreover, both Tsai-Hill and Hashin[7] criteria are used to obtain a better identification of the most damaged zones of the columns and understand their failure modes. Finally, the main conclusions of this numerical study are presented.

[7] Hashin damage criterion was used only in the reference column (unprotected and exposed to fire in one side), also allowing to estimate its respective failure load.

8.2. Numerical models

8.2.1. Introduction

Aiming at simulating the fire behaviour of pultruded GFRP columns, a two-step procedure was adopted: the thermal response of the profiles was first obtained using numerical models within *ANSYS Fluent* [18] framework and the thermal results (variation of temperature distribution with time) were subsequently used as input data to the FE models developed within *ABAQUS Standard* [113][8] framework to obtain the thermo-mechanical response of pultruded GFRP columns. In the thermal study (*cf.* chapter 6), two-dimensional models were developed to evaluate the evolution of temperatures in the cross-section of the unprotected and protected GFRP profiles subjected to different fire exposure (either in one- or three-side). The numerical temperature curves were consistent with the experimental ones, despite the several assumptions adopted and the complexity involved in this heat transfer problem, including conduction, radiation and convection inside the tubular section.

8.2.2. Description of numerical models

FE model labelling and mesh

The labelling of the FE models is summarized in Table 19, including the type of fire exposure, the applied load level considered and its time duration. As shown in Table 19, columns were labelled according to the following nomenclature: (i) fire protection (U – unprotected; CS – CS protected); (ii) fire exposure (E1 – one-side; E3 – three-side), (iii) load level (L1 – 6.7% room temperature axial strength; L2 – 13.4% room temperature axial strength). Four uniform load and time-dependent models were considered (U-E1-L1, CS-E1-L1, U-E3-L1, U-E1-L2), all with elastic material behaviour (no material damage) and identification of initial failure though Tsai-Hill criterion. A fifth model (U-E1-LV) with the load varied from 0 to P_u (ultimate load) and progressive failure included through Hashin's damage criteria was considered. In this model, the mechanical properties were assumed fixed for the time t = 16 min, at which the collapse of column U-E1-L1 occurred experimentally.

In the FE model of the protected column (CS-E1-L1), the mechanical (stiffness and strength) contribution of the passive fire protection to the axial and flexural deformations and stresses was neglected[9]. Additionally, there is also a lack of information in the literature regarding both

[8] This software did not allow the performance of two-dimensional thermal analysis considering heat transfer though simultaneous conduction, radiation and convection inside the tubular section. Consequently, it was decided to perform the thermal (2D) and mechanical (3D) analysis using different software, *ANSYS Fluent* and *ABAQUS Standard*, respectively.

[9] Using mechanical homogenization principles, it may be concluded that the CS protection allowed an increase of approximately 11% of the room temperature axial stiffness of the unprotected columns. In fact, the axial shortening measurements registered in S1 columns after load application (before beginning fire exposure) were

GFRP-CS interface and thermo-mechanical properties of material CS. Despite modelling the steel blocks for the reaction supports, only a GFRP part was considered.

Table 19: Labelling of numerical models.

FE Models	Series	Protection	Exposure	Load level	Criterion	Damage
U-E1-L1	S1	Unprotected (U)	1 side (E1)	P=55 kN (L1)	Tsai-Hill	No
CS-E1-L1	S1	Calcium silicate (CS)	1 side (E1)	P=55 kN (L1)	Tsai-Hill	No
U-E3-L1	S2	Unprotected (U)	3 sides (E3)	P=55 kN (L1)	Tsai-Hill	No
U-E1-L2	S3	Unprotected (U)	1 side (E1)	P=110 kN (L2)	Tsai-Hill	No
U-E1-LV	S1	Unprotected (U)	1 side (E1)	0≤P≤Pu (LV)	Hashin	Yes

Regarding the FEs used, the time-dependent models (U-E1-L1, CS-E1-L1, U-E3-L1, U-E1-L2) adopted solid FEs, while the load-dependent model U-E1-LV considered shell FEs because the solid ones do not allow the damage progression – Hashin criterion is only available for shell FEs. For models U-E1-L1, CS-E1-L1, U-E3-L1 and U-E1-L2, the GFRP columns were discretised using eight-node solid elements with reduced integration (C3D8R). The cross-section of GFRP columns was meshed uniformly with 4 and 50 elements across the thickness and along the height, respectively, and with 450 elements along the length. To reduce the computational time of the analyses, only half of the profile was modelled assuming conditions of symmetry in transversal direction, as schematized in Figure 109. Then, the FE mesh had a total of 165,232 elements and 209,250 nodes.

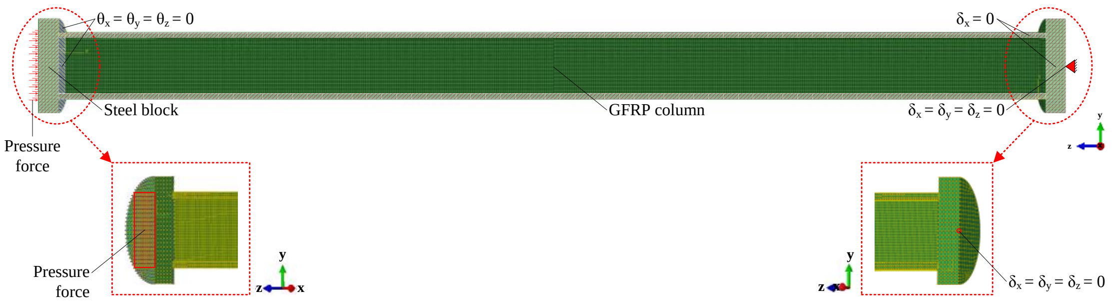

Figure 109: Geometry, mesh and boundary conditions of FE models.

The model U-E1-LV was meshed using eight-node continuum shell elements with reduced integration (SC8R). Continuum shell elements were assumed as three-dimensional bodies, with 4 layers across the width of each flange and 12 layers across the webs height. In each one of these layers, the temperature-dependent mechanical properties were considered, *i.e.*, the assign of different materials depending on the numerical temperatures obtained in chapter 6 was made. The cross-section of GFRP column was meshed uniformly with 4 and 50 elements across the

0.68 mm (U-E1-L1) and 0.80 mm (CS-E1-L1). Thus, the mechanical contribution of the passive fire protection system may be neglected.

thickness and height, respectively, and 750 elements along the length. As a result, a mesh with a total of 589,568 elements and 737,940 nodes was used.

Boundary, loading and thermal conditions

The mechanical response of GFRP columns was modelled considering symmetric conditions with respect to y-z plane (plane of symmetry) and, therefore, displacements in x-axis were fully restrained ($\delta_x = 0$), as shown in Figure 109. The load (pressure force) was applied through a steel bearing plate (left side of Figure 109) with free axial deformation (z-axis) but restrained (null) rotations ($\theta_x = \theta_y = \theta_z = 0$). In opposite (right) side, the steel plate was allowed to rotate freely but it was fixed against displacement ($\delta_z = 0$), as illustrated in Figure 109. The interface between the GFRP profile and steel blocks was modelled using surface-to-surface contact interaction with hard normal contact and rough tangential behaviour. Constant pressures of 5.5 and 11.0 MPa were applied to left bearing plate for load levels L1 and L2 (see Table 19), respectively, corresponding to half of the total loads (55 and 110 kN) due to symmetry simplification. For LV, compressive load was incrementally increased up to P_u (ultimate load).

The variation of nodal temperatures with fire exposure time was previously obtained from the two-dimensional thermal analysis (presented in chapter 6) and considered herein as input to the mechanical analyses. Considering the test setup used (see section 5.2.3.), the temperature variation along the length of the profiles was not constant and, therefore, longitudinal temperatures were discretized in three parts, and were considered uniform in each of these parts. Figure 110 shows the longitudinal distribution of temperatures assumed, in which three different parts were considered: (i) 2D numerical temperatures (exposed part); (ii) half of 2D numerical temperatures (unexposed part); and (iii) initial temperature set equal to 20 ºC (exterior part). Since neither the experimental nor the numerical distribution of temperatures along the longitudinal direction (z-axis) was known, these assumptions were considered in order to simulate the mechanical response of the GFRP columns.

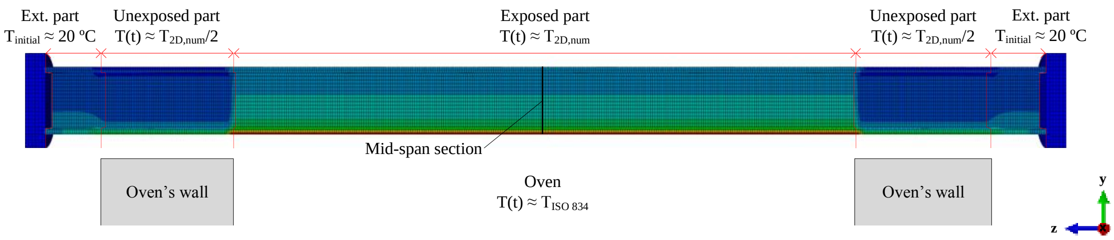

Figure 110: Temperature distribution assumed along the length of GFRP columns.

Failure and damage criteria

In order to estimate the initial failure of GFRP columns under fire exposure, the Tsai-Hill criterion [62] was used in time-dependent models (U-E1-L1, CS-E1-L1, U-E3-L1, U-E1-L2). In this criterion, the interaction between acting stresses and material strength components was considered according to the Eq. (15) – *cf*. section 7.3.3.

When Tsai-Hill index reaches the unit value ($I_F = 1.0$) at a given point, it indicates that such point achieved the onset of failure. For a given (calculated) stress state, this criterion allows the distinction between the damaged ($I_F > 1.0$) and undamaged ($I_F < 1.0$) state of the column. However, it should be emphasized that this failure criterion has no influence on the stiffness degradation and strength of the GFRP columns: it only identifies the zones that are more susceptible to present failure, but this "failure" does not introduce any type of reduction in the mechanical properties of the material.

In order to estimate the load carrying capacity of GFRP columns under fire exposure and to predict their collapse, the Hashin damage criterion [61] was used in the load-dependent model U-E1-LV. In opposition to the Tsai-Hill criterion, which proposes a single equation to predict failure initiation, Hashin criterion takes into account the material progressive damage by considering four failure modes (indexes): (i) fibre tension index ($F_{f,T}$), (ii) fibre compression index ($F_{f,C}$), (iii) matrix tension index ($F_{m,T}$) and (iv) matrix compression index ($F_{m,C}$). In this criterion, the following equations are used,

$$F_{f,T} = \left(\frac{\hat{\sigma}_{11}}{S_{T,1}}\right)^2 + \alpha\left(\frac{\hat{\sigma}_{12}}{S_{12}}\right)^2 \leq 1.0 \text{ and } \hat{\sigma}_{11} \geq 0 \tag{18}$$

$$F_{f,C} = \left(\frac{\hat{\sigma}_{11}}{S_{C,1}}\right)^2 \leq 1.0 \text{ and } \hat{\sigma}_{11} < 0 \tag{19}$$

$$F_{m,T} = \left(\frac{\hat{\sigma}_{22}}{S_{T,2}}\right)^2 + \left(\frac{\hat{\sigma}_{12}}{S_{12}}\right)^2 \leq 1.0 \text{ and } \hat{\sigma}_{22} \geq 0 \tag{20}$$

$$F_{m,C} = \left(\frac{\hat{\sigma}_{22}}{2S_{23}}\right)^2 + \left[\left(\frac{S_{C,2}}{2S_{23}}\right)^2 - 1\right]\frac{\hat{\sigma}_{22}}{S_{C,2}} + \left(\frac{\hat{\sigma}_{12}}{S_{12}}\right)^2 \leq 1.0 \text{ and } \hat{\sigma}_{22} < 0 \tag{21}$$

where $\hat{\sigma}_{11}$, $\hat{\sigma}_{22}$ and $\hat{\sigma}_{12}$ are the applied effective stresses, $S_{T,i}$, $S_{C,i}$ and S_{ij} are tensile, compressive and shear strengths and α is a coefficient (set by default to 0.0) that accounts for the shear stress contribution to fibre breakage in tension criterion. The effective stresses $\hat{\sigma}$ are computed by means of,

$$\hat{\sigma} = M\sigma, \text{where } M = \begin{bmatrix} 1/(1-d_f) & 0 & 0 \\ 0 & 1/(1-d_m) & 0 \\ 0 & 0 & 1/(1-d_s) \end{bmatrix} \tag{22}$$

where M is the damage operator, σ is applied stress and d_f, d_m and d_s are indexes that reflect the current state of fibre, matrix and shear damage, respectively, given by,

$$d_f = \begin{cases} d_f^{tens} & \text{if } \hat{\sigma}_{11} \geq 0 \\ d_f^{comp} & \text{if } \hat{\sigma}_{11} < 0 \end{cases} \tag{23}$$

$$d_m = \begin{cases} d_m^{tens} & \text{if } \hat{\sigma}_{22} \geq 0 \\ d_m^{comp} & \text{if } \hat{\sigma}_{22} < 0 \end{cases} \tag{24}$$

$$d_m = 1 - (1 - d_f^{tens})(1 - d_f^{comp})(1 - d_m^{tens})(1 - d_m^{comp}) \tag{25}$$

in which the subscripts "tens" and "comp" correspond to tensile and compressive modes, respectively. The difference between stress states (before and after damage) in a material point should be responsible for a sudden drop of strength of the structure to which that point belongs and also a decrease of its post-damage stiffness (softening stage). This computation requires the definition of four different fracture energy parameters, one for each failure mode.

In Hashin damage criterion, the elasticity matrix is affected by the state of fibre, matrix and shear damage, which consequently reduces the stresses in GFRP material; the damage evolution law (available in *ABAQUS* FE package) is based on the energy dissipated during the damage process and linear material softening [101]. Contrarily to Tsai-Hill criterion, in which the elasticity matrix is affected by temperature-dependent material properties, the Hashin criterion also considers the reduction of elasticity matrix with the state of damage in GFRP material. When any of the failure indexes attains the limit value (1.0) in a given point, the stress state in that damaged point is computed by means of,

$$\begin{Bmatrix} \sigma_{11} \\ \sigma_{22} \\ \sigma_{12} \end{Bmatrix} = \frac{1}{D} \begin{bmatrix} (1-d_f)E_{11} & (1-d_f)(1-d_m)\nu_{21}E_{11} & 0 \\ (1-d_f)(1-d_m)\nu_{12}E_{22} & (1-d_f)E_{22} & 0 \\ 0 & 0 & (1-d_s)G_{12}D \end{bmatrix} \begin{Bmatrix} \epsilon_{11} \\ \epsilon_{22} \\ \epsilon_{12} \end{Bmatrix} \tag{26}$$

where σ_{ij} are the applied stresses, ϵ_{ij} is a strain component, E_{11}, E_{22} and G_{12} are longitudinal, transversal and shear moduli, ν_{12} and ν_{21} are Poisson ratios, and $D = 1 - (1 - d_f)(1 - d_m)\nu_{12}\nu_{21}$.

Material properties

The GFRP material was modelled assuming an orthotropic behaviour using *ABAQUS Standard*, in which the three elastic moduli, Poisson's ratios and shear moduli corresponding to material's principal directions were assigned. Taking into account the mechanical properties measured in experimental tests (Table 20), the following room temperature compressive properties were considered (the corresponding source is indicated in brackets): longitudinal modulus E_L = 31.0 GPa (full-section elastic modulus); transverse modulus E_T = 8.3 GPa (compressive transverse modulus); out-of-plane modulus E_Z = 3.5 GPa (compressive modulus of polymeric matrix); shear modulus G_{LT} = 3.6 GPa (full-section and material shear modulus); ν_{LT} = 0.27 (coupon tests)[10]; longitudinal strength σ_L = 416.4 MPa (determined from coupon tests in compression); transversal strength σ_T = 93.1 MPa (determined from coupon tests in compression); shear strength τ_{LT} = 37.0 MPa (determined from coupon tests in shear). All moduli and strengths were assumed to vary with temperature according to curves depicted in Figure 111, while the Poisson's ratios were considered temperature-independent. The thermal expansion of the GFRP material was defined according to the values reported in the literature [25] and was assumed temperature-independent in both longitudinal ($\alpha_{long} = 6.7\times10^{-6}$) and transversal ($\alpha_{trans} = 22.0\times10^{-6}$) directions. These values are also in agreement with the ones previously used (see section 7.3.1.), where a parametric study was performed on GFRP beams. The steel material parts, corresponding to the steel blocks placed at the end sections, were defined with temperature independent isotropic properties (E_{steel} = 210 GPa, ν_{steel} = 0.3).

Table 20: Mechanical properties of the GFRP profiles at room temperature.

Mechanical property	Elastic modulus [GPa]	Ultimate strength [MPa]
Flexural longitudinal	$E_{L,flex} = 28.0 \pm 6.1$	$\sigma_{L,flex} = 352.7 \pm 76.1$
Tensile longitudinal	$E_{L,tens} = 39.9 \pm 2.7$	$\sigma_{L,tens} = 336.5 \pm 87.7$
Compressive longitudinal	$E_{L,comp}* = 25.3 \pm 2.5$	$\sigma_{L,comp} = 416.4 \pm 22.2$
Compressive transversal	$E_{T,comp}* = 8.3 \pm 1.8$	$\sigma_{T,comp} = 93.1 \pm 14.9$
Interlaminar shear	$G_{LT} = 3.6 \pm 0.3$	$\tau_{LT} = 37.0 \pm 2.9$

* "Apparent" modulus, as it includes the effects of local crushing at the extremity sections (edges) of coupons.

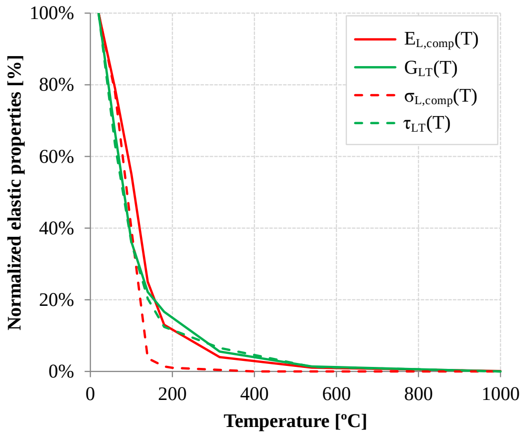

Figure 111: Variation with temperature of the compressive and shear moduli/strengths.

As mentioned, the use of Hashin damage criterion also requires the knowledge of GFRP fracture energies (FE), which were defined based on some preliminary experimental tests [121]. The fracture energies assumed for room temperature are: (i) $FE_{L,comp}$ = 45 N/mm (longitudinal compressive failure mode); and (ii) $FE_{T,comp}$ = 20 N/mm (transversal compressive failure mode).

[10] In the other planes, this value of shear modulus was assumed, while a value of 0.11 was adopted for the Poisson's ratio.

Since no information was found in the literature, the variation with temperature of the fracture energies in compression ($FE_{L,comp}$ and $FE_{T,comp}$) was assumed equal to that of the longitudinal compressive ($E_{L,comp}(T)$) modulus.

Methodology and analysis

In the fire resistance tests of time-dependent models (U-E1-L1, CS-E1-L1, U-E3-L1, U-E1-L2), three steps were defined: (i) an initial step to impose the boundary conditions and initial nodal temperatures (20 ºC); (ii) a mechanical load step (general, static) to apply the constant pressure; and (iii) a thermal load step (with a time step of 1 min) to impose the nodal temperatures as function of the time. These are the so-called thermo-mechanical loading models. For comparison purposes for axial and flexural deformations (sections 8.3.1. and 8.3.2.), they were also used only for thermal loading, in which the mechanical compressive load was absent. In this case, the labelling excludes the capital "L" – *e.g.* U-E1-L1 is the thermo-mechanical loading model of the unprotected column under one-side exposure and lowest load level, while U-E1 is the same model without compressive load.

Transient linear analyses were carried out considering a total time of 60 min and a time step of 1 min. It was possible to predict the fire behaviour of the GFRP columns tested (chapter 5), namely axial and flexural deformations. Nevertheless, the analyses were not successfully completed in most of the numerical simulations due to numerical convergence difficulties. The durations of the numerical simulations were: U-E1-L1 (t = 39 min), CS-E1-L1 (t = 60 min), U-E3-L1 (t = 9 min), U-E1-L2 (t = 25 min). These "numerical" durations were however higher that the corresponding experimental ones. In the load-dependent model (U-E1-LV), a two-step procedure was defined: (i) an initial step to impose the boundary conditions and the nodal temperatures computed for t = 16 min (time of experimental failure observed); (ii) a mechanical load step (general, static) to increase the pressure up to collapse of the column. In this model, an initial imperfection[11] (in both flexural and axial directions) caused by thermal expansion of GFRP column was imposed. The results obtained from these simulations are presented and discussed in the next section.

8.3. Numerical results and discussion

In this section, the numerical results are presented and discussed. In sections 8.3.1. and 8.3.2., the evolution of column axial and flexural behaviours with fire exposure time is assessed and compared with experimental measurements. In section 8.3.3., the evolution of stress distributions in both longitudinal and transversal directions of the reference column (U-E1-L1)

[11] The referred initial imperfection applied was determined from model U-E1 where only thermal loading was applied (*i.e.*, no mechanical loading).

is presented and the effects of fire protection, fire exposure and applied load level are discussed in terms of stress patterns. Finally, in sections 8.3.4. and 8.3.5., the failure and damage of GFRP columns is investigated through the use of Tsai-Hill failure criterion (time-dependent models) and Hashin damage criterion (load-dependent model), respectively.

8.3.1. Axial behaviour

Figure 112 presents the variation of axial deformation with fire exposure time obtained from both numerical analyses and experimental tests. During the first 5 min, a slight axial elongation (positive) caused by the thermal expansion of GFRP material was measured in reference column U-E1-L1 (unprotected and one-side exposed). In this period, a perfect agreement was found between the results of model U-E1 (only thermal loading) and experimental ones. However, the models U-E1-L1 and U-E1-L2 (both with thermal and mechanical loadings) exhibited only axial shortening (negative). In the fire protected column, the axial shortening experimentally registered was much higher that the numerical one. Despite the overall fair qualitative agreement between the numerical and experimental curves for the unprotected columns, such consistency was not observed for the protected column: the numerical axial shortening values of CS-E1-L1 were considerably lower than those experimentally measured (CS-E1-L1(exp)), as shown in Figure 112(a). These differences might be due to (i) the variation of nodal temperatures with fire exposure time (the numerical temperatures were slightly lower than those measured, in particular at the webs); (ii) the test setup conditions (the misalignments in test setup, friction in supports and column geometrical imperfections might play a key role); (iii) the thermal degradation of mechanical properties (*e.g.* the reduction compressive modulus); and (iv) the creep effect. This last effect, not considered in the models, is consistent with the fact that experimental deformations are generally higher than numerical ones.

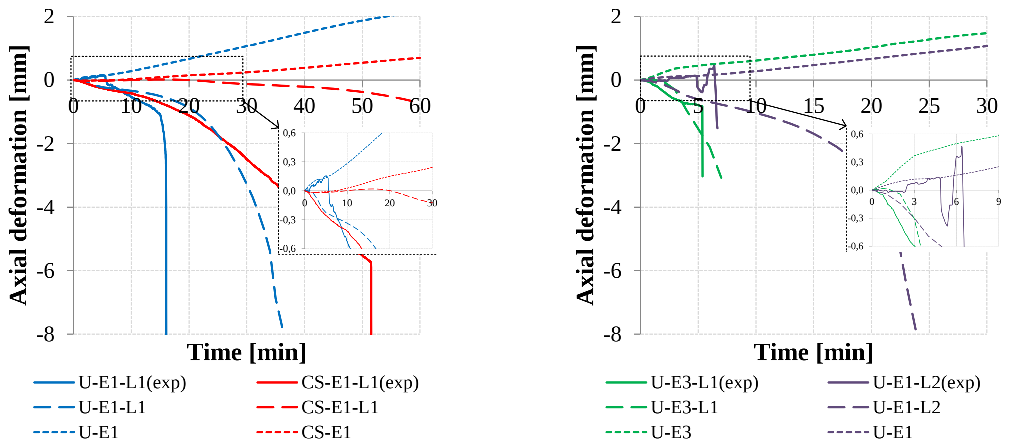

(a) (b)

Figure 112: Variation of axial deformation with fire exposure time for columns (a) U-E1-L1/CS-E1-L1 and (b) U-E3-L1/U-E1-L2 – mid-span section (positive-elongation; negative-shortening).

Aiming at quantifying the potential influence of creep effect in the mechanical response of the GFRP columns, a semi-empirical equation proposed by Dutta and Hui [118] was used. As mentioned (*cf.* section 8.1.), these authors performed an experimental investigation on the creep rupture of GFRP composites at different temperatures (25, 50 and 80 ºC). Based on Findley's equation, Dutta and Hui [118] proposed the following semi-empirical equation,

$$\varepsilon_{\mathrm{creep}}(\mathrm{t}) = \varepsilon_0 + \mathrm{p}\left(\frac{\mathrm{t}}{\mathrm{t}_0}\right)^{\beta(\mathrm{T}/\mathrm{T}_0)} \tag{27}$$

where $\varepsilon_{\mathrm{creep}}$ is creep strain, t is time (in hours), ε_0 is initial strain (set as null), p is a coefficient applied to time ratio (t/t_0) and β is a coefficient applied to temperature ratio (T/T_0). In that study, parameters p and β were set as 45 and 0.29, respectively, as a result of a curve fitting from the experimental data measured in the compression creep test at 80 ºC.

In order to estimate the influence of creep deformation in the protected column (CS-E1-L1, the longer test where the importance of creep effects was expected to be higher), the instant in which the average temperature (T_m)[12] at the mid-span section reaches 80 ºC was determined. Considering the evolution of numerical temperatures in column CS-E1-L1, it was concluded that the average temperature at the mid-span section attains 80 ºC after 23 min of fire exposure. Using Eq. (27) and considering only the length directly exposed to fire, it can be estimated that the creep strain for T_m = 80 ºC (corresponding to t = 23 min) would be about 825 μm/m and the axial shortening increase would be approximately 0.8 mm. It should also be highlighted that the axial shortening is 0.1 mm after 23 min of fire exposure, and that value is 12.5% of the axial shortening caused by creep. This prediction confirms the potential behavioural influence of creep (namely, in axial deformations) and explains, to a certain extent, the differences found between some numerical and experimental results (*cf.* Figure 112).

The unprotected column exposed to fire in three sides (U-E3-L1 and U-E3-L1(exp)) shortened quickly during the first 6 min, as a result of the severe temperature increase registered. The overall tendency of the numerical results was consistent with the experimental data, both presenting a significant shortening during that initial period. In opposition, the increase of load level in the unprotected column (U-E1-L2(exp)) led to its experimental collapse after 9 min. In this case, the numerical model U-E1 provided an initial axial elongation consistent with experimental data, while such behaviour was not observed in model U-E1-L2. The collapse of columns U-E3-L1 and U-E1-L2 occurred only 6 and 9 min after burners' ignition, respectively. Therefore, few conclusions may be drawn from the comparison between numerical and

[12] The average temperature at mid-span section was calculated considering the average of the temperatures at the middle of bottom (P13-P14) and top (P2-P3) flanges (*cf.* Figure 114).

experimental results and the differences observed may be due to the same factors referred above.

8.3.2. Flexural behaviour

Figure 113 shows the variation of transversal deflection with fire exposure time obtained from the numerical analyses and measured in the experimental tests. According to experimental results, the GFRP columns moved downwards (towards the heating source) as a result of the temperature gradient in the cross-section's profile and the material thermal expansion. This initial descending movement (corresponding to the initial negative values) was less perceptible in the protected column because the thermal insulation conferred by the fire protection allowed the reduction of the thermal gradient across the cross-section's height. That deflection downwards, associated to thermal expansion effect, was only observed only in models U-E1, CS-E1 and U-E3. Nevertheless, the deflections obtained from these models were significantly lower than those measured from fire tests. With the exception of the protected column (CS-E1-L1), the overall tendency of the remaining numerical curves (U-E1-L1, U-E3-L1 and U-E1-L2) was different from the experimental ones (*cf.* Figure 113). In these models, the columns started deflecting upwards as a consequence of the fire exposure and, subsequently, a progressive loss of profiles' axial stiffness occurred. The ascending movement observed in all models is in agreement with the experimental results – this movement upwards was registered after a descending one. Although meaningless negative vertical displacements were observed in columns CS-E1-L1 and U-E3-L1 (thus, corresponding to a descending movement), the overall trend is to revert these displacements to positive ones (ascending movement) for increasing fire exposure – this behaviour was qualitatively similar to that observed in the experimental tests.

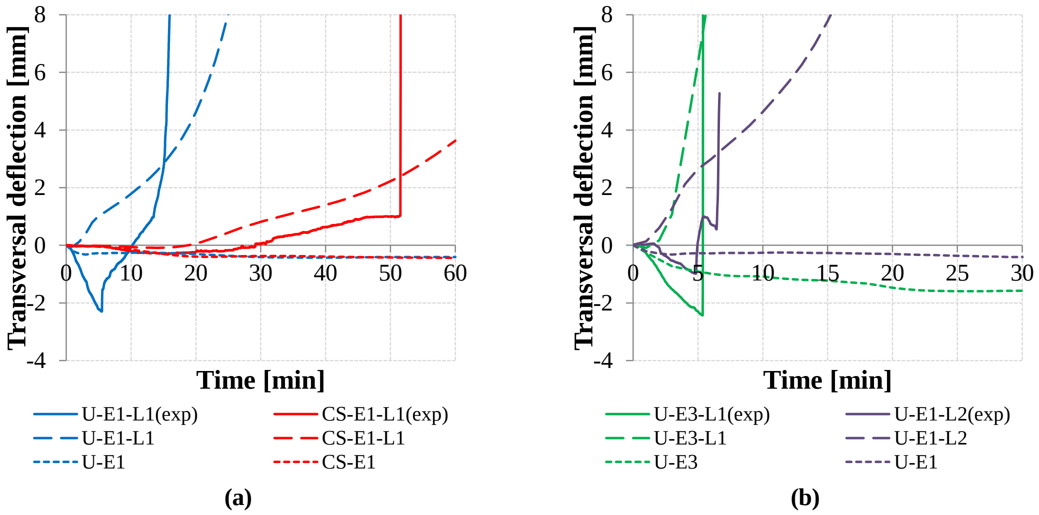

Figure 113: Variation of transversal deflection with fire exposure time for columns (a) U-E1-L1/CS-E1-L1 and (b) U-E3-L1/U-E1-L2 – mid-span section.

8.3.3. Stress distribution

In this section, the models were used to study the evolution of stresses with fire exposure time (in practice, not possible to measure in fire tests, especially in walls directly exposed to fire). To achieve this goal, fifteen elements along the height of the mid-span section (see Figure 110) of the GFRP columns were selected and distributed as follows (Figure 114): four elements (P1-P4) at the centre of top flange, seven elements (P5-P11) along the web height and four elements (P12-P15) at the centre of bottom flange. In this section, the stress distribution and its time evolution are described for the reference column U-E1-L1; then, the stress patterns of the reference column U-E1-L1 are compared to those of columns CS-E1-L1, U-E3-L1 and U-E1-L2, to evaluate the influence of fire protection, fire exposure and applied load level, respectively, on their behaviour.

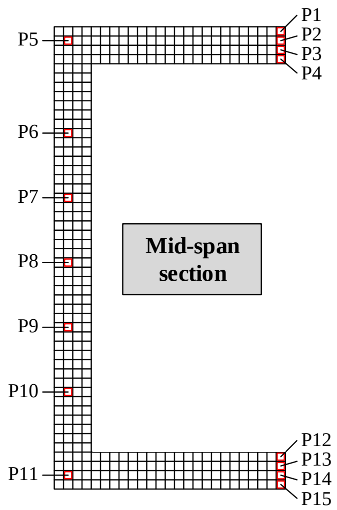

Figure 114: Finite elements (P1-P15) selected for stress distribution analysis – mid-span section.

Unprotected column with one-side fire exposure: U-E1-L1 (reference)

Figure 115 presents the evolution of normal stresses in the longitudinal direction (σ_{11}) of mid-span section of column U-E1-L1 in its top flange (P1-P4, Figure 115(a)), web (P5-P11, Figure 115(b)) and bottom flange (P12-P15, Figure 115(c)). During the first 10 min, a significant reduction in the longitudinal stresses is observed in the bottom flange (P12-P15), which was caused by the rise of temperature. Consequently, σ_{11} stresses increased in the web (P6-P10), particularly in its lower part, due to the axial stiffness reduction of the bottom flange – the exception is P11, whose σ_{11} curve is similar to those observed in the bottom flange (P12-P15). It was also observed a slight increase in longitudinal stresses acting on the top flange (P1-P4), namely the inner layer (P4), although this increase was considerably lower than that registered in the web.

After that initial period, the longitudinal stresses remained approximately unaltered in the bottom flange (~1.0-9.0 MPa), while they presented a slight decrease (between 10-25 min) at top flange (particularly in P3-P4). In parallel, the rise of temperature at the webs caused a progressive stiffness reduction and, consequently, a decrease in longitudinal stresses (see Figure 115). Then, an increase of the longitudinal stresses in the inner layer of the bottom flange (P12) was observed, most likely due to axial stiffness reduction of the top flange. The increase of this localized stress in the bottom flange was closely related to the temperature at element P12, which was significantly lower than those registered at elements P13-P15[13]. According to the numerical results, a clear stress reduction occurred in the top flange as a result of the temperature increase in the overall cross-section. Similarly, the longitudinal stresses in the upper part (P6-P8) of the webs started decreasing due to temperature increase, thus causing an increase of σ_{11} stresses in the web lower part (P9-P10).

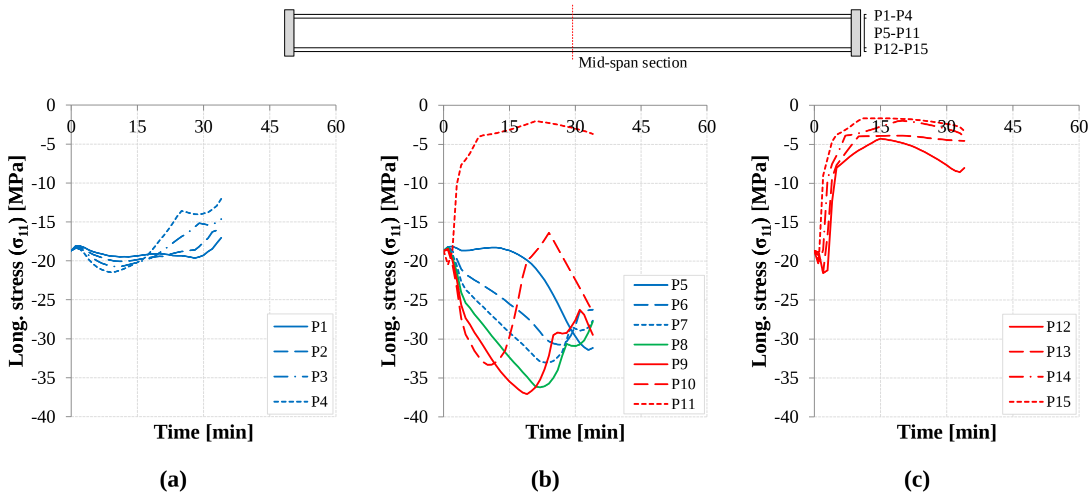

Figure 115: Evolution of longitudinal stresses (σ_{11}) in column U-E1-L1 at (a) top flange (P1-P4), (b) web (P5-P11) and (c) bottom flange (P12-P15) – mid-span section.

Generally speaking, it can be stated that longitudinal stresses in the webs increased significantly due to the quick drop of bottom flange axial stiffness in the first 10 min. After that, it can be seen that the progressive heating of the cross-sections caused huge stress variations: all curves (except P5 and P11) display local minima, which denotes a certain stress transfer between the several points of the web along its height. The material thermal expansion, considered in the numerical models, also influences moderately the evolution of longitudinal stresses, especially in the initial period (~10 min).

Figure 116 presents the evolution of normal stresses in the transversal direction (σ_{22}) of mid-span section of column U-E1-L1 in its top flange (P1-P4, Figure 116(a)), web (P5-P11,

[13] For instance, after 30 min of fire exposure, the numerical temperatures at elements P12, P13, P14 and P15 are 411, 512, 624 and 747 °C, respectively.

Figure 116(b)) and bottom flange (P12-P15, Figure 116(c)). Although being null at the onset of fire exposure, the transversal stresses increased in the first 3 min, particularly in the bottom flange. In this flange, tensile (P12, P13) and compressive (P14, P15) stresses were observed as a result of the considerable temperature gradients imposed, which tended to zero after that initial period (*cf*. Figure 116(c)). Additionally, the variation of the web transversal stresses is small and the minor compressive stresses (lower than 1.0 MPa) tend to zero. With the exception of P1 and after an initial insignificant variation, the σ_{22} stresses in the top flange tend to uniform values associated to through-thickness stress gradient (tension in P1-P2 and compression in P3-P4). Taking into account these results, it can be stated that transversal stresses developed particularly in the bottom flange, but these were expectedly much lower than the longitudinal stresses (see Figure 115) because of the 1D nature of column behaviour.

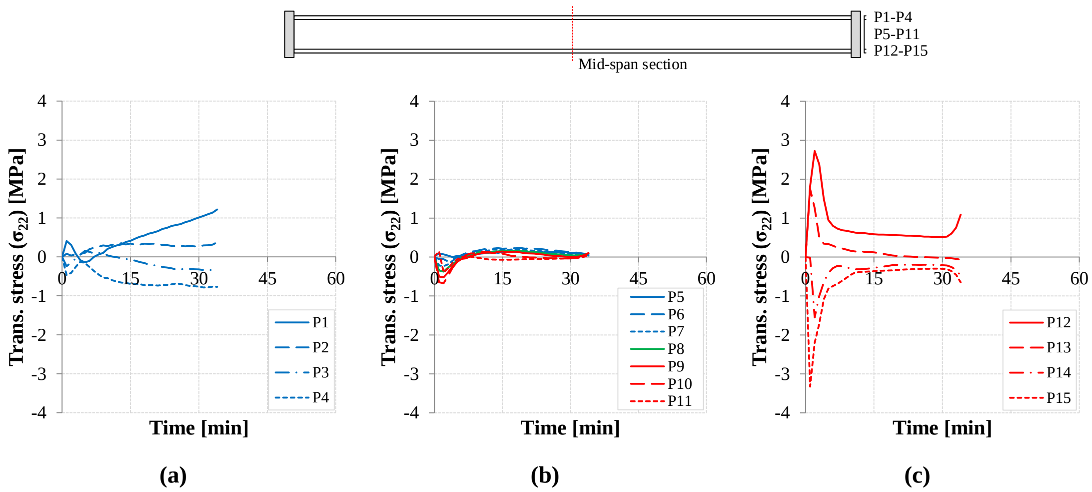

Figure 116: Evolution of transversal stresses (σ_{22}) in column U-E1-L1 at (a) top flange (P1-P4), (b) web (P5-P11) and (c) bottom flange (P12-P15) – mid-span section.

Figure 117 presents the time evolution of shear stresses (σ_{12}) in the web (P5-P11)[14] of column U-E1-L1. Considering the variation of σ_{12} stresses with fire exposure time, it can be stated that a gradual increase was observed as a result of transversal deflection, which was caused by temperature increase and thermal degradation of the mechanical properties (particularly in the lower part of cross-section). Because the columns deflected upwards (moving away from the oven) due to the progressive loss of axial stiffness in the bottom flange, the shear stresses expectedly increased in the web.

[14] The stress evolutions in both top (P1-P4) and bottom (P12-P15) flanges are not shown herein because they are meaningless (nearly null for the entire duration of numerical simulations).

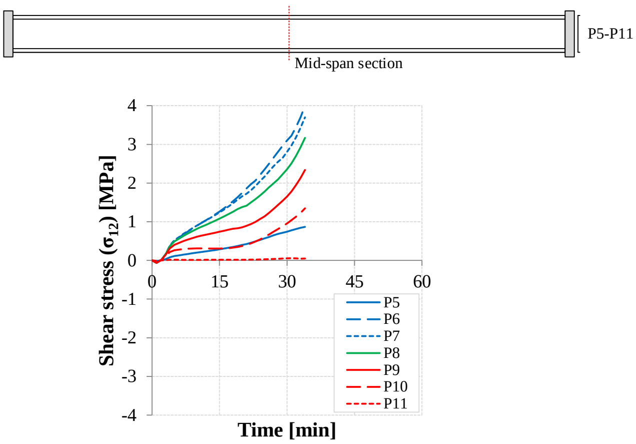

Figure 117: Shear stresses (σ_{12}) in column U-E1-L1 at web (P5-P11) – mid-span section.

Effect of fire protection: CS-E1-L1 *vs.* U-E1-L1

Aiming at studying the effect of fire protection on the evolution of stress distributions, the numerical results obtained for one-side exposed columns U-E1-L1 and CS-E1-L1 (unprotected and protected with CS boards, respectively) are compared. In Figure 118(a), the evolution of longitudinal stresses (σ_{11}) along the web's height (y) of columns U-E1-L1 and CS-E1-L1 is presented. Initially (t = 0 min), the longitudinal stress diagram is uniform (σ_{11} = 18.7 MPa) in both columns. After 15 min of fire exposure, longitudinal stresses in column U-E1-L1 (i) decreased significantly near the bottom flange (P11) due to rapid increase of temperatures, (ii) increased considerably in the central part of web (P6-P10) as a consequence of axial stiffness loss at the bottom flange, and (iii) remained approximately uniform near the top flange (P5). In opposition, longitudinal stress diagram in column CS-E1-L1 remained approximately uniform (*cf.* Figure 118(a)) for t = 15 min.

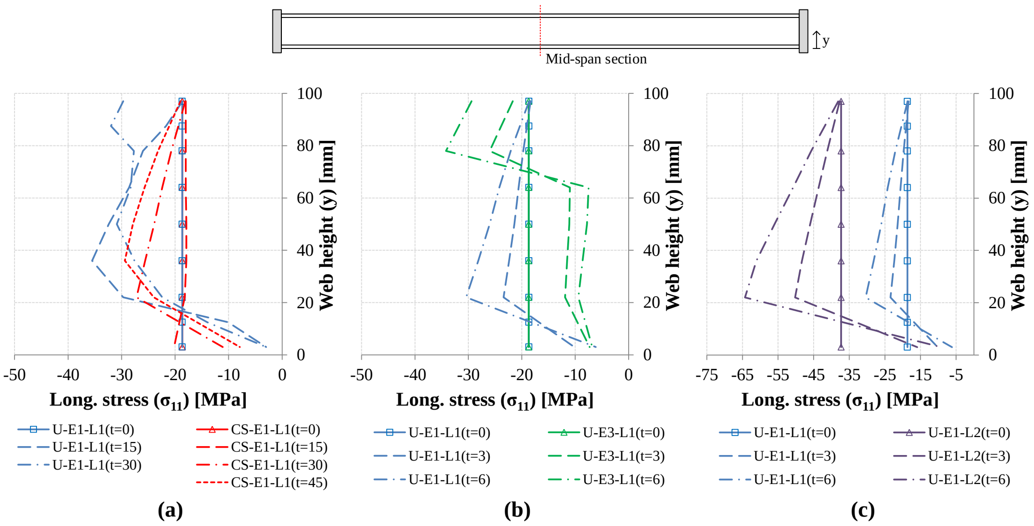

Figure 118: Comparison of longitudinal (σ_{11}) stresses evolution (a) for columns U-E1-L1/CS-E1-L1 (at 0, 15, 30 and 45 min), (b) for columns U-E1-L1/U-E3-L1 (at 0, 3 and 6 min) and (c) U-E1-L1/U-E1-L2 (at 0, 3 and 6 min) – mid-span section.

Effect of type of fire exposure: U-E3-L1 *vs*. U-E1-L1

With the purpose of evaluating the influence of the type of fire exposure on the GFRP columns response, Figure 118(b) shows the evolution of longitudinal stresses (σ_{11}) along the profile's height (y) of columns with one-side (U-E1-L1) and three-side (U-E3-L1) fire exposures.

In column U-E3-L1, the shape of longitudinal stress diagram change from uniform to a highly nonlinear one after only 3 min of fire exposure. In comparison with column U-E1-L1, the longitudinal stresses at a significant part of web/bottom flange (P7-P11) decreased due to axial stiffness reduction in this zone associated to the rapid increase of temperatures across the tubular section. In parallel, the high stresses migrate to the upper part of web/top flange (P5-P6), which is the less heated zone. With the evolution of time exposure, this stress pattern amplifies (in Figure 118(b), see the stress distribution after 6 min). The fire exposure also influences the neutral axis position: the web neutral axis is located very close to the bottom flange in column U-E1-L1 (one-side exposure) but nearer the top flange in column U-E3-L1 (three-side exposure). However, it is seen that the maximum compressive stress level (23-25 MPa for t = 3 min, 30-33 MPa for t = 6 min) is not influenced by the type of fire exposure.

Effect of load level: U-E1-L2 *vs*. U-E1-L1

In order to assess the effect of the applied load level on the GFRP columns response, Figure 118(c) shows the evolution of longitudinal stresses (σ_{11}) along the profile's height (y) of columns under compressive loads of 6.7% (U-E1-L1) and 13.4% (U-E1-L2) of room temperature axial strength.

The shape of the longitudinal stress diagram in column U-E1-L2 (*cf*. Figure 118(c)) was similar to that of the reference column (U-E1-L1), while the stress magnitudes were very dissimilar. As a consequence of load level increase, higher initial stresses were observed (37.3 MPa, instead of 18.7 MPa), as expected. The longitudinal stresses (i) increased significantly in the web (in particular, at element P10) due to the temperature increase in the lower part of profile, (ii) decreased near the bottom flange (P11) for the same reason, and (iii) remained almost constant at the upper part of profile (P5). Also, it should be noted that the mentioned stress concentration at P10, where σ_{11} stresses increased from 37.3 to 64.3 MPa, might explain the premature failure (9 min) observed in column U-E1-L2. In resume, as expected, the applied load level influences a lot the magnitude of longitudinal stresses, but does not affect the position of neutral axis and the shape of the stress diagram.

8.3.4. Initial failure: Tsai-Hill criterion

In order to investigate the initial failure of GFRP columns under fire action and to better understand some of the experimental results, the Tsai-Hill failure criterion [62] was implemented in the time-dependent models, as described in section 8.2.2. Herein, the time evolutions of Tsai-Hill failure index and residual section index are presented and discussed.

Tsai-Hill index and stress ratios: reference column (U-E1-L1)

As shown in Eq. (15), the expression of Tsai-Hill index comprises four terms hereafter designated by quadratic stress ratios $(\sigma/\sigma_u)^2$ for (i) longitudinal stresses $(\sigma_{11}/\sigma_{u,11})^2$, (ii) transversal stresses $(\sigma_{22}/\sigma_{u,22})^2$, (iii) shear stresses $(\sigma_{12}/\sigma_{u,12})^2$, and (iv) combined longitudinal-transversal stresses $\sigma_{11}\sigma_{22}/(\sigma_{u,11})^2$. Thus, the Tsai-Hill index enables the identification of the stress components that contribute the most to the initial failure of the columns. Again, the analysis was started with the unprotected and one-side exposed column (U-E1-L1). Figure 119 (top and bottom flange) and Figure 120 (web) depict the time evolution of these ratios and Tsai-Hill index (I_F) for column U-E1-L1.

From the observation of Figure 119 and Figure 120, it may be clearly stated that the longitudinal stresses (σ_{11}) were the most influential to failure index as the (blue) curves always precede the other stress curves, in terms of time evolution. Regarding the evolution of Tsai-Hill index in flanges (I_F – black curves in Figure 119), it is clear that the bottom flange initial failure ($I_F = 1.0$ at P13-P14) occurred for $t = 3$ min (well before experimental collapse), while the top flange initial failure did not occur during the simulation ($I_F \approx 0.6$ at P2-P3, after 34 min of fire exposure). Concerning the evolution of Tsai-Hill index in the web (I_F – black curves in Figure 120), it is also evident that the web initial failure occurred in its bottom part ($I_F = 1.0$ at P11) for $t = 3$ min (well before experimental collapse), while the web initial failure occurred in its middle part ($I_F = 1.0$ at P8) for $t = 27$ min (after experimental collapse) and in its top part it did not occur during the simulation ($I_F \approx 0.2$ at P5, after 34 min of fire exposure). Thus, it can be stated that column's collapse was triggered by the initial failure of bottom flange and bottom part of the web, mostly due to longitudinal stresses (σ_{11} – blue curves) and lesser to transversal stresses (σ_{22} – green curves) and interaction between them ($\sigma_{11}\sigma_{22}$ – light green curves). This predicted and initial failure mode is consistent with the observed experiments.

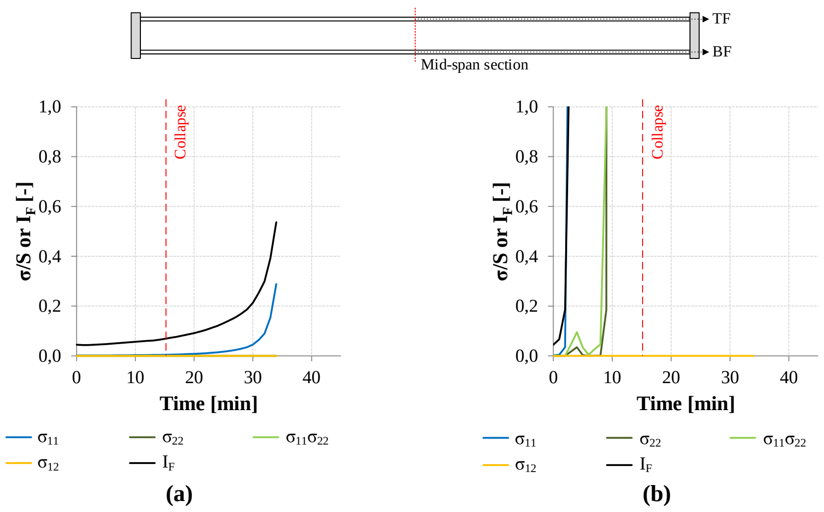

Figure 119: Stress ratios (σ/σ_u) and Tsai-Hill index (I_F) evolution in the flanges of column U-E1-L1 at: (a) P2-P3 (TF) and (b) P13-P14 (BF) – mid-span section.

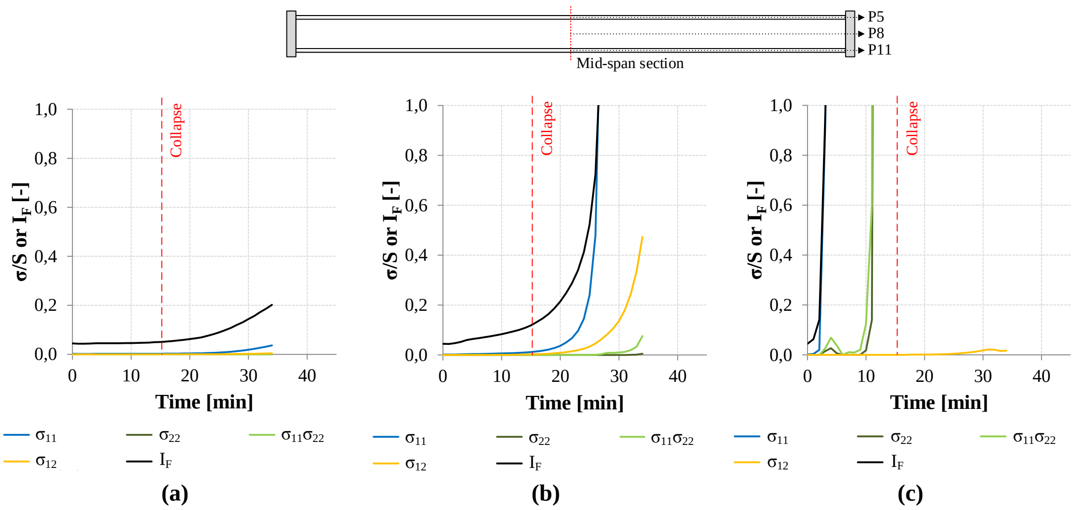

Figure 120: Stress ratios (σ/σ_u) and Tsai-Hill index (I_F) evolution in the web of column U-E1-L1 at: (a) P5, (b) P8 and (c) P11 – mid-span section.

Tsai-Hill index: all columns

In order to compare the numerical results obtained from the different time-dependent models and to predict the columns' initial failure, the variation of Tsai-Hill index (I_F) at the middle of top flange (TF – P2-P3), web (W – P8) and bottom flange (BF – P13-P14) with fire exposure time is presented in Figure 121.

The initial failure mode of column U-E1-L1 predicted by Tsai-Hill criterion (failure of bottom flange and bottom part of the web) was partially observed in the protected column (CS-E1-L1), in which the initial failure occurred in the bottom flange (I_F = 1.0 at P13-P14) for t = 27 min (well before experimental collapse), while the web initial failure did not occur during the simulation ($I_F \approx 0.24$ at P8, after 60 min of fire exposure).

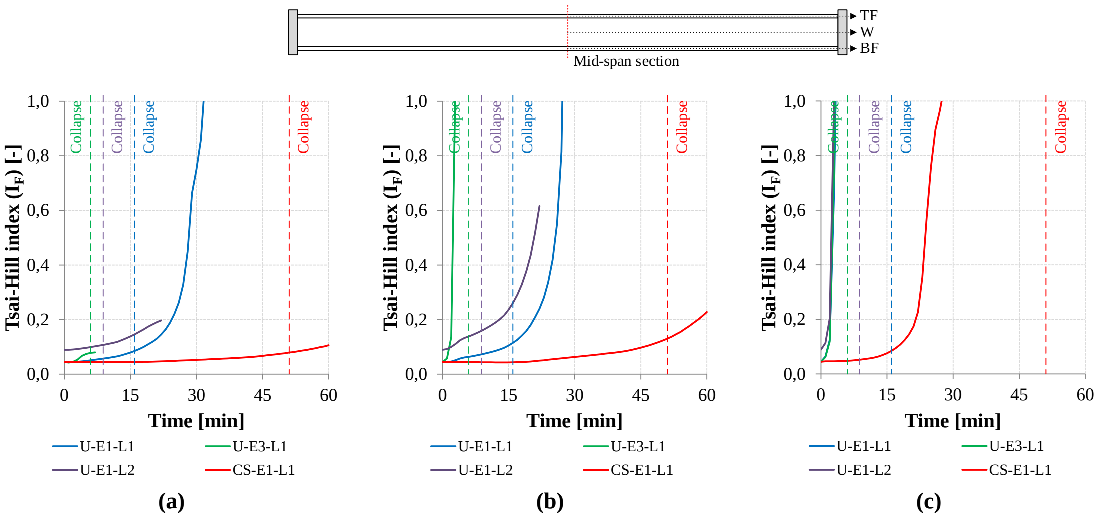

Figure 121: Comparison of Tsai-Hill index (I_F) evolution at (a) top flange (P2-P3), (b) web (P8) and (c) bottom flange (P13-P14) for all columns – mid-span section.

As expected, the results shown above indicate that the Tsai-Hill criterion provided conservative estimates of the fire resistance of all GFRP columns. This is explained by the fact that this criterion only considers the stress interaction and does not take into account the material stiffness degradation when $I_F > 1.0$.

Residual section index

With the purpose of predicting the collapse of columns, the residual section index (I_R) was also calculated. It is defined as the ratio between the area of each part (top flange, web, bottom flange) of the tubular section that remained with the Tsai-Hill index below the unit value ($I_F < 1.0$) and the corresponding total area of that part. This index was determined using Eq. (16) – *cf*. section 7.3.3.

Figure 122 presents the evolution of residual section index (I_R) with fire exposure time, contributing for a better understanding of columns' failure. According to this index and considering the experimental fire resistances, the following conclusions can be drawn: (i) columns U-E1-L1 and CS-E1-L1 collapsed due to bottom flange failure (I_R = 0%) and to partial web failure ($I_R \approx$ 85%); (ii) collapse of column U-E3-L1 (three-side exposed) was caused by bottom flange failure (I_R = 0%), as well as web failure (I_R = 18%); and (iii) column U-E1-L2 (subjected to the load level increase) collapsed due to bottom flange failure only (I_R = 0%). It should be noted that these conclusions are in agreement with those previously mentioned, as well as with those observed in the experimental campaign (chapter 5).

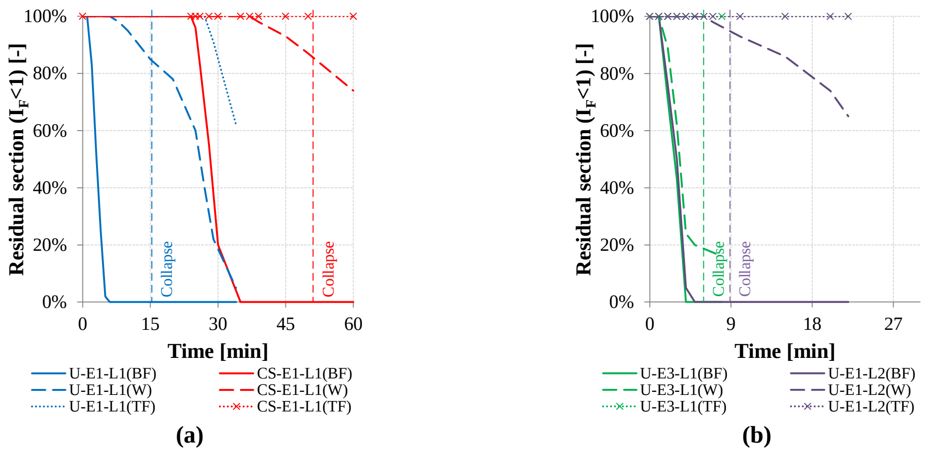

Figure 122: Residual section ($I_F < 1$) evolution at top flange (TF), web (W) and bottom flange (BF) of (a) columns U-E1-L1/CS-E1-L1 and (b) columns U-E3-L1/U-E1-L2 – mid-span section.

8.3.5. Progressive failure: Hashin damage criterion

The results shown previously were not affected by the stress level in each point of the columns, even if these were above the GFRP material's strengths. Using now the fifth model (U-E1-LV), which had an experimental failure after 16 min of fire exposure, it will be possible to perform an incremental analysis considering the mechanical properties at t = 16 min and use the Hashin damage criterion to identify the progressive damage and collapse of the reference column. The results of this analysis are presented in Figure 123, Figure 124 and Figure 125. Figure 123 shows the variation of compressive load and the axial shortening. From the observation of this figure, it may be concluded that (i) linear elastic behaviour is found for compressive load up to 27.1 kN (for which initial damage occurred at the interface between the exposed and unexposed parts of the column – point I), (ii) axial stiffness reduction was observed beyond this load (nonlinear behaviour), (iii) initial damage occurred at the bottom flange for the load of 76.4 kN (point II), and (iv) collapse of the column took place for the peak load of 88.4 kN (point III).

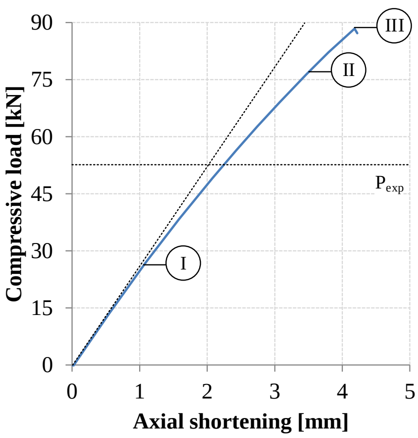

I — Initial damage at the interface between exposed (T) and unexposed (T/2) parts

II — Initial damage at the bottom flange

III — Collapse of column U-E1-LV (peak load)

P_{exp}	55.0 kN	
P_{num} (I)	27.1 kN	
P_{num} (II)	76.4 kN	(+39% P_{exp})
P_{num} (III)	88.4 kN	(+61% P_{exp})

Figure 123: Compressive load *vs.* axial shortening curve obtained from the nonlinear analysis (using Hashin damage criterion) in column U-E1-LV at failure (t = 16 min).

According to the four failure modes of Hashin's criterion (see Eqs. (18)-(21)), the collapse of column U-E1-LV occurred due to fibre compression. Although the failures by matrix compression and matrix tension also appeared in some regions of the web, they may be neglected when compared to the fibre compression failure. Therefore, the evolution of longitudinal compressive damage is presented in Figure 124 for the three load levels depicted in Figure 123 (I, II and III). In Figure 124, the longitudinal compressive damage[15] is shown at three different load levels: (I) the initial damage (P = 27.1 kN), (II) the bottom flange initial damage (P = 76.4 kN) and (III) the column collapse (P = 88.4 kN). Figure 125 shows the variation of longitudinal (Figure 125(a)) and transversal (Figure 125(b)) stresses at bottom flange (P12-P15) with the axial shortening of column U-E1-LV.

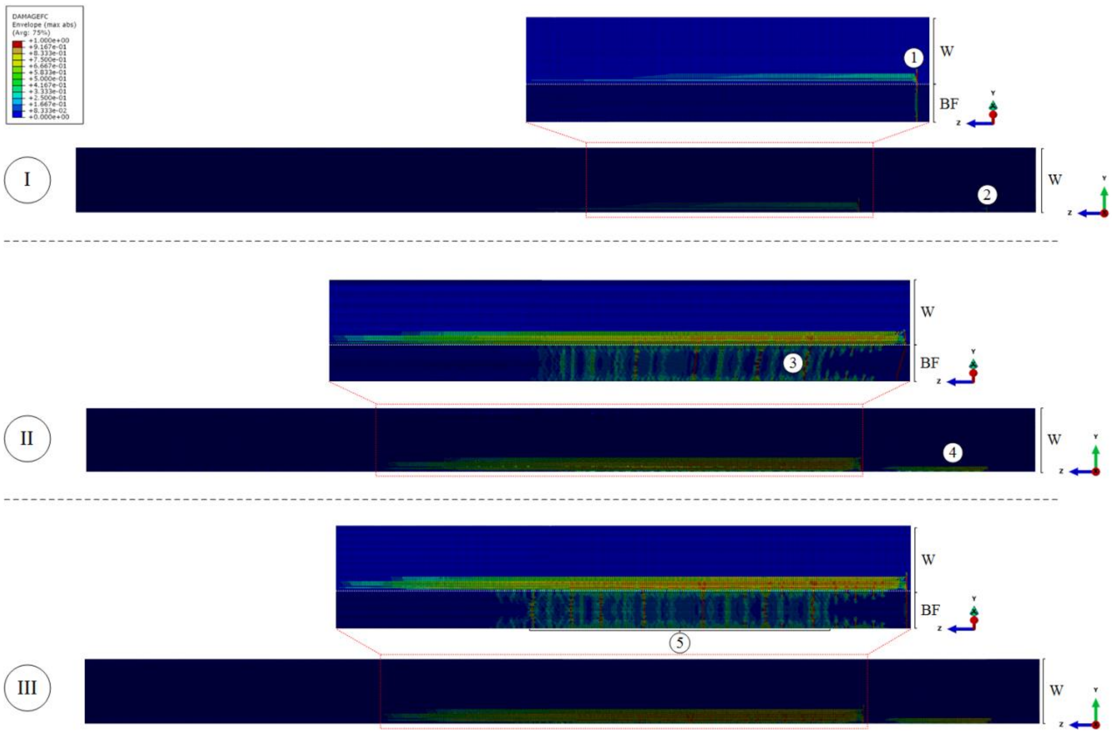

Figure 124: Longitudinal compressive damaged zones in column U-E1-LV for different load levels ("I", "II" and "III").

For load level I, longitudinal compressive damage (region (1)) was observed at the interface between "exposed part" and "unexposed part" (previously indicated in Figure 110). The stress concentration in this zone was caused by the discontinuity in the material mechanical properties between "exposed" and "unexposed" parts. Longitudinal compressive damage was also observed at the interface between "unexposed part" and "exterior part" (region (2)). Therefore, the referred damage was mainly caused by the longitudinal temperature distribution imposed (*i.e.*, it did not completely reproduce the experiments carried out in this thesis). For the load level I, a progressive decrease in the longitudinal compressive stresses at the bottom flange

[15] Red colour indicates fully damaged points (d = 1.0), while blue colour denotes undamaged ones (d = 0.0).

(elements P12-P15) was observed (*cf.* Figure 125(a)). Simultaneously, transversal tensile stresses progressively increased in the bottom flange, as shown in Figure 125(b). This significant transversal stress gradient developed through the thickness of the bottom flange would certainly cause its delamination, which was observed in the experimental tests but was not considered in the current U-E1-LV. Moreover, the delaminated layers would most likely buckle for low levels of compressive stresses due to their reduced thickness. Thus, it can be stated that the absence of delamination effects in the current model also introduces a virtual stiffening effect that provides fictitious (non-realistic) strength to the column for upper load levels. When the column load attains 76.4 kN, fully damaged elements (red colour, d = 1.0) were observed at the bottom flange, as shown in Figure 124 (in particular, at region (3)). Figure 124 also shows the spread/increase of the damaged areas in region (4). Finally, the collapse of column U-E1-LV occurred when the compressive load reaches 88.4 kN and the longitudinal compressive damage in different zones are presented in region (5) (*cf.* Figure 124).

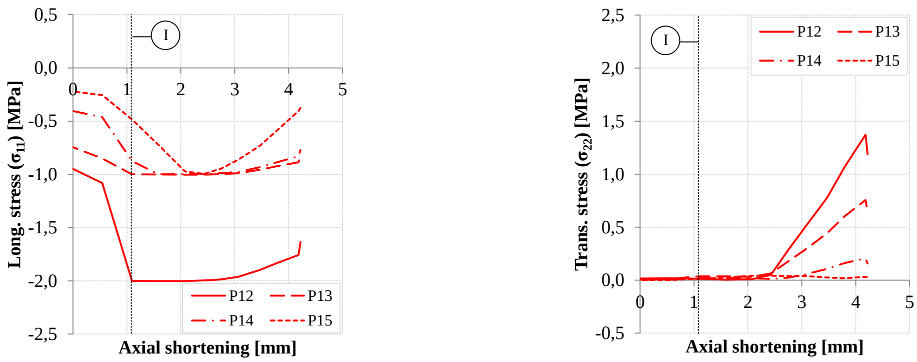

(a) **(b)**

Figure 125: Variation of (a) longitudinal and (b) transversal stresses with axial shortening in the bottom flange (P12-P15) of column U-E1-LV – region (3).

The collapse load in the experimental test was 55 kN, which is 72% of load level II (bottom flange initial damage) and 62% of load level III (column collapse). The 38% difference between experimental and numerical collapse loads is high but considering the plethora of complex phenomena involved and the uncertainty of their associated parameters, it can be affirmed that the model U-E1-LV correctly captures the behavioural aspects of GFRP column under fire exposure. Recall that phenomena like viscoelasticity (creep and time-dependent behaviour) and delamination (through-thickness damage and physical separation) were not considered, which would certainly lower the collapse load predicted by the numerical model. Additionally, the adopted values of fracture energy for GFRP materials are yet uncertain (unavailable in literature) and further studies are needed to obtain reliable data on this parameter. Nevertheless, the model agreed with the experimental results obtained in this thesis, thus confirming (i) the location of failure section (where longitudinal compressive damage at the bottom flange occurred at first – region (3)) and (ii) the cause of failure mode (according to this model, the collapse occurred due to bottom flange compression).

8.4. Conclusions

This chapter presents a numerical investigation on the fire resistance of pultruded GFRP columns, compared and validated against experimental results. This numerical study focused on the evaluation of several effects, such as the use of a fire protection system, the imposition of different fire exposure conditions and the application of distinct load levels. The following conclusions are drawn:

- GFRP columns exposed to elevated temperatures exhibited progressive shortening due to thermal degradation of mechanical properties caused by temperature increase in cross-sections. In opposition to the experimental measurements, where a slight initial elongation was registered in some specimens, the numerical models presented only axial shortening that may have been caused by some uncertainties regarding the thermal expansion coefficient adopted. It should also be noted that the numerical models provided a lower axial deformation rate (in particular, in the protected column) than the experimental tests, and this was probably caused by the non-consideration of the creep phenomenon.

- Regarding the transversal deflection, a movement towards the opposite direction of heating source was observed, which was attributed to the increasing eccentricity of the applied load with respect to the resistant cross-section. However, the numerical results did not follow the experimental ones in the initial stage. The former showed an ascending movement of the columns while the latter exhibited a descending one. Most likely, this behavioural difference was caused by the thermal expansion coefficients considered and was more evident in the unprotected columns (higher thermal gradients).

- The shape of longitudinal stress diagrams changed from uniform (room temperature) to highly nonlinear (fire exposure time). In comparison with the reference column (unprotected, one-side exposed, load level equal to 6.7% of axial strength), the influence of fire protection, type of fire exposure and load level on the column behaviour was different. The calcium silicate protection decreases the magnitude of longitudinal stresses to a reasonable extent, but does not affect too much the position of neutral axis and the shape of the stress diagram. The change from one- to three-side fire exposure influenced hugely the shape of stress diagram and neutral axis position, migrating this from the bottom to the top of the web. However, this fire exposure change did not affect much the maximum compressive stress. The increase in applied load level influenced proportionally the magnitude of longitudinal stresses, but did not affect the position of neutral axis and the stress diagram shape.

- As expected, the Tsai-Hill criterion provided conservative estimates of the fire resistance of all GFRP columns. According to the Tsai-Hill criterion, the initial failure of GFRP columns occurred near the mid-span section, being consistent with the experimental results. As expected, the longitudinal stresses were the most influential to failure index, while transversal and shear stresses were clearly less influential. Taking into account this failure criterion, the one-side exposed columns under an applied load of 6.7% of axial strength (either protected or unprotected) would have collapsed when the entire bottom flange and part of the webs (~15%) reached the limit value of failure criterion. The unprotected column with three-side exposure and applied load level of 6.7% of axial strength would collapse due to bottom flange and web failure, while the unprotected column with one-side exposure with applied load level of 13.4% of axial strength would collapse due to bottom flange failure only. These results were in agreement with those observed in the experiments.

- The strength and collapse mode of reference column (unprotected, one-side exposure, applied load level of 6.7% of axial strength) was also predicted using Hashin damage criterion. The progressive damage analysis overestimated the load capacity of the column. However, it allowed the correct identification of failure location and column collapse mode observed in the experimental tests. Bearing in mind the several intricate phenomena involved but not considered in the current models (creep and viscosity, through-thickness delamination) and the uncertainty of certain parameters (*e.g.*, fracture energies), it can be affirmed that the current models show a good performance and promising potential to predict the complex behaviour of GFRP column under fire exposure. A wealth of additional experimental data will be needed to improve the accuracy of such models.

Part IV:

Conclusions and future developments

Chapter 9:

Conclusions and future developments

9.1. Conclusions

In the last decades, pultruded glass fibre reinforced polymer (GFRP) profiles have been increasingly used in civil engineering applications. When compared to traditional materials (namely steel, reinforced concrete and timber), they present advantages such as high strength, low self-weight, improved durability and reduced maintenance requirements. Despite these advantageous properties, some drawbacks are still hindering the widespread use of pultruded GFRP profiles, namely their high deformability, the susceptibility to buckling phenomena, the occurrence of brittle failure modes, the perceived poor fire behaviour and the lack of widely accepted design codes and guidelines.

The fire behaviour of GFRP profiles in particular – the object of the present thesis – is an issue that has been raising well founded concerns, not only due to the inherent combustibility of the material, but also due to the limited understanding of the complex physico-chemical and mechanical phenomena involved when GFRP materials and structures are exposed to elevated temperature and fire. Despite the efforts made in the past decade to investigate the fire reaction and fire resistance behaviour of GFRP members, when the present work was started the understanding of many aspects was still very limited. This evidence also explains the lack of design guidance in this specific aspect.

In order to obtain further insights about the fire behaviour of pultruded GFRP profiles, experimental and numerical investigations were developed in the framework of this thesis. The experimental programme focused on the characterization of the thermo-physical and thermo-mechanical properties of GFRP material, and on the fire resistance behaviour of GFRP beams and columns. In the numerical investigations, the thermal response of GFRP profiles exposed to fire was simulated, as well as the mechanical response of GFRP beams and columns under fire exposure.

The overall results obtained in this thesis confirm that the fire issue is a matter of concern posing considerable limitations to the use of GFRP profiles in buildings. In order to fulfil the applicable requirements in terms of fire reaction and fire resistance performance, tailored fire protection systems need to be applied and the structural fire design needs to be duly articulated with the architectural design.

The following subsections summarize the main conclusions that can be drawn from the present thesis.

9.1.1. Experimental study

In order to investigate the shear behaviour of pultruded GFRP material at elevated temperatures, in-plane shear tests were performed on small-scale coupons at eight different temperatures (varying from 18 to 180 ºC). The shear tests carried out in the framework of the present thesis confirmed the susceptibility of shear strength and modulus to elevated temperatures. As an example, shear strength and modulus retentions, compared to the values measured at room temperature, are 12% and 22% at 180 ºC, respectively. In fact, even for moderate temperatures (60 ºC), likely to be attained in outdoor applications in certain climates, the shear strength and modulus suffer quite significant reductions of 64% and 69%, respectively. From a qualitative point of view, the variation of shear strength with temperature measured in the present study (from Iosipescu test) was in general agreement with that reported in the literature (from 10º off-axis tensile tests). However, in the present study, the shear strength reduction occurs for lower temperatures, which may be explained by the influence of tensile stresses in the 10º off-axis setup. Finally, it should be noted that the experiments presented herein were the first to report the variation of shear modulus with temperature of pultruded GFRP material (earlier studies addressed only the shear strength).

At a structural level, comprehensive experiments were conducted about the fire behaviour of pultruded GFRP beams and columns with square tubular cross-section, in which both thermal and mechanical responses were investigated.

For one-side fire exposure, all fire protection systems used were effective in delaying the heating of the GFRP material throughout the tubular profile cross-section and, consequently, in improving the fire performance of GFRP beams and columns. Calcium silicate protection was more effective in providing thermal insulation to the bottom flange, while the water-cooling systems (in particular with flowing water) were more effective in protecting the webs and top flange. In GFRP beams, agglomerated cork and rock wool boards were also effective in delaying the heating of the cross-section. These three passive fire protection systems improved considerably the fire performance of GFRP beams, with fire resistance increasing from 36 min (unprotected beam) to 75-83 min (protected beams). Regarding the water-cooling protection, it proved to be the most effective solution, since the beam protected with this active system did not collapse even after 120 min of fire exposure, which is consistent with previous works reported in the literature. Similar results were also observed in the fire resistance tests performed on GFRP columns, in which the fire endurance was increased from 16 min (without protection) to 51 min (with passive protection) and more than 120 min (with water-cooling).

Results obtained show that the fire behaviour of pultruded GFRP beams and columns is severely affected by the number of sides exposed to fire. For three-side exposure, the temperatures in the top flange and particularly in the webs (now directly exposed to fire) suffered a substantial increase compared to one-side exposure. Consequently, the fire resistance of unprotected beams suffered a drastic reduction, from 36 min (one-side exposure) to about 8 min; the same occurred with unprotected columns, whose fire resistance was reduced from 16 min (one-side exposure) to 5 min. Once more, the calcium silicate protection slowed down considerably the temperature increase across the profile's cross-section, allowing to increase the fire endurance of both beams and columns (compared to unprotected members), respectively five (beams) and seven (columns) times. Indeed, calcium silicate protection provided the best fire performance for three-side exposure. However, now the 60 min threshold was not attained in none of the types of structural members. For three-side fire exposure, it should also be noted that the efficacy of the water-cooling system used in the beams (a thin layer of water running over the bottom flange) was drastically affected; since it did not provide any fire protection to the webs (which were now directly exposed to fire), these section walls presented premature failure. The efficacy of the water-cooling systems used in the GFRP columns (full section) was also remarkably affected, particularly the one with flowing water.

The load level increase caused a moderate reduction of the fire resistance of GFRP beams and columns. In beams, the fire resistance decreased 14%-20% as a result of increasing the load level in 60%. In GFRP columns, a load level increase of 100% caused also a significant decrease in fire resistance (~50-75%). Such results were naturally attributed to the stress level increase in the section walls and to the temperature dependency of the GFRP mechanical properties, which varies according to the stress state. Taking into account the service load levels and the different types of fire exposure tested, it can be stated that the fire resistance of GFRP beams was generally higher than that observed in columns. This is attributed to the higher residual strength in tension at elevated temperature when compared to compression.

In terms of mechanical response during fire exposure, the beams without passive fire protection suffered a rapid increase of mid-span deflection during an initial stage, as a consequence of the stiffness loss of the bottom flange. After that initial period, in general, the deformations increased progressively up to failure. Beams with passive fire protection presented a similar overall response, but the increase of vertical displacements was delayed. In the columns without passive fire protection, a slight axial elongation during an initial period was observed, which was caused by material thermal expansion; subsequently, a progressive axial shortening up to failure was registered, as a result of compressive stiffness decrease. Columns with fire protection also exhibited a progressive axial shortening up to collapse, but such deformations were delayed. In terms of transversal (out-of-plane) deformation, at first, the columns presented a descending movement (towards the heating source) due to the temperature gradients throughout the cross-section height; then, they started presenting an ascending movement, which was caused by the increasing eccentricity of the applied load.

The GFRP beams tested in this experimental campaign collapsed in a brittle manner due to one or more of the following modes: (i) compression (flexural) failure of the top flange, with wrinkling of this section wall; (ii) compressive (vertical) and shear failure of the upper part of the webs (under applied loads), in some cases with material wrinkling; and (iii) shear failure (sinking) of the webs. The fire resistance tests indicate that the failure of pultruded GFRP beams occurs when the glass transition temperature of the GFRP material is approached or exceeded in parts of the section under axial/transversal compression and/or shear.

The structural collapse of GFRP columns occurred due to the formation of a hinge at a cross-section located near the central part of columns, which seems to have been triggered either at the bottom flange (one-side exposure) or at the bottom flange and webs (three-side exposure). At failure, the profiles' walls exhibited a wrinkling type of failure with material crushing and delamination. In some cases, damage at the top flange was also registered, in the form of either cracking or wrinkling. It should also be mentioned that, in general, when failure occurred the average temperature of the section walls had already attained the glass transition temperature or at least the onset glass transition temperature of the GFRP material.

Overall, the results obtained confirm that the fire endurance of pultruded GFRP profiles is a matter of concern for building applications. Although it is possible to extend considerably the fire endurance of GFRP structural members using passive and active fire protection systems, their fire resistance behaviour is strongly dependent on the number of sides exposed to fire. The results obtained in this thesis highlight the interest of integrating/embedding GFRP beams in building floors and of integrating GFRP columns in walls/facades; this architectural option prevents those GFRP members from being exposed to fire in three or four sides.

9.1.2. Numerical and analytical studies

As mentioned, a numerical study about the thermal response of pultruded GFRP profiles was carried out in this thesis with the purpose of investigating in further depth the effects of using different fire protection systems and of different types of fire exposure, and also to develop accurate simulation tools. Besides the results of the experiments conducted in the frame of this thesis, the thermal models were also validated through the simulation of previous fire resistance experiments performed on multicellular panels by Tracy [24].

The finite volume models developed in this thesis confirmed previous findings of López [17] that when GFRP tubular profiles are exposed to fire the heat transfer occurs through conduction, radiation and convection inside the cavities of the cross-section. The numerical results obtained confirmed also that the non-consideration of heat exchanges due to internal radiation and convection affects considerably the evolution of temperatures and provides less accurate temperature predictions (compared to experimental data). Despite the complexity involved in this heat transfer problem and the several assumptions taken into account, the evolution with time of numerical temperatures were in relative good agreement with the data obtained in the experiments.

The numerical models also provided further insights about the effectiveness of the different fire protection systems in delaying the heating of GFRP tubular profiles and multicellular panels. For one-side fire exposure, the numerical results confirmed the higher efficacy of water-cooling in delaying the temperature increase at webs and top flanges and the higher efficacy of calcium silicate in providing thermal insulation to the bottom flange. The numerical models confirmed also the remarkable reduction of the efficacy of water-cooling system for three-side exposure. In this case, the passive fire protection provided more thermal insulation, which is also in agreement with the experimental results. Compared to one-side exposure, three-side exposure involves a much faster temperature increase in the webs and top flange.

After simulating the thermal response of pultruded GFRP profiles exposed to elevated temperatures, numerical (finite element) and analytical (beam theory) models were developed in order to simulate the mechanical response of beams exposed to fire. Similarly, numerical (finite element) models were developed to simulate the mechanical response in fire of pultruded GFRP columns. These numerical investigations provided interesting insights about the most relevant *kinematic* (deflections) and *static* (stresses) issues involved in the mechanical response of those structural members, thus complementing the experiments.

The analytical and numerical results obtained show that the thermal expansion coefficient affects considerably the mechanical response of GFRP beams, which is in line with other works previously reported in the literature. In particular, such effect is more noticeable in unprotected beams during an initial period, when they are exposed to higher thermal gradients in the cross-section. In opposition, such effect proved to be much less relevant in the columns' mechanical response.

The numerical and analytical results obtained for beams presented a general good agreement with the experimental data. With the exception of the unprotected beam exposed to fire in three sides, the numerical models developed were able to simulate the fire behaviour of GFRP beams, presenting accurate predictions of the evolution of mid-span deflection with time. The analytical models also provided good agreement with the experimental data, although various simplifying assumptions were considered.

The numerical models of the GFRP columns simulated the progressive axial shortening behaviour under exposure to elevated temperature, as a result of the axial stiffness decrease and thermal degradation of mechanical properties. However, unlike the test data, none of the models depicted an initial axial elongation (registered in some of the columns tested). It should also be noted that the numerical models retrieved lower axial deformation rates (in particular, in the protected column), when compared to the experiments; this difference was attributed to the non-consideration of the creep phenomenon in the models. Regarding the transversal deformation, a progressive ascending movement (away from the heating source) was simulated, which was attributed to the increasing eccentricity of the applied load. The models did not reproduce the (limited) descending movement observed at the first stage of some tests, which had been ascribed to the temperature gradient installed in the cross-section and thermal expansion effects.

Regarding the stress analysis of GFRP beams, the numerical models showed that the linear longitudinal stress diagram initially observed becomes highly nonlinear as a result of the heating process, presenting stress concentrations at (i) both top and bottom parts of the web for one-side exposed beams, and (ii) top part of the cross-section for three-side exposed beams. In the protected beams, although this behaviour was less evident, the mentioned nonlinearity was also observed.

The shear stress diagram in GFRP beams was asymmetric with respect to the web centre as a result of stress concentrations at the top of the profile and shear deformation effect. For one-side fire exposure, its shape remained qualitatively the same, regardless of the time of fire exposure and the application of fire protection. On the other hand, for three-side fire exposure, shear stresses (i) decreased in the web during an initial period due to the direct fire exposure of this section wall, and (ii) increased in the web after that initial period of fire exposure as a consequence of the heating of the top flange.

The numerical models showed also that the transversal stresses developed in the GFRP beams were almost negligible, compared to longitudinal and shear ones. Only in the sections below the bearing plates, transversal stresses developed in the top flange and web of the unprotected beam due to the sharp corner of the plate; these stresses were not significantly affected by the heating of the cross-section. In the remaining sections, such concentration of transversal stresses was not observed in the top flange and webs. In opposition, transversal stresses were developed in the bottom flange along the exposed length, which were caused by thermal expansion effects.

In what concerns the stress analysis of GFRP columns, uniform stress fields were observed in the columns at room temperature, presenting (relatively) high longitudinal stresses and null transversal and shear ones, as expected. The longitudinal stresses across the profile's height became highly nonlinear as a result of the beginning of fire exposure. While the one-side exposed columns presented a stress concentration at the lower part of web (caused by the reduction of compressive modulus at the bottom flange), the three-side exposed columns presented a stress increase at the upper part of the webs and top flange (caused by the axial stiffness reduction at the bottom flange and also at a significant part of webs). It should also be noted that transversal stresses were irrelevant and that shear stresses increased slightly due to transversal deformation.

In the numerical investigations of both GFRP beams and columns, the Tsai-Hill failure (initiation) criterion was used with the purpose of identifying the zones of GFRP profiles that were more sensitive to failure when exposed to fire. According to the numerical results obtained, the collapse of GFRP beams was caused by top flange and webs (top part) failure, which was generally consistent with experimental failure modes observed. In opposition, for three-side fire exposure, the collapse of the unprotected beam occurred due to bottom flange and webs failure, which was not entirely in agreement with the experimental observations (webs failure). Regarding the load level increase, the failure criterion used was not able to accurately capture the influence of the load level on the fire resistance of GFRP beams, which may be explained by (i) inaccuracy of the thermo-mechanical properties considered; (ii) small difference between compressive loads used; and (iii) non-consideration of material damage.

According to the Tsai-Hill failure criterion, the failure of GFRP columns would occur near the central section. In this case, the longitudinal stresses were the most influential to the failure index, while transversal and shear stresses were clearly less prominent, as expected. The one-side exposed columns were predicted to collapse mainly due to compressive failure of the bottom flange, while the collapse of three-side exposed columns was predicted to be due to webs and bottom flange failure. These results were in agreement with those observed in the experiments. The Tsai-Hill failure analysis did not allow to determine with accuracy the fire resistance of pultruded GFRP beams and columns, as it does not include progressive material damage. However, it provided interesting insights about the failure mechanisms observed in the fire resistance tests.

For the simulation of the GFRP columns, the Hashin damage initiation criterion was also considered in the numerical models together with a damage progression law in order to estimate the maximum load (strength) of a reference column, unprotected and under one-side fire exposure. This preliminary progressive damage analysis (in which fracture energy values had to be assumed) overestimated (by about 60%) the load capacity of the GFRP column at failure (such overestimation was attributed to the uncertainty regarding the fracture energy values at elevated temperature). However, it allowed confirming the location of the failure section and it did reproduce the failure mode observed in the experimental work.

As discussed in the thesis, there are still several uncertainties regarding the numerical and analytical simulation of the fire behaviour of GFRP structural members, mostly concerned with the material properties needed as input, such as (i) the variation of thermo-physical properties with temperature (*e.g.*, the thermal expansion coefficient); (ii) the variation of mechanical properties with temperature, especially for temperatures above the decomposition temperature of the polymer matrix; (iii) creep, which was not considered in these simulations; (iv) delamination; and (v) the definition of failure criteria and damage propagation at elevated temperature. In addition, in the present study, there were also some uncertainties about the thermal and mechanical boundary conditions used in the experiments. Despite these uncertainties, it may be stated that the mechanical response of pultruded GFRP beams and columns exposed to fire was successfully simulated, especially taking into account the complexity of the problem.

9.2. Recommendations for future developments

The experimental and numerical studies presented in this thesis provided a better understanding of the fire behaviour of pultruded GFRP beams and columns. However, many issues remain open and need to be investigated in further depth. In this section, the current research needs and recommendations for future investigations in this field are highlighted.

9.2.1. Experimental investigations

In what concerns the fire behaviour of pultruded GFRP profiles, further experimental research should focus on the following topics:

- Characterization of the thermo-physical properties (specific heat, thermal conductivity, emissivity) at elevated temperature;
- Full characterization of the mechanical properties (in compression, tension and shear, in different directions) at elevated temperature, especially for temperatures above the decomposition temperature of the polymer matrix; it is particularly relevant to assess the compressive behaviour of GFRP material at elevated temperature, namely the variation of the compressive modulus with temperature;
- Characterization of the creep behaviour (in compression, tension and shear) at elevated temperature;
- Characterization of the thermal expansion coefficient (in different directions) as a function of temperature;
- Development of test methods to determine intralaminar fracture energy of pultruded GFRP material, not only at room temperature but also at elevated temperatures;

- Characterization of thermo-physical properties of materials used in passive fire protection systems;
- Development of new fire protection solutions, more adapted to pultruded GFRP members, possibly directly incorporated in the pultrusion process;
- Performing further fire resistance tests on GFRP profiles and panels, measuring the temperature distribution along their length and the material strains during fire exposure;
- Characterization of the mechanical behaviour of bolted and bonded connections between GFRP structures at elevated temperature and under fire exposure.

9.2.2. Numerical and analytical investigations

As a result of the numerical study developed in the framework of this thesis, the following topics should be investigated in further depth:

- Development of three-dimensional thermal models to simulate the thermal response of GFRP profiles and panels exposed to fire, considering as input the full set of temperature-dependent thermo-physical properties referred in the preceding subsection;
- Simulation of the mechanical behaviour of pultruded GFRP structural members considering (i) the above mentioned thermo-mechanical properties, (ii) the (potential) mechanical contribution of fire protection materials, (iii) the variation of thermal expansion coefficient with temperature, (iv) the creep behaviour at elevated temperature, and (v) delamination under compression;
- Implementation of appropriate damage criteria for pultruded GFRP material at elevated temperature, which should provide more accurate predictions of the fire resistance of structural members; such more advanced failure criteria should consider damage propagation and stress redistribution;
- Optimization of the fire performance of GFRP members, namely through the definition of new structural shapes with a cross-section geometry better suited to resist fire;
- Optimization of existing and development of new fire protection solutions that allow improving the fire endurance of GFRP members;
- Development of new analytical formulas to design pultruded GFRP structures under fire. These formulae should be calibrated against a large data set of experimental results, which include those presented in this thesis. This task will be of paramount relevance in the proposal of the first generation of design codes.

References

[1] J.P. Busel, J.D. Lockwood, *Product selection guide: FRP composite products for bridge application*, The market development alliance of the FRP composites industry, Harrison, NY, 2000.

[2] J.R. Correia, *Fibre-reinforced polymer (FRP) composites*, in Materials for Construction and Civil Engineering (Editors: M.C. Gonçalves, F. Margarido), Materials for Construction and Civil Engineering: Science, Processing, and Design, Springer, Dordrecht, 2015.

[3] J.R. Correia, *GFRP Pultruded Profiles in Civil Engineering: Hybrid Solutions, Bonded Connections and Fire Behaviour*, PhD Thesis in Civil Engineering, IST, Technical University of Lisbon, 2008.

[4] J.R. Correia, M.M. Gomes, J.M. Pires, F.A. Branco, Mechanical behaviour of pultruded glass fibre reinforced polymer composites at elevated temperature: Experiments and model assessment, *Composite Structures*, 98, 303-313, 2013.

[5] A.P. Mouritz, A.G. Gibson, *Fire Properties of Polymer Composite Materials*, Springer Netherlands, 2006.

[6] J.R. Correia, Y. Bai, T. Keller, A review of the fire behaviour of pultruded GFRP structural profiles for civil engineering applications, *Composite Structures*, 127, 267-287, 2015.

[7] J.J. Massot, Glass Reinforced Plastics Heavy Load Flooring for Offshore Platforms, *in Proceedings of Composite Materials in the Offshore Industry*, Institut Français du Pétrole: Rueil-Malmaison, France, 1994.

[8] T. Keller, C. Tracy, E. Hugi, Fire endurance of loaded and liquid-cooled GFRP slabs for construction, *Composites Part A: Applied Science and Manufacturing*, 37(7), 1055-1067, 2006.

[9] C. Ludwig, J. Kippers, E. Hugi, K. Wakili, Thermal and Thermo-Mechanical Investigation of Polyester based Composite Beams, in *Fourth International Conference on FRP Composites in Civil Engineering*, Zurich, 2008.

[10] J.R. Correia, F.A. Branco, J.G. Ferreira, Y. Bai, T. Keller, Fire protection systems for building floors made of pultruded GFRP profiles: Part 1: Experimental investigations, *Composites Part B: Engineering*, 41(8), 617-629, 2010.

[11] Y. Bai, E. Hugi, C. Ludwig, T. Keller, Fire performance of water-cooled GFRP columns. I: fire endurance investigation., *Jounal of Composite for Construction*, 15(3), 404-412, 2011.

[12] T. Morgado, *Fire resistance behaviour of GFRP pultruded profiles (in Portuguese)*, MSc dissertation in Civil Engineering, IST, Technical University of Lisbon, 2012.

[13] International Standards Organization, *Fire resistance tests. Elements of building construction – Part 1: General requirements*, 1999.

[14] Y. Bai, T. Keller, Y. Vallée, Modeling of stiffness of FRP composites under elevated and high temperatures, *Composites Science and Technology*, 68(15–16), 3099-3106, 2008.

[15] Y. Bai, T. Keller, J.R. Correia, F.A. Branco, J.G. Ferreira, Fire protection systems for building floors made of pultruded GFRP profiles – Part 2: Modeling of thermomechanical responses, *Composites Part B: Engineering*, 41(8), 630-636, 2010.

[16] T. Keller, C. Tracy, A. Zhou, Structural response of liquid-cooled GFRP slabs subjected to fire – Part II: Thermo-chemical and thermo-mechanical modeling, *Composites Part A: Applied Science and Manufacturing*, 37(9), 1296-1308, 2006.

[17] C. López, *Numerical modelling of the thermomechanical behaviour of GFRP pultruded profiles subjected to fire*, PhD thesis in Civil Engineering, IST, Technical University of Lisbon, 2016.

[18] ANSYS inc, *Commercial software ANSYS Fluent*, version 14.5, 2012.

[19] Y. Bai, T. Keller, Modelling of mechanical response of FRP composites in fire, *Composites: Part A*, 40, 731-738, 2009.

[20] A.G. Gibson, Y.S. Wu, J.T. Evans, A.P. Mouritz, Laminate theory analysis of composites under load in fire, *Jounal of Composite Materials*, 40(7), 639-658, 2006.

[21] J.V. Bausano, J.J. Lesko, S.W. Case, Composite life under sustained compression and one sided simulated fire exposure: Characterization and prediction, *Composites Part A: Applied Science and Manufacturing*, 37(7), 1092-1100, 2006.

[22] P.M.H. Wong, J.M. Davies, Y.C. Wang, An experimental and numerical study of the behaviour of glass fibre reinforced plastics (GRP) short columns at elevated temperatures, *Composite Structures*, 63, 33-43, 2004.

[23] J.R. Correia, *Composites of polymeric matrix (in portuguese)*, IST Press, Lisbon, 2012.

[24] C.D. Tracy, *Fire endurance of multicellular panels in an FRP building system*, PhD thesis in Civil Engineering, École Polytechnique Fédérale de Lausanne, 2005.

[25] L. C. Bank, *Composites for Construction: Structural Design with FRP Materials*, John Wiley & Sons, 2006.

[26] J.R. Correia, *Pultrusion of advanced composites*, in Advanced Fibre-Reinforced Polymer (FRP) Composites for Structural Applications (Editor: J. Bai), Woodhead Publishing Limited, 2013.

[27] A. Zhou, T. Keller, Joining techniques for fiber reinforced polymer composite bridge deck systems, *Composite Structures*, 69(3), 336-345, 2005.

[28] J.A. Gonilha, J.R. Correia, F.A. Branco, Creep response of GFRP–concrete hybrid structures: Application to a footbridge prototype, *Composites Part B: Engineering*, 53, 193-206, 2013.

[29] M.F. Sá, A.M. Gomes, J.R. Correia, N. Silvestre, Creep behavior of pultruded GFRP elements – Part 1: Literature review and experimental study, *Composite Structures*, 93, 2450-2459, 2011.

[30] M. Garrido, J.R. Correia, F.A. Branco, T. Keller, Creep behaviour of sandwich panels with rigid polyurethane foam core and glass-fibre reinforced polymer faces: Experimental tests and analytical modelling, *Journal of Composite Materials*, 48, 2237-2249, 2013.

[31] J.M. Sousa, J.R. Correia, S. Cabral-Fonseca, Durability of Glass Fibre Reinforced Polymer Pultruded Profiles: Comparison Between QUV Accelerated Exposure and Natural Weathering in a Mediterranean Climate, *Experimental Techniques*, 40(1), 207-219, 2016.

[32] J.M. Sousa, J.R. Correia, S. Cabral-Fonseca, A.C. Diogo, Effects of thermal cycles on the mechanical response of pultruded GFRP profiles used in civil engineering applications, *Composite Structures*, 116, 720-731, 2014.

[33] B. Tang, Fiber reinforced polymer composites application in USA, in *Proceedings of first Korea/USA road workshop*, 1997.

[34] T. Keller, *Use of fibre reinforced polymers in bridge construction*, Structural Engineering Documents, Volume 7, IABSE, Zurich, 2003.

[35] Fiberline Composites, *https://fiberline.com*, (accessed in 2017).

[36] Strongwell Corporation, *http://www.strongwell.com*, (accessed in 2017).

[37] *Fiberline design manual*, Fiberline Composites, 1995.

[38] A. Landesmann, C.A. Seruti, E.M. Batista, Mechanical Properties of Glass Fiber Reinforced Polymers Members for Structural Applications, *Materials Research*, 18(6), 1372-1383, 2015.

[39] PUL-AERO project (TWI and Cranfield University), *http://www.pul-aero.eu*, (accessed in 2016).

[40] F. Nunes, *Structural behaviour of FRP pultruded beams and columns*, PhD thesis in Civil Engineering, IST, Technical University of Lisbon, 2016.

[41] C.E. Bakis, L.C. Bank, V.L. Brown, E. Cosenza, J.F. Davalos, J.J. Lesko, S.H. Rizkalla, T.C. Triantafillou, Fiber-reinforced polymer composites for construction – state of the art review, *Journal of Composites for Construction*, 6(2), 73-87, 2002.

[42] T. Keller, Recent all-composite and hybrid fibre-reinforced polymer bridges and buildings, *Progress in Structural Engineering and Materials*, 6(2), 132-140, 2001.

[43] P. Cassity, D. Richards, J. Gillespie, Compositely acting FRP deck and girder system, *Structural Engineering International*, 12, 71-75, 2002.

[44] J.R. Correia, *Advanced fibre-reinforced polymer (FRP) composites for structural applications: 9. Pultrusion of advanced fibre-reinforced polymer (FRP) composites*, Elsevier Inc. Chapters, 2013.

[45] FRP Engineering, *www.frpengineering.net*, (accessed in 2017).

[46] C. Burgoyne, Advanced Composites in Civil Engineering in Europe, *Structural Engineering International*, 9, 267-273, 1999.

[47] Composites World, *www.compositesworld.com*, (accessed in 2017).

[48] B. Karlsson, J.G. Quintiere, *Enclosure Fire Dynamics*, CRC Press, Taylor & Francis, Boca Raton, 2000.

[49] European Committee for Standardization (CEN), *Eurocode 1: Actions on Structures. Part 1-2: Actions on structures exposed to fire*, 2002.

[50] A. Samanta, M.R.E. Looyeh, S. Jihan, J. McConnachie, *Thermo-mechanical assessment of polymer composites subjected to fire*, The Robert Gordon University, Aberdeen, 2004.

[51] J.C. Hilado, *Flammability Handbook for Plastics*, Technomic Publishing Co., Lancaster, USA, 1990.

[52] T.I. Dimitrienko, Thermomechanical behaviour of composite materials and structures under high temperatures: 1. Materials, *Composites Part A: Applied Science and Manufacturing*, 28(5), 453-461, 1997.

[53] B.Y. Lattimer, J. Ouellette, Properties of composite materials for thermal analysis involving fires, *Composites Part A: Applied Science and Manufacturing*, 37(7), 1068-1081, 2006.

[54] J.B. Henderson, J.A. Wiebelt, M.R. Tant, A model for the thermal response of polymer composite materials with experimental verification, *Journal of Composite Materials*, 19(6), 579-595, 1985.

[55] J.B. Henderson, J.A. Wiebelt, M.R. Tant, G.R. Moore, A method for the determination of the specific heat and heat decomposition of composite materials, *Thermochimica Acta*, 57(2), 161-171, 1982.

[56] M.R. Tant, J.B. Henderson, C.T. Boyer, Measurement and modelling od the termochemical expansion of polymer composites, *Composites*, 1(1), 73-100, 1985.

[57] Y. Bai, T. Vallée, T. Keller, Modeling of thermo-physical properties for FRP composites under elevated and high temperature, *Composites Science and Technology*, 67(15–16), 3098-3109, 2007.

[58] A.P. Mouritz, Z. Mathys, A.G. Gibson, Heat release of polymer composites in fire, *Composites Part A: Applied Science and Manufacturing*, 18(5), 313-325, 2006.

[59] P.M.H. Wong, Y.C. Wang, An experimental study of pultruded glass fibre reinforced plastics channel columns at elevated temperatures, *Composite Structures*, 81(1), 84-95, 2007.

[60] Y. Bai, T. Keller, Pultruded GFRP tubes with liquid-cooling system under combined temperature and compressive loading, *Composite Structures*, 90(2), 115-121, 2009.

[61] Z. Hashin, Failure Criteria for Unidirectional Fiber Composites, *Journal of Applied Mechanics*, 47, 329-334, 1980.

[62] R.M. Jones, *Mechanics of composite materials*, 2nd edition, Tayler & Francis, 1999.

[63] Y. Bai, T. Keller, A kinetic model for predicting stiffness and strength of FRP composites in fire, in *Proceedings of the Fifth International Conference of Composites in Fire*, Newcastle, 2008.

[64] I. Rosa, *Mechanical behaviour of FRP composite materials at elevated temperature (in Portuguese),* MSc dissertation in Civil Engineering, IST, Technical University of Lisbon, 2016.

[65] C.A. Mahieux, K.L. Reifsnider, S.W. Case, Property modeling across transition temperatures in PMC 's : Part I - Tensile Properties, *Applied Composite Materials*, 42, 217-234, 2001.

[66] K. Wang, B. Young, S.T. Smith, Mechanical properties of pultruded carbon fibre-reinforced polymer (CFRP) plates at elevated temperatures, *Engineering Structures*, 33(7), 2154-2161, 2011.

[67] Y. Bai, T. Keller, Modeling of strength degradation for fiber-reinforced polymer composites in fire, *Journal of Composite Materials*, 43(21), 2371-2385, 2009.

[68] ASTM D 5379/D 5379M - 05, *Standard Test Method for Shear Properties of Composite Materials by the V-Notched Beam Method*, West Conshohocken, ASTM, 2010.

[69] E.J. Barbero, *Introduction to Composite Materials Design*, Taylor & Francis, 1998.

[70] J.M. Hodgkinson, *Mechanical Testing of Advanced Fibre Composites*, CRC Press, 2000.

[71] J.R. Correia, F.A. Branco, J.G. Ferreira, The effect of different passive fire protection systems on the fire reaction properties of GFRP pultruded profiles for civil construction, *Composites Part A: Applied Science and Manufacturing*, 41(3), 441-452, 2010.

[72] British Standards, *Fire resistance tests - Part 2: Alternative and additional procedures*, 1999.

[73] European Committee for Standardisation, *Reinforced plastics composites - Specifications for pultruded profiles*, Brussels, 2002.

[74] Sofalca, *www.sofalca.pt*, (accessed in 2012).

[75] Rockwool, *www.rockwool.co.uk*, (accessed in 2012).

[76] Promat, Technical information of Calcium Silicate: Promat PROMATECT (Type H). 2012.

[77] Technical Fibre Products, Technical information of Intumescent Mat: Tecnofire 60853A mineral. 2012.

[78] CIN, Technical information of Intumescent Coating: 7H-960 C-THERM HB. 2009.

[79] I. Rosa, T. Morgado, J. R. Correia, J. Firmo, N. Silvestre, Shear behaviour of FRP composite materials at elevated temperature, 22(3), 2018.

[80] J.P. Firmo, M.R. Arruda, J.R. Correia, Numerical simulation of the fire behaviour of thermally insulated reinforced concrete beams strengthened with EBR-CFRP strips, *Composite Structures*, 126, 360-370, 2015.

[81] J.P. Firmo, J.R. Correia, Fire behaviour of thermally insulated RC beams strengthened with NSM-CFRP strips: Experimental study, *Composites Part B: Engineering*, 76, 112-121, 2015.

[82] E. Nigro, G. Cefarelli, A. Bilotta, G. Manfredi, E. Cosenza, Fire resistance of concrete slabs reinforced with FRP bars. Part I: Experimental investigations on the mechanical behavior, *Composites Part B: Engineering*, 42(6), 1739-1750, 2011.

[83] V.K.R. Kodur, L.A. Bisby, Evaluation of fire endurance of concrete slabs reinforced with fibre-reinforced polymer bars, *Journal of Structural Engineering*, 131, 34-43, 2005.

[84] Portuguese National Laboratory of Civil Engineering (LNEC), *E 364: Fire safety. Fire resistance of construction elements. Test methods and classification criteria (in Portuguese)*, Lisbon, 1990.

[85] Decree-law 220/2008, *Legal Regime for Fire Safety in Buildings (in portuguese)*, 2008.

[86] V.K. Jain, *Fire Safety In Buildings*, Taylor & Francis, 1996.

[87] A. Moreira, *Fire resistance behaviour of GFRP pultruded tubular and I-section columns (in Portuguese)*, MSc dissertation in Civil Engineering, IST, Technical University of Lisbon, 2014.

[88] G.A. Kardomateas, G.J. Simitses, V. Birman, Structural integrity of composite columns subject to fire, *Journal of Composite Materials*, 43(9), 1015-1033, 2009.

[89] A. Orefice, G. Mancusi, L. Feo, F. Fraternali, Cohesive interface behaviour and local shear strains in axially loaded composite annular tubes, *Composite Structures*, 160, 1126-1135, 2017.

[90] T. Vallée, T. Tannert, R. Meena, S. Hehl, Dimensioning method for bolted, adhesively bonded, and hybrid joints involving Fibre-Reinforced-Polymers, *Composites Part B: Engineering*, 46, 179-187, 2013.

[91] F. Stazi, M. Giampaoli, L. Nisi, M. Rossi, P. Munafò, Mechanical performance reduction of GFRP specimens with polyester matrix exposed to continuous condensation, *Composites Part B: Engineering*, 99, 330-339, 2016.

[92] M. Rajaei, D.-Y. Wang, D. Bhattacharyya, Combined effects of ammonium polyphosphate and talc on the fire and mechanical properties of epoxy/glass fabric composites, *Composites Part B: Engineering*, 113, 381-390, 2017.

[93] J. Michels, R. Widmann, C. Czaderski, R. Allahvirdizadeh, M. Motavalli, Glass transition evalutation of commercially available epoxy resins used for civil engineering applications, *Composites Part B: Engineering*, 77, 484-493, 2015.

[94] S.M. Raoof, D.A. Bournas, Bond between TRM versus FRP composites and contrete at high temperatures, *Composites Part B: Engineering*, 127, 150-165, 2017.

[95] K. Dong, K. Hu, Development of bond strength model for CFRP-to-contrete joints at high temperatures, *Composites Part B: Engineering*, 95, 264-271, 2016.

[96] J.P. Firmo, J.R. Correia, L.A. Bisby, Fire behaviour of FRP-strengthened reinforced concrete structural elements: A state-of-the-art review, *Composite Structures*, 80, 198-216, 2015.

[97] E. Nigro, A. Bilotta, G. Cefarelli, G. Manfredi, E. Cosenza, Performance under fire situations of concrete members reinforced with FRP rods: bond models and design nomograms, *Jounal of Composite for Construction*, 16(4), 395-406, 2012.

[98] Y. Bai, T. Keller, *High Temperature Performance of Polymer Composites*, Wiley VCH, 2014.

[99] J.P. Firmo, J.R. Correia, P. França, Fire behaviour of reinforced concrete beams strengthened with CFRP laminates: Protection systems with insulation of the anchorage zones, *Composites Part B: Engineering*, 43(3), 1545-1556, 2012.

[100] C. López, C. Tiago, J.R. Correia, A coupled fluid flow/heat transfer model: application to the analysis of a GFRP tubular cross-section under fire exposure, in *7th Inthernational conference on advanced computational engineering and experimenting*, Madrid, 2013.

[101] inc ANSYS, *ANSYS Fluent Theory Guide*, 2013.

[102] M.F. Modest, *Radiative Heat Transfer*, Series in Mechanical Engineering McGraw-Hill, 1993.

[103] European Committee for Standardization (CEN), *Eurocode 1: Actions on Structures: Part 1.2: Actions on Structures Exposed to Fire*, 2002.

[104] J.M. Mimoso, *Theoretical bases for building applications - technical information for buildings*, LNEC, Lisbon, 1987.

[105] The Engineering Toolbox, *www.engineeringtoolbox.com*, (accessed in 2016).

[106] J.P. Holman, *Heat Transfer*, 10th edition, McGraw-Hill, Inc., 2010.

[107] F. Incropera, D. DeWitt, T. Bergman, A. Lavine, *Fundamentals of Heat and Mass Transfer*, John Wiley & Sons, Ltd, 2006.

[108] K. Avila, D. Moxey, A. Lozar, M. Avila, D. Barkley, B. Hof, The Onset of Turbulence in Pipe Flow, *Science*, 333(6039), 192-196, 2011.

[109] J. Pallares, I. Cuesta, F.X. Grau, Laminar and turbulent Rayleigh–Bénard convection in a perfectly conducting cubical cavity, *International Journal of Heat and Fluid Flow*, 23(3), 346-358, 2002.

[110] A.G. Gibson, P.N.H. Wright, Y.-S. Wu, C.P. Gardiner, The Integrity of Polymer Composites during and after Fire, *Journal of Composite Materials*, 38(15), 1283-1307, 2004.

[111] A.G. Gibson, Y.-S. Wu, J.T. Evans, A.P. Mouritz, Laminate theory analysis of composites under load in fire, *Journal of Composite Materials*, 40(7), 639-658, 2007.

[112] R.M. Sullivan, A Coupled Solution Method for Predicting the Thermalstructural Response of Decomposing, Expanding Polymeric Composites, *Jounal of Composite Materials*, 27(4), 408-434, 1993.

[113] Dassault Systèmes Simulia Corp., *Commercial software ABAQUS Standard*, version 6.13, 2013.

[114] Y. C. Wang, P. M. H. Wong, V. Kodur, An experimental study of the mechanical properties of fibre reinforced polymer (FRP) and steel reinforcing bars at elevated temperatures, *Composite Structures*, 80, 131-140, 2007.

[115] F.T. Wallenberger, J.C. Watson, H. Li, PPG Industries inc, *Glass Fibers*, ASM International, 2001.

[116] W. Sun, *Temperature effects on material properties and structural response of polymer matrix composites*, PhD thesis in Civil Engineering, École Polytechnique Fédérale de Lausanne, 2015.

[117] S. Timoshenko, *Theory of Elasticity*, 2nd edition, McGraw-Hill, 1970.

[118] P.K. Dutta, D. Hui, Creep rupture of a GFRP composite at elevated temperatures, *Computers and Structures*, 76(1), 153-161, 2000.

[119] S.E. Boyd, S.W. Case, J.J. Lesko, Compression creep rupture behavior of a glass/vinyl ester composite subject to isothermal and one-sided heat flux conditions, *Composites Part A: Applied Science and Manufacturing*, 38(6), 1462-1472, 2007.

[120] B. Budiansky, N.A. Fleck, Compressive failure of fiber composites, *Journal of the Mechanics and Physics of Solids*, 41(1), 183-211, 1993.

[121] L. Almeida-Fernandes, N. Silvestre, J.R. Correia, Assessment of fracture thoughness of pultruded GFRP composites, in *8th Inthernational Conference on Thin-Walled Structures*, Lisbon, 2018.